DOCTORAL SCHOOL

UNIVERSITY OF MILANO-BICOCCA

Department of **Environmental and Earth Sciences**

PhD program in **Geological, Chemical and Environmental Sciences**

Cycle **XXXVIII**

Curriculum in **Geological Sciences**

From Thermal Preconditioning To Slope Instability In Alpine Permafrost Rock Slopes

Luca Cifeca Recinella

876304

Supervisor *Prof. Paolo Frattini*

Tutor: *Prof. Giovanni Battista Crosta*

Coordinator: *Prof. Marco Giovanni Malusà*

Academic Year 2026/2027

ABSTRACT

Warming trends in Alpine permafrost are reshaping the stability of high-mountain rock slopes and the long-term performance of the infrastructure built upon them, yet the mechanism linking gradual thermal change to discrete failure remains poorly constrained. This thesis argues that instability and thermal disturbance in permafrost-affected rock masses follow a consistent two-stage logic: decades of thermally driven weakening at ice-filled discontinuities progressively erode the structural strength of a rock mass, or the thermal integrity of the ground hosting an engineered structure, long before the outcome becomes visible. A second, distinct process then converts that latent weakness into an observable outcome, for natural rock slopes, a discrete triggering event; for engineered infrastructure, a persistent, self-sustaining thermal perturbation. Resolving this two-stage logic and demonstrating that it can be captured by physically grounded, minimally calibrated models rather than treated as an unpredictable hazard, is the central objective of the work.

The framework is built and progressively stress-tested across four case studies of increasing physical complexity and decreasing data availability. It is first validated on two instrumented, non-permafrost cliffs in the Italian Alps, the Scaiùn cliff and Monte Colodri, where finite-element thermo-mechanical simulations are projected along the radar line of sight and directly benchmarked against ground-based InSAR displacement fields. This establishes that slope geometry, rather than material properties, exerts the primary control on thermally induced deformation, and provides a validated baseline for the permafrost-specific chapters that follow.

The framework is then applied to the Sas da Lech dolomite pillar in the Dolomites, a warm-permafrost setting with a documented 2018 collapse and a multi-depth borehole record. Here, an extended one-dimensional analytical heat-flow model, incorporating localized fracture advection, latent-heat effects at the zero-curtain, and cold-air trapping, reproduces the non-conductive thermal dynamics of the fractured pillar, while a purpose-built, hardware-independent thermal-compensation algorithm isolates irreversible structural kinematics from thermo-elastic sensor noise. Three-dimensional strength-reduction analyses show that gravitational and structural loading alone cannot explain the 2018 failure, and that decades of climate-driven degradation of ice-filled discontinuities

were the necessary long-term precondition exploited by a discrete, short-term precipitation trigger.

The same preconditioning–trigger logic is then formalised and generalised through the 2025 Cima Falkner rock avalanche, a large-scale event reconstructed from multi-temporal point-cloud, satellite InSAR, and three-dimensional thermal and mechanical modelling. A novel episodic thermo-hydromechanical framework, which explicitly decouples slow conductive preconditioning from discrete hydrological shocks, resolves a structural limitation shared by existing continuous-forcing models, and reproduces the exact timing of the 2025 collapse using strictly uncalibrated, laboratory-constrained parameters, without requiring complete volumetric ice ablation as a prerequisite for failure. Independent three-dimensional strength-reduction analysis corroborates this result: plastic strain localises spontaneously along the exact post-event failure plane without any predefined sliding surface.

Finally, the same monitoring–modelling logic is transferred to an operating cable-car infrastructure at Punta Helbronner, where a shaft embedded in cold bedrock is shown, through multi-year monitoring and validated two- and three-dimensional thermal modelling, to act not as a passive structure but as a persistent, non-seasonal heat source that is still working its way toward thermal equilibrium years after construction. Independent validation against borehole data reveals a systematic, conduction-only modelling bias that converges, in both sign and physical explanation, with an equivalent bias independently identified at Sas da Lech, indicating that conduction-only thermal models of fractured Alpine permafrost bedrock should generally be expected to underestimate, rather than overestimate, the true thermal disturbance.

Across natural and anthropogenically forced settings alike, from a collapsed rock pillar to an actively heated infrastructure shaft, thermal preconditioning emerges as the common, decades-long process governing both catastrophic failure and slow structural disturbance, whether it culminates in a discrete trigger or in a still-evolving perturbation. Taken together, these four case studies and their associated methodological advances provide a physically grounded, transferable and testable framework for anticipating instability and thermal disturbance in permafrost-affected rock slopes and the infrastructure built upon them.

Table of Contents

CHAPTER 1 INTRODUCTION 1
1.1 Motivation and scope 1
1.2 Thesis Outline 5
1.3 Research Questions 8
CHAPTER 2 LITERATURE REVIEW 10
2.1 Mountain Permafrost in the European Alps 10
2.2 Rockfalls and rock-slope instabilities at high elevation 15
2.3 Thermal processes, monitoring and thermo-mechanical modelling of rock slopes 19
2.3.1 Thermal regime of Rock Walls 20
2.3.2 Thermal damage mechanisms 22
2.3.3 Monitoring of Thermally Sensitive Rock Slopes 24
2.3.4 Numerical Modelling Approaches 25
2.4 High-altitude infrastructures on permafrost-affected rock 27
CHAPTER 3 INTEGRATED GBINSAR AND THERMO-MECHANICAL MODELING FOR ROCK SLOPE DISPLACEMENT ANALYSIS ACROSS GEOMETRICAL COMPLEXITIES 31
3.1 Aim 31
3.2 Study areas and geological–climatic setting 32
3.2.1 Scaiùn cliff (Val Masino, Central Alps) 34
3.2.2 Monte Colodri (Sarca Valley, Southern Alps) 35
3.3 GBInSAR monitoring 36
3.3.1 Scaiùn cliff 37
3.3.2 Monte Colodri 38
3.4 Thermo-mechanical numerical modelling 41
3.4.1 Mathematical models 42
3.4.2 Overall modelling workflow 43
3.4.3 Simplified geometry thermo-mechanical models 44
3.4.4 Real-geometry thermo-mechanical models 52
3.4.5 Parametric sensitivity analyses 56
3.5 Integration of thermo-mechanical modelling and GBInSAR data 58
3.5.1 Detrending of GBInSAR time series and isolation of the thermal component 59

3.5.2 Reconstruction of FEM-based LOS displacement maps 60
3.5.3 Data Elaboration and model validation 62
3.6 Discussion 66
3.6.1 Insights from simplified geometries 66
3.6.2 Model sensitivity 69
3.6.3 Applicability to real geometries 69
3.6.4 Limitations of the isotropic material assumption 70
3.6.5 Methodological advancements in data representation 71
3.6.6 Comparison with field measurements 73
3.7 Case Study Conclusion 75
CHAPTER 4 THERMO-MECHANICAL AND KINEMATIC EVOLUTION OF A WARMING PERMAFROST ROCK PILLAR (SAS DA LECH, DOLOMITES) 78
4.1 Aim 78
4.2 Study area 79
4.2.1 Geological and Geomorphological setting 79
4.2.2 Air Temperature and Climate Context 81
4.2.3 Pillar geometry and discontinuities analysis 83
4.3 Methodology and Theoretical Background 85
4.3.1 Monitoring layout 85
4.3.2 Geomechanical Laboratory Characterization 87
4.3.3 Theoretical background: 1D heat transfer and permafrost thermal regime 89
4.3.4 Phase changes and zero-curtain effect 90
4.3.5 Modeling localized thermo-hydro-mechanical anomalies 91
4.3.6 Thermo-mechanical coupling and kinematics of borehole snaking 92
4.3.7 Thermal compensation algorithm of rock displacements 94
4.3.8 3D transient thermal modelling setup 96
4.3.9 3D mechanical stability analysis setup 97
4.4 Results 99
4.4.1 Subsurface Thermal Regime 99
4.4.2 Conductive baseline and deep anomalies 101
4.4.3 Deep Kinematics – Borehole Deformation 105
4.4.4 Isolation of the Geotechnical residual 107
4.4.5 Surface Fracture Kinematics and thermal decoupling 108
4.4.6 3D FEM thermal modeling: present-day validation and climate projections 110

4.4.7 3D mechanical stability and failure kinematics: pre- and post-2018 collapse 113
4.5 Discussion 118
4.5.1 Thermo-mechanical Preconditioning vs. Hydro-meteorological Triggering 118
4.5.2 Localized Advective Heat Transport and Thermo-mechanical Feedback119
4.5.3 Permafrost Rock Mechanics at the Melting Point 120
4.5.4 The Analytical Thermal-Compensation Approach 121
4.6 Case Study Conclusion 122
CHAPTER 5 THERMAL PRECONDITIONING UNLOCKS EPISODIC HYDROLOGICAL TRIGGERS IN PERMAFROST ROCKWALL COLLAPSE 125
5.1 Aims 125
5.2 Study Area 126
5.2.1 Regional Instability context 126
5.2.2 Geological and Geomorphological Setting 128
5.2.3 Regional Climatic Setting and Hydrological Anomaly 130
5.3 Kinematic Evolution and Failure Reconstruction 132
5.3.1 Multi-temporal Aerial Imagery and Fracture Aperture Evolution 132
5.3.2 EGMS Satellite InSAR Kinematics 133
5.3.3 Point Cloud Change Detection and Volumetric Budget 134
5.4 Methodology and Theoretical Background 137
5.4.1 The Calibration Trap: Structural Limitations of Existing Models 137
5.4.2 Episodic Thermo-hydromechanical Framework 138
5.4.3 3D Thermal Modelling Setup 143
5.4.4 3D Mechanical Stability Analysis Setup 147
5.5 Results 148
5.5.1 Resolving the Calibration Trap 148
5.5.2 Isolating the Trigger: The 0-mm Precipitation Control 152
5.5.3 3D Thermal Regime 153
5.5.4 3D Mechanical Stability and Emergent Failure Plane 159
5.6 Discussion 162
5.6.1 Mechanics of Thermal Preconditioning and Hydrological Triggering . 162
5.6.2 From Cold-trapping to Advective Bypass 164
5.6.3 The Seasonal Heartbeat and Precursory Kinematics 165
5.6.4 FEM vs. 1D: Complementary Roles and the Decoupling of Forcings .. 166

5.6.5 Regional Validation of the Thermal Regime: Independent Air- and Ground-Temperature Evidence 167
5.6.6 Regional Implications in a Warming Cryosphere 170
5.6.7 Model Limitations and position in literature 171
5.7 Case study conclusion 175

CHAPTER 6 A PERSISTENT ANTHROPOGENIC HEAT SOURCE IN COLD BEDROCKS: THE PUNTA HELBRONNER CABLE-CAR SHAFT 178
6.1 Aim and case study 178
6.2 Study Area 179
6.2.1 Geological and geomorphological setting 179
6.2.2 Air Temperature and climate context 181
6.2.3 Infrastructure: Skyway cable car 183
6.3 Methodology and Theoretical Background 185
6.3.1 Regional Permafrost probability map 185
6.3.2 Monitoring Layout 187
6.3.3 2D Thermal FEM setup 189
6.3.4 3D Thermal FEM setup 190
6.4 Results 194
6.4.1 Near-surface and borehole rock temperature 194
6.4.2 Shaft internal temperature 199
6.4.3 Shaft radial temperature 201
6.4.4 2D thermal analysis results 202
6.4.5 3D thermal analysis results 206
6.5 Discussion 211
6.5.1 A coupled Natural-Anthropogenic thermal regime 211
6.5.2 Model validation and the direction of the residual bias 212
6.5.3 Model limitations and position in literature 213
6.5.4 Implication for High-Altitude Infrastructure on Permafrost 215
6.6 Case study Conclusion 216

CHAPTER 7 CONCLUSION 218
7.1 Summary of the thesis 218
7.2 Answers to the Research Questions 219
7.2.1 RQ1 - Geometric controls on thermo-mechanical response 219
7.2.2 RQ2 - Modelling conductive and advective heat transport in fractured rock 220

7.2.3 RQ3 - Preconditioning versus triggering in permafrost rockwall collapse221
7.2.4 RQ4 - Simulating instability under progressive permafrost degradation222
7.2.5 RQ5 - Permafrost degradation and high-altitude infrastructure 223
7.2.6 Cross-chapter synthesis: a recurring physical pattern 223
7.3 Original contributions and methodological advances 224
7.4 Limitations 225
7.5 Practical and management implications 227
7.6 Future perspectives and recommendations 228
7.7 Closing remarks 229

List of Figures

Figure 1 APIM (Alpine Permafrost Index Map (Boeckli et al., 2012b)) for the entire European Alps chain with three zooms on the study area discussed in this thesis. 4

Figure 2 Articulation of methods and data across the four case studies of the thesis. Rows group the three method families; columns correspond to the four case studies, ordered by increasing physical complexity. Differences in the methods deployed between sites reflect differences in data availability. 7

Figure 3 Schematic representation of permafrost configuration. In the purple box, the active layer displays the portion affected by seasonal freezing and thawing. Within the designated blue box, the permafrost body remains permanently frozen throughout the changing seasons. The red box delineates the area of elevated temperatures, which exceed 0°C, attributable to geothermal heat flow. 11

Figure 4 Rockfalls distribution according to climate anomaly e considering the a) season occurrence, b) elevation, c) volume and d) permafrost (Paranunzio et al., 2016) ST: Short-Term T anomaly; Rapid warming; superficial thaw/melt. WT: Widespread T anomaly; Persistent warming across multiple time scales. LT: Long-Term T anomaly; Sustained warming affecting deeper ground/permafrost. RT: Rainfall (Precipitation) anomaly. Influence of water pressure/infiltration (with/without T anomaly).NO: No anomaly; Trigger likely non-climatic or not captured by the variables. 16

Figure 5 Schematic figure of resistance behaviour in function of temperature (Adapted from (Bommer et al., 2010)). The plot show how in correspondence of warm permafrost the resistance decrease significantly. 17

Figure 6 Photo of cliff fall in Dolomite a) Cima Lastei; b) Sassolungo; c) Carè Alto; d) Gran Vernel. 19

Figure 7 Results of temperature model of Matterhorn (4478m a.s.l.) with two future scenarios: 100years (dashed line) and 200years (dot line). In this work the author assumes a warming scenario of +3C/100years (Noetzli & Gruber, 2009). 22

Figure 8 a) Numerical model considering an isotropic material (Wegmann & Keusen, 1998) a1) pre-building a2) with elevator shaft and a3) with cooling system. b) Observatory and monitoring system, in the plot it's possible to observe data before and after the construction with an inverse relationship between temperature and

displacements, with irreversible strain caused by excavation of the shaft and ice melting inside the fracture..... 29

Figure 9: Location and geological maps of the two study areas in the Italian Alps: (a) Scaiùn cliff, Val Masino-Cataeggio (SO); (b) Monte Colodri, Arco di Trento- (TN). .. 33

Figure 10 :(a) View of the Scaiùn cliff and monitoring area; (b) Displacement along LOS for POIs #30, #32, #35. The white point indicates the approximate location of the displayed points of observation. 38

Figure 11 Monte Colodri from frontal view showing:(a) the identified main moving sectors; (b) LOS displacement map for long-term measurements (269 day, October 2023 - July 2024). 40

Figure 12 Simplified pillar shape with a surrounding area (model box) and corresponding mesh used in the analyses: (a) Lateral view; (b) Frontal view. The different colors represent the 288 portions generated from horizontal, vertical, and oblique planes. The minimum mesh size is 1 m and the maximum one is 15 m. Numbers within circles refer to the surface identification. Surfaces (1) and (2) represent the faces of the domain where displacement constraints (red symbol) and no-flux conditions were applied. At surface (3), (4), (5), (6), and (7) the temperature input signals were applied. 46

Figure 13 Numerical results for simulation with the homogeneous external temperature: (a-e) Pillar geometry cross section showing the temperature distribution at different time instants during the year. Figures (a, c) represent the minimum and maximum air temperatures, respectively; other figures (b, d, e) are intermediate values. In the plot the input sinusoidal air temperature (dashed line) and the temperature for 11 different points along the central vertical of the pillar, are represented (continuous lines). 47

Figure 14 Numerical results for simulation in which the homogeneous external temperature is imposed displacement at different time instants (corresponding to those in Figure 13). The graph shows the total vertical displacement for points P1 to P11 together with the imposed external air temperature. 48

Figure 15 Different air temperature time series as a function of face exposure(a) applied to domain. Total displacement results for: (d) Frontal view during summer season; (e) Lateral view during summer season; (d) Frontal view during winter season; (g) Lateral view during winter season. The graphs show: (b) Temperature distribution for the same points (as in Figure 13); and (c) corresponding displacement. 49

Figure 16 Geometry and mesh of the simplified convex rock wall shape used in the analysis: (a) Lateral view; (b) Frontal view. The mesh size of the convex shape is 2 m, and for the rest of the domain, it varies up to 20 m. Numbers indicate the faces where boundary conditions were applied. 50

Figure 17 Time series of displacement during one year of simulation along different Z-position in the central part of geometry. 51

Figure 18 (a) Control points along the convex surface at a fixed Z-elevation; (b) Time series of air temperature adopted for Scaiun case for the year 2023; (c) Total displacement time series for each control point; (d) V/H (vertical-to-horizontal displacements) ratio. 52

Figure 19 Numerical simulation results with non-uniform thermal input: (a) Scaiun mesh used for analyses and section (black line) (b) and (c) temperature and displacement distributions in the section, respectively, at winter season. 54

Figure 20 Monte Colodri numerical results at winter season with aspect effect (a) and (b) mesh in frontal and lateral view, respectively with a vertical section (black line); (c) temperature distribution along the section and (d) displacement distribution along the section. 55

Figure 21 Results of parametric analyses in terms of displacement and vertical stress for each simulation listed in Table 2focusing on a single node and at changing: (a) Young's Modulus (E); (b) Thermal Conductivity(α); (c) Specific Heat (Cv); (d) Thermal Expansion Coefficient variation (CET). The values shown in these graphs are extracted in the same position of POI 30 (Figure 10). 57

Figure 22 Comparison of displacement time series along the LOS for the Scaiùn cliff: in-situ measurements (solid line, with suffix M) versus calculated displacements (dashed line, with suffix C). The grey line represents the air temperature. 62

Figure 23 Scaiùn map of displacement along LOS for the month of July, presented from different viewpoints: (a) left side; (b) frontal; (c) right side. Grey shape indicate the position of radar. 64

Figure 24 Monte Colodri map of LOS displacement calculated from FEM simulation at different months: (a) January; (b) March; (c) July; (d) November. 65

Figure 25 Sketches and plots of the expected movements for the three main geometries a_1) pillar element with bending and torsional movement, b_1) stocky prism movement, c_1) convex (half-truncated cone) scheme movement; a_2) and a_3) displacement and

temperature along the vertical (A-A') and horizontal (B-B') directions, respectively, for the pillar case (dashed lines for uniform external temperature, continuous lines for non-uniform external temperature), b_2) and b_3) displacement and temperature along the vertical (A-A') and horizontal (B-B') direction, respectively, for the case of stocky cubic scheme; c_2) and c_3) displacement and temperature along the vertical (A-A') and horizontal (B-B') directions, respectively for the case of convex scheme. 68

Figure 26 Comparative example of Monte Colodri LOS displacement maps generated with different cell sizes: from (a) and (b) larger cells (e.g., 1.4°×1.4°); to (c) and (d) smaller cells (e.g., 0.45°×0.8°). 73

Figure 27 Comparison between measured LOS displacement maps from GBInSAR (left-hand side) and calculated maps from FEM analysis (right-hand side) for (a) (a') the Scaiùn cliff and (b) (b') the Monte Colodri. The computed maps were prepared using a resolution of 0.45°×0.45° and 1.2° × 1.2°, respectively, projecting FEM displacements in the LOS direction. 74

Figure 28 Lateral view (from the west) of the Sas da Lech pillar a) pre-event and b) post event of 2018 that involves up to 3500m^3 of rock represented by white dashed line on the pre-event photo. c) frontal view of the pillar after the failure event and showing the main central fracture cutting in half the pillar. 80

Figure 29 Geological Map of the Sella Group where the location of the Sas da Lech pillar and of the 2018 failure is marked inside a black circle (modified after 1:50.000 geological map n. 028 La Marmolada). 81

Figure 30 a) Air temperature time series registered at Cima Pisciadù (3000m a.s.l.) meteorological station; b) altitude-adjusted air temperature time series compared to rock surface temperatures registered at the base of the Sas da Lech pillar (2700m a.s.l.) at 0.23m depth. 82

Figure 31 a-b) E-W component of normal vectors calculated on LiDAR point cloud observed from north-east (a) and northwest (b); c) Stereoplot with 138 poles of main joints measured on site and by Cloude Compare, and mean planes of the six main joint sets. S0 corresponds to the bedding. 84

Figure 32 a) BHTV for borehole DMS01 in which a melted ice during the drilling started at 11.75m depth; b) BHTV for borehole DMS02 in which a large fracture of about 0.6m at 13/14m depth is observed. A third horizontal boreholes was drilled between the two DMS without interesting evidence during the BHTV investigation..... 85

Figure 33 Monitoring approach adopted at the Sas da Lech pillar: a) ERT acquisition, b) 3 DMS extensometers (Ext21,22,23) for the superficial opening fractures, c) Aerial photogrammetry and LiDAR acquisition, d) 2 DMS multiparametric column (DMS1 and DMS2), e) Geoprecision temperature chain, and f) terrestrial laser scanner acquisition. The DMS columns and temperature chain are located inside three 21m long boreholes (2 horizontal and 1 inclined of 35°, long line red and blue). 86

Figure 34 Annual air temperature time series for RCP4.5 and RCP8.5 climate scenarios up to 2100 used as input boundary conditions in thermal analysis. The 2004–2024-time interval includes the measurements acquired at the Pisciadù station whereas the future time series are built on global scenarios. 97

Figure 35 a) Boxplot showing the variability of temperature at each sensor along the Geoprecision thermal chain; b) Geoprecision temperature heat map with profiles at different days (d1) along the column and time series at different depths (d2). 101

Figure 36 Comparison of measured thermal regimes against a purely conductive 1D heat transfer model for the DMS01 (a–c), DMS02 (d–f), and Geoprecision (g–i) boreholes. The left column (a, d, g) displays the thermal trumpet curves, plotting the minimum and maximum measured temperatures alongside the theoretical 1D conductive envelopes. The center column (b, e, h) shows the depth-time heatmaps of the in-situ measured temperatures. The right column (c, f, i) presents the corresponding theoretical heatmaps generated by the 1D diffusion model, highlighting the deviations between purely conductive predictions and the actual advection-influenced field data. 102

Figure 37 Depth-dependent thermal wave propagation and apparent velocity analysis for the DMS01 (a–d), DMS02 (e–h), and Geoprecision (i–l) boreholes. Panels (a, e, i) show the global sinusoidal fitting of the temperature time series at various depths. The phase lag (b, f, j) and amplitude attenuation (c, g, k) of the measured data (solid blue lines) are compared against theoretical limits calculated for low and high thermal diffusivity bounds (0.5 and 1.0 × 10^{-6} m^2/s, represented by red and blue dashed lines, respectively). Green dots in the phase lag panels indicate the R^2 value of the sinusoidal fit. Panels (d, h, l) display the computed apparent vertical thermal velocity from the measured data (solid black lines) compared to the constant theoretical velocities associated with the bounding diffusivity values. 103

Figure 38 Displacement profile along the columns DMS01 (a) and DMS02 (b) at different dates. The BHTV images are shown at the top of each plot, to show the correspondence of displacement with the main fractures. 105

Figure 39 Time series of extensometer located at 2 m, 13 m, and 17 m from the surface along the DMS02. Deformation is expressed as compression (negative) and extension (positive) and plotted together with rock temperature measured in the same module. 106

Figure 40 Application of the semi-empirical thermal-kinematic model to the DMS2 dataset to separate cyclic thermal snaking from underlying geotechnical displacement. a) Comparison between measured borehole temperatures (solid lines) and the calibrated theoretical thermal diffusion model (dashed lines) over depth. Colors indicate different months of the year. b) Measured cumulative deformation projected along the specified azimuth, containing both the seasonal thermal snaking and the long-term geotechnical drift. c) Time-series comparison at specific depths (M3, M7, M18) for extensometric deformation: local displacements (solid lines) against pure thermal-model predictions. d) Geotechnical residual displacement over time, obtained by subtracting the theoretical thermal model from the real projected deformation. e) Pure kinematic response generated by the semi-empirical model, predicting the seasonal expansion and contraction (snaking) based on theoretical temperature variations. f) Kinematic prediction using the actual measured temperature profiles as input for the theoretical snaking model, providing a baseline for expected thermal strain. 108

Figure 41 Surface extensometer records and thermal decoupling for Ext21 (a, b), Ext22 (c, d) and Ext23 (e, f), August 2024 – March 2026. Left column: cumulative displacement showing the raw signal, the thermally corrected net signal, the fitted long-term linear trend with its annual rate, and the detrended residual. Right column: high-pass filtered air temperature against raw displacement increment; the slope of the linear fit gives the equivalent coefficient of thermal expansion α_eq of each rock–sensor system. Applying the analytical decoupling procedure described in section 4.3.7 successfully filtered this thermal noise. The empirical equivalent coefficients of thermal expansion ($\boldsymbol{\alpha eq}$) back calculated for the instrumented fractures were $\mathbf{7.7 \times 10 - 6}$°C^{-1} for Ext21, $\mathbf{2.3 \times 10 - 6}$°C^{-1} for Ext22, and $\mathbf{1.85 \times 10 - 5}$°C^{-1} for Ext23. The significant deviation of these site-specific values from the nominal theoretical expansion coefficient of steel ($\mathbf{1.20 \times 10 - 5}$ °C^{-1}) confirms that field measurements must account for the

bulk response of the coupled rock-sensor system rather than relying on material-specific theoretical values. 109

Figure 42 Validation of the thermal model against Geoprecision borehole temperatures at four depths: (a) 0.2 m, (b) 1.5 m, (c) 4.5 m and (d) 15 m. red lines show measured temperatures, while simulations are reported using two alternative surface boundary conditions: daily air temperature forcing (T_{air}; blue) and near-surface rock temperature forcing derived from the shallowest Geoprecision sensor (T_{rock}; green). e) Scatter plot of measured vs calculated temperatures at different depths..... 111

Figure 43 a) Temperature distribution from the 3D FEM simulation along an EW cross section of the pillar in January 2025; b-c) Temperature distribution for RCP4.5 and RCP8.5 climate scenarios at 2100 and d) Scenario-based evolution of simulated temperatures at 0.2, 1.5, 4.5 and 15 m depth under RCP4.5 and RCP8.5. The marked black line in a, b and c represent the 0°C isotherm, and the thick one the 1°C isotherm. 113

Figure 44 Pre-collapse SRM result (M6, FoS = 3.13): a) total displacement contours at incipient instability and illustrating a lateral detachment mechanism mainly controlled by the back discontinuity, b) equivalent plastic strain in the rock mass at incipient instability, showing localization adjacent to the back structural domain and c) back-interface relative displacement (normal component), highlighting deformation concentration along the controlling discontinuity. 115

Figure 45 Post-collapse weakened SRM result (M7, FoS = 1.58): a) total displacement contours at incipient instability (left: frontal view from North; right: lateral view from West) indicating progressive mobilization of the standing pillar and a valley-facing (frontal) detachment mechanism; b) equivalent plastic strain in the rock mass at incipient instability, showing a broader inelastic zone compared to the pre-collapse case and c) frontal-interface relative displacement along the central fracture (normal component), showing a concentrated deformation band along the valley-facing discontinuity associated with the predicted forward failure mode. 116

Figure 46 Thermo-mechanical displacement response derived from numerical modelling. Left panel: temporal evolution of XY displacement at different depths obtained from the 3D thermo-elasto-plastic model over the simulation period, showing a marked seasonal cyclicity and strong attenuation of amplitude with depth. Right panel: depth profiles of XY displacement for representative warm (red) and cold (blue) seasons

from the 3D model, compared with the corresponding 1D FDM results (upper curves), which include the effect of column snaking and extensometric modules. The 3D results highlight the thermo-induced displacement component and its localization within the shallow domain, whereas the 1D FDM outputs provide a bulk estimate of displacement magnitude..... 117

Figure 47 Cumulative precipitation from May to September with the important event the week before the 2018 collapse in which 120mm of rain fell in the Sas da Lech area. 119

Figure 48 Validation of the analytical thermal-compensation method using an independent monitoring dataset for a thermally forced exfoliation monitoring system (after Collins et al 2016) (a, c, e) corrected by dummy sensor data (cyan) and corrected by the filtering approach (light blue). Best linear fitting of Collins corrected data (black line) and of the analytical compensated series (blue); (b, d, f): High-frequency displacement–temperature relationship for the same dataset, illustrating the hysteretic cloud following phase alignment and enabling derivation of an equivalent thermal expansion coefficient (α_{eq})..... 122

Figure 49 Large volume rockfalls in the Dolomites are migrating to higher elevations in response to permafrost degradation. (a) Regional distribution and volume of rockfalls in Trentino–Alto Adige and Veneto (symbol size proportional to event volume). The white square indicates the Cima Falkner study site. (b) Site location overlaid on the Alpine Permafrost Index Map. The 2025 collapse (white dot) occurred within the continuous permafrost zone. (c) Spatio-temporal distribution of rockfall events. Event frequency increases post-2000, with a distinct upward migration of large-volume events (>10^5 m^3) above 3,000 m a.s.l. during the last decade. 128

Figure 50 Geological Map of the Cima Falkner (red circle) area (Modified from the CARG Geological MAP 059 Tione di Trento Castellarin, Dal Piaz, et al., 2005)..... 130

Figure 51 pre-collapse kinematic acceleration and surviving basal ice confirm failure occurred prior to complete volumetric ablation. (a′, a″) pre-event aerial imagery (September 2021 and June 2025) documenting progressive pre-failure creep, with rear fracture apertures reaching 2.0–2.5 m prior to the main collapse. (a‴) High-resolution UAV orthophoto of the highly dilated crest following the July 27, 2025, precursory event. (b, c) post-collapse field photographs (July and August) highlighting massive surviving ice candles (blue arrows) preserved within deep tension fractures and exposed basal

scarps. (d) European Ground Motion Service (EGMS) displacement time series (2019–2023) for seven Persistent Scatterers (PS) on the Cima Falkner peak block (descending orbit; inset shows PS locations). Continuous lines represent Lowess-smoothed datasets, revealing a distinct kinematic acceleration initiating in December 2020 (dashed vertical line). 133

Figure 52 Point cloud analysis. a) Stereoplot of main joint sets; b) and c) 2.5D Volume difference computed from the pre- and post-failure DEMs results and showing the volume involved during the main collapse event of August 2025. 135

Figure 53 DEM cross-section comparison. Red lines: 4 August 2025 (post-main collapse); green: 27 July 2025 (post-first collapse); blue: 2022 baseline; grey: 2014 baseline. Lower panel: deposit extent and thickness from DoDs (LiDAR 2025 vs. 2022). Red arrows indicate main displacement directions from the source zone. 136

Figure 54 Short term headscarp evolution. (a) M3C2 distance between August 2025 and January 2026 point clouds; (b-c) Detailed view of the 700 m^3 detached block..... 137

Figure 55 Catastrophic failure is driven by the decoupling of long-term thermal preconditioning and transient hydromechanical shocks. Left: Schematic of the structural block geometry. Progressive secular warming drives conductive heat into the rock mass, exponentially reducing the shear strength of the deep ice candle. As the rock-ice interface approaches 0°C, extreme precipitation bypasses the remaining ice anchor via marginal flow, generating transient hydrostatic overpressures. Right: Three-phase stability evolution (1940–2025). Phase 1 (Cold-trapping): Infiltrating water refreezes, growing the ice candle and maximizing the Factor of Safety (FoS). Phase 2 (Plateau & slow decay): Long-term conductive ablation degrades baseline ice cohesion. Phase 3 (Seasonal heartbeat): Episodic rainstorms generate acute hydro-mechanical shocks (transient FoS drops). Subsequent drainage and refreezing allow episodic effective stress recovery, maintaining marginal stability through 2024 and into the extreme wet conditions of 2025. 139

Figure 56 a) Aspect Map from ArcGIS Pro; b) Solar radiation calculated from DEM, Slope and Aspect and c) Solar radiation distribution during every month for each aspect position..... 145

Figure 57 Episodic hydromechanical forcing resolves the premature failure paradox while preserving deep basal ice. (a–d) Comparison of continuous (a, c) and episodic (b, d) atmospheric forcing models for daily air temperature and precipitation. (e) Spatio-

temporal thermal evolution map (1940–2040). The overarching top ice depth trajectory is virtually identical under continuous (light blue line) and episodic (dark blue line) forcing, governed predominantly by latent heat. (f, g) Decadal depth profiles of rock temperature (f) and the corresponding temperature-dependent ice shear strength (g). In (f), continuous lines represent the hottest day of the respective year, while dotted lines represent August 1st. (h–m) Long-term evolution of ice depth, fracture opening (red lines; h, i), and Factor of Safety (FoS; l, m). The grey vertical band highlights the critical failure divergence: continuous forcing (l) imposes an artificial downward trend, driving the FoS below unity (dashed line) prematurely. Conversely, the episodic framework (m) captures episodic poro-elastic recovery, delaying the definitive FoS drop below unity until the exact timing of the 2025 collapse. 150

Figure 58 0-mm precipitation control simulation isolates thermal preconditioning and confirms the necessity of hydromechanical triggers. (a, b) Evolution of ice depth, fracture opening (a), and Factor of Safety (FoS) (b) under continuous thermal forcing with zero precipitation. (c, d) Corresponding outputs under episodic thermal forcing with zero precipitation. The grey vertical band indicates the timing of the August 2025 collapse. In the complete absence of infiltration and subsequent hydrostatic shocks, thermal degradation alone causes a progressive, decadal decline in baseline stability. However, the FoS consistently remains above unity (>1.0) across the entire simulated period in both modelling approaches. This control run mechanically validates that while secular warming acts as a critical preconditioning factor by degrading ice shear strength, extreme transient hydrostatic forcing is strictly required to induce the final catastrophic failure. 152

Figure 59 Cross-sections of the FEFLOW conductive-plus-latent-heat (piFreeze) temperature field: (a) North–South and (b) West–East vertical sections at the date of collapse (1 August 2025); colors represent temperature distribution (°C), with the white contour marking sliding surface. c) Location of the fifteen systematically distributed monitoring points (P1–P15) across the inferred rupture surface, colored by long-term temperature trend (°C yr^{-1}); the gradient from warming to cooling values across the surface reflects variable aspect and exposure. d) Modelled temperature evolution at the fifteen points over the simulated record; most locations remain within a narrow sub-zero band, while point P4 shows the largest seasonal amplitude, indicating the greatest sensitivity to atmospheric forcing. 154

Figure 60 Vertical temperature-depth profiles at the location of maximum ice thickness along the rupture surface, showing monthly profiles from August 2024 to July 2025 (color gradient, blue to red) and the profile at the time of collapse (August 2025, dashed line). The active layer thickness (ALT), defined as the depth at which the envelope of monthly profiles converges to 0 °C, is 9.8 m (dash-dot line). 155

Figure 61 FEFLOW conductive-plus-latent-heat (piFreeze) temperature field mapped on the post-collapse point cloud, showing a cold rupture surface (blue tones) contrasting with the surrounding, sun-exposed rockmass surface (red tones, computed considering solar radiation) at the date of the collapse event. 156

Figure 62 Internal thermal response of the slope across three 3D FEM modelling scenarios. Left column (a, a1, a2, a3): conduction only (Scenario A). Centre column (b, b1, b2, b3): conduction plus fluid convection/advection in deep fractures (Scenario B). Right column (c, c1, c2, c3): conduction plus convection/advection in mid-depth fractures (Scenario C). Top row (a–c): winter temperature cross-sections. Second row (a1–c1): summer temperature cross-sections (see nodal thermal temperature color scale). Third row (a2–c2): temperature time series (January 2022 – August 2025) at ten monitored points distributed along the back-fracture sliding surface (locations indicated in panel a). Bottom row (a3–c3): transient temperature-depth profiles spanning from January 2024 to the failure date (August 1, 2025). Note how the depth profiles in the convective scenarios (b3, c3) demonstrate significant thermal anomalies propagating deep into the rock mass, actively driving basal temperatures into the critical transitional regime (–5°C to 0°C) compared to the heavily damped, purely conductive baseline (a3). 158

Figure 63 FEM-SRM results for the four geomechanical scenarios. Left column: total displacement magnitude (m); right column: equivalent plastic strain for Cases 1–3 and interface normal relative displacement for Case 4. Case 1 (mixed elasto-plastic, active sliding surface; FoS = 2.24): displacements localized in the summit block, plastic strain confined to the imposed sliding surface. Case 2 (fully plastic, active sliding surface; FoS = 2.06): broader displacement field with distributed yielding geometrically consistent with the observed failure plane. Case 3 (fully plastic, no sliding surface; FoS = 2.17–2.21): plastic strain localizes spontaneously along the same band as Cases 1–2, confirming that the failure plane is an emergent structural feature independent of any predefined kinematic constraint. Case 4 (elastic rock mass, plastic interfaces only; FoS = 4.50): displacements reduced by an order of magnitude with no continuous failure band,

demonstrating that bulk yielding is essential to drive instability; interface slip alone is insufficient. 160

Figure 64 Mean annual air temperature (MAAT) of four confirmed-permafrost Alpine boreholes (Zugspitze, Stelvio, Piz Pisciadù, Piz Boè) plotted against elevation, together with the two Brenta Dolomites stations (Grostè massif) used for extrapolation to the Cima Falkner failure zone. The solid and dotted red lines show the Alimonta MAAT projected upward using the locally measured lapse-rate range (0.43–0.53 °C per 100 m); the shaded blue band marks the marginal/warm-permafrost window (MAAT between −2 and 0 °C). The Cima Falkner failure zone (2,850–2,999 m) falls within the MAAT envelope of all four boreholes, at the warm end alongside the lithologically identical Piz Boè record. 168

Figure 65 View from Est of Punta Helbronner with a cable car arrive at 3488m a.s.l. 178

Figure 66 Geological Map of Monte Bianco area in which Punta Helbronner is located. 180

Figure 67 Number of days per year with sub-zero daily air temperature at Punta Helbronner (2008–2023), colour-graded relative to the 15-year reference mean (273 days/year). 181

Figure 68 a) Mean seasonal cycle of daily air temperature at Punta Helbronner (2008–2023), showing the monthly mean, the minimum–maximum range and ±1 standard deviation; b) Annual mean air temperature over three consecutive five-year periods (2008–2012, 2013–2017, 2018–2022), with individual annual values shown in the background and period means highlighted. 183

Figure 69 Section of concrete shaft with elevator and visitor gallery (Dimensione Ingenierie s.r.l., 2009). 185

Figure 70 Raster maps of MAAT, PISR and MARST used to calculate the probability of permafrost occurrence map, according to Magnin et al., 2019) with a zoom on the Mont Blanc Massif, where Punta Helbronner is located. 187

Figure 71 Orthophoto of the Punta Helbronner site showing the location of the monitoring boreholes: shallow ARPA boreholes (yellow triangles), deep ARPA boreholes (blue circles), and deep DMS-instrumented points (red triangles), the shaft itself (center) and the external validation borehole (~37.8 m to the SE). 188

Figure 72 2D mesh represents a section of concrete shaft. The red line indicates the line in which results are extracted. 190

Figure 73 a) Eight-class aspect map (N, NE, E, SE, S, SW, W, NW) derived from the site's high-resolution DEM, used to construct the radiative boundary condition of the 3D FEFLOW model; b) Corresponding potential incoming solar radiation (Wh/m²) derived from the same DEM. 192

Figure 74 Ground surface temperature (GST, left panels, sensors at 0.10, 0.30 and 0.55 m) and borehole temperature (right panels, thermistor chains to maximum depths of 11.7 m East, 6.8 m West and 9.6 m South) at a-b) East, c-d) West and e-f) South aspects. 196

Figure 75 Vertical temperature profile at the external DMS borehole (0–70 m depth, ~37.8 m from the shaft), colored by acquisition date from 2 December 2025 (dark blue/purple) to 22 June 2026 (red). 199

Figure 76 Maximum, minimum, mean and mode of the air temperature recorded inside the shaft by each module of the vertical multiparametric column (2.5 m spacing), over the full monitoring period, from the shaft base (Module 0) to the shaft head near the surface infrastructure (Module 24). 200

Figure 77 Time series of temperature around the shaft registered at different vertical depth and at different distance from shaft in two different orientation (SE -SW) in which a) 0.1m b) 0.6m and c) 1.1m distance from shaft. 202

Figure 78 Results from 2D steady analysis in terms of temperature in function of distance from shaft for all case. 204

Figure 79 Temperature evolution in the first 24h after concrete hydration exothermic reaction. 205

Figure 80 Extraction geometry for the 3D FEFLOW model results. a) Plan view of the model domain (~220 × 220 m), showing the shaft, the eight compass directions used for extraction, the 50 m reference point (dashed circle) and the position of the external monitoring borehole (70 m); b) detail of the extraction grid around the shaft, showing the eight directions at six fixed distances from the shaft wall (0.5, 1, 2, 5, 10 and 15 m). 206

Figure 81 Modelled temperature field in vertical cross-section through the shaft: a) North–South section; b) West–East section. Contour lines mark isotherms; note the sharply bounded warm column corresponding to the shaft, embedded in colder, permafrost-consistent rock, and the aspect-related warming of the ground surface on the more sun-exposed side of each section. 207

Figure 82 Horizontal temperature profiles as a function of distance from the shaft wall (0.5, 1, 2, 5, 10 and 15 m), for the eight compass directions, at three characteristic depths: shaft top, mid-depth and shaft base. 207

Figure 83 Vertical temperature profiles from the shaft top to its base, at six fixed distances from the shaft wall (0.5, 1, 2, 5,10 and 15 m), for each of the eight compass directions (N, NE, E, SE, S, SW, W, NW). 208

Figure 84 Simulated temperature time series over the fifteen-year period during which the shaft was thermally active, at 1 m, 5 m and 10 m from the shaft wall (rows), at shaft top, mid-depth and shaft base (columns), for the eight compass directions, compared against the 50 m reference point (dashed line). 210

List of Tables

Table 1 Parameters of material used in numerical analysis. 45

Table 2 List of performed parametric analyses and values adopted for the parameters together with the refence ones (Set 02). In bold the values changed from the initial ones. 56

Table 3 Mean and standard deviation of each parameter measured with laboratory test for Dolomia Principale samples..... 88

Table 4 Parameters used in entire domain for thermal analysis..... 96

Table 5 Rock mass mechanical properties adopted in the MIDAS model for the SRM analyses and Interface mechanical properties adopted in the mechanical model for the SRM analyses. Five parameter sets (Set 1–Set 5) were defined including initial interface cohesion c and initial friction angle φ, normal and shear stiffness (k_n, k_s) and dilatancy angle. Cohesion and friction angle are bold since they are varied during the numerical simulations. 98

Table 6 Summary of SRM numerical simulations. The analysis considers two geometry states (pre-2018: back-analysis – BA2018, and post-2018 collapse: future failure scenario) and three fracture configurations: (F1) back discontinuity only; (F2) back and central discontinuities; and (F3) central discontinuity only. The interface strength parameters assigned to each case correspond to Sets 1–5 in Table 5. 99

Table 7 Recent annual cumulative precipitation (2020–2025) highlighting the severe dry biennium (2022–2023) preceding the 2025 anomalous peak. The 2025 value is cumulative from 1 January to 1 August 2025 (date of collapse), not a full calendar-year total. 131

Table 8 Material properties used for the FEFLOW FEM thermal analysis. 146

Table 9 Constitutive parameters for the 3D FEM mechanical analysis (MIDAS FEA). 147

Table 10 Comparison of SRM-reduced interface parameters at failure with literature values for ice-filled rock discontinuities. 163

Table 11 Thermal parameters used for the rock and shaft-concrete domains in the 3D FEFLOW model. 191

Chapter 1
INTRODUCTION

1.1 **Motivation and scope**

High-mountain terrain is undergoing rapid changes, with the European Alps being among the regions where these changes are most evident. The phenomenon of rising air temperatures and the increasing frequency of unusually warm summers are modifying the thermal boundary conditions of rock walls, debris-covered slopes, and high-elevation plateaus. In this particular setting, permafrost is of significance as it is a thermal condition that governs the tendency of water within the ground, particularly within fractures and pores in bedrock, to occur as ice, liquid water, or a mixture of both. The presence and state of ice have been demonstrated to influence the behaviour of discontinuities (Gruber & Haeberli, 2007; Harris et al., 2009). Consequently, permafrost conditions have the potential to affect the stability of fractured rock masses and the evolution of alpine slopes. Permafrost in the Alps is characterised by its discontinuity and spatial heterogeneity, with its occurrence frequently in close proximity to the melting point, particularly in steep bedrock settings. This near-zero condition is of critical importance: when temperatures are close to 0 °C, relatively small changes can alter the duration and frequency of thawed periods in fractures and near-surface rock (Gruber & Haeberli, 2007). Observations from mountainous regions and those situated at high latitudes demonstrate that permafrost temperatures have increased over recent decades. European mountain permafrost exhibits a discernible warming trend in borehole data since the early 2000s (Noetzli et al., 2024). These trends provide compelling evidence to support the hypothesis that warm permafrost environments in the Alps are among the most sensitive to ongoing climate change. The consequences of such changes are of particular concern in the context of both natural hazards and infrastructure. In terms of potential hazards, numerous studies have indicated that rockfalls and rock-slope failures in high-elevation rock walls frequently occur during unusually warm summers and heatwaves, suggesting that the warming of rock-wall permafrost can act as a relevant conditioning factor, although it is rarely the sole cause (Ravanel et al., 2017). The pivotal observation is that temperature alone does not

necessarily induce failure; rather, it is the cumulative effect of thermal conditions on the mechanical integrity of ice-affected discontinuities that can significantly enhance their susceptibility to failure when additional drivers such as precipitation events, water pressure in fractures, progressive damage, or stress redistribution act (Krautblatter et al., 2013). This interaction is particularly plausible in marginal or warm permafrost conditions, where the system operates near the phase-change threshold. Infrastructure in high-altitude regions, such as cable cars, summit stations, and mountain huts, is often established on fractured bedrock in cold environments. In this particular instance, permafrost constitutes not merely a natural boundary condition; it is also subject to local modification by the infrastructure itself. Excavations, lined shafts, heat input from buildings, and altered airflow can create thermal anomalies in the surrounding rock mass. These anomalies have the potential to lead to differential settlement, long-term deformation, and increased maintenance needs. This aspect is of increasing relevance, given that the reliability and safety of infrastructure located at high elevations is contingent upon a stable foundation response over the course of decades, in the context of boundary conditions that are no longer stationary.

Despite the growing attention, understanding and anticipating instability in permafrost-affected rock slopes remains challenging for three practical reasons. Firstly, the behaviour of rock-slope systems in steep bedrock is primarily governed by structural elements. Discontinuities in the bedrock define the kinematic behaviour and potential release surfaces, while intact rock bridges and the presence of roughness provide resistance. Secondly, the processes through which warming affects stability are not directly observable at the scale of a rock wall. Whilst temperature can be measured, the quantification of ice content, water circulation, and changes in fracture aperture are more challenging in situ. Thirdly, observations and models frequently delineate the system in disparate measurement spaces. For instance, radar interferometry quantifies displacements along the sensor line of sight, while numerical models generate three-dimensional displacement and stress fields. In the absence of an explicit strategy to ensure comparability of these outputs, a comparison of models with data can become qualitative and potentially misleading. The motivation for this thesis stems from the need for a consistent and transferable framework to interpret permafrost-related instability in steep alpine bedrock, one that combines monitoring and modelling in a way that is physically coherent, practically usable, and capable of distinguishing between competing mechanisms rather than merely describing observations. The scope is deliberately

concentrated on steep rock slopes and rock walls, where structural control is paramount and permafrost conditions can approach 0 °C, making the system highly sensitive to relatively small thermal perturbations.

The work pursues this objective along three interconnected lines. The first is the development and validation of a model–data comparison strategy in which numerical outputs are explicitly transformed into the same observational space as the field measurements for instance, by projecting finite-element displacement fields along the radar line of sight of ground-based InSAR systems. This ensures that agreement or disagreement between models and data carries a precise geometric meaning rather than remaining qualitative. The second line concerns the extension of standard one-dimensional conduction models to account for the thermal complexity of highly fractured rock masses, where open discontinuities act as preferential pathways for air circulation and water infiltration, introducing advective heat transport and latent-heat effects that conduction alone cannot reproduce. The third line addresses a structural limitation of existing geomechanical frameworks: current models that apply continuous atmospheric forcing systematically misrepresent the failure chronology of permafrost-affected rock slopes, requiring physically implausible parameter adjustments to match observed collapse times. This thesis introduces an episodic thermo-hydromechanical formulation that decouples long-term conductive preconditioning from discrete hydrological shocks, resolving this calibration paradox and providing a physically grounded explanation for the observed pattern of late-summer, rain-triggered failures in Alpine permafrost environments. These three lines of investigation are developed and tested across four case studies of increasing complexity and decreasing data availability. Two instrumented non-permafrost rock slopes in the Italian Alps, the Scaiùn cliff and Monte Colodri, serve as the validation testbed for the model–data comparison workflow, allowing the thermally driven component of ground-based InSAR displacement fields to be isolated and quantified. The Sas da Lech dolomite pillar in the Dolomites (Figure 1), which experienced a 3,500 m^3 collapse in September 2018, provides a warm-permafrost setting where multi-depth borehole records enable direct validation of the extended thermal models and where strength reduction analyses reveal how a statically stable pre-collapse configuration can be driven to failure by climate-driven degradation of ice-filled discontinuities. The August 2025 Cima Falkner (Figure 1) rock fall, involving approximately 5.7×10^5 m^3 in the Brenta Dolomites, offers an unprecedented natural laboratory in which the episodic framework is applied without calibration, successfully

reproducing the exact timing of failure and demonstrating the transferability of the approach to large, poorly instrumented events. Finally, the Punta Helbronner (Figure 1) cable-car station on the Mont Blanc massif allows the interaction between engineered infrastructure and the surrounding permafrost to be quantified, showing how shaft-related heat input creates localized warm anomalies whose spatial extent depends on elevation and background thermal conditions. In summary, this thesis advances the understanding of permafrost-related rock-slope instability by moving beyond descriptive monitoring towards mechanism-based interpretation, by extending the physical realism of thermal and mechanical models to account for processes that standard approaches systematically neglect, and by demonstrating, across sites ranging from instrumented pillars to large uninstrumented rock slope, that a consistent integrated framework can reduce interpretive ambiguity and support quantitative hazard assessment in one of the most thermally sensitive environments on Earth.

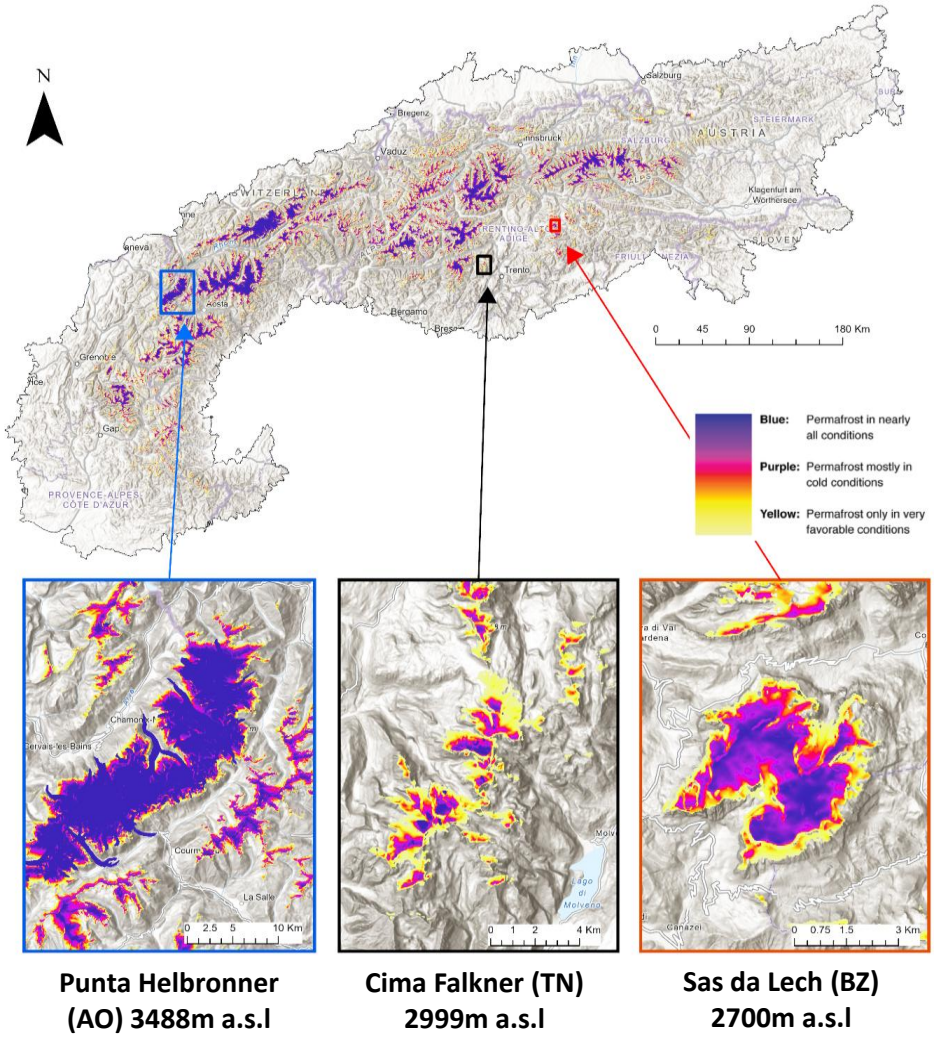


Figure 1 APIM (Alpine Permafrost Index Map (Boeckli et al., 2012b)) for the entire European Alps chain with three zooms on the study area discussed in this thesis.

1.2 **Thesis Outline**

This thesis is organized into seven chapters.

Chapter 1 introduces the scientific and societal context of Alpine permafrost and rock-slope instability, presents the motivation and scope of the work, and formulates the five research questions that structure the investigation. Section 1.3 identifies the chapters in which each question is addressed.

Chapter 2 presents the background and literature review. It first synthesizes current knowledge on Alpine permafrost and climate change, rockfalls and rockwall erosion in high mountain environments, and permafrost-related slope instabilities. It then reviews the specific issues posed by high-altitude infrastructure founded on permafrost and finally discusses thermal monitoring strategies and numerical modelling approaches in permafrost-affected rock slopes.

Chapter 3 investigates the thermo-mechanical response of rock slopes subjected to cyclic temperature forcing, using both idealized and real geometries through numerical modeling and GBInSAR data. Parametric FEM simulations are carried out to explore the influence of slope geometry, material properties and boundary temperatures. The results are compared with GBInSAR displacement measurements at two non-permafrost sites, providing a validation benchmark for the modelling approach and a methodological foundation for the subsequent permafrost-focused chapters.

Chapter 4 focuses on the Pisciadù–Sas da Lech rock pillar in the Dolomites, which is affected by warm permafrost and experienced a large pillar collapse in 2018. An integrated monitoring system combining borehole probes, surface displacement sensors, and geophysical surveys is presented. The observations are interpreted through a novel analytical thermal-compensation algorithm and an extended one-dimensional heat-flow model that incorporates localized fracture advection and latent-heat effects. Three-dimensional thermo-mechanical modelling is then used to assess the role of permafrost degradation in the observed instability and to explore the residual hazard of the current post-collapse configuration.

Chapter 5 presents the 2025 Cima Falkner rock avalanche as a large-scale case study in the Brenta Dolomites. Drawing on multi-temporal point-cloud change detection, seismic records and satellite InSAR data, the chapter reconstructs the failure sequence and its volumetric budget. A novel thermo-hydromechanical framework is introduced that decouples long-term conductive preconditioning from episodic hydrological shocks,

resolving a fundamental calibration paradox in existing geomechanical models and identifying the mechanism by which thermal degradation of ice-filled discontinuities creates a vulnerability window that episodic rainfall events can exploit as a trigger.

Chapter 6 addresses the Punta Helbronner site in the Mont Blanc massif, where a cable-car shaft is embedded in permafrost-affected bedrock. Drawing on multi-year borehole and shaft monitoring, the chapter applies two- and three-dimensional thermal modelling to characterize the coupled natural and anthropogenic thermal regime of the rock mass. The analysis quantifies the persistent, non-seasonal heat source represented by the shaft, the spatial extent of the resulting thermal anomaly in the surrounding bedrock, and the systematic bias introduced by conduction-only modelling in fractured permafrost rock. The scope of this chapter is deliberately thermal: it characterizes the perturbation of the ground thermal regime rather than its mechanical consequences.

Chapter 7 summarizes the main conclusions of the thesis, provides explicit answers to the five research questions formulated in Chapter 1, highlights the original contributions and methodological advances, discusses the limitations of the study, and outlines recommendations and perspectives for future research and monitoring activities in Alpine permafrost rock slopes.

The methodological articulation of the thesis is summarized in Figure 2, which maps the three method families — monitoring and data acquisition, thermal modelling, and mechanical modelling — onto the four case studies. The four sites are ordered by increasing physical complexity, from the purely geometric, thermo-elastic response of non-permafrost cliffs (Chapter 3), through phase-change and permafrost degradation at Sas da Lech (Chapter 4), to episodic hydro-mechanical triggering at Cima Falkner (Chapter 5), and finally to anthropogenic thermal forcing at Punta Helbronner (Chapter 6). The methods deployed differ between sites not arbitrarily, but as a direct consequence of data availability: where borehole temperature records exist, thermal models are validated directly against them; where they do not, the modelling strategy is adapted accordingly.

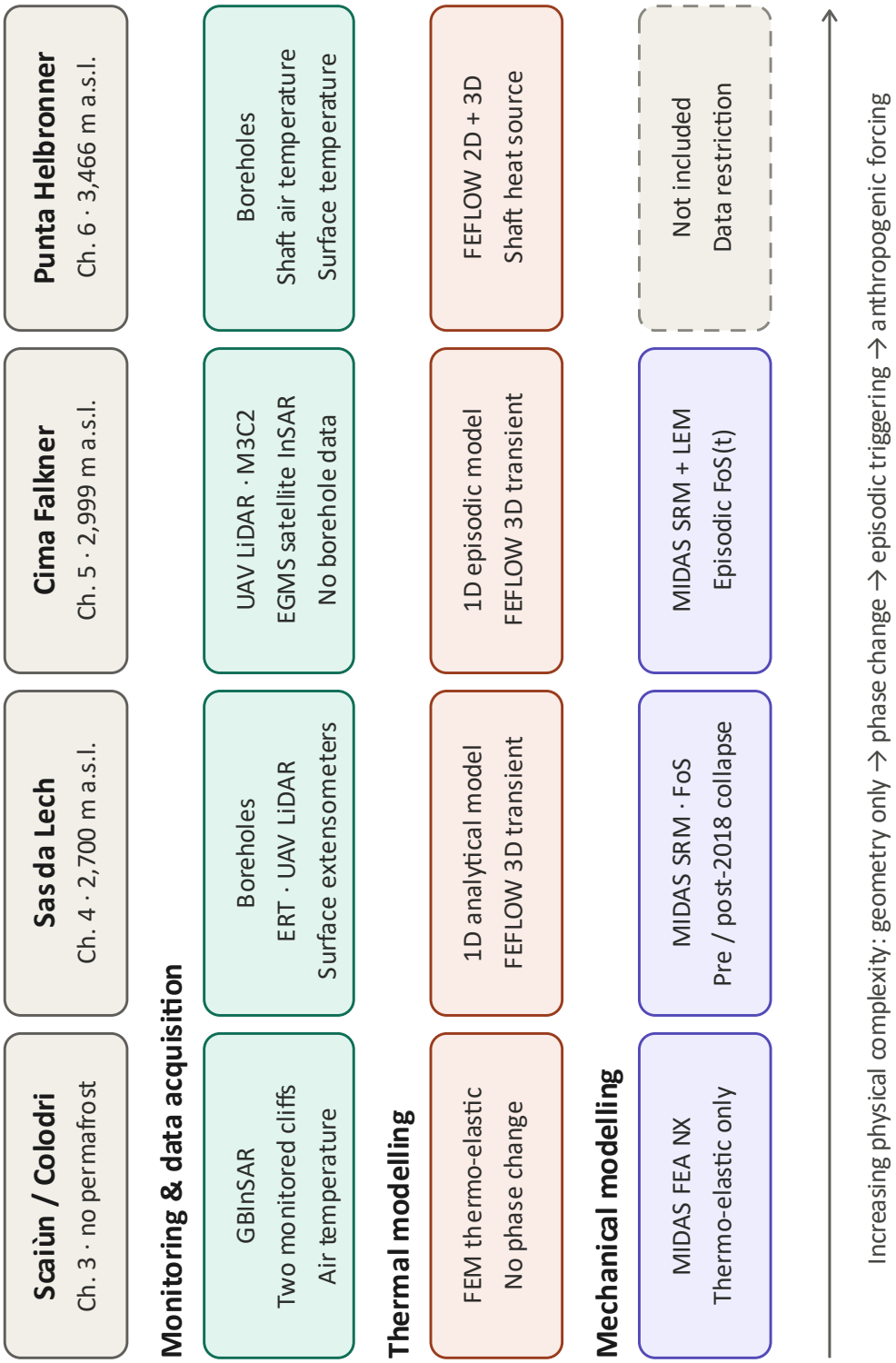


Figure 2 Articulation of methods and data across the four case studies of the thesis. Rows group the three method families; columns correspond to the four case studies, ordered by increasing physical complexity. Differences in the methods deployed between sites reflect differences in data availability.

1.3 **Research Questions**

Against this background, the thesis is organized around five explicit research questions that define its scientific scope and connect its individual case studies into a coherent investigative framework.

RQ1. ***In thermally sensitive high-mountain environments, and separating geometric controls from geomechanical responses, what are the thermo-mechanical effects directly attributable to the geometry of potentially unstable rock elements?***

This question addresses the need to isolate the role of morphology, pillar slenderness, wall curvature, slope aspect, in governing the amplitude, spatial distribution and mode of thermally induced deformation, and is examined in Chapter 3.

RQ2. ***Given the local temperature distribution in a high-altitude rock wall, how can the subsurface thermal regime be modelled in a way that accounts for both conductive and advective heat transport?***

Standard one-dimensional conduction models systematically fail to capture the thermal behaviour of highly fractured rock masses, where open discontinuities act as preferential pathways for air and water circulation. This question is addressed in Chapter 4.

RQ3. ***In high-altitude environments characterised by alpine permafrost conditions, which factor predisposes a rock mass to collapse, and which acts as the ultimate triggering mechanism?***

The distinction between long-term thermal preconditioning and discrete short-term triggers is central to understanding and anticipating catastrophic failure and is investigated in Chapters 4 and 5.

RQ4. ***How can high-altitude instability phenomena be simulated in a way that explicitly accounts for the progressive deterioration of physico-mechanical properties with temperature, and specifically with permafrost degradation?***

This question is addressed in Chapters 4 and 5, through analyses that incorporate temperature-dependent interface properties and a thermo-hydromechanical framework that decouples long-term conductive preconditioning from episodic hydrological shocks.

RQ5. ***What influence or interaction exists between permafrost degradation and the presence of high-altitude infrastructure?***

Engineering structures modify the local thermal boundary conditions of the surrounding rock mass, potentially amplifying permafrost degradation beyond what the regional climate alone would produce. This question is examined in Chapter 6.

The detailed state-of-the-art and the physical background underlying these processes are presented in Chapter 2.

Chapter 2
LITERATURE REVIEW

This chapter reviews the state of knowledge on alpine mountain permafrost and its relevance for high-elevation rock-slope instability. It first introduces permafrost as a ground thermal condition and describes its vertical structure in the specific context of steep, fractured bedrock. It then summarizes the main climatic and topographic controls that govern where Alpine permafrost forms, how it evolves under warming, and why warm, near-zero conditions are especially critical. Building on this basis, the chapter discusses evidence linking cryo-hydro-thermal processes to instability activity and outlines the monitoring and modelling approaches commonly used to interpret deformation and temperature distribution in rock walls. Finally, it contextualizes these processes through high-altitude infrastructures founded on permafrost-affected rock masses.

2.1 **Mountain Permafrost in the European Alps**

Permafrost is commonly defined as ground like soil, sediment, rock and/or ice, that remains at or below 0 °C for at least two consecutive years, regardless of ice content. This definition emphasizes that permafrost is a thermal state, not a material class (Gruber, 2012; Gruber & Haeberli, 2007; Smith, 1989). In Alpine environments, permafrost can occur in unconsolidated deposits and in intact or fractured bedrock, where water stored in pores and discontinuities may be liquid, frozen, or partially frozen. Importantly, 0 °C is not a universal freezing threshold: salinity, pressure, and pore geometry can depress the freezing point, allowing unfrozen water to persist below 0 °C, particularly where thin liquid films remain adsorbed on mineral surfaces (Haeberli et al., 1993; Matsuoka & Murton, 2008). For steep bedrock, this distinction matters because even small changes in temperature near the melting point can shift the balance between ice and liquid water in fractures, with direct consequences for stiffness, shear resistance, and hydraulic connectivity (Gruber & Haeberli, 2007; Haeberli et al., 2010).

From a cryological perspective, it is useful to distinguish dry permafrost, in which no ice is present, from wet permafrost, where ice and liquid water coexist in pores or fractures, as these states imply very different thermal buffering capacities and mechanical behaviour (Gruber & Haeberli, 2007; Harris et al., 2003). Near the surface, permafrost terrain typically organized into a seasonally affected active layer overlying perennially frozen ground. In winter, a freezing front propagates downward; in summer, a thawing front propagates downward, producing an active-layer thickness that depends on surface temperatures, thermal properties, moisture, snow cover, and topographic factors such as elevation, aspect, and slope angle (Christiansen, 2005; Harris et al., 2003; Riseborough et al., 2008). The boundary between the seasonally thawed layer and the underlying frozen ground is the permafrost table, while the permafrost base is the lower limit where temperatures exceed 0 °C due to geothermal heat flux (Christiansen, 2005; Gruber, 2012) (Figure 3).

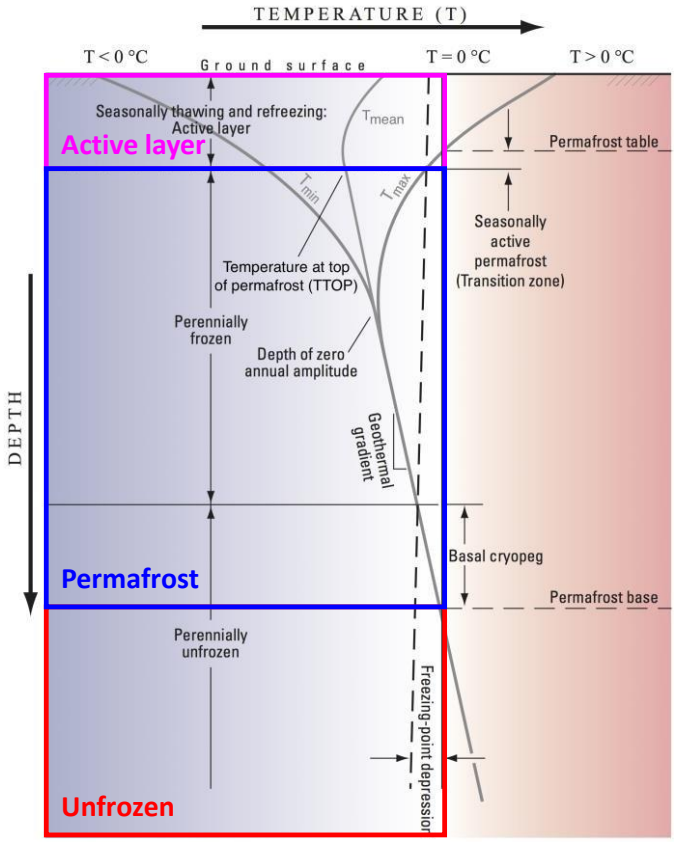


Figure 3 Schematic representation of permafrost configuration. In the purple box, the active layer displays the portion affected by seasonal freezing and thawing. Within the designated blue box, the permafrost body remains permanently frozen throughout the changing seasons. The red box delineates the area of elevated temperatures, which exceed 0°C, attributable to geothermal heat flow.

Because heat propagates diffusively, temperature oscillations at the surface penetrate with attenuation and phase lag. Daily cycles usually affect only the upper decimeters of

rock, whereas seasonal cycles can reach several meters to a few tens of meters depending on thermal diffusivity (Carslaw et al., 1962; Kukkonen & Šafanda, 2001). At greater depth, multi-decadal trends related to climate change are expressed as a slowly evolving background signal on which shorter oscillations are superimposed (Riseborough et al., 2008). Near 0 °C, phase change introduces strong latent-heat effects, damping seasonal amplitudes and often producing a zero curtain during freezing and thawing, when temperatures linger near the melting point for extended periods (Haeberli et al., 1993). In steep fractured bedrock, these thermal processes govern the distribution of ice and liquid water within discontinuities and therefore act as a direct control on rock-mass mechanical behaviour. The depth of zero annual amplitude (ZAA), the subsurface level where the seasonal ground-temperature signal becomes negligible, operationally defined where annual amplitude drops below approximately 0.1 °C, provides a practical reference depth for describing the thermal state of rock walls and their long-term warming (Gruber & Haeberli, 2007; Magnin et al., 2015). In steep alpine bedrock permafrost, ZAA commonly occurs deeper than approximately 10 m, and the temperatures measured at or just below this depth primarily reflect multi-annual climatic trends rather than short-term variability.

Across the European Alps, mountain permafrost is discontinuous and strongly controlled by local boundary conditions. At the scale of the Alpine arc, permafrost is generally more likely above approximately 2,500 m a.s.l. on north-facing slopes and above approximately 2,800–3,000 m a.s.l. on south-facing slopes, but these thresholds vary substantially depending on snow conditions, terrain shape, and substrate properties (Boeckli et al., 2012a; Gruber, 2012; Haeberli, 1973; Haeberli et al., 1993). Mapping and modelling initiatives such as PERMAKART, PermaNET, and PERMOS show that ridges, shaded cliffs, talus slopes, and debris-covered plateaus may host permafrost, while nearby areas at similar elevation can be permafrost-free due to different radiative and snow regimes (Boeckli et al., 2012a; Haeberli et al., 1993; Magnin et al., 2024). This spatial patchiness is particularly important for bedrock slopes, where fracture-controlled ice acts as a transient cementing agent that is highly sensitive to warming (Gruber & Haeberli, 2007; Magnin et al., 2015; Noetzli et al., 2007).

The thermal state of rock permafrost reflects the balance between atmospheric forcing, radiation, snow cover, and subsurface conduction, with local contributions from advective heat transport by water or air circulation within fractures (Gruber, 2012; Magnin et al., 2017; Noetzli & Gruber, 2009). Snow cover is often a first-order control, but its effect is not monotonic. Thick and persistent snow can insulate the ground in winter

and maintain subsurface temperatures near 0 °C; thin or patchy snow can allow strong winter cooling and favor permafrost preservation if cold conditions persist (Luetschg et al., 2008). Observations show that early snow onset may protect the ground from winter cold and promote warming, whereas delayed or intermittent snow cover permits deeper freezing (Draebing et al., 2017; Magnin et al., 2017). These snow–radiation interactions are strongly modulated by microtopography and wind redistribution, so that meter-scale contrasts in insulation may occur even on the same rock wall. Where open fractures allow the circulation of air or infiltrating meltwater, advective heat transport can locally dominate over conduction, producing thermal shortcuts that deliver atmospheric temperature signals to depths far greater than purely conductive processes would permit (Gruber & Haeberli, 2007; Hasler et al., 2011).

On multi-decadal timescales, monitoring and modelling document widespread permafrost warming across the Alpine arc. Borehole records in rock and debris indicate increasing ground temperatures in the upper tens of meters, with particularly pronounced changes at sites close to the lower permafrost limit and in warm permafrost conditions (Etzelmüller et al., 2022; Harris et al., 2003; Magnin et al., 2024; Noetzli et al., 2024). In many sites, the active layer has thickened, while deeper thermal signals can lag surface trends by decades because the subsurface retains a memory of past climate (Noetzli & Gruber, 2009; Riseborough et al., 2008). Recent analyses indicate that European mountain permafrost has warmed by more than 1 °C per decade at certain cold bedrock sites, matching the rates observed in Arctic lowlands (Noetzli et al., 2024). Long-term investigations of the response of alpine ground temperatures to the rising 0 °C isotherm further confirm a systematic upward shift of thermal conditions in bedrock permafrost over the period 1955–2021, with implications for the depth and persistence of ice-bearing zones in steep rock walls (Kenner et al., 2024). In steep rock walls, the response is strongly controlled by aspect and geometry: south-facing faces and convex ridges tend to warm faster than shaded, concave walls (Magnin et al., 2015; Magnin et al., 2017; Noetzli et al., 2007). Extreme warm summers, notably those of 2003, 2015, and 2022, can produce step-like perturbations, rapidly deepen the active layer and increase temperatures at depth beyond what would be expected from gradual trends alone (Cathala et al., 2024; Gobiet et al., 2014; Ravanel et al., 2017).

Monitoring is central to constraining these processes, yet steep rock faces remain under-represented relative to debris slopes and accessible plateaus. Key observables include ground- or rock-surface temperature (GST/RST), which integrates air

temperature, radiation, and snow cover, and the bottom temperature of snow cover (BTS), measured near the end of winter at the ground–snow interface (Haeberli, 1973; Haeberli et al., 1993). Long-term borehole measurements remain the backbone of Alpine permafrost observation. Networks such as PERMOS and PermaFrance provide multi-depth time series in debris and bedrock permafrost, documenting active-layer thickness, warming trends, and the response to extreme summers (Etzelmüller et al., 2022; Magnin et al., 2015; Magnin et al., 2024; Noetzli et al., 2024). Dedicated monitoring campaigns in steep bedrock, such as the decade-long dataset from the Matterhorn Hörnligrat (Weber et al., 2019), have demonstrated that even in well-studied crystalline massifs, the thermal regime of permafrost-affected rock walls remains highly variable in space and time, and that structural heterogeneity can produce sharp thermal contrasts within individual rock walls. Alpine-wide initiatives such as PermaNET further promote combined strategies integrating GST/BTS, boreholes, geophysics, and modelling for mapping and monitoring design (Boeckli et al., 2012a; Harris et al., 2003; Scandroglio et al., 2021).

A recurring challenge in steep rock is the interpretation of monitoring data, since the same measured temperature signature can reflect different combinations of snow insulation, radiation, and latent-heat effects. Seasonal records often contain characteristic phases linked to snow dynamics and phase change (Stocker-Mittaz et al., 2002). During snow-free periods, GST/RST can show strong diurnal variability and track atmospheric forcing closely. Once the snowpack becomes sufficiently thick, daily fluctuations are damped and the ground–snow interface approaches a quasi-steady winter equilibrium temperature reflecting the balance between subsurface heat flux and snow insulation (Haeberli, 1973). During melt periods, a near-0 °C plateau is common while meltwater is present and latent heat dominates. In steep rock slopes, these concepts remain valid but become harder to generalize because meter-scale snow variability and complex three-dimensional radiative effects such as shading, reflections, and local incidence angles, can produce sharply different thermal boundary conditions within the same rock wall (Gruber, 2012; Magnin et al., 2015). This is one reason why distributed sensor networks and complementary observations, including time-lapse snow mapping and geophysical imaging, are increasingly used when thermal datasets are intended to constrain site-scale, three-dimensional modelling (Haeberli et al., 2010; Scandroglio et al., 2021).

Taken together, alpine permafrost emerges as a three-dimensional and highly heterogeneous element of the mountain cryosphere. Warming trends are clear at regional scale, but steep bedrock remains a critical knowledge gap because the most unstable

source areas are often the least instrumented, and stability is frequently governed by warm, degrading conditions near 0 °C where small thermal shifts translate into large changes in ice–water partitioning and effective mechanical properties. This transitional near-zero regime, where temperature controls the phase state of water in fractures, and thereby the stiffness and shear resistance of discontinuities, is therefore the central physical setting for the instability processes investigated in the following sections.

2.2 **Rockfalls and rock-slope instabilities at high elevation**

High-elevation rock slopes in the Alps are characterised by steep cliffs and ridges where the rock mass is subdivided into blocks and pillars by faults, joints, and bedding planes. Rockfalls, sudden detachments from steep rock walls followed by free fall, bouncing, sliding, and rolling, are among the most widespread and hazardous processes in these settings (Varnes, 1978). Other forms of instability include cliff falls (De Blasio et al., 2018; Whalley, 1974), rockslides, rock avalanches, and deep-seated gravitational slope deformations, which may involve larger volumes but are typically less frequent. Among these instability types, the sudden collapse of large rock pillars and isolated towers represents one of the most hazardous mechanisms, threatening mountain infrastructure, trails, and human lives through the combination of difficult predictability, high impact energy, and long runout distances (Ravanel et al., 2017; Weber et al., 2025).

Rockfall occurrence reflects the interaction between long-term predisposition and short-term triggers. Predisposition is primarily controlled by lithology, intact rock strength, and rock-mass structure: the orientation, persistence, and connectivity of discontinuity sets define the kinematics of potential failures and the size of releasable volumes. Progressive damage and weathering reduce rock-bridge area and promote crack opening over time. In high-mountain environments, these processes are strongly influenced by thermal cycling, freeze–thaw activity, permafrost degradation, intense rainfall, and, occasionally, earthquakes (Bonometti et al., 2026; Crosta & Agliardi, 2003; Frattini et al., 2008; Paranunzio et al., 2016; Valagussa et al., 2014). The spatial and temporal distribution of documented rockfall events in the Alps shows a clear correlation with climatic anomalies, with events concentrated during anomalously warm summers, periods of intense precipitation, and at elevations consistent with permafrost occurrence (Figure 4; Paranunzio et al., 2016). Recent work emphasizes that cryospheric controls intensify above approximately 2,500 m a.s.l., where seasonal frost, discontinuous rock

permafrost, and glaciated terrain often overlap, making high-elevation slopes disproportionately sensitive to warming and snow-cover changes (Draebing et al., 2022).

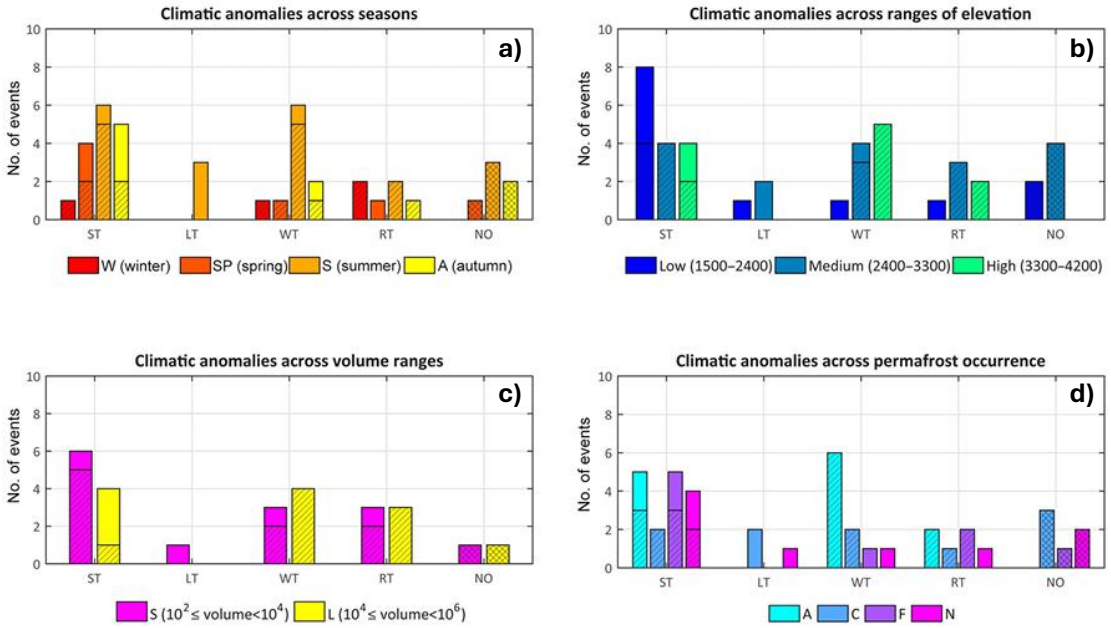


Figure 4 Rockfalls distribution according to climate anomaly e considering the a) season occurrence, b) elevation, c) volume and d) permafrost (Paranunzio et al., 2016) ST: Short-Term T anomaly; Rapid warming; superficial thaw/melt. WT: Widespread T anomaly; Persistent warming across multiple time scales. LT: Long-Term T anomaly; Sustained warming affecting deeper ground/permafrost. RT: Rainfall (Precipitation) anomaly. Influence of water pressure/infiltration (with/without T anomaly).NO: No anomaly; Trigger likely non-climatic or not captured by the variables.

In recent decades, the European Alps have experienced a marked increase in the frequency and magnitude of rockfalls and rockslides originating from high-altitude rock walls, affecting both crystalline massifs, such as the Mont Blanc area, and sedimentary carbonate groups, including the Dolomites and the Limestone Alps (Ravanel & Deline, 2011; Savi et al., 2021). This escalating trend is widely attributed to climate change, which strongly alters the thermo-mechanical and hydro-thermal equilibrium of rock masses through permafrost degradation, deeper active-layer thawing, and modified snow-cover dynamics (Draebing et al., 2022; Noetzli et al., 2024). The primary driver of enhanced instability at high elevations is the progressive warming of ice-filled fractures toward 0 °C, which drastically reduces the shear resistance of rock–ice interfaces and compromises the integrity of intact rock bridges (Krautblatter et al., 2013; Mamot et al., 2018). The relationship between temperature and the resistance of frozen discontinuities is strongly non-linear: experimental evidence demonstrates that warming interstitial ice from −10 °C to −0.5 °C reduces the shear strength of ice-filled joints by up to 60–78%,

with the steepest strength loss concentrated in the interval between −2 °C and 0 °C (Davies et al., 2001; Mamot et al., 2018). This behaviour is schematically illustrated in Figure 5, which shows how warm permafrost conditions correspond to the most critical stability regime. In addition, extreme heatwaves generate intense thermo-elastic stresses and cyclic fatigue, driving progressive fracture propagation that can culminate in catastrophic failure even without a discrete external trigger (Collins & Stock, 2016; Collins et al., 2018, 2019).

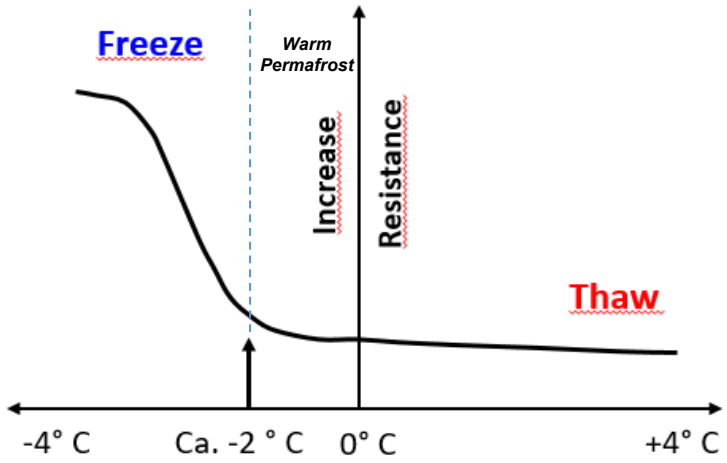


Figure 5 Schematic figure of resistance behaviour in function of temperature (Adapted from (Bommer et al., 2010)). The plot show how in correspondence of warm permafrost the resistance decrease significantly.

Permafrost thaw is increasingly recognized as a major contributor to rockfall activity in Alpine settings. In rock permafrost, ice in fractures contributes to shear resistance and structural integrity; as temperatures rise, this contribution diminishes, especially near the melting point (Krautblatter et al., 2013). Warm permafrost, roughly −2 to 0 °C, therefore, represents a critical stability regime in which modest thermal perturbations can lead to disproportionate changes in ice content, unfrozen water fraction, and mechanical response. A crucial distinction has emerged in recent literature between two temporally separated processes: long-term thermal preconditioning, through which decades of climate-driven warming progressively degrade the mechanical contribution of ice-filled discontinuities without necessarily producing failure, and discrete short-term triggers like intense rainfall, snowmelt, or extreme heat pulses, that exploit the accumulated weakness to initiate collapse (Cathala et al., 2024; Leinauer et al., 2024). This decoupling between preconditioning and triggering is central to understanding why many Alpine rockfalls occur abruptly in late summer following seemingly ordinary precipitation events, and

why predicting their exact timing remains elusive despite a well-established understanding of the underlying mechanisms.

Thermo-cryogenic processes progressively weaken rock masses through stress accumulation, microcracking, and crack propagation (Deprez et al., 2020; Matsuoka & Murton, 2008; Mayer et al., 2023). Hydrological processes amplify these effects: as fractures thaw, permeability may increase, promoting infiltration and advective heat transport that can deepen thaw beyond conduction-only expectations (Krautblatter & Hauck, 2007; Magnin et al., 2015). Infiltrating meltwater or rainfall can simultaneously deliver advective heat to depth and generate transient hydrostatic overpressures within the fracture network, producing a combined mechanical and thermal shock that may far exceed what purely conductive warming would accomplish over the same timeframe (Hasler et al., 2011; Offer et al., 2025). Snow-cover variability modulates these dynamics by controlling winter insulation and the timing and intensity of spring meltwater inputs.

Field evidence increasingly links warm permafrost conditions to rockfall activity. In the Mont Blanc massif, inventories document an increase in rockfall frequency since the 1990s, with peaks during exceptionally warm summers (Magnin et al., 2024; Ravanel et al., 2017). Tree-ring reconstructions in the Swiss Alps support this relationship, indicating higher rockfall frequencies in warm summers particularly after the 1980s (Stoffel et al., 2024). Terrestrial laser scanning studies on steep permafrost-affected cliffs report high erosion rates following glacier retreat and extreme summers, reinforcing the coupling between thermal forcing and rock-wall retreat (Courtial-Manent et al., 2024). Statistical analyses further indicate that rock temperatures can be anomalously high days to weeks before detachment, and that deeper scar depths are often associated with permafrost or near-zero thermal conditions (Legay et al., 2021). At regional scale, a large share of documented failures occurs on slopes where mean annual rock surface temperatures remain below approximately 3 °C (Cathala et al., 2024). Recent detailed monitoring campaigns on freestanding rock pillars, most notably the decade-long dataset from the Matterhorn Hörnligrat, culminating in the pillar collapse of June 2023, have provided direct field validation of the progressive destabilization pathway, demonstrating how seasonal water infiltration into permafrost fractures accelerates mechanical weakening over multi-annual timescales until a threshold is crossed (Weber et al., 2025).

Although many classic permafrost–rockfall studies focus on crystalline massifs, dolomitic and carbonate landscapes are also markedly affected by climate-driven destabilization. Due to their specific structural setting, characterised by pervasive joint

networks, high secondary porosity, and distinct thermal properties, dolomitic massifs exhibit high vulnerability to thermal forcing and water circulation (Bonometti et al., 2026). The intricate fracture networks in these lithologies promote complex three-dimensional heat transfer and advective processes that cannot be fully captured by traditional conduction-only models, making their thermal and mechanical behaviour particularly challenging to characterize and predict. Regional analyses in the eastern Alps indicate an increase in slope instabilities from the early 2000s, with detachment elevations migrating upward by several hundred meters, interpreted in the context of frost cracking and permafrost thaw (Savi et al., 2021). Work specifically on dolomitic cliffs of the eastern Alps shows that rockfall occurrence correlates with summer temperatures, daily thermal amplitude, and freeze–thaw frequency (Bonometti et al., 2026). Representative examples of cliff falls in the Dolomites are shown in Figure 6, illustrating the scale and morphological impact of such events. In this context, the Sella Group and the Brenta Dolomites are well suited for integrated monitoring aimed at disentangling the structural, thermal, and hydrological controls on instability in transitional permafrost zones, a challenge that the case studies presented in Chapters 4 and 5 directly address.



Figure 6 Photo of cliff fall in Dolomite a) Cima Lastei; b) Sassolungo; c) Carè Alto; d) Gran Vernel.

2.3 Thermal processes, monitoring and thermo-mechanical modelling of rock slopes

The thermal behaviour of rock masses in cold environments is governed primarily by conduction, phase change of water, and locally advective heat transport through open discontinuities (Draebing et al., 2014; Noetzli & Gruber, 2009). The relative importance of these three processes varies with depth, fracture density, and the availability of infiltrating water or circulating air, making the thermal regime of steep permafrost-

affected rock walls inherently heterogeneous and difficult to characterize from surface observations alone. Understanding how thermal forcing translates into mechanical response, through stress redistribution, progressive damage, and ultimately failure, requires an integrated approach that combines field monitoring with physically based numerical modelling. The following subsections review the state of knowledge on each of these three components.

2.3.1 *Thermal regime of Rock Walls*

Under purely conductive conditions and without phase change, temperature evolution in a rock mass follows the classical heat-flow equation, and periodic surface forcing produces damped, phase-lagged signals at depth. The depth of penetration of a periodic thermal signal scales with the square root of the product of thermal diffusivity and forcing period, meaning that diurnal cycles affect only the uppermost decimeters of rock, seasonal cycles penetrate to several meters, and multi-decadal climate trends reach tens of meters over time (Carslaw et al., 1962). These fundamental conductive dynamics produce a characteristic trumpet-shaped envelope of temperature extremes with depth, converging toward the mean annual surface temperature at the depth of zero annual amplitude. Temperature measurements at or below this depth therefore reflect long-term climatic trends rather than short-term atmospheric variability, and deviations from the expected conductive profile constitute direct evidence of non-conductive heat transfer processes.

In permafrost-affected rock, phase change introduces strong non-linearities that substantially modify this conductive baseline. Latent heat buffers temperature variations near 0 °C, slows signal propagation, and prolongs transitional periods during both freezing and thawing. The resulting zero-curtain effect, a near-isothermal plateau at the melting point, can persist for weeks to months in ice-bearing fractures, delaying the penetration of both summer warming and winter cooling beyond what purely conductive models predict (Haeberli et al., 1993). This latent-heat buffering is particularly pronounced where fracture networks concentrate ice and water, producing strongly localized thermal anomalies that are invisible to surface temperature sensors but critical for the mechanical integrity of the rock mass.

In fractured bedrock, thermal behaviour is rarely uniform. Contrasts among intact rock, ice-filled fractures, air-filled voids, and water pathways produce locally variable thermal gradients and potentially anisotropic effective heat transfer. Open fractures can support air or water circulation, introducing advective heat transport that may locally dominate

over conduction. Where infiltrating meltwater or rainfall percolates into cold fractures, it delivers sensible heat directly to depth, creating thermal shortcuts that can thaw ice-bearing discontinuities far faster than conductive warming alone (Gruber & Haeberli, 2007; Hasler et al., 2011). Air circulation through connected fracture systems produces a different advective regime, characterised by strong seasonal asymmetry: cold dense air sinks into fractures in winter, trapping cold temperatures at depth, a phenomenon known as cold-air trapping, while summer ventilation is comparatively inefficient. This asymmetric convection selectively preserves permafrost beyond the depths expected from surface thermal conditions (Hasler et al., 2011).

Three-dimensional geometry strongly controls the subsurface temperature field. Modelling at sites such as the Matterhorn and Aiguille du Midi has demonstrated how ridges, spurs, and convex topography experience faster and deeper thaw than adjacent concave or shaded areas, making them preferential locations for ice-bearing instabilities (Figure 7; Noetzli et al., 2007; Noetzli & Gruber, 2009). Coupled thermal and hydrological finite-element simulations have further shown how water flow in rock-wall permafrost modifies temperature distributions relative to purely conductive predictions, with saturated and flowing conditions producing systematically warmer conditions at depth (Magnin & Josnin, 2021). These three-dimensional and multi-process thermal effects are central to interpreting field monitoring data in steep Alpine rock walls and motivate the modelling approaches described in Section 2.3.4.

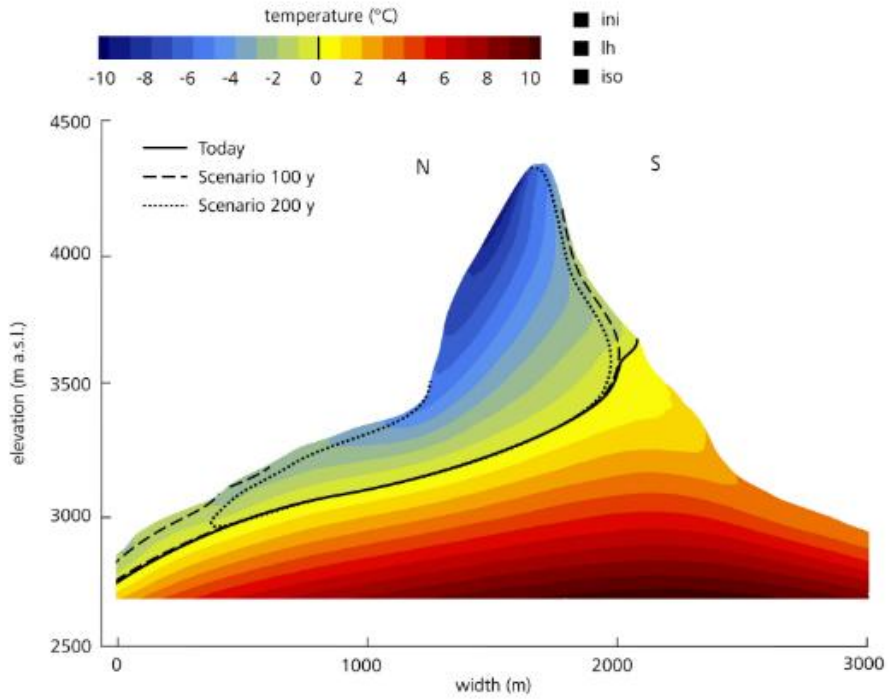


Figure 7 Results of temperature model of Matterhorn (4478m a.s.l.) with two future scenarios: 100years (dashed line) and 200years (dot line). In this work the author assumes a warming scenario of +3C/100years (Noetzli & Gruber, 2009).

2.3.2 *Thermal damage mechanisms*

These thermal regimes connect directly to damage mechanisms through a chain of physical processes spanning from the grain scale to the slope scale. Freeze–thaw activity, frost cracking, and thermal fatigue progressively weaken rock masses through stress accumulation, microcracking, and crack propagation (Matsuoka & Murton, 2008; Deprez et al., 2020). While volumetric expansion of freezing water can contribute under confined conditions, ice segregation driven by cryo-suction is widely recognized as the dominant frost-cracking mechanism in many periglacial settings.

Under a temperature gradient, freezing fronts draw unfrozen water toward the freezing zone through cryo-suction. Taber (1929) proved experimentally that frost heave is an open system in which ice lenses grow by drawing in external water rather than solely through in-situ water expansion, while Everett (1961) provided the thermodynamic proof that the curvature of the ice–water interface in micropores creates a pressure difference that allows ice to push outward while water is sucked inward. For a sub-zero temperature T, the pressure difference between ice and coexisting water scales approximately as 1.2 MPa per degree of undercooling below 0 °C, a magnitude sufficient to exceed the tensile strength of granite or limestone under appropriate conditions. However, this suction force

can only generate fracture growth if liquid water can migrate to the freezing front. Because hydraulic conductivity decreases dramatically at very low temperatures as unfrozen water films thin to nanometer scale, the most effective window for frost cracking is not the coldest temperature range but a relatively narrow interval, often cited as −3 °C to −8 °C, where cryo-suction is strong enough to drive fracture propagation yet permeability remains sufficient to sustain ice lens growth (Anderson, 1998; Hales & Roering, 2009; Walder & Hallet, 1985). This frost cracking window commonly coincides with the active layer and upper permafrost zone in Alpine rock walls, and repeated cycles can gradually reduce rock-bridge area and increase fracture connectivity over years to decades (Draebing & Krautblatter, 2019).

The mechanical behaviour of ice-filled fractures is particularly critical in warm permafrost settings, where temperatures approach the melting point. The shear strength of rock–ice interfaces is strongly temperature-dependent and collapses over a narrow thermal interval near 0 °C. Systematic laboratory experiments on limestone–ice and mica-rich interfaces demonstrate that warming interstitial ice from −10 °C to −0.5 °C reduces shear stress at failure by 64–78 % for normal stresses representative of 4–30 m of rock overburden (Mamot et al., 2018). At a given temperature, the shear resistance decreases further with decreasing normal stress, meaning that shallow, low-confinement ice-filled fractures in steep rock walls are particularly vulnerable to thermal weakening. Near 0 °C, the unfrozen water film at the ice–rock interface thickens, reducing the effective contact area between solid ice and rock, lowering cohesion, and making the joint susceptible to creep and progressive failure. At colder temperatures, for instance at −5 °C, the water film thin, ice bites harder into rock asperities, and both cohesion and total shear resistance increase substantially (Krautblatter et al., 2013). This temperature-dependent strength envelope provides the physical basis for understanding why warm permafrost conditions, roughly −2 to 0 °C, represent the most critical stability regime, and why relatively modest warming can produce disproportionately large reductions in rock-mass integrity (Davies et al., 2001; Mamot et al., 2018). Recent experimental work has further quantified the shear strength of the ice–rock interface as a function of temperature, normal stress, and surface roughness, providing improved parameterizations for stability models (Su et al., 2024).

Beyond fracture-scale processes, thermo-mechanical fatigue provides an additional pathway to weakening at the slope scale, even in the absence of freezing. Daily and seasonal heating and cooling generate cyclic strains; at the grain scale, differences in

mineral thermal expansion coefficients induce stresses and microcracking, while at the slope scale, gradients between sunlit surfaces and cooler interiors produce bending and curvature, concentrating tensile and shear stresses in the outer decimeters to meters of rock (Collins & Stock, 2016; Collins et al., 2018, 2019; Eppes & Keanini, 2017). Field observations and monitoring confirm that temperature cycles drive measurable fracture opening and closure and progressive damage accumulation over seasonal timescales (Gunzburger & Merrien-Soukatchoff, 2011; Mufundirwa et al., 2011), while numerical studies show that thermo-elastic stresses can propagate to depths exceeding 100 m in large rock slopes, contributing to long-term instability (Gischig et al., 2011).

In real slopes, thermal, hydraulic, and mechanical processes are tightly coupled. As fractures thaw, permeability often increases, enabling infiltration of snowmelt and rainfall and potentially raising pressures where drainage is limited by low-permeability zones or still-frozen layers (Etzelmüller et al., 2022; Phillips et al., 2017). Conversely, fracture opening and evolving connectivity alter flow pathways and can enhance advective heat transport, deepening thaw beyond conduction-only expectations. Capturing these feedbacks requires multi-parameter monitoring strategies that simultaneously constrain the thermal, hydrological, and kinematic state of the slope.

2.3.3 *Monitoring of Thermally Sensitive Rock Slopes*

Multi-sensor monitoring is central to constraining the coupled thermo-mechanical behaviour of permafrost-affected rock walls and to providing the observational basis against which physically based models can be validated. Key thermal observables include rock-surface temperature loggers, which integrate atmospheric forcing with radiative and snow-cover effects, and thermistor chains installed in boreholes, which provide direct multi-depth measurements of the subsurface thermal regime and its seasonal evolution (Harris et al., 2009; Magnin et al., 2015). Non-uniform sensor spacing, dense near the surface to capture strong gradients, progressively wider with depth to monitor long-term trends, significantly improves the diagnostic power of borehole datasets for distinguishing conductive from advective heat transfer signatures.

Geophysical methods, and in particular electrical resistivity tomography (ERT), provide spatially distributed information on the frozen–unfrozen state of the rock mass that borehole measurements alone cannot deliver. The marked contrast in electrical resistivity between frozen and unfrozen rock, increasing by one to several orders of magnitude across the phase transition, allows the imaging of active-layer geometry, ice-

bearing zones, and their temporal evolution under warming (Hilbich et al., 2008; Krautblatter & Hauck, 2007; Scandroglio et al., 2021). Laboratory calibration of the temperature–resistivity relationship for the specific rock types at each site is essential for quantitative interpretation of field ERT surveys (Krautblatter et al., 2010).

For kinematic monitoring, Ground-Based Interferometric Synthetic Aperture Radar (GBInSAR) provides millimetric line-of-sight precision over large slope areas at high temporal resolution, independent of daylight and adverse weather conditions (Leva et al., 2003, 2005; Tarchi et al., 2003). Its ability to provide spatially distributed displacement fields, rather than the point measurements of crackmeters or extensometers, makes it particularly valuable for identifying thermally sensitive sectors and detecting early kinematic precursors to failure. When combined with in-situ sensors and thermal measurements, GBInSAR enables the separation of thermo-elastic seasonal signals from genuine irreversible slope deformation (Woods et al., 2021). Satellite InSAR, including the European Ground Motion Service (EGMS) based on Sentinel-1 data, complements ground-based radar by providing pre-event displacement histories at sites without permanent instrumentation, extending the observational record to the years or decades preceding a failure (Costantini et al., 2022). Point-cloud change detection from repeated terrestrial or UAV-borne laser scanning and photogrammetry quantifies volumetric rock-mass loss and surface geometry changes between epochs, providing the geometric validation data essential for constraining numerical failure scenarios (Lague et al., 2013).

The integration of these complementary sensor systems thermal, geophysical, kinematic, and topographic within a consistent monitoring framework reduces interpretive ambiguity and provides the multi-variable datasets required to test physically based models of permafrost-related instability. This integrated approach is adopted throughout the case studies presented in Chapters 3 to 6.

2.3.4 *Numerical Modelling Approaches*

Numerical modelling complements monitoring by translating thermal forcing into stress redistribution, progressive damage, and discontinuity-driven kinematics at scales that in-situ sensors cannot resolve. Finite element, finite difference, and distinct element methods have been used to simulate temperature fields, thermo-elastic stresses, and fracture behaviour in both seasonally frozen and permafrost conditions (Collins et al., 2019; Gischig et al., 2011; Greif et al., 2017; Marmoni et al., 2020; Mufundirwa et al., 2011). At the thermal level, three-dimensional FEM simulations have demonstrated how

topographic complexity, aspect, curvature, and altitude control permafrost distribution and the propagation of warming in realistic Alpine geometries (Noetzli et al., 2007; Noetzli & Gruber, 2009), while coupled thermal–hydrological formulations have shown how water circulation modifies temperature distributions beyond what conduction alone would predict (Magnin & Josnin, 2021).

At the mechanical level, more recent work explicitly incorporates temperature-dependent material properties to capture the progressive strength loss of permafrost-affected discontinuities as warming approaches the melting point. The temperature-dependent mechanical model of Mamot et al. (2021) provides a transferable framework for assessing the stability of degrading permafrost rock slopes, demonstrating that even modest warming within the −2 to 0 °C range can drive the system from stable to unstable configurations. Strength Reduction Method (SRM) analyses applied to three-dimensional FEM geometries allow the factor of safety and the dominant failure kinematics to be identified across a range of structural and interface-strength scenarios, making it possible to distinguish between static structural predisposition and the transient weakening required to initiate collapse (Boffelli & Calvetti, 2023; Mamot et al., 2021).

A recognized limitation of standard modelling approaches is that they typically apply continuous atmospheric forcing, coupling rockfall occurrence directly to mean air temperature anomalies or to time-averaged thermal and hydrological energy inputs, thereby distributing climatic energy linearly over time and imposing an artificial, monotonic decline in simulated stability. This framework systematically misrepresents the failure chronology of permafrost-affected rock slopes, requiring physically implausible parameter adjustments to match observed collapse times. The physical mechanism through which decades of slow thermal preconditioning are translated into an instantaneous, event-triggered collapse mediated by discrete hydrological shocks that exploit the accumulated mechanical weakness, is not captured by these continuous-forcing paradigms and remains an active frontier of geomechanical research. This challenge motivates the modelling framework developed in Chapter 5, where an episodic thermo-hydromechanical formulation explicitly decouples the long-term conductive trajectory from episodic hydrological triggers.

2.4 **High-altitude infrastructures on permafrost-affected rock**

Permafrost degradation does not only affect natural rock slopes: it represents an increasingly critical challenge for the engineering structures that human activity has established in high-altitude environments. Cable cars, summit stations, mountain huts, and telecommunication towers are frequently found on fractured bedrock in cold environments where the ground thermal state has historically been assumed to be stable. The interaction between permafrost and engineering structures has been a concern in mountain regions since at least the mid-20th century (Arenson & Jakob, 2017). Warming-induced thaw of ice in pores, fractures, and ice lenses can alter the physical and mechanical properties of rock and debris, causing settlement, creep-like deformation, and loss of bearing capacity. In the European Alps, early observations already reported damage to high-altitude buildings and lift stations founded on permafrost, highlighting that stability depends not only on regional climate trends but also on local heat transfer from structures and construction activities.

Several classic cases in the Zermatt region of Switzerland illustrate this sensitivity. Facilities at Gornergrat, Hohtälli, Stockhorn, Unterrothorn, Trockener Steg, Schwarzsee, and Klein Matterhorn experienced differential settlement and deformation attributed to permafrost degradation, reinforcing the need for long-term monitoring and mitigation adapted to evolving ground thermal conditions (King & Kalisch, 1998; Ulrich & King, 1993). A well-known example is the chairlift at Grächen (2,453 m a.s.l.), constructed on permafrost where a approximately 20 m thick frozen layer had been identified (Phillips et al., 2007). Shortly after construction, significant foundation displacements were observed and one station was eventually abandoned; investigations linked the failure to local melting triggered by the heat released during concrete curing, demonstrating how the construction process itself can perturb the thermal regime and accelerate degradation before the structure is even operational.

Another emblematic case is Jungfraujoch at approximately 3,550 m a.s.l., where the Sphinx observatory was expanded in the 1990s (Wegmann & Keusen, 1998). Extensive investigations included deep borehole temperature and deformation monitoring. During construction, an inverse relationship between temperature increase and deformation was observed, consistent with fracture-ice melting and thermally induced weakening. Thermal modelling incorporating geothermal flux, radiative forcing, and measured boundary temperatures supported the reconstruction of permafrost evolution and informed design

choices, including active cooling and structural measures aimed at reducing heat transfer into the rock mass and maintaining long-term serviceability. The numerical model developed at Jungfraujoch, illustrating the pre-construction baseline, the perturbation induced by the elevator shaft, and the effect of an active cooling system, is shown in Figure 8 and provides one of the earliest examples of the integrated thermal modelling approach adopted for permafrost-affected infrastructure sites. Beyond individual cases, recent syntheses have quantified how widespread permafrost-related infrastructure problems are and which mechanisms are most recurrent. In a comprehensive review in the French Alps, Duvillard et al. (2019) analyzed 947 infrastructures located on permafrost or potentially underlain by permafrost, identifying a subset that experienced repeated damage, severe deterioration, or destruction over roughly three decades, associated with subsidence, creep, frost-related displacement, and rockfall impacts. While severe impacts affect a minority of structures, consequences can be substantial and are likely to increase as warming progresses. In response, modern design strategies increasingly favor adaptation and reversibility (Bommer et al., 2010). The Pardorama restaurant at Ischgl, Austria (2,624 m a.s.l.) is a representative example: after damage to earlier buildings, the current structure is supported by adjustable foundations with hydraulic jacks that allow re-levelling as differential settlement develops. Other common approaches include elevating structures to enhance air circulation, introducing insulation or ventilated coarse fills beneath foundations, and using thermally optimised supports that reduce heat input to the ground. In parallel, monitoring has become standard practice for critical infrastructure, pairing temperature measurements with deformation tracking, using levelling, GNSS, inclinometers, extensometers, GBInSAR and, increasingly, numerical modelling to interpret trends and guide maintenance decisions.

A dimension of the infrastructure problem that has received comparatively less attention is the active thermal perturbation that engineered elements impose on the surrounding rock mass

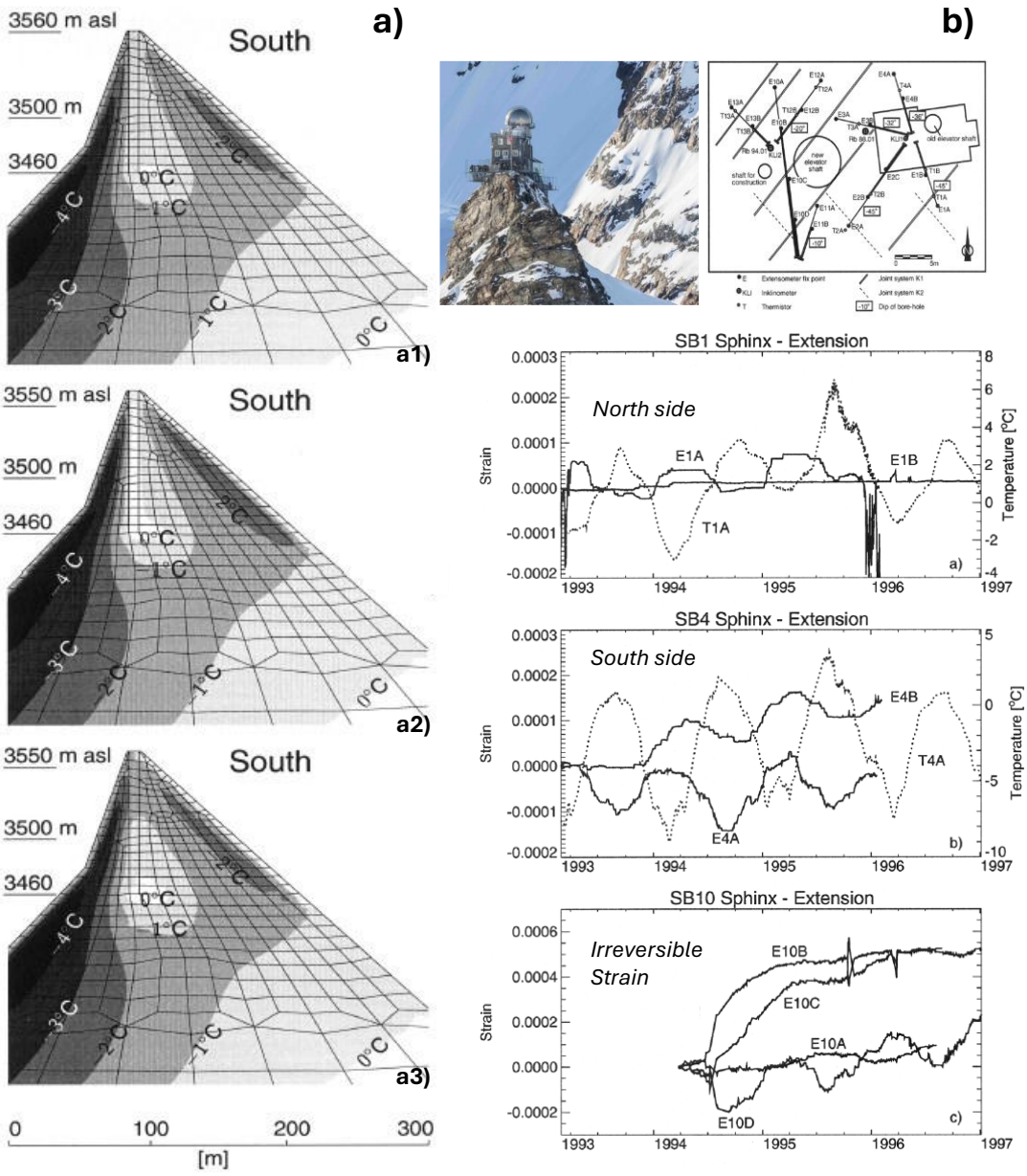


Figure 8 a) Numerical model considering an isotropic material (Wegmann & Keusen, 1998) a1) pre-building a2) with elevator shaft and a3) with cooling system. b) Observatory and monitoring system, in the plot it's possible to observe data before and after the construction with an inverse relationship between temperature and displacements, with irreversible strain caused by excavation of the shaft and ice melting inside the fracture.

Concrete shafts, foundation galleries, and heated interiors act as persistent heat sources that can create localized warm anomalies extending several meters into the surrounding bedrock, potentially destabilizing ice-bearing discontinuities that would otherwise remain frozen under natural boundary conditions. The spatial extent and intensity of such perturbations depend on the thermal contrast between the structure and the surrounding rock, on the geometry of the installation, and critically on the background permafrost conditions, meaning that the same infrastructure may have very different impacts

789 depending on elevation and aspect. Quantifying these structure-induced thermal
790 anomalies and evaluating their implications for foundation stability and for the
791 surrounding natural rock mass, represents the focus of Chapter 6, where the Punta
792 Helbronner cable-car station on the Mont Blanc massif is used as a case study to address
793 Research Question 5.
794

Chapter 3
INTEGRATED GBINSAR AND THERMO-MECHANICAL MODELING FOR ROCK SLOPE DISPLACEMENT ANALYSIS ACROSS GEOMETRICAL COMPLEXITIES

3.1 **Aim**

The focus of this chapter is on the thermo-mechanical behaviour of a large high-mountain rock slope subjected to climatic temperature forcing, in a setting where permafrost is not the dominant control. While Chapter 2 has shown that permafrost degradation plays a key role in many Alpine rock-slope instabilities, it has also emphasized that purely thermal and thermo-mechanical processes such as thermal expansion and contraction, thermo-fatigue and temperature-driven stress redistribution are important in both permafrost and non-permafrost environments.

Most previous numerical studies have either modelled the thermal regime of rock slopes at large scales using purely conductive models or investigated thermo-mechanical effects at small scales (meters to tens of meters) using finite element or distinct element approaches. In contrast, this chapter presents a large-scale, three-dimensional thermo-mechanical finite element (FE) model of a high-alpine rock slope and evaluates its ability to reproduce observed slope deformation measured by ground-based InSAR (GBInSAR). The aim is twofold: (i) to assess how far a continuum thermo-mechanical FE approach can capture the observed spatio-temporal patterns of displacement at slope scale, and (ii) to identify the main controls and limitations affecting such models in a non-permafrost context.

In the framework of the research questions formulated in Chapter 1, this chapter directly addresses Research Question 1: *what are the thermo-mechanical effects directly attributable to the geometry of potentially unstable rock elements, separating geometric controls from geomechanical responses?* By systematically varying slope morphology from idealized pillar and convex wall geometries to real Alpine cliff topographies and by projecting numerical outputs along the radar line of sight for direct comparison with

GBInSAR measurements, the chapter establishes that geometry is not a secondary modulator of thermally induced deformation but its primary control. The results provide the methodological and conceptual baseline that the subsequent chapters extend to permafrost-affected settings, where phase-change processes and irreversible structural kinematics are superimposed on the purely thermo-elastic response characterised here.

3.2 **Study areas and geological–climatic setting**

Thermo-mechanical finite element framework is applied to two representative non-permafrost rock slopes in the Italian Alps: Scaiùn cliff in Val Masino (Central Alps) and Monte Colodri in the Sarca Valley (Southern Alps) (Figure 9). Although they differ in lithology, structural setting and elevation both sites are characterised by steep, highly fractured rock faces directly overlooking inhabited areas and transport or recreational corridors. In both cases, diurnal and seasonal temperature gradients, combined with complex discontinuity networks, provide favorable conditions for thermally driven stress redistribution and rock-mass damage in the absence of permafrost. These two slopes therefore offer complementary testbeds to investigate large-scale thermo-mechanical behaviour in non-frozen rock masses and to assess the capability of the modelling approach to reproduce observed deformation patterns derived from GBInSAR monitoring data.

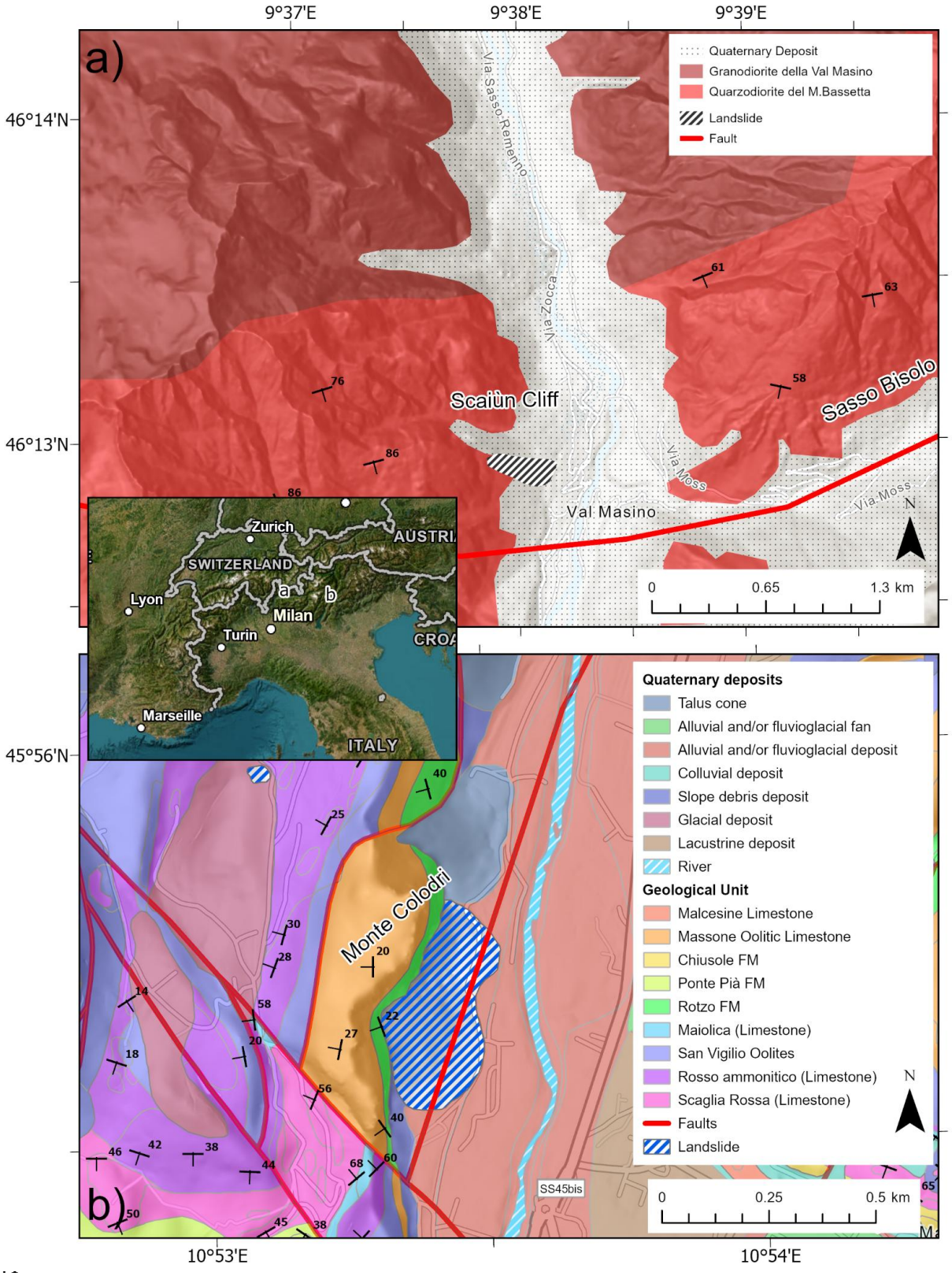


Figure 9: Location and geological maps of the two study areas in the Italian Alps: (a) Scaiùn cliff, Val Masino-Cataeggio (SO); (b) Monte Colodri, Arco di Trento- (TN).

3.2.1 *Scaiùn cliff (Val Masino, Central Alps)*

Val Masino is a tributary valley of the Valtellina Valley in Northern Italy (Figure 9a), characterised by a rugged, high-relief Alpine landscape with elevations ranging from about 580 m a.s.l. (Ponte del Baffo) to 3,678 m a.s.l. (Monte Disgrazia). The morphology reflects a glacially shaped valley system framed by steep slopes and narrow ridges.

From a geological point of view, the area lies north of the Tonale Tectonic Line and is predominantly underlain by intrusive rocks of the Tertiary Val Masino pluton. Metamorphic units of the Margna Crystalline Complex and the Languard–Tonale system also occur locally, consisting of mica schists, gneisses, quartzites and amphibolites with variable foliation. South of the Tonale Line, the structural framework is governed by major lineaments such as the Val d'Agua Line and the Cataeggio Fault, which control lithological boundaries and the dip direction of structural surfaces, generally trending northwards.

Quaternary surface deposits are heterogeneous and include Late Glacial and Holocene moraines, talus cones, alluvial fans, river terraces and peat-rich infill of glacially overdeepened basins. The slopes of Val Masino have a long history of rock-slope instabilities, mainly large-block rockfalls and rockslides. Notable examples are the failures at Sasso Bisolo Mt–Pezza in 1931, 1977 and 1991, influenced by local quarrying and strongly controlled by the foliation in the serizzo gneiss (Crosta, 1992), and a large rockfall at Ponte del Baffo in 1961.

Among the most critical slopes is the Scaiùn cliff, located above the village of Cataeggio at the south-eastern margin of the Masino–Bregaglia pluton. The rock face is composed of tonalite and granodiorite (locally termed serizzo) and is fringed by extensive debris cones and boulder fields at its base, attesting to intense and recurrent rockfall activity. Decametric boulders are embedded within the built-up area, highlighting the long-term exposure of the village to rockfall hazard.

The rock mass is structured by several joint sets. The two dominant families, K1 (163/59°) and K2 (165/86°), define the primary release planes. Additional joint sets K3 (69/86°), K4 (94/53°) and K5 (263/81°) contribute to lateral delimitation and form isolated rock prisms prone to planar sliding and toppling. These structural conditions were confirmed by photogrammetric analyses and GBInSAR data following the 4 February 2019 rockfall, which involved more than 7,900 m³ of rock and highlighted the role of persistent discontinuities and foliation-parallel failure surfaces (Dei Cas et al., 2021). Laboratory

877 tests indicate a linear thermal expansion coefficient for the serizzo of about 0.0061 mm/m
878 °C.
879 The regional climate is Alpine, with cold winters and mild summers. The mean annual
880 daytime temperature is approximately 10 °C, while mean nocturnal values are around 1
881 °C, yielding a mean daily temperature of about 6 °C. In summer, average temperatures
882 range between ~20 °C during the day and ~11 °C at night, whereas in winter they decrease
883 to about –1 °C (daytime) and –9 °C (night-time). Mean annual precipitation is around
884 1,980 mm, of which roughly 80–85 % falls as rain and the remainder as snow or hail.
885 June is typically the wettest month, while January is the driest. These conditions imply
886 strong seasonal thermal gradients in the cliff, but permafrost is not expected at the
887 elevation of Scaiùn, so thermo-mechanical processes act in a non-permafrost context.

888 3.2.2 *Monte Colodri (Sarca Valley, Southern Alps)*

889 The second study area is Monte Colodri, a prominent carbonate cliff overlooking the town
890 of Arco in the southern part of Trentino (Autonomous Province of Trento) (Figure 9b).
891 Arco is located in the middle Sarca Valley north of Lake Garda, at an elevation of about
892 90 m a.s.l., and is surrounded by steep limestone and dolomite massifs. Major reliefs in
893 the area include Monte Brento (1,545 m) and Monte Casale (1,632 m) to the north; Monte
894 Stivo (2,059 m), Monte Velo and Monte Creino to the north-east; and Monte Biaìna
895 (1,413 m), Monte Baone and Monte Colodri to the west. Monte Colodri rises directly
896 above the urban area and is a well-known destination for rock climbing and tourism.
897 Geologically, the area belongs to the Southern Alps, within the Trentino Platform domain
898 (CARG sheet 080 “Riva del Garda”, ISPRA). It lies within a major structural bundle
899 trending predominantly NNE–SSW, bounded to the west by the Ballino Line and to the
900 east by the Adige Valley Line. Monte Colodri is located between the Rudere di San
901 Martino fault and the northern branch of the eastern Val Lomasone fault (LOE). These
902 tectonic structures define uplifted structural prisms bounded by high-angle reverse faults
903 and associated transpressional features, mainly formed during the Valsuganese phase
904 (Upper Miocene).
905 Monte Colodri is largely composed of Mesozoic carbonate rocks, predominantly Dolomia
906 Principale (Upper Carnian–Norian) and, to a lesser extent, Grey Limestones (Lower Lias)
907 (Castellarin, Picotti, et al., 2005). Dolomia Principale crops out as thick, light-grey, well-
908 bedded banks affected by intense fracturing and locally overprinted by secondary

faulting. Surface and deep karst features are common. This combination of lithology, fracturing and karstification makes the slope highly susceptible to rockfall and localized instabilities.

The main joint sets structuring the rock mass are K1 (65/66°), K2 (18/82°) and K3 (298/83°), which together define potential release planes and wedges. Rockfall events, local detachments and toppling have been repeatedly reported and mapped in the IdroGEO national inventory, confirming active instability in the cliff sector overlooking the town and climbing routes.

The local Alpine climate is significantly modulated by the presence of Lake Garda, which produces relatively mild conditions compared to the inner Alps. Summers are warm, with maximum conditions in July characterised by mean daytime temperatures of about 23 °C and nocturnal values around 14 °C. Winters are cool but not extreme, with January mean daytime temperatures of about 2 °C and nocturnal averages around –6 °C. On an annual basis, the mean temperature is approximately 8 °C, with average daytime and night-time values of about 13 °C and 4 °C, respectively. Mean annual precipitation is on the order of 1,900–1,950 mm, with a marked maximum in late autumn (typically November) and rain accounting for roughly 85 % of total precipitation. Snow and hail represent the remaining fraction and are generally confined to the coldest months.

Also in this case, permafrost conditions are absent at the elevation of Monte Colodri, but strong diurnal and seasonal temperature gradients, combined with the fractured carbonate rock mass and karst features, provide an ideal setting to investigate large-scale thermo-mechanical effects in non-permafrost rock slopes.

3.3 **GBInSAR monitoring**

GBInSAR data provide the main constraint on slope-scale kinematics at both Scaiùn and Monte Colodri and are used in this chapter to quantify displacement patterns and to evaluate the performance of the thermo-mechanical finite element models. In both sites, radar measurements capture millimetric to centimetric displacements over seasonal time scales, allowing the separation of thermally driven, reversible components from longer-term trends.

3.3.1 *Scaiùn cliff*

A permanent Ground-Based interferometric Synthetic Aperture Radar (GBInSAR; LiSALab, operated by Ellegi Srl) is installed on the western side of Val Masino at an elevation of ~800 m a.s.l. The system images the east-facing Scaiùn cliff across the valley with an oblique, upward-looking line-of-sight (LOS) that covers elevations up to more than 1,500 m a.s.l. In the adopted sign convention, negative LOS displacements correspond to movement towards the radar (i.e. downslope components), whereas positive LOS displacements indicate motion away from the radar (i.e. upslope components).

In 2024, the system acquired more than 300 radar images. For the purposes of this study, the data were processed using 24-hour averages, in order to reduce short-term atmospheric artefacts and thermal noise while preserving the seasonal signal. The resulting time series reveal a clear seasonal pattern, with substantial deformation concentrated in the central sector of the slope. In this area, mean annual LOS displacements of about –9 mm were observed, with maximum cumulative values reaching approximately –31 mm over the year. These magnitudes are consistent with previous monitoring years, which showed mean annual displacements of about –9 mm in 2023 and –11 mm in 2022, suggesting a persistent and relatively stable pattern of slow movement. The temporal evolution indicates small, positive LOS displacements during summer, interpreted as thermally induced expansion of the rock mass, possibly linked to joint opening and minor outward bulging. In contrast, autumn and early winter are characterised by pronounced negative displacements, locally up to ~ –10 mm/month, indicating downslope motion towards the radar. These phases are consistent with thermal contraction, joint closure and, potentially, limited frost-related effects in fractures at higher elevations.

A total of 55 Points of Interest (POIs) were defined across the imaged cliff. Only the central group exhibits statistically significant motion above the noise level, with POI #30 reaching a cumulative displacement of –25.1 mm in 2024 (Figure 10). All other sectors, including the southern and northern parts of the cliff and the 2019 collapse area, remain within the instrumental noise threshold (±0.4 mm), indicating overall stability of those portions of the slope. The upward and across-valley LOS geometry is crucial for interpreting these trends, as it enhances sensitivity to downslope movements in the central sector while reducing sensitivity to motion parallel to the cliff face in peripheral areas.

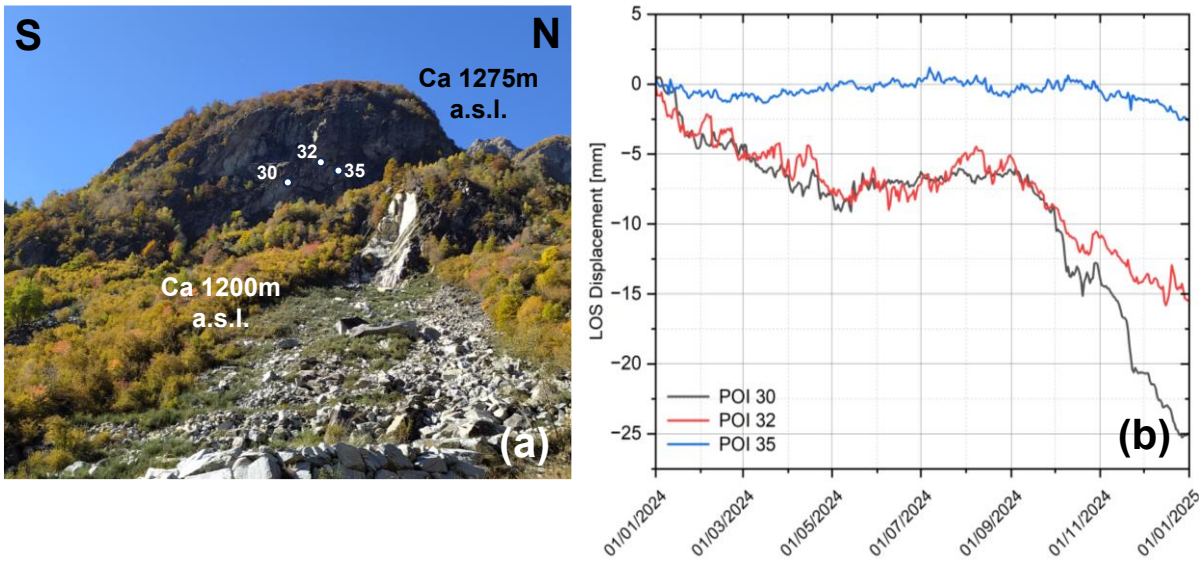


Figure 10 :(a) View of the Scaiùn cliff and monitoring area; (b) Displacement along LOS for POIs #30, #32, #35. The white point indicates the approximate location of the displayed points of observation.

3.3.2 *Monte Colodri*

As described in Section 3.2, the Monte Colodri cliffs are strongly fractured and include two prominent rock pillars with a total estimated volume of ~33,000 m³. These pillars are separated from the main rock mass by sub-vertical discontinuities roughly parallel to the slope, defining potentially unstable prisms. To monitor their stability and the behaviour of the surrounding cliff, a GBInSAR system was deployed episodically at a stable vantage point, and several monitoring campaigns were carried out.

A key campaign took place in July 2024 and lasted three days, twelve hours and nineteen minutes, yielding 1,030 radar images. This dataset was compared with an initial reference acquisition in October 2023 and with a third campaign conducted in April–May 2024. The three datasets together allow the assessment of both long-term deformation over ~266 days (October 2023–July 2024) and medium-term changes over ~80 days (April–July 2024).

During the July 2024 campaign, the slope appeared kinematically stable at short time scales: average LOS displacements over the entire cliff were around –0.1 mm, with a standard deviation of ~0.3 mm, well within the noise level. This is consistent with previous observations and confirms the absence of rapid or accelerating movements during the monitored period.

However, comparison with the October 2023 baseline reveals a more articulated seasonal pattern. The data indicate an initial phase of motion towards the radar during winter, followed by a gradual reversal to motion away from the radar during spring and early summer. This cycle suggests a thermo-mechanical response of the rock mass to daily and seasonal temperature changes, with winter contraction and summer expansion producing small but detectable LOS displacements.

Specific sectors of the cliff, labelled E, E1 and G, show slightly enhanced activity, with peak LOS displacements of about –3.5 mm, –3.0 mm and +1.8 mm, respectively (Figure 11). Despite these peaks, mean displacements in these zones remain below 1 mm. A sector previously considered stable, labelled L, exhibits new deformation signatures during the fourth campaign, with cumulative displacements up to –1.2 mm. This suggests that this area may be more sensitive to thermal forcing or subtle structural changes than previously recognized and warrants closer observation in future campaigns.

The comparison with the April–May 2024 campaign highlights a general trend of backward motion (away from the radar) between late spring and mid-summer, with average displacements ranging between ~0.3 mm and 1.5 mm depending on the sector, and local peaks up to ~4.1 mm. These spatial differences in response likely reflect variations in rock-mass structure, fracture density and exposure to solar radiation along the cliff. Overall, the magnitude and temporal pattern of displacements support the interpretation that the observed movements are primarily thermally driven and do not, at present, indicate imminent structural instability.

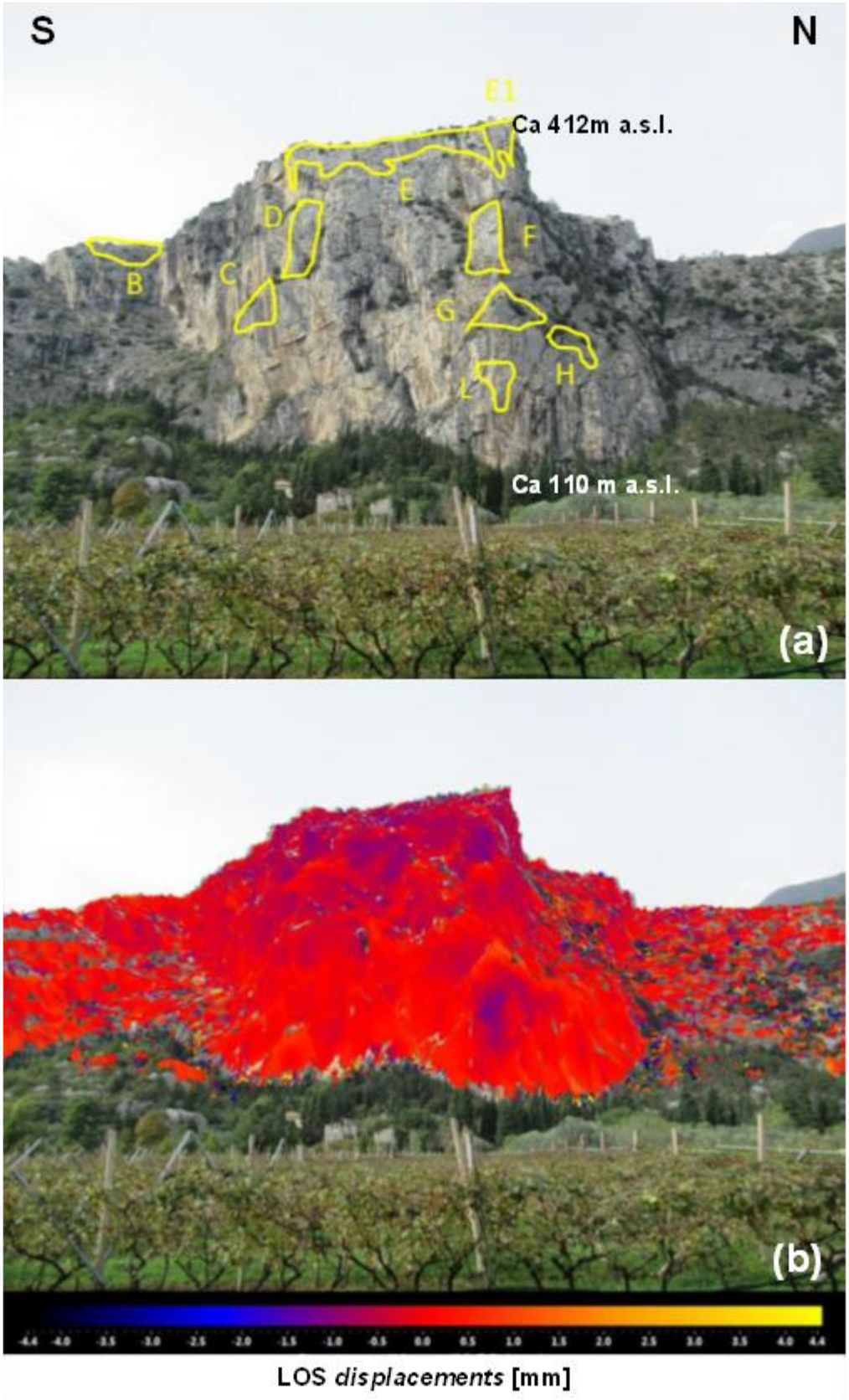


Figure 11 Monte Colodri from frontal view showing:(a) the identified main moving sectors; (b) LOS displacement map for long-term measurements (269 day, October 2023 - July 2024).

The GBInSAR datasets from Scaiùn and Monte Colodri provide spatially distributed, millimetric LOS displacement fields and time series over seasonal to multi-annual time scales in two non-permafrost, thermally sensitive rock slopes. At several POIs the records include both a long-term component, with episodes of acceleration, and a superimposed seasonal signal that correlates with temperature forcing. In this chapter, the GBInSAR information is used in two complementary ways. First, LOS displacement maps computed over selected time windows are compared with synthetic LOS maps derived from the FEM simulations for the same periods, in order to assess whether the models reproduce the observed spatial pattern of deformation; in this case, neither measured nor modelled maps are detrended, and the comparison is mainly qualitative because the FEM results represent only the thermo-mechanical component of deformation. Second, detrended GBInSAR time series at selected POIs are compared with modelled LOS displacement histories at the corresponding locations, focusing on the seasonal component. This dual strategy allows us to jointly evaluate the spatial consistency and temporal phasing of the thermo-mechanical finite element models with respect to the radar observations.

3.4 **Thermo-mechanical numerical modelling**

The overarching goal is to investigate how seasonal thermal forcing translates into stress redistribution and surface displacements at slope scale in rock masses, and to test to what extent a continuum thermo-mechanical finite element (FEM) approach can reproduce the kinematic patterns observed by GBInSAR.

To this end, the modelling strategy is organized in three levels of increasing realism:

1. idealized, simplified geometries, used to explore the basic thermo-mechanical response of steep rock slopes under controlled boundary condition
2. real-geometry models of the Scaiùn and Monte Colodri cliffs, constrained by geological, structural and climatic information.
3. projection of FEM displacements into the radar line-of-sight (LOS) and comparison with GBInSAR data, using both spatial displacement maps and POI time series.

This multi-step approach allows separating general thermo-mechanical effects that depend mainly on slope geometry and material properties from site-specific responses controlled by actual topography, discontinuity patterns and exposure to radiation.

3.4.1 *Mathematical models*

This section briefly introduces the mathematical model used in the subsequent numerical simulations.

A thermal model is based on the energy balance equation, expressed in its integral form as:

$$-\int_{\partial\Omega} q \cdot \hat{n}\, dS + \int_{\Omega} r d\Omega = \int_{\Omega} c\rho \frac{\partial T}{\partial t} d\Omega \quad (1)$$

in which c is the specific heat, ρ is the material density, T is the temperature, r is the source or sink of heat, q is the heat flux vector, $\hat{n}$ is the outward normal vector and Ω is the integration domain while $\partial\Omega$ is its boundary. Furthermore, the heat flux is given by the Fourier's law, given by:

$$q = -\boldsymbol{k}\, \nabla T \quad (2)$$

being $\boldsymbol{k}$ is the conductivity tensor and ∇ is the nabla operator. Since the material is considered thermally isotropic ($\boldsymbol{k} = k\boldsymbol{I}$), equation (1) after substituting equation (2) into (1) become:

$$\int_{\partial\Omega} (k\, \nabla T) \cdot \hat{n}\, dS + \int_{\Omega} r d\Omega = \int_{\Omega} c\rho \frac{\partial T}{\partial t} d\Omega \quad (3)$$

Applying the divergence theorem and since the balance equation must be met for any domain Ω, the above equation becomes:

$$\nabla \cdot (k\, \nabla T) + r = c\rho \frac{\partial T}{\partial t} \quad (4)$$

which is the classical differential equation of heat flow whose main unknown is the temperature function $T = T(t, x, y, z)$.

To fully define the problem, an initial condition is required, having the form:

$$T(t = 0, x, y, z) = T_0(x, y, z) \quad (5)$$

being $T_0(x, y, z)$ is the initial spatial temperature distribution. The boundary domain is divided into two parts: one part ($\partial\Omega_N$) where no heat flux is imposed, that is:

$$q \cdot \hat{n} = -\, k\, \nabla T \cdot \hat{n} = 0 \quad (6)$$

and ($\partial\Omega_D$) where the temperature is imposed, i.e.:

$$T(t, x, y, z) = T_D(t, x, y, z) \quad (7)$$

where $(x, y, z) \in \partial\Omega_D$ and T_D is the air temperature. As no heat source/sinks are considered in the subsequent simulations, the term $r = 0$.

The mechanical behavior of the materials is assumed to be linear elastic, and the following constitutive law is imposed:

$$\boldsymbol{\sigma} = \boldsymbol{K}^{el}\boldsymbol{\varepsilon} \tag{8}$$

being $\boldsymbol{\sigma}$ and $\boldsymbol{\varepsilon}$ are the stress and strain tensors, respectively, $\boldsymbol{K}^{el}$is the elastic stiffness tensor depending on material Young's Modulus and Poisson ratio.

3.4.2 *Overall modelling workflow*

The numerical workflow adopted in this chapter comprises the following main steps:

3.4.2.1 Thermal forcing and boundary conditions

Seasonal thermal forcing is prescribed at the slope surface using temperature boundary conditions representative of each site. These are derived from available climatic data and on-site measurements and reproduce the annual temperature cycle over the rock face. At depth, a fixed temperature or geothermal gradient is imposed, ensuring that the lower boundary remains insensitive to short-period fluctuations. Lateral boundaries are treated so as to minimise artificial lateral heat fluxes.

3.4.2.2 Simplified thermo-mechanical models

Before addressing the real slopes, thermo-mechanical FEM models are set up for two simplified slope geometries that mimic the typical height and inclination of steep Alpine cliffs in granitoid and dolomitic rocks. These idealized models are subjected to the same type of seasonal surface forcing and mechanical loading (self-weight, constraints at the base) as the real-geometry models, but without the complexity of real topography. They are used to explore how slope height, inclination and material parameters control the depth and magnitude of thermally induced stresses and displacements, and to provide a conceptual reference for interpreting the behaviour of the actual sites.

3.4.2.3 Real-geometry thermo-mechanical models

In a second step, three-dimensional thermo-mechanical FEM models are constructed for the Scaiùn and Monte Colodri slopes using digital elevation data and structural information described in Section 3.2. The computational domains extend beyond the

observed cliff faces to reduce boundary effects, and mechanical constraints are applied at the base and lateral boundaries in a way that reproduces the large-scale stress state while allowing realistic deformation of the slope sectors imaged by GBInSAR. The same type of seasonal thermal forcing is imposed at the exposed rock surfaces, with site-specific amplitudes and mean values.

3.4.2.4 Extraction of modelled displacements

For each simulation, three-dimensional displacement fields are computed over the seasonal cycle. These fields are sampled at surface nodes corresponding to the areas imaged by GBInSAR and at selected POIs. In a later step, these displacements will be projected along the radar LOS to generate synthetic LOS maps and modelled time series directly comparable to the GBInSAR measurements.

3.4.2.5 Comparison with GBInSAR

The comparison with GBInSAR is carried out at two levels. First, cumulative LOS displacement maps over selected time windows are used to assess whether the models reproduce the main spatial pattern of deformation (active vs. stable areas, sign of movement, relative intensity among sectors). In this case, neither the FEM nor the GBInSAR maps are detrended, and the comparison is mainly qualitative because the FEM simulations represent only thermo-mechanical deformation, whereas the radar maps include all deformation components. Second, detrended GBInSAR time series at selected POIs are compared with modelled LOS displacement histories at the same locations, focusing on the seasonal component. This provides a more quantitative test of the thermo-mechanical response simulated by the models.

In the following, the setup and results of the simplified geometry models are first presented, followed by the real-geometry simulations for Scaiùn and Monte Colodri and the detailed FEM–GBInSAR comparison.

3.4.3 *Simplified geometry thermo-mechanical models*

Thermo-elastic analyses were first carried out on simplified geometries to investigate the response of steep rock slopes subjected to sinusoidally varying external temperature conditions. The goal of this preliminary work is to clarify the main thermo-mechanical processes and provide a reference framework for interpreting the more complex real-geometry simulations.

3.4.3.1 Pillar geometry

The first simplified model consists of a prismatic pillar with trapezoidal base embedded in a surrounding model box. The pillar is discretized into 288 sub-volumes using 8 horizontal, 3 vertical and 7 oblique planes. The mesh comprises 134,934 linear tetrahedral elements and 25,948 nodes (Figure 12). The material properties, denoted as Set 01 in Table 1

Table 1 Parameters of material used in numerical analysis.

PARAMETER	Set 01	Set 02
Young's module $[N/m^2]$	7.50E+10	1.00E+10
Poisson's ratio [-]	0.3	0.3
Unit weight $[kN/m^3]$	27.4	25
Thermal Expansion Coefficient $[1/K]$	8.00E-06	5.00E-06
Thermal Conductivity $[J/(m \cdot day \cdot K)]$	260000	216000
Specific Heat $[J/(kg \cdot K)]$	900	900

Mechanical boundary conditions

To prevent rigid-body motion, displacement constraints are applied:

- along the z-direction on surface 2
- along the x-direction on surface 1,
- along the y-direction along the intersection between surfaces 1 and 2.

This combination removes rigid translations and rotations while allowing thermo-elastic deformation of the system.

Thermal boundary conditions

Convective boundary conditions are applied to all external surfaces except surfaces 1 and 2, where a no-flux condition is imposed. The prescribed air temperature varies according to:

$$T(t) = T_0 + Asin\left(\frac{2\pi}{t_p}t + \varphi_0\right) \quad (9)$$

where T_0 is the initial temperature, A is the temperature amplitude, t_p is the period, and φ_0 is the initial angle phase. Hence, the maximum and minimum temperatures are $T_0 + A$ and $T_0 - A$, respectively. This function approximates real meteorological data collected at a weather station. The initial condition for the entire system was a uniform temperature of $0°C$.

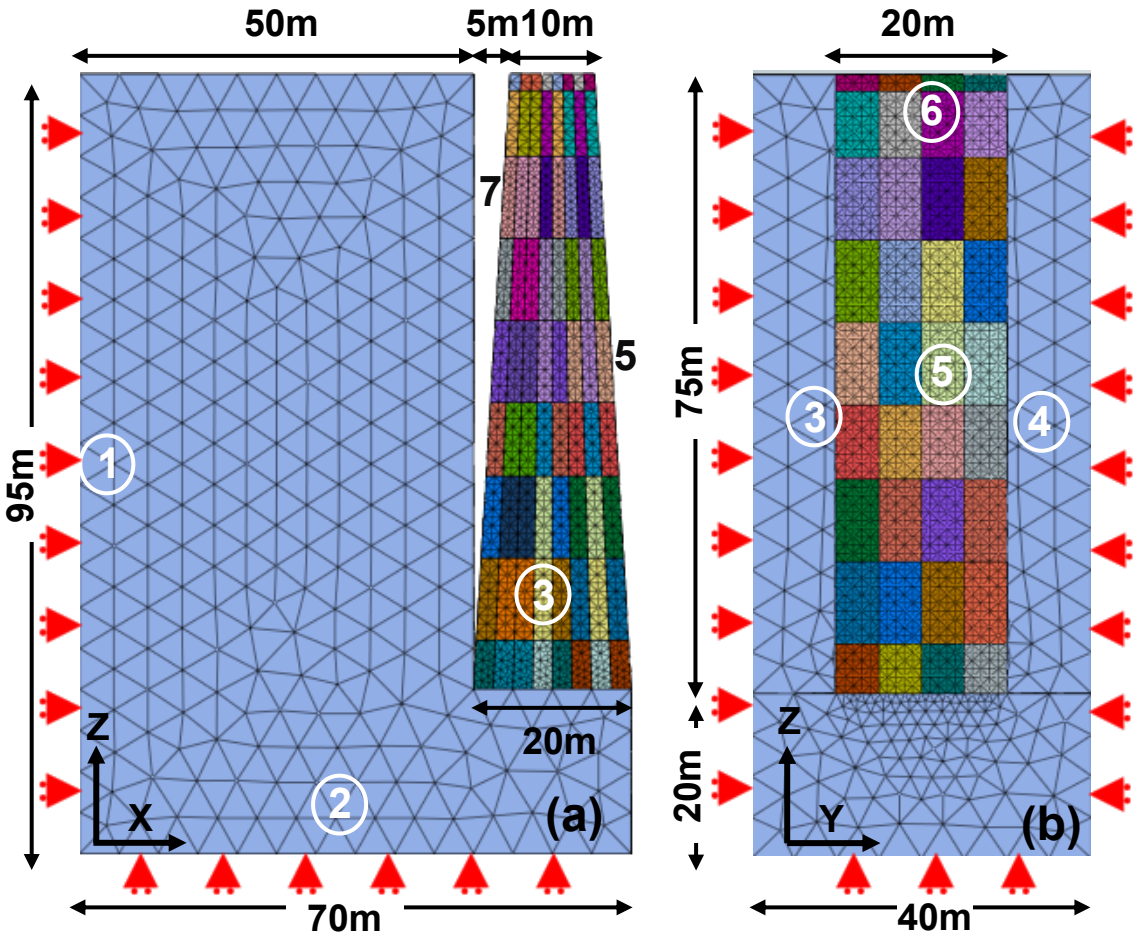


Figure 12 Simplified pillar shape with a surrounding area (model box) and corresponding mesh used in the analyses: (a) Lateral view; (b) Frontal view. The different colors represent the 288 portions generated from horizontal, vertical, and oblique planes. The minimum mesh size is 1 m and the maximum one is 15 m. Numbers within circles refer to the surface identification. Surfaces (1) and (2) represent the faces of the domain where displacement constraints (red symbol) and no-flux conditions were applied. At surface (3), (4), (5), (6), and (7) the temperature input signals were applied.

The analysis is structured in three stages:

1. application of gravity to establish an in-situ stress state.
2. clearing of the computed displacements, so that subsequent displacements represent only thermo-elastic effects.
3. application of the thermal load over many years to simulate the seasonal cycle.

The results show a thermal front propagating into the domain with a delay relative to the boundary input (Figure 13). Beyond the first year, still influenced by initial conditions, the temporal evolution becomes periodic. Because the pillar is small relative to the model

box, its thermal regime is mainly controlled by the boundary conditions; the box acts as a thermal reservoir, storing heat in summer and releasing it in winter.

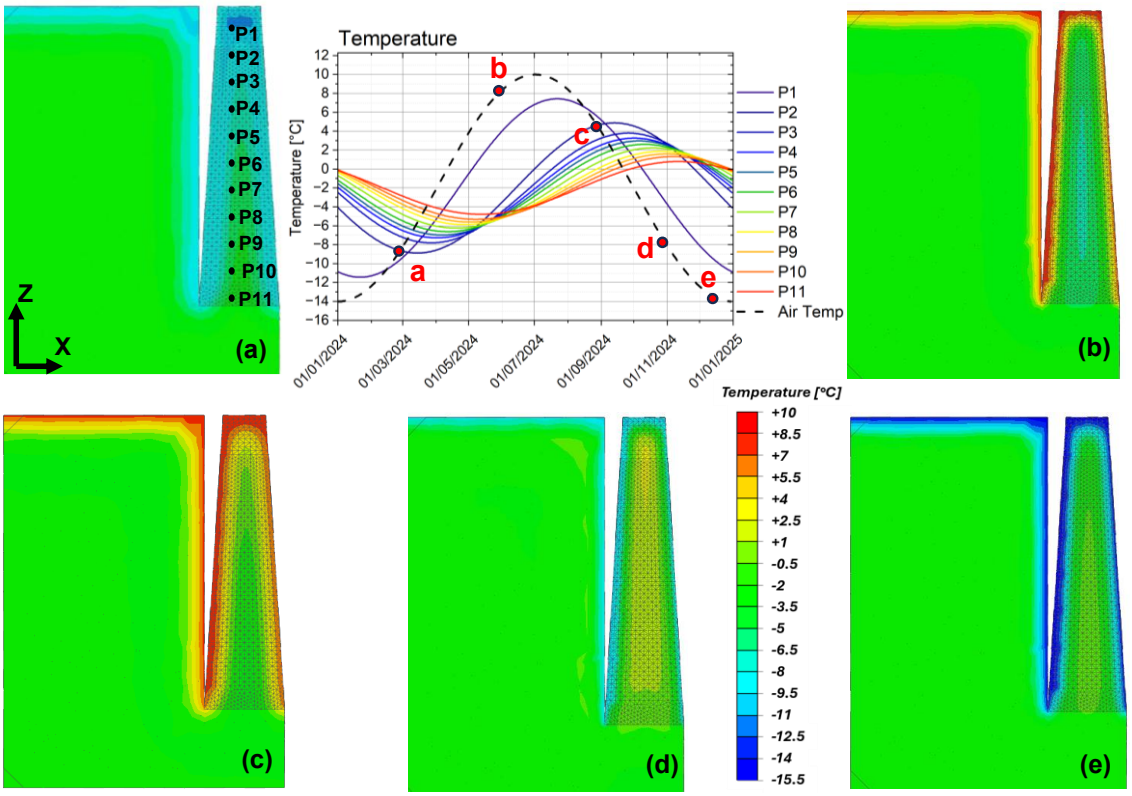


Figure 13 Numerical results for simulation with the homogeneous external temperature: (a-e) Pillar geometry cross section showing the temperature distribution at different time instants during the year. Figures (a, c) represent the minimum and maximum air temperatures, respectively; other figures (b, d, e) are intermediate values. In the plot the input sinusoidal air temperature (dashed line) and the temperature for 11 different points along the central vertical of the pillar, are represented (continuous lines).

Temperature inhomogeneities within the pillar translate into inhomogeneous strain and stress fields, producing non-uniform displacements (Figure 14). At the macroscopic scale, the pillar deflects, with the top moving in the *x*-direction. The magnitude and direction of deflection vary throughout the year, between roughly +0.002 m and −0.004 m at the top. During cold months, internal temperatures remain higher than the sub-zero ambient air; during warm months, the pillar core exceeds 0 °C. The pillar therefore undergoes seasonal expansion in summer and contraction in winter (Figure 14a-d-e). In winter it appears smaller than its initial configuration (black outlines in Figure 14) due to contraction; similar behaviour is observed in spring when the cold front reaches the pillar center. In summer and autumn, the pillar appears larger due to expansion (Figure 14b-c). Real displacements are on the order of millimeters and are visually amplified in the figures.

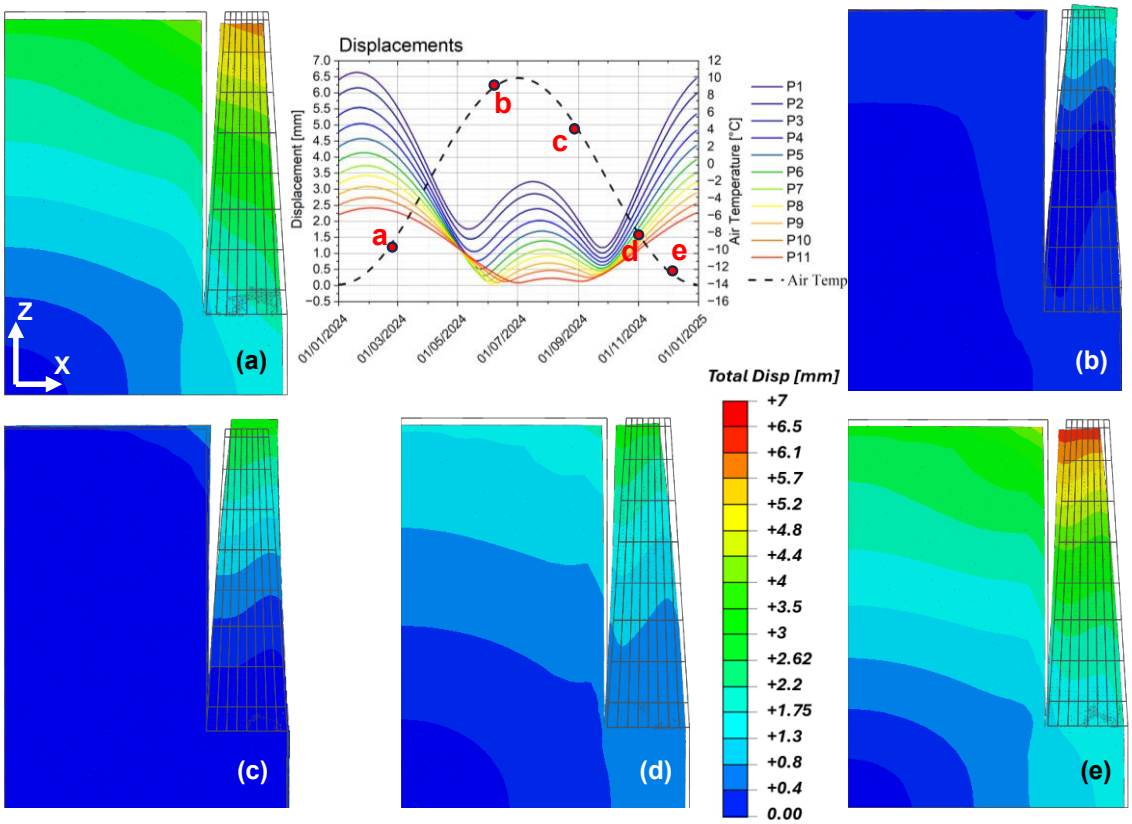


Figure 14 Numerical results for simulation in which the homogeneous external temperature is imposed displacement at different time instants (corresponding to those in Figure 13). The graph shows the total vertical displacement for points P1 to P11 together with the imposed external air temperature.

Subsequently, a second simulation was run to account for reduced solar exposure on the north face. The pillar's lateral surfaces were grouped according to the imposed boundary conditions. For faces 3, 5 and 6, the same sinusoidal boundary condition was maintained. For faces 4 and 7, an additional vertical temperature gradient was imposed, from −1 °C at the top to −4 °C at the base, linearly interpolated with height and superimposed on the sinusoidal function applied to faces 3, 5 and 6.

This gradient produces an asymmetric temperature field and, consequently, an asymmetric deformational response. Warmer portions of the pillar experience larger thermal expansion than colder zones, generating differential deformation across cross-sections (Figure 15). The global response is torsional, with progressive rotation of the pillar's longitudinal axis. In Figures 5–7, dashed lines represent air temperature, while continuous lines show temperature or displacement time series at points P1–P11.

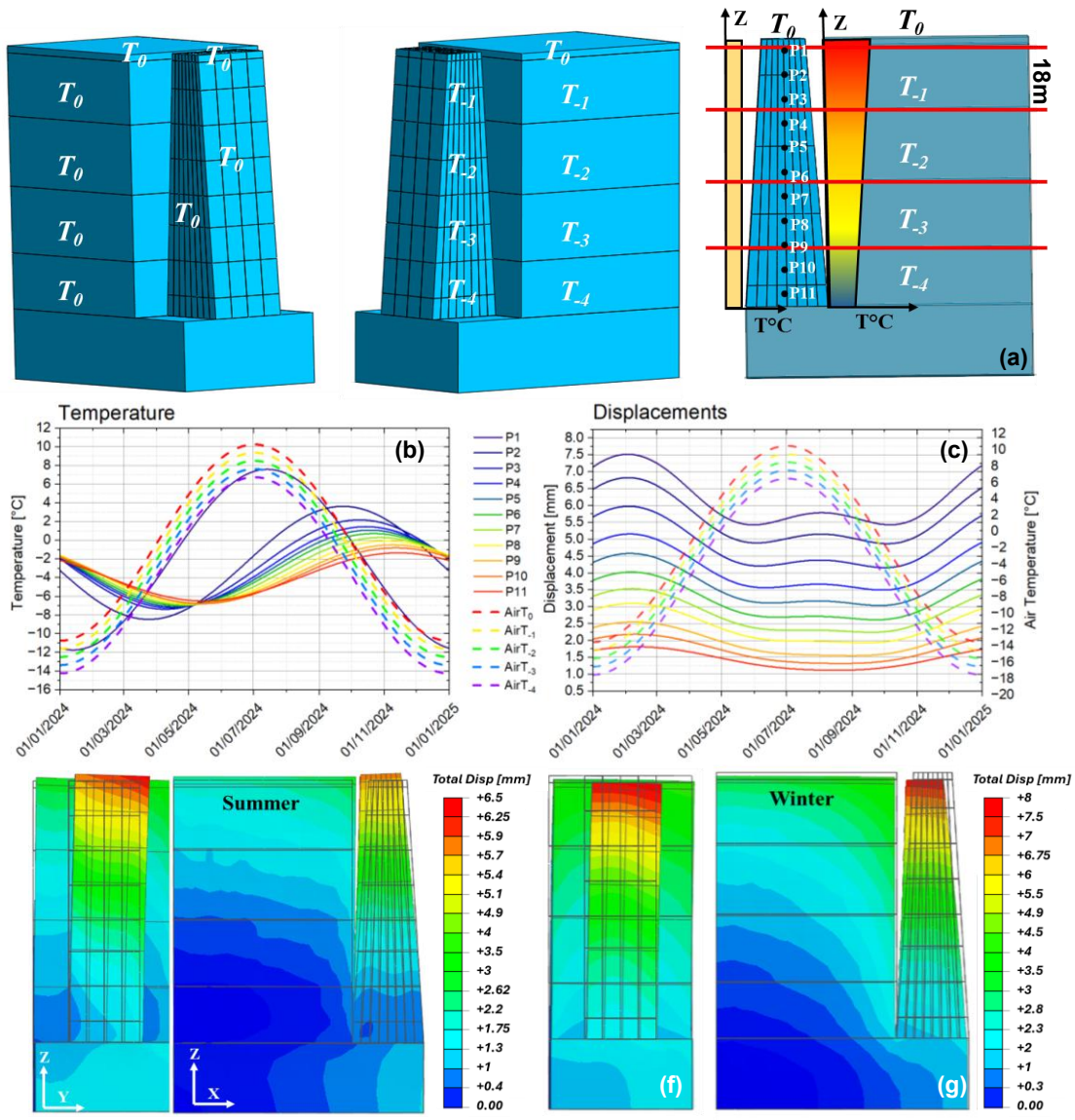


Figure 15 Different air temperature time series as a function of face exposure(a) applied to domain. Total displacement results for: (d) Frontal view during summer season; (e) Lateral view during summer season; (d) Frontal view during winter season; (g) Lateral view during winter season. The graphs show: (b) Temperature distribution for the same points (as in Figure 13); and (c) corresponding displacement.

3.4.3.2 Convex rock wall

The second simplified geometry represents a convex rock face (Figure 16), approximated by a half-truncated cone. The half-cone is rigidly connected at its base and rear face to a larger surrounding model box, so the system behaves as a single solid. The box is similar in concept to that used in the pillar model but has larger dimensions (Figure 16). Only half of the domain is modelled, exploiting symmetry to reduce computational cost.

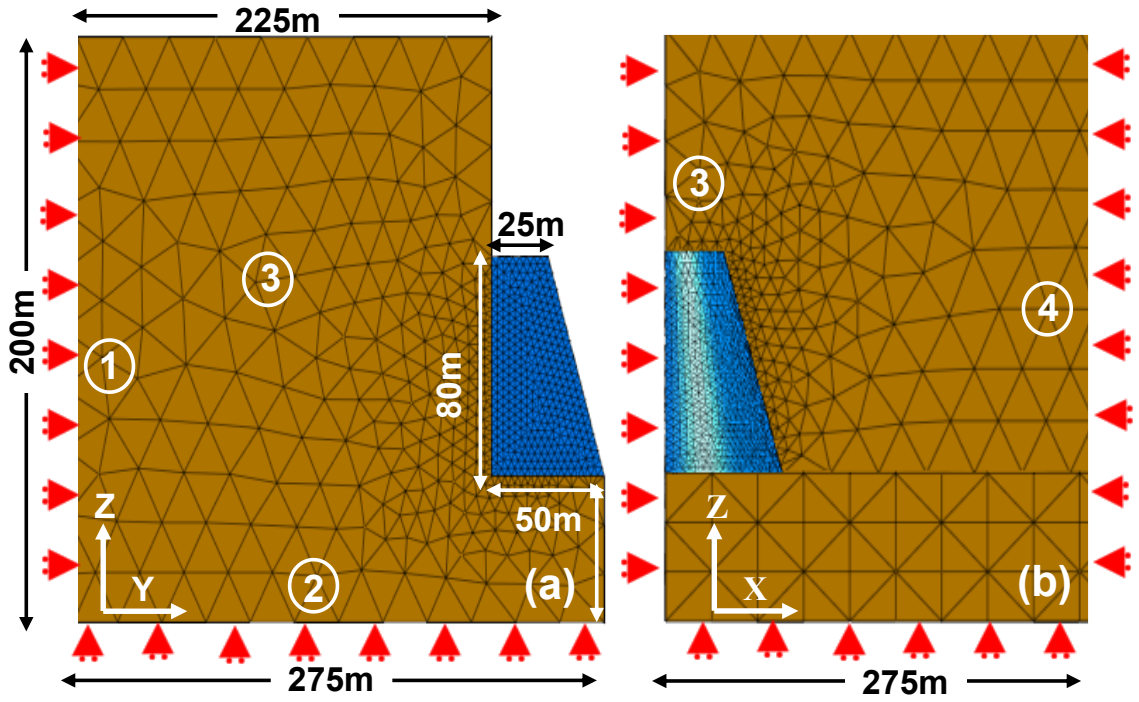


Figure 16 Geometry and mesh of the simplified convex rock wall shape used in the analysis: (a) Lateral view; (b) Frontal view. The mesh size of the convex shape is 2 m, and for the rest of the domain, it varies up to 20 m. Numbers indicate the faces where boundary conditions were applied.

A sensitivity analysis was conducted to define the extent of the surrounding domain so as to avoid boundary artefacts while limiting model size. A width of 275 m was adopted. The mesh consists of 36,492 elements and 7,275 nodes. The material is linear elastic and isotropic, with properties corresponding to Set 01 (Table 1). The mesh size is 2 m on the convex face and up to 20 m in the surrounding box.

Displacement constraints are applied along:

- the *z*-direction on surface 2,
- the *x*-direction on surfaces 3 and 4,
- the *y*-direction on surface 1

Convective thermal boundary conditions are applied to all external surfaces except surfaces 1–4, where a no-flux condition is imposed. The initial temperature is 0 °C, and gravity acts on the entire domain.

Because long-term site-specific thermal conditions are unknown and initial conditions can influence results, the system is first brought to a quasi-steady state by applying a sinusoidal temperature input for 40 years. Displacements are then cleared, and an additional two years of simulation are run with the external temperature function shown in Figure 18b.

Temperature evolution is qualitatively similar to the pillar case: a thermal front propagates into the domain with a phase lag relative to the boundary forcing. Here, however, the convex wall and box form a single body, so thermal inertia acts differently than in the pillar model. Displacement time series extracted after the spin-up (Figure 17) show that vertical displacements along the z-axis are small, as the thickness of the thermally affected layer is nearly constant with elevation.

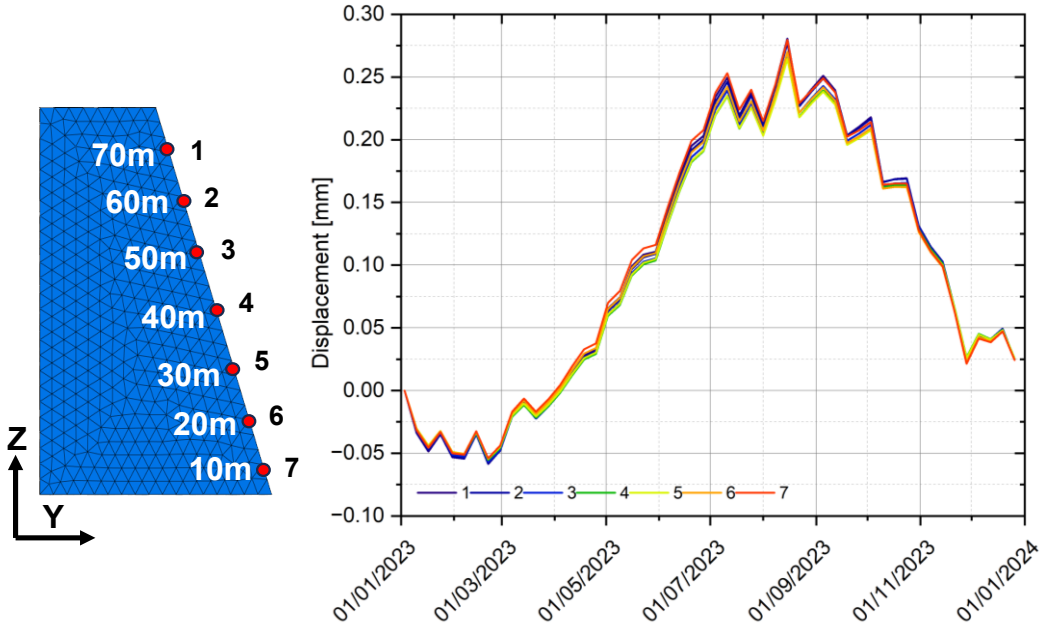


Figure 17 Time series of displacement during one year of simulation along different Z-position in the central part of geometry.

Displacements along the convex surface at constant elevation (Figure 18) reveal that points in the central, more curved sector experience larger displacements than those nearer the edges. Maximum displacements occur in summer, reaching about +0.3 mm in the central area. The ratio between vertical displacement (V, along z) and horizontal displacement $H = \sqrt{x^2 + y^2}$ranges from 0.43 to 0.51, indicating that vertical components account for roughly 40–50% of total horizontal movement (Figure 18d).

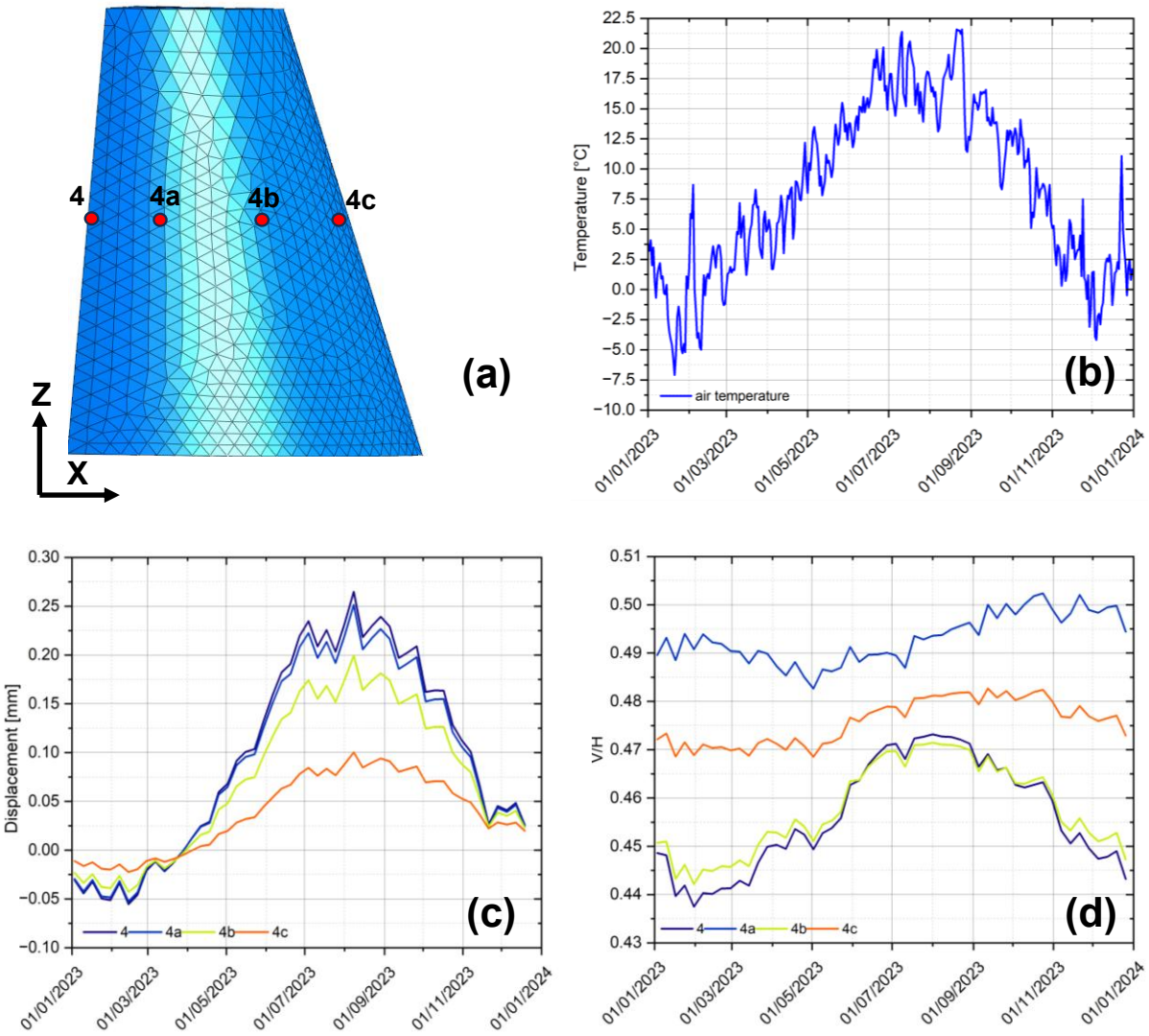


Figure 18 (a) Control points along the convex surface at a fixed Z-elevation; (b) Time series of air temperature adopted for Scaiun case for the year 2023; (c) Total displacement time series for each control point; (d) V/H (vertical-to-horizontal displacements) ratio.

3.4.4 *Real-geometry thermo-mechanical models*

Having explored the simplified cases, thermo-mechanical analyses were extended to the actual geometries of Scaiùn cliff and Monte Colodri. These models incorporate realistic topography and orientation and use site-specific thermal forcing.

3.4.4.1 Topography generation

The 3D geometries of Scaiùn cliff and Monte Colodri were derived from high-density LiDAR point clouds. The raw point clouds contained both terrain and non-terrain elements (e.g. vegetation, temporary structures). They comprised 26,740,890 points (10 cm resolution) for Scaiùn and 6,680,884 points (20 cm resolution) for Monte Colodri.

The clouds were pre-processed in CloudCompare© to improve accuracy and reduce artefacts. Points associated with dense vegetation or irrelevant features were selectively removed. The cleaned clouds were interpolated to generate Digital Terrain Models (DTMs) with 2 × 2 m resolution, chosen as a compromise between geometric detail and computational cost.

From the DTMs, 5 m contour lines were extracted and imported into MIDAS FEA NX to construct the external surface of the numerical domains. This workflow produced 3D surfaces that closely match the observed slope morphologies and provide the geometric basis for meshing and boundary-condition definition.

3.4.4.2 Scaiùn cliff

The mesh used for Scaiùn cliff consists of 95,770 elements and 19,118 nodes. Seasonal temperature forcing is applied at the external surface to reproduce annual air-temperature variations. The initial temperature of the domain was set to -12°C, corresponding to the first value of the thermal input sine wave. This choice was made to prevent excessively high stress levels at the simulation's commencement due to the difference between the initial conditions and the initial value of the boundary condition, which could have adversely affected the displacement outcomes by distorting the thermal and mechanical behavior of the system.

Displacement constraints are applied along the coordinate directions and correspond to no-flux thermal boundaries on specific surfaces, consistent with simplified models. Two types of analyses are performed:

- thermo-elastic analysis with uniform thermal input.
- thermo-elastic analysis with non-uniform thermal input that accounts for slope aspect.

In the second case, two distinct air-temperature time series are applied to north- and south-facing surfaces, with a 10 °C difference to approximate the effect of solar radiation. A MATLAB script is used to compute normal vectors for surface elements (Figure 19a) and to classify them by aspect. Material properties correspond to Set 02 (Table 1), and gravity is applied to the whole domain.

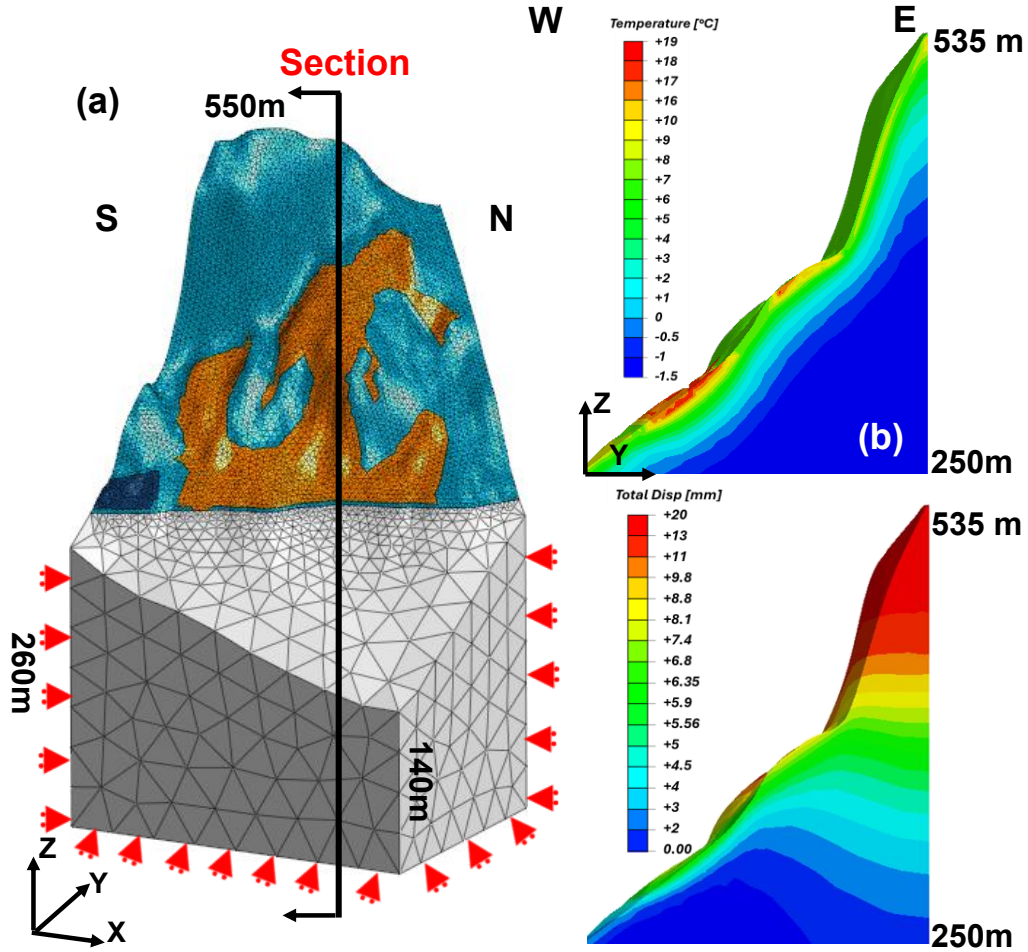


Figure 19 Numerical simulation results with non-uniform thermal input: (a) Scaiun mesh used for analyses and section (black line) (b) and (c) temperature and displacement distributions in the section, respectively, at winter season.

The uniform-temperature simulations confirm and generalize the behaviour seen in the simplified geometries and are not discussed further. In the aspect-dependent case, south-facing surfaces systematically exhibit higher temperatures. This anisotropic boundary condition induces a non-uniform temperature gradient, which controls the internal temperature distribution (Figure 19b) and the displacement field (Figure 19c). Larger deformations occur in areas subjected to higher thermal loads.

3.4.4.3 Monte Colodri

The same procedure is applied to Monte Colodri. The mesh, representing a relatively large area, is partitioned into separate parts to limit computational cost and consists of 82,983 elements and 15,201 nodes. The sinusoidal temperature input is derived from a nearby meteorological station and corrected for elevation. The initial temperature was 0 C.

As for Scaiùn, an initial long simulation is run to reach a steady state; displacements are then cleared, and a subsequent period is simulated to quantify thermally induced displacements. A 10 °C difference is imposed between north- and south-facing surfaces.

Displacement constraints are applied along the z-axis on surface 2, along the x-axis on surface 3 and along the y-axis on surface 1 (Figure 20a-b). These constraints correspond to no-flux boundaries. Gravity is applied to the domain, and material properties correspond to Set 02 (Table 1).

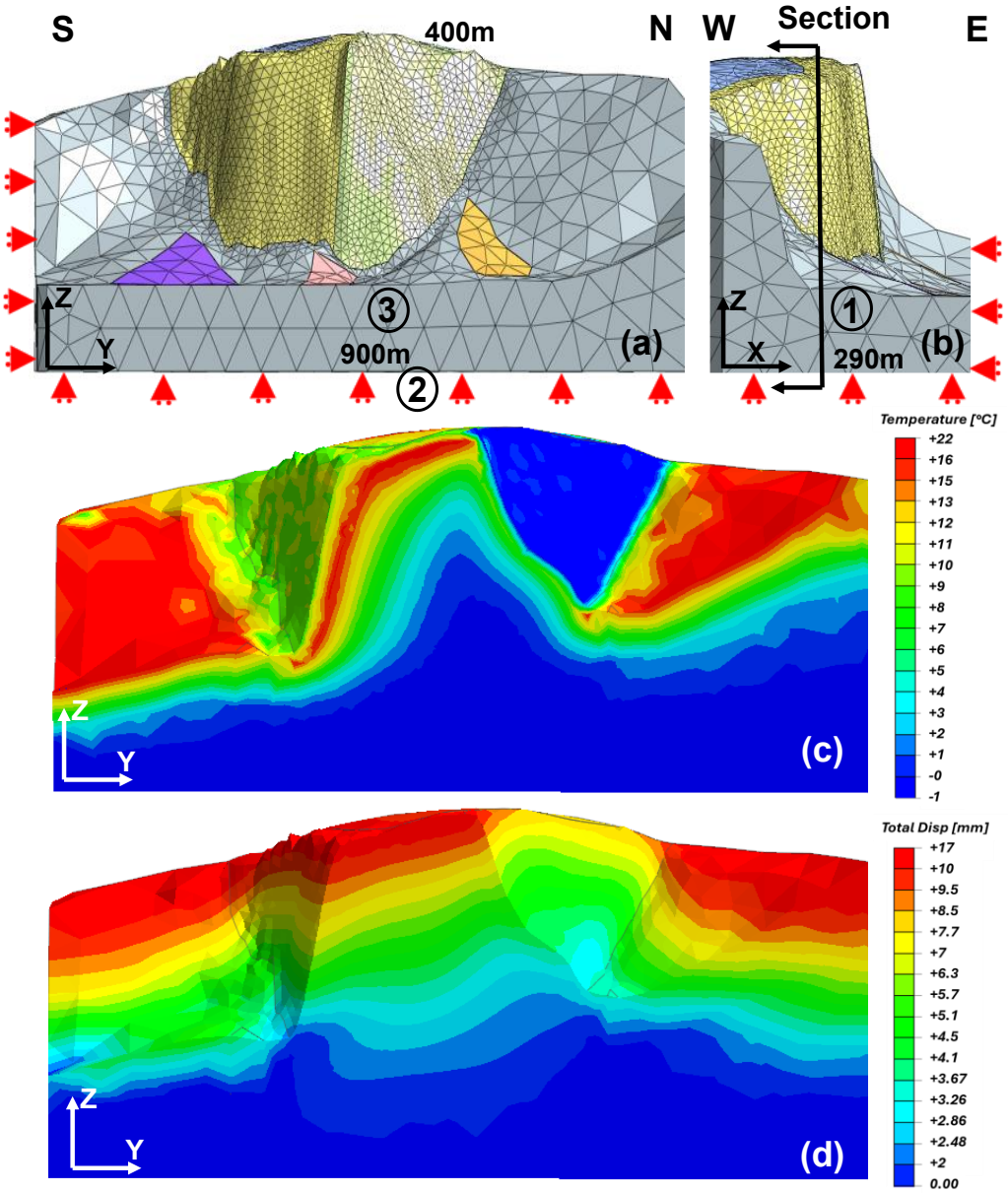


Figure 20 Monte Colodri numerical results at winter season with aspect effect (a) and (b) mesh in frontal and lateral view, respectively with a vertical section (black line); (c) temperature distribution along the section and (d) displacement distribution along the section.

Temperature distribution along a vertical section (Figure 20b-c) clearly shows the influence of aspect, with warmer southern faces and cooler northern faces. This pattern controls the displacement field (Figure 20d), with larger displacements in the southern sector, which expands more than the northern sector in the same direction. Overall, a stretching of the model box and cliff is observed in the direction of maximum thermal expansion.

3.4.5 *Parametric sensitivity analyses*

To assess the influence of the main thermo-mechanical parameters on the model response, a parametric analysis was performed using a Scaiùn mesh. Each parameter varied independently with respect to the reference configuration (Set 02 in Table 1), while all other parameters were kept constant. Table 2 lists the simulations and parameter values.

Table 2 List of performed parametric analyses and values adopted for the parameters together with the refence ones (Set 02). In bold the values changed from the initial ones.

Simulation	Young's module $[N/m^2]$	Specific Heat $[J/(kg*K)]$	Thermal Conductivity $[J/(m*day*K)]$	Thermal Expansion Coeff $[1/K]$
Set 02	1.00E+10	900	216000	5.00E-06
Para_E01	**5.00E+10**	900	216000	5.00E-06
Para_E02	**1.00E+09**	900	216000	5.00E-06
Para_K01	1.00E+10	900	**172800**	5.00E-06
Para_K02	1.00E+10	900	**259200**	5.00E-06
Para_Cv01	1.00E+10	**500**	216000	5.00E-06
Para_Cv02	1.00E+10	**1200**	216000	5.00E-06
Para_CET01	1.00E+10	900	216000	**2.00E-06**
Para_CET02	1.00E+10	900	216000	**1.00E-05**

Figure 21 summarizes the results in terms of displacement and vertical stress at a representative node located at the same position as POI 30 (Figure 10). Each panel shows the effect of varying one parameter relative to the reference case: (a) Young's modulus, (b) thermal conductivity, (c) specific heat, (d) thermal expansion coefficient.

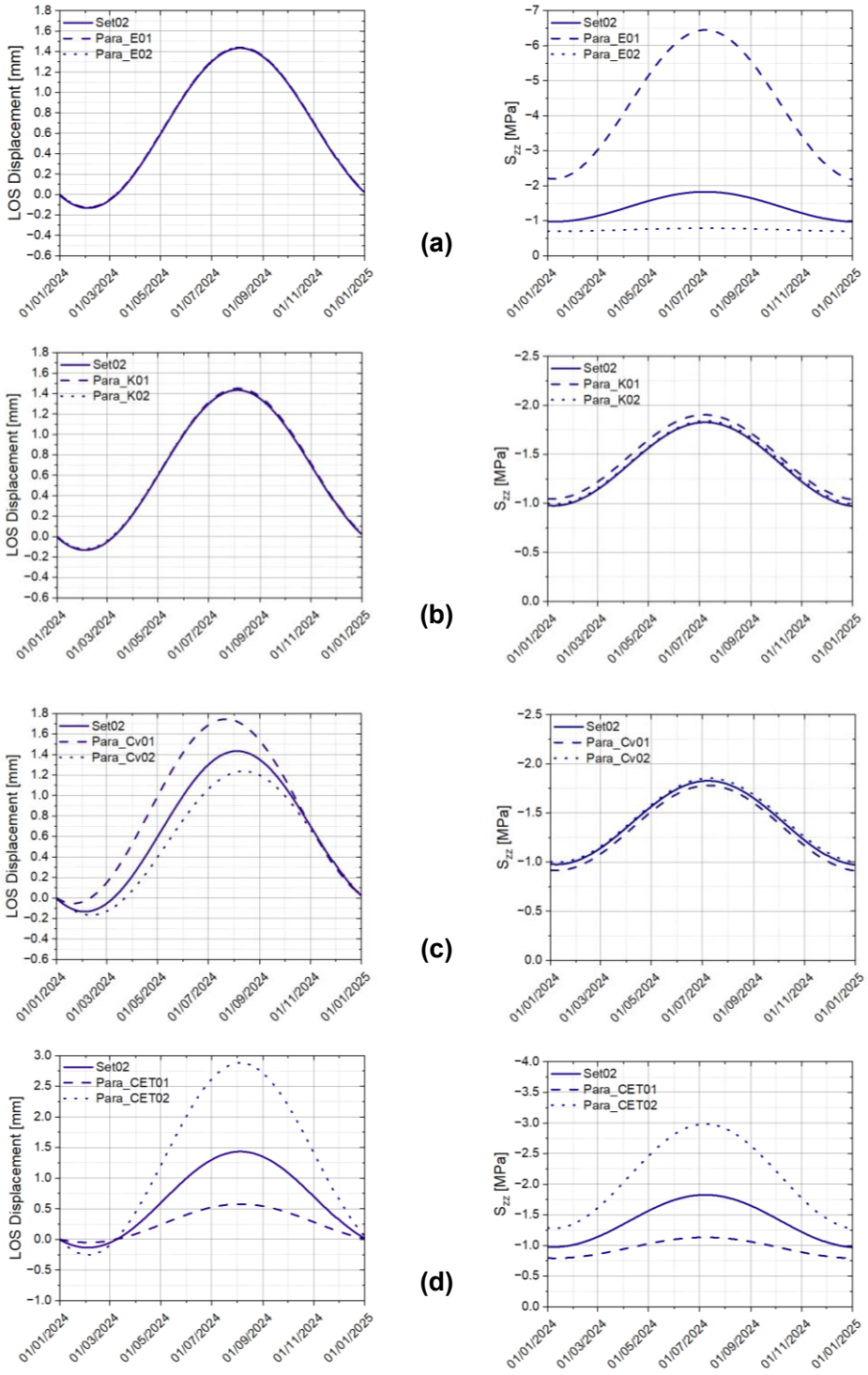


Figure 21 Results of parametric analyses in terms of displacement and vertical stress for each simulation listed in Table 2focusing on a single node and at changing: (a) Young's Modulus (E); (b) Thermal Conductivity(α); (c) Specific Heat (Cv); (d) Thermal Expansion Coefficient variation (CET). The values shown in these graphs are extracted in the same position of POI 30 (Figure 10).

The analysis revealed distinct influences of each parameter on the thermo-mechanical behavior of the system. The elastic modulus (Figure 21a) affects significantly vertical stress, but this does not substantially alter the distribution or magnitude of displacements,

as the induced deformations are primarily governed by the thermal expansion coefficient and the thermal field. It is important to note that if stress variation exceeds the failure condition, changes in stiffness could induce progressive rock degradation.

While thermal conductivity governs the rate of heat diffusion within the domain, it was found to have a marginal effect on both displacement and stress (Figure 21b). Because no modification of the temperature distribution occurs, changes in conductivity do not modify the displacements observed along the line of sight (LOS). Instead, variations in heat diffusion rate primarily influence the time required to reach a given thermal distribution.

The specific heat (Figure 21c) exhibited a direct influence on the thermo-mechanical response. Higher specific heat values indicate a greater thermal capacity of the medium, meaning more energy is required to induce a temperature increase. This effectively dampens thermal gradients over time, leading to a reduction in the amplitude of induced deformations and, consequently, observable displacements. Conversely, lower specific heat values cause the material to heat up more quickly under the same heat flow, forming sharper and more localized thermal gradients that produce more pronounced displacements without significantly affecting the vertical stress field.

The thermal expansion coefficient (Figure 21d) exerts the most direct and proportional control over the displacement field. An increase in the thermal expansion coefficient causes an amplification of the thermally induced deformation, increasing its intensity without altering the spatial distribution of the displacement field. In this case, the vertical stress field is also significantly affected because increasing the thermal expansion coefficient an increment of the vertical stress peak was observed. We stress that in the analyses an isotropic material was considered

3.5 **Integration of thermo-mechanical modelling and GBInSAR data**

The thermo-mechanical finite-element simulations and the GBInSAR observations were jointly analyzed with two complementary objectives: (i) to verify whether a purely thermo-elastic model, parameterized at slope scale, can reproduce the main features of the seasonal displacement signals measured by radar; and (ii) to explore how the viewing geometry and the post-processing choices affect the interpretation of thermally driven

slope deformation. To this end, the comparison was carried out both in the time domain, using detrended point time series, and in the spatial domain, by reconstructing synthetic LOS displacement maps from the FEM results and confronting them with GBInSAR displacement maps for the same sectors of the slopes.

In both case studies, the GBInSAR data show a combination of a long-term trend (interpreted as progressive, partly irreversible deformation and/or damage accumulation) and a seasonal cyclic component largely controlled by temperature. The numerical models, in contrast, describe only the reversible thermo-elastic response of an idealized, homogeneous rock mass subjected to cyclic thermal forcing, without explicitly representing hydrological effects, inelastic processes or spatial mechanical heterogeneities. The integration of the two therefore requires careful preprocessing of the radar time series and an appropriate projection of the FEM displacement field along the radar line-of-sight.

3.5.1 *Detrending of GBInSAR time series and isolation of the thermal component*

For the time-series comparison, the GBInSAR LOS displacements were analyzed at selected Points of Interest (POIs) representing the most active sectors identified in the previous sections

At each POI, the raw displacement time series $u_{LOS}(t)$ typically exhibits:

- a monotonic or weakly accelerating component, attributed to long-term creep, progressive rock-mass damage and/or other non-thermal contributions; and
- a superimposed seasonal oscillation, which correlates with air-temperature variations and is interpreted as thermally driven expansion–contraction of the rock mass.

Since the numerical simulations are designed to reproduce only the seasonal, reversible component, the long-term trend in the GBInSAR data was removed prior to comparison. The detrending procedure adopted is intentionally simple and conservative:

1. **Selection of a reference year**

For each POI, one full year of radar monitoring is considered (e.g. January–December 2024 for Scaiùn), in order to capture at least one complete thermal cycle.

2. Estimation of the non-seasonal trend

A straight line is interpolated between the displacement at the beginning and at the end of the reference period, i.e. between $u_{LOS}(t_{\text{start}})$ and $u_{LOS}(t_{\text{end}})$. This linear function represents the non-seasonal, long-term contribution (combining progressive deformation and possible instrument biases) and is denoted as $\mathrm{u_{TREDN}(t)}$

3. Extraction of the seasonal component

The detrended displacement is then computed as:

$$u_{seasonal}(t) = u_{LOS}(t) - u_{TREND}(t)$$

so that $u_{seasonal}(t)$ isolates the oscillatory component primarily associated with thermal forcing.

4. Comparison with FEM outputs

The detrended GBInSAR series $u_{seasonal}(t)$ is finally compared with the FEM LOS displacement computed at the corresponding position and projected along the same LOS direction. In this way, both curves represent predominantly thermo-elastic responses, even if the radar data may still retain minor contributions from other processes.

3.5.2 *Reconstruction of FEM-based LOS displacement maps*

While time-series analysis allows a pointwise comparison, one of the keys aims of this work is to reconstruct slope-scale displacement fields from the FEM simulations that are directly comparable with GBInSAR LOS maps. To this end, a dedicated post-processing workflow was developed to convert the 3D FEM displacement field into synthetic radar-like maps.

The procedure can be summarized as follows:

1. Selection of reference and comparison times

For each real geometry (Scaiùn and Monte Colodri), the thermo-elastic model is run over multiple synthetic years until a dynamic steady state is reached. The displacement field at the last day of the previous synthetic year is chosen as reference configuration. All subsequent displacements are expressed as increments with respect to this reference, mimicking the way GBInSAR maps show displacements relative to an initial epoch.

2. Projection along the radar line-of-sight

For every FEM node located on the slope surface, the total 3D displacement vector $u(x, y, z, t)$ is projected along the radar LOS direction $n_{LOS}(t)$ using:

$$u_{LOS}(t) = u(t) * n_{LOS}$$

The LOS direction is defined according to the actual geometry of the GBInSAR installation (upward and across-valley configuration for Scaiùn; frontal, slightly oblique view for Monte Colodri).

3. Definition of a radar-like angular grid

Instead of working in Cartesian coordinates, the synthetic maps are built in a radar coordinate system, discretized in azimuth and zenith angles. The angular ranges corresponding to the illuminated slope are subdivided into regular cells, each representing one "pixel" of the radar image.

4. Aggregation of nodal values into LOS cells

For each cell of the angular grid, all FEM nodes whose direction, as seen from the radar position, falls within the azimuth/zenith bounds of that cell are identified. The LOS displacement values of these nodes are then aggregated (typically using the mean or median) to assign a single LOS displacement to the cell. Cells without nodes remain empty and appear as gaps in the synthetic map.

5. Choice of cell size and resolution

Several combinations of angular cell size were tested. Large cells tend to smooth the displacement field and improve spatial continuity but may hide localized patterns; very small cells better capture spatial variability but create many empty cells due to limited nodal density. For Scaiùn, a cell size of about 0.45° × 0.45° was found to provide a reasonable compromise between detail and completeness, whereas for Monte Colodri a 1.2° × 1.2° grid was adopted to reduce empty areas and obtain a continuous map while maintaining meaningful spatial resolution.

6. Selection of representative months

For Monte Colodri, four synthetic maps were produced for months representative of the main seasons (January, March, July, November), in order to visualize the full seasonal cycle of thermo-elastic response. For Scaiùn, maps were generated for the period corresponding to the summer maximum (e.g. July), which is most relevant for comparison with the radar data.

Importantly, no detrending is applied to the FEM maps: the displacements represent the incremental thermo-elastic response during the selected synthetic year relative to the chosen reference configuration. The detrending procedure is used only for the GBInSAR time series at selected POIs, not for the spatial maps. As a consequence, FEM maps inherently show only the thermal component, whereas GBInSAR maps integrate thermal and non-thermal contributions accumulated over the considered time window. This introduces an inevitable amplitude difference but does not prevent a qualitative comparison of the spatial patterns of deformation.

3.5.3 *Data Elaboration and model validation*

3.5.3.1 Scaiùn cliff

After isolating the seasonal component of the GBInSAR LOS signal, the comparison with the thermo-elastic FEM output indicates a good agreement in the overall temporal evolution of displacements. Measured and computed time series show a similar seasonal waveform, with coherent warm-season expansion and cold-season contraction trends, supporting the interpretation that the dominant cyclic component observed by radar is largely thermo-elastic in origin (Figure 22).

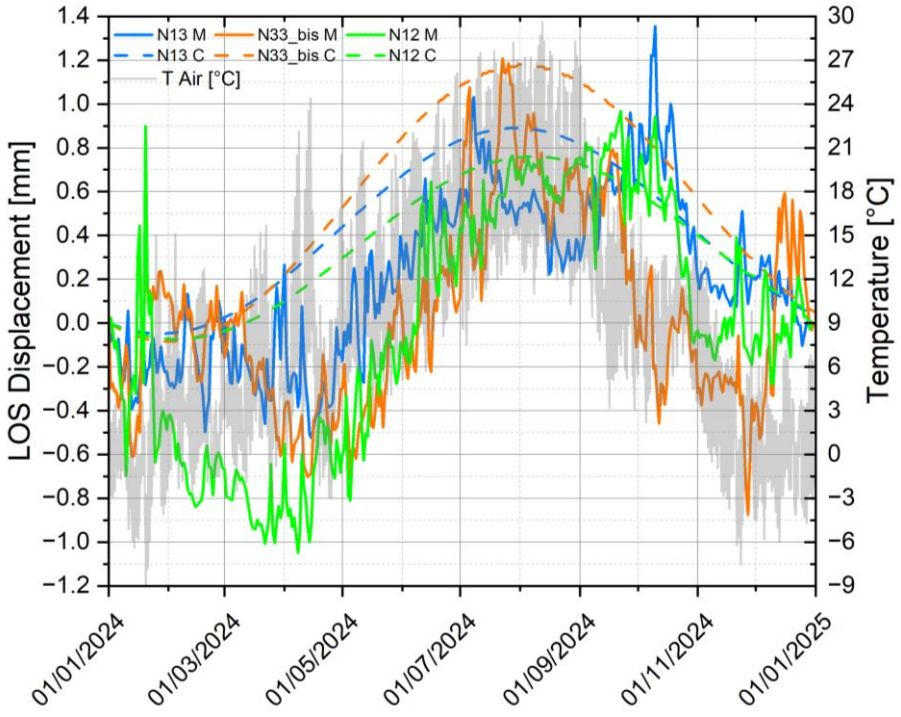


Figure 22 Comparison of displacement time series along the LOS for the Scaiùn cliff: in-situ measurements (solid line, with suffix M) versus calculated displacements (dashed line, with suffix C). The grey line represents the air temperature.

Despite this agreement, two systematic differences emerge. First, a phase shift is observed: the simulated signal slightly anticipates the peak summer displacements and the subsequent winter contraction compared to the GBInSAR series, with the mismatch being more evident during the contraction phase. This behaviour is consistent with the idealized thermal forcing used in the numerical setup and with the timing of the maximum temperature in the reference year, which can delay the thermal response recorded in the field relative to the model.

Second, amplitude differences are present between calculated and measured seasonal displacements. This is expected because the FEM simulations were conceived as a qualitative representation of the slope-scale thermo-elastic response rather than a calibrated tool for reproducing absolute magnitudes. In addition, residual non-thermal contributions may still be embedded in the measured seasonal component, especially where progressive deformation and damage accumulation are significant over the same period. Within this framework, the cyclic signal is interpreted as predominantly thermo-elastic and directly comparable to the numerical prediction, whereas the removed long-term component is attributed to irreversible processes not included in the elastic formulation. The potential coupling between repeated thermal cycles and progressive damage cannot be quantified with the available monitoring window and the adopted modelling assumptions.

At the slope scale, FEM-derived LOS maps provide a spatial validation of the same mechanism inferred from the time-series comparison. The reconstructed displacement fields show negligible displacements in the early months and a progressive expansion towards summer, followed by a gradual contraction during cooling. Importantly, maps generated from different viewpoints highlight that the apparent LOS signal can vary depending on viewing geometry, but the seasonal expansion–contraction pattern remains robust (Figure 23).

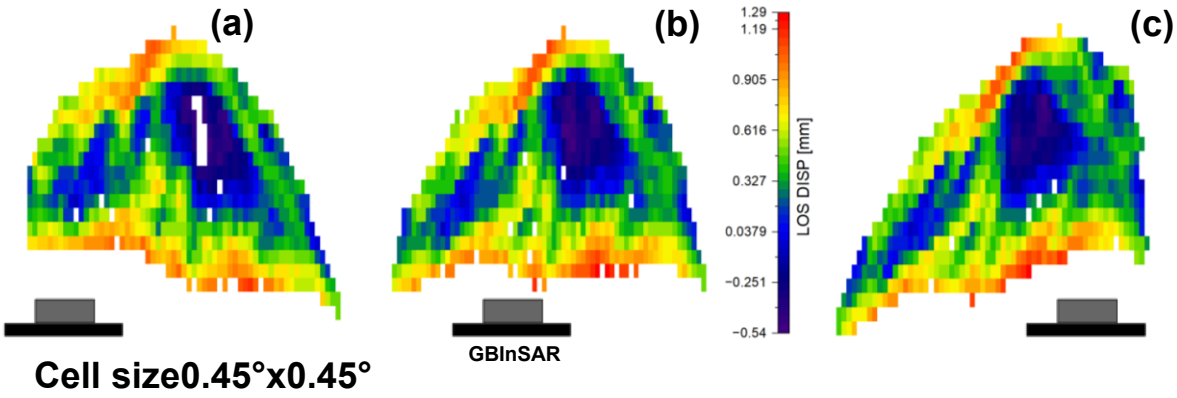


Figure 23 Scaiùn map of displacement along LOS for the month of July, presented from different viewpoints: (a) left side; (b) frontal; (c) right side. Grey shape indicate the position of radar.

Overall, the combined time-series and map-based comparisons support the ability of a purely thermo-elastic slope-scale model to reproduce the timing and spatial coherence of the thermally driven deformation at Scaiùn, while acknowledging that irreversible processes control the long-term trend measured by GBInSAR.

3.5.3.2 Monte Colodri

For Monte Colodri, the FEM-based LOS displacement maps reconstructed for representative months outline a clear seasonal thermo-elastic cycle (Figure 24). Displacements are negligible in January, while progressive deformation develops during the warming phase. The model predicts the strongest response in the south-facing sector, where thermal expansion generates LOS displacements moving away from the sensor and reaching up to ~2 mm in summer conditions. This spatial contrast reflects the stronger thermal forcing expected on sun-exposed sectors.

In the northern portion of the wall, the model shows a weaker and locally different response, including areas with positive LOS displacements that are interpreted as a secondary mechanical effect induced by the expansion of the southern sector (mechanical coupling within the rock mass). During autumn and winter, the simulated wall progressively returns toward its initial configuration as temperatures decrease, delineating a reversible cycle consistent with an elastic thermo-mechanical behaviour.

Overall, the Monte Colodri results indicate that the thermo-elastic model is able to identify (i) the seasonal timing of the response and (ii) the spatial hierarchy of thermally sensitive sectors, with the largest displacements systematically associated with the most exposed portion of the rockwall. This supports the use of the FEM outputs as a physically based interpretative layer for slope-scale GBInSAR products, particularly for

distinguishing thermally driven deformation patterns from longer-term irreversible components that are not represented in the elastic formulation.

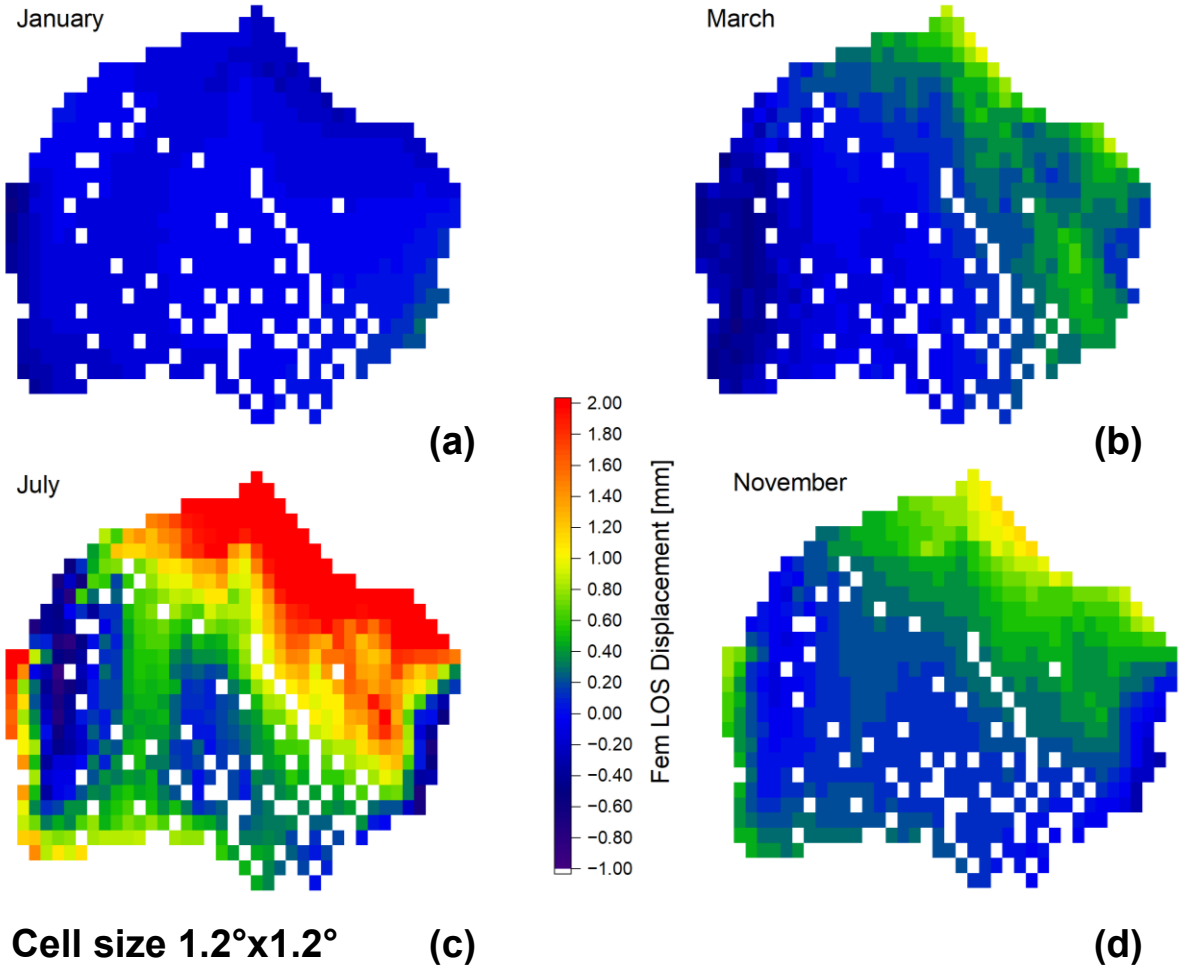


Figure 24 Monte Colodri map of LOS displacement calculated from FEM simulation at different months: (a) January; (b) March; (c) July; (d) November.

Overall, the integrated analysis demonstrates that:

- at point scale, detrended GBInSAR time series and FEM outputs share a similar seasonal behaviour, with differences that can be explained by the idealized nature of the thermal forcing and by neglected processes.
- at slope scale, the synthetic LOS displacement fields capture the same zones of enhanced deformation highlighted by radar monitoring, especially in sun-exposed and geometrically complex sectors such as pillars, convex walls and slope breaks.
- the workflow for reconstructing FEM-based LOS maps provides a practical bridge between numerical simulations and GBInSAR products, allowing the

model to be used both as an interpretative tool for existing monitoring data and as a predictive framework to identify rock masses and geometries most sensitive to thermal loading.

3.6 **Discussion**

Numerical simulations conducted in this study provide a detailed analysis of the thermo-mechanical behavior of rock slopes subjected to seasonal thermal cycles. Despite utilizing continuous medium models, they were parameterized with mechanical properties representative of a fractured rock mass. A key aspect emerging from this work is the crucial role played by geometry, boundary conditions, and slope aspect in controlling both the amplitude and the spatial distribution of stress and strain fields.

3.6.1 *Insights from simplified geometries*

In simplified geometries, the differences between the pillar and the convex rock wall models underscore the importance of shape in responding to thermal stresses and this become important for monitoring data interpretation and for possible long-term fatigue induced failure. The pillar model, characterized by a high vertical aspect ratio, typical of many mountains area, exhibited more pronounced vertical displacements at the top, reaching values of the order of 6-7 mm when subjected to a real daily air temperature time series. This finding is consistent with the physical principle that, for the same thermal expansion coefficient and temperature variation, taller structures accumulate greater absolute deformations. Similarly, Gischig et al. (2011), modeled the large Randa rock slope instability with a 2D FEM approach, highlighting cumulative and cycling displacements up to 1-5 mm at depths of 100 m, with larger deformations concentrated in the less constrained portions of the slope.

Conversely, the curved geometry showed more uniform displacements along the vertical axis but with noticeable lateral variations at the same height. These variations are attributable to the curvature, which localizes the heat flow. These results align with observations by Greif et al., (2017), who reported annual cyclic deformations of 1-2 mm in the Pravčická brána natural arch, where stresses and strains accumulate in the curved part of arch, emphasizing the influence of geometry on thermal stress concentration.

From a methodological perspective, the adopted modeling approach incorporated idealized boundary conditions to simulate realistic constraints: blocked displacements at

the base to represent the anchorage to the bedrock, and free surfaces laterally and superiorly to simulate natural exposure. However, it is important to acknowledge that while these conditions enable the capture of general trends, they may neglect secondary effects related to the presence of pre-existing fractures or anisotropies, which are known to locally influence the deformation field, with an amplification of the thermal effects at fracture tips.

A particularly notable result from the pillar model, under varying thermal input conditions, was the initiation of torsional deformation, with displacement differences of up to 1.5 mm between the exposed and unexposed sides. This finding is in line with experiments by Villarraga et al. (2021), which demonstrated that repeated thermal cycles on limestone samples induce anisotropic degradation of elastic properties and cumulative deformations between 0.1 and 0.5 mm after 900 cycles. Although the model used in this study is elastic, the observation that even small temperature differences can produce relevant torsional effects underlines the need to consider such phenomena in real slope monitoring data analysis and stability models.

In Figure 25, three sketches illustrate the various types of movement observed in the numerical simulations for both warm (red arrows) and cold (blue arrows) seasons, along with the corresponding displacement and temperature distributions for vertical (A-A') and horizontal profiles (B-B'). For the pillar scheme (Figure 25a1, a2 and a3) two subcases were considered: uniform and non-uniform external temperature. For a uniform external temperature, a bending movement was observed, characterized by a maximum displacement at the top and a minimum at the bottom. The magnitude of these displacements was more pronounced in the warm season than in the cold season, and their directions were opposite. For a non-uniform external temperature, the pillar was subjected to a torsional movement, with displacement magnitudes consistently greater in the warm season. For all subcases within the warm season, the temperature increased along the vertical direction. In the horizontal direction, the temperature exhibited a convex trend with a minimum observed in the middle of the pillar.

The stocky cubic-like scheme (Figure 25 b_1, b_2 and b_3) displayed a spatially non-uniform expansion and contraction cycle during warm and cold seasons, respectively. Specifically, the movement on the left-hand side (south-facing) was greater than that on the right-hand side (north-facing). This discrepancy is attributed to differences in external temperature due to ground surface aspect. No significant displacement was observed at

the base due to imposed mechanical constraints and the substantial mass. In the warm season, temperature increased with elevation, exhibiting a quasi-bilinear trend. Along the horizontal direction, the temperature showed a non-symmetric convex trend, influenced by the temperature difference between the north and south faces and their respective surface areas.

For the convex scheme (half-truncated cone, Figure 25 c_1, c_2 and c_3), only uniform external temperature was considered. In this configuration, geometry played a crucial role in controlling the displacement distribution. The displacement magnitude was greatest in the middle of the convex surface and progressively decreased towards the lateral directions. In all analyzed cases, displacements were more substantial in the warm season compared to the cold season. During the warm season, temperature increased with elevation and exhibited a decreasing trend from the external surface inward.

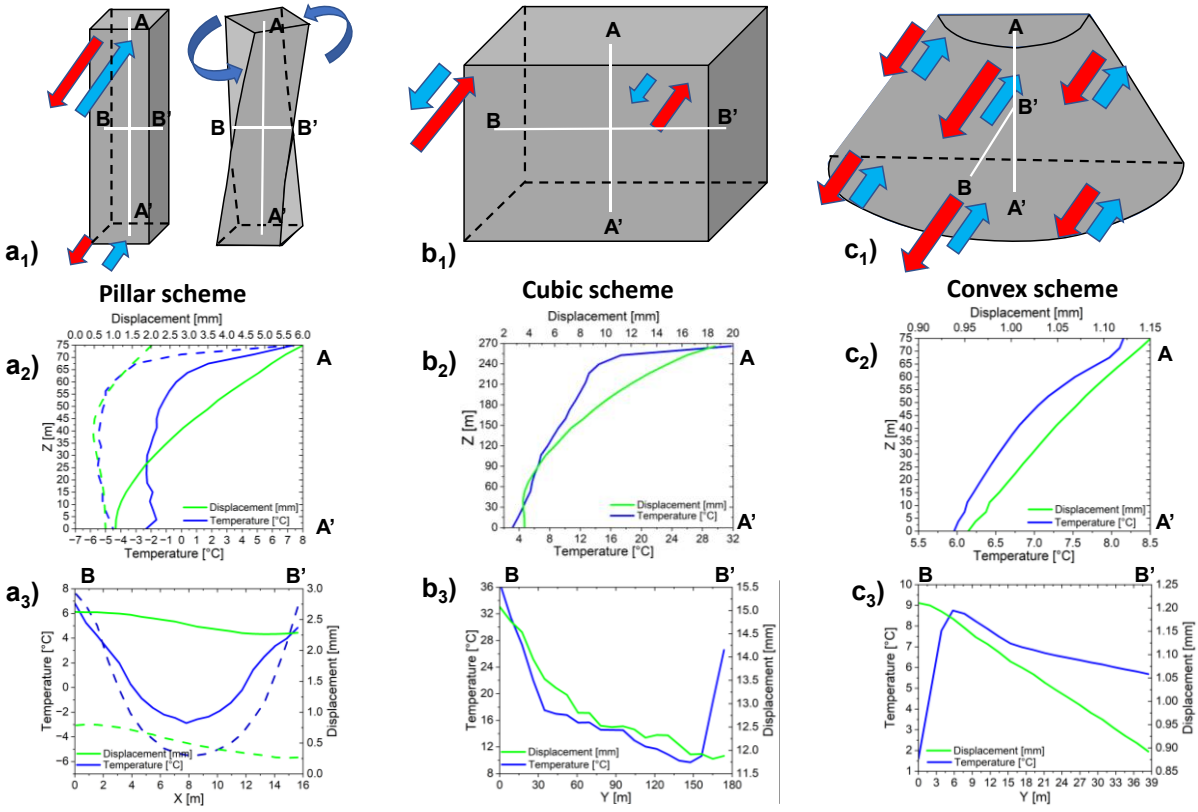


Figure 25 Sketches and plots of the expected movements for the three main geometries a_1) pillar element with bending and torsional movement, b_1) stocky prism movement, c_1) convex (half-truncated cone) scheme movement; a_2) and a_3) displacement and temperature along the vertical (A-A') and horizontal (B-B') directions, respectively, for the pillar case (dashed lines for uniform external temperature, continuous lines for non-uniform external temperature), b_2) and b_3) displacement and temperature along the vertical (A-A') and horizontal (B-B') direction, respectively,

for the case of stocky cubic scheme; c_2) and c_3) displacement and temperature along the vertical (A-A') and horizontal (B-B') directions, respectively for the case of convex scheme.

3.6.2 *Model sensitivity*

In the parametric analyses, the role of the key parameters was investigated to characterize their individual effects on the displacement and temperature fields, and the following considerations can be stated. The elastic modulus predominantly influences the stress field, affecting both its distribution and magnitude, whereas its impact on the displacement field is negligible. This effect on the stress field was also revealed by Gischig et al., (2011), who reported peak-to-peak stress variations of up to ±50% within the range of Young' Modulus they investigated. Thermal conductivity primarily influences the speed at which heat propagates through the domain, with only a marginal effect on displacement and stress fields. Specific heat, conversely, directly influences the displacement field by controlling the thermal inertia of the medium, thereby affecting the distribution of thermal gradient and the sensitivity to temperature changes. It does not, however, significantly impact the stress field. Finally, the thermal expansion coefficient is the only parameter affecting simultaneously the stress and displacement fields, directly controlling the intensity and extent of the overall thermo-elastic response, and as a consequence could be also analyzed by considering anisotropy

3.6.3 *Applicability to real geometries*

In simulations of real geometries, particularly for the Monte Colodri site, the analysis successfully reproduced the expected seasonal trend of LOS displacements, with maximum values up to $+2\ mm$ in the south-facing portion. This behavior is consistent with high solar exposure and aligns with GBInSAR monitoring data. The comparatively smaller displacements observed in the north portion highlight the importance of considering thermal gradients related to exposure, as highlighted by Collins & Stock, (2016), who documented daily fracture openings of up to $1.27\ cm$ on the sun-exposed granite exfoliation slabs. Mufundirwa et al. (2011) also reported daily openings of up to $0.21\ mm$ even for modest temperature variations. A significant implication of the results obtained from the simplified pillar geometry is their potential applicability to real slope configurations. At the Monte Colodri site, despite its more intricate overall morphology, the southern sector of the slope includes conspicuous protruding rock formations that can

be morphologically and mechanically assimilated to isolated pillars. It is evident that these structures, due to their vertical elongation, partial isolation, and enhanced solar exposure, are subject to boundary conditions and thermal loads comparable to those simulated in the idealized model. Consequently, the displacement patterns observed in the simulations, including increased vertical expansion at the top and torsional deformations due to differential heating, can be reasonably anticipated in these natural sub-structures. This correspondence reinforces the interpretative value of the idealized models, which, despite their simplified nature, effectively capture fundamental physical processes directly transferable to real-world cases. The presence of pillar-like morphologies within complex slopes is also suggested to locally amplify thermo-mechanical effects, and therefore these should be explicitly considered in slope-scale numerical simulations and hazard assessments.

Of particular interest is the heat accumulation effect observed in the area behind the base of the pillar in the simplified geometry. In this region, heat tends to concentrate, generating a persistent thermal gradient that locally amplifies deformations. This result highlights how heat primarily accumulates in the most superficial layers, penetrating and concentrating within the first meters of the domain. This observation aligns with Mamot et al. (2021), whose numerical analysis of permafrost rock slopes revealed that thermal variations significantly impact the first 5–7 meters below the surface, leading to both progressively increasing displacements and a marked reduction in the safety factor and slope stability. Although Mamot et al. (2021) employed an explicit discontinuity approach while the present study adopts a continuous and homogenized model, the remarkable consistency in our results underscores the dominant role of surface heat in the deformation response of slopes. This finding strengthens the interpretation that thermal variations can act as significant triggers for the initiation of rock slope instability, even in the absence of explicit fractures but unfortunately almost no data are available at lower elevations to improve an internal temperature distribution.

3.6.4 *Limitations of the isotropic material assumption*

In the numerical analysis we adopted isotropic and homogeneous thermal and mechanical properties (Table 1) a clear simplification of the behaviour of many foliated and layered rocks. Numerous laboratory studies have shown that elastic stiffness and strength can vary significantly with orientation in metamorphic rocks, reflecting both

crystallographic preferred orientation and foliation-related microcrack fabrics (Johnson & Wenk, 1974). Likewise, marbles and other polycrystalline carbonates display strong anisotropy of linear thermal expansion, with coefficients that differ by factors of ~1.5–2 or more between directions of maximum and minimum dilatation, systematically aligned with rock fabric and crystal orientation (Luque et al., 2010; Siegesmund et al., 2000) Thermal conductivity also tends to be anisotropic in foliated and bedded rocks: measurements on Alpine rocks and fine-grained sedimentary rocks show that conductivity and diffusivity are typically higher parallel to foliation or bedding than normal to it, with parallel values exceeding perpendicular ones by up to factors of ~1.5–3.8 (Labus & Labus, 2018). Neglecting such thermo-mechanical anisotropy is therefore expected to influence primarily the magnitude and local orientation of stress concentrations (e.g. favoring earlier shear or tensile localization along weak fabric-related directions), and to slightly modify the distribution of thermally induced strains and torsion-related stress peaks. However, in the present set of simulations the emergence and overall pattern of stress concentrations are mainly controlled by the geometry of the modelled rock volumes and by the imposed boundary conditions; the torsional stress concentrations observed in the pillar examples represent a specific manifestation of this behaviour and are therefore expected to remain qualitatively robust even if anisotropic property tensors were introduced. A fully anisotropic thermo-mechanical formulation, explicitly linked to site-specific fabric and directional property measurements, lies beyond the scope of this first modelling step but represents an important direction for future work.

3.6.5 *Methodological advancements in data representation*

The reconstruction of displacement maps from the numerical models reveals that, unlike GBInSAR which provides continuous and high spatial resolution data, the FEM results are constrained by the nodal discretization. Although introducing a limitation in capturing finer local effects, the adoption of a slope-scale domain allowed for the generation of displacement fields comparable to GBInSAR data, thereby improving the readability of the numerical results. This represents a significant step forward compared to studies which used coupled numerical models to simulate rock slope response at small scale and at shallow depth or based on superficial disturbance and measurement.

The generation of LOS displacement maps from the FEM simulations required a post-processing step involving the projection of nodal displacements onto a 2D grid defined in radar coordinates. This grid was constructed by discretizing the azimuth and zenith angle intervals (i.e., the viewing geometry of the radar) into cells of variable size. Each cell aggregates the displacements of all the FEM nodes falling within its angular boundaries, effectively creating a spatial raster representation of the modeled displacements. The dimensions of these angular cells can vary, being either square or rectangular, as shown in the comparative example. The choice of cell size significantly affects the readability and representativeness of the final maps. Larger cells (e.g., 1.4°×1.4°) tend to "flatten" the map, smoothing out details and potentially masking local variations, while smaller cells (e.g., 0.45°×0.8°) better capture spatial variability but may result in many empty cells due to the limited number of nodes available in some regions, leading to white gaps. Multiple configurations were tested to identify the optimal compromise between spatial resolution and completeness of the information. This process was particularly important because, in contrast to measurement data, FEM results are inherently limited to the spatial distribution of mesh nodes requiring careful spatial aggregation to be meaningfully compared with radar-derived LOS displacement data. In the case of Monte Colodri, shown in Figure 26, a 1.2°×1.2°-degree cell size was adopted as the best balance between spatial continuity and resolution, allowing for the reconstruction of a coherent displacement pattern while minimizing the presence of empty areas.

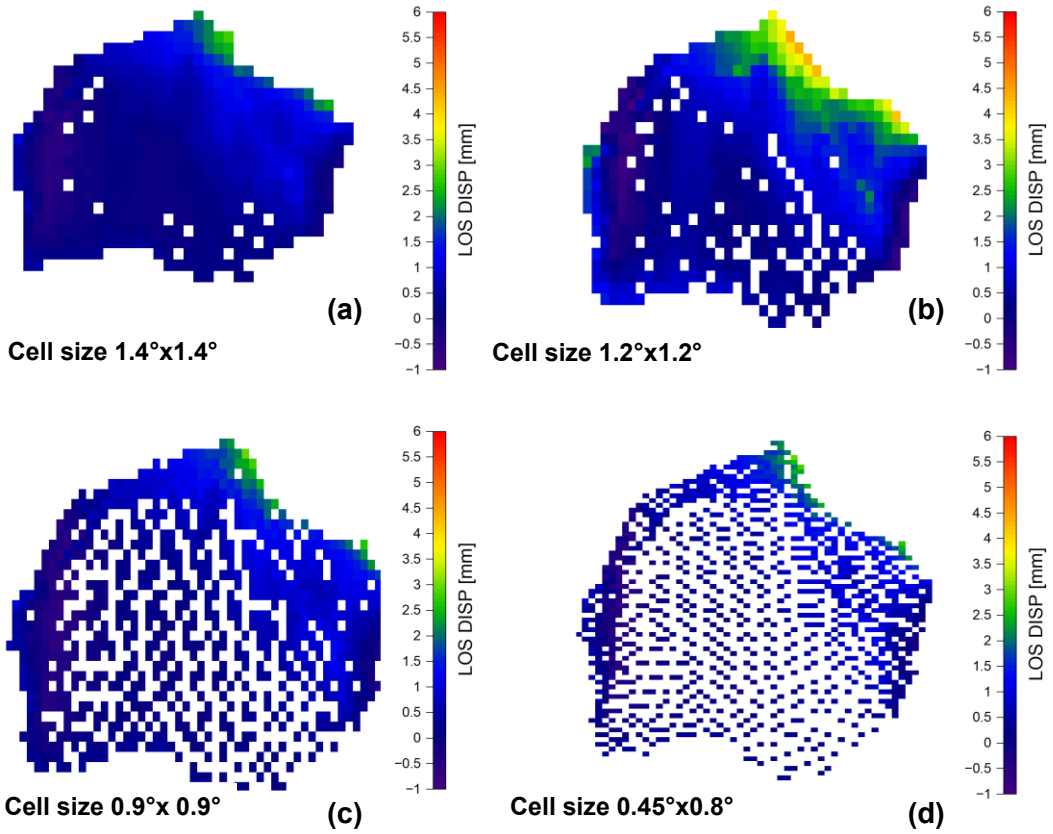


Figure 26 Comparative example of Monte Colodri LOS displacement maps generated with different cell sizes: from (a) and (b) larger cells (e.g., 1.4°×1.4°); to (c) and (d) smaller cells (e.g., 0.45°×0.8°).

3.6.6 *Comparison with field measurements*

The comparison between the measured GBInSAR and FEM modeled LOS displacement maps for both the Scaiun and Monte Colodri sites reveals key differences and similarities essential for interpreting the model outcomes. A fundamental distinction lies in the nature of the data: the GBInSAR measurements represent cumulative displacements over time, whereas FEM results reflect instantaneous elastic responses to thermal forcing. This inherent difference also explains potential disparities in the sign of displacement between measured and simulated data, as the numerical model isolates the thermal component, whereas monitored data integrate the total deformation signal, including other mechanical or hydrological influences. As described in data elaboration, detrending the measured time series to isolate the cyclic component provides a more coherent basis for comparison (Figure 22). In the Scaiun case, despite the different displacement scales, more accentuated in the measured map due to a longer observation

period (January to July), some consistent patterns emerge. Both map types exhibit slightly negative LOS displacements in the central, more stable zone. Concurrently, positive values are concentrated at the base of the slope in the modelled data. This lower-slope anomaly corresponds to a morphological change in gradient, suggesting a geometrically driven amplification of thermal displacement at concave breaks, a phenomenon also visible in the in-situ measurements.

Conversely, for the Monte Colodri site, where both maps refer to a similar time window (October to July) and share comparable displacement scales, the sign of displacement is inverted in the most mobile sectors. This inversion is again attributable to the thermal-only nature of the numerical model. Nonetheless, the spatial distribution of the moving areas demonstrate consistency, with both maps highlighting displacement concentration in the southern exposed portion of the slope. This spatial coherence, despite the conceptual and mechanical simplifications of the adopted FEM approach, confirms the ability of thermo-mechanical models to identify thermally sensitive sectors of rock slopes and supports the interpretation of real slope dynamics based on numerical results.

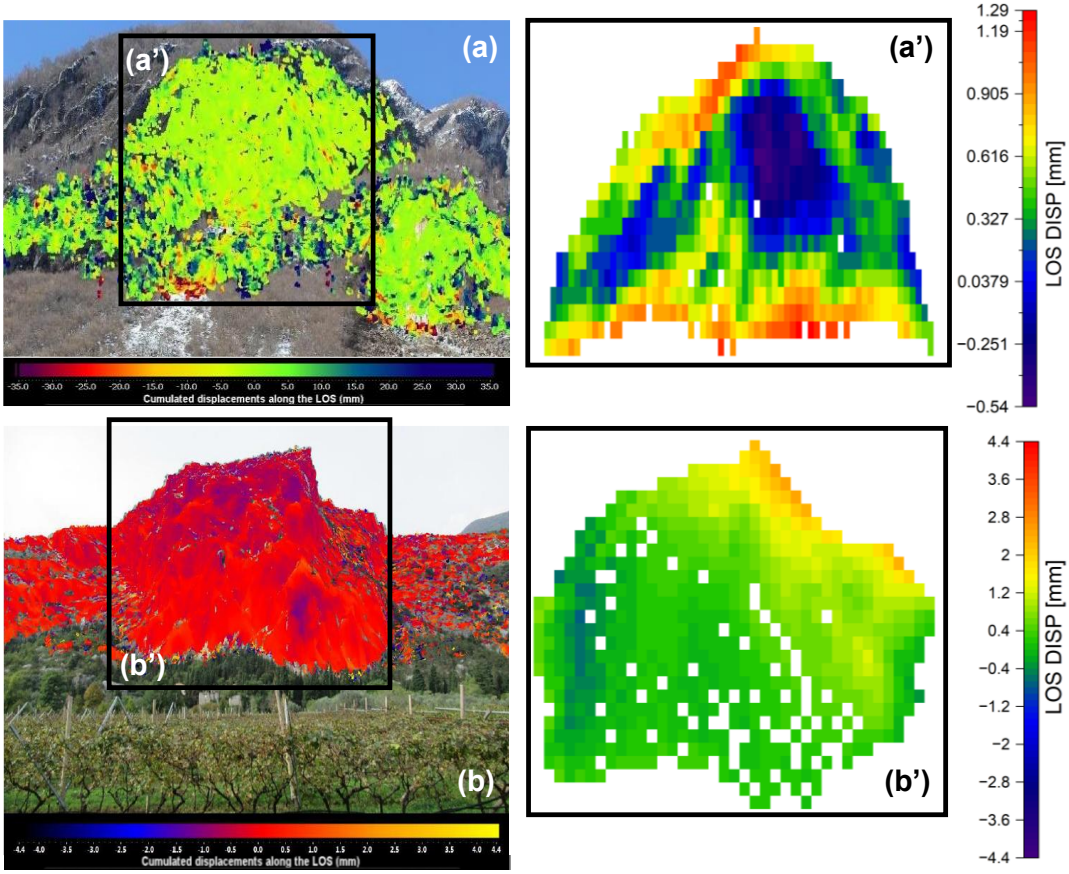


Figure 27 Comparison between measured LOS displacement maps from GBInSAR (left-hand side) and calculated maps from FEM analysis (right-hand side) for (a) (a') the Scaiùn cliff and (b)

(b') the Monte Colodri. The computed maps were prepared using a resolution of 0.45°×0.45° and 1.2° × 1.2°, respectively, projecting FEM displacements in the LOS direction.

3.7 **Case Study Conclusion**

This study provides a comprehensive analysis of the mid-term thermo-mechanical behavior of rock slopes subjected to thermal forcing, using finite element simulations, for both simplified and real geometries. Our findings demonstrate that rock masses, modelled by a continuous approach with mechanical properties representative of fractured media, exhibit deformation patterns qualitatively similar in spatial distribution to observed field data when subjected to cyclic thermal inputs.

In direct response to Research Question 1, the results establish that the thermo-mechanical effects attributable to the geometry of potentially unstable rock elements are substantial, systematic, and geometry specific. Isolated pillars with high vertical aspect ratios develop torsional displacement modes under asymmetric thermal forcing; convex rock walls localize thermal stress at their apex, amplifying displacements relative to planar surfaces of identical extent; and slope aspect controls the spatial hierarchy of deformation, with sun-exposed sectors consistently exhibiting larger and earlier seasonal expansion than shaded faces. These geometry-dependent responses define the dominant kinematic signature of thermally forced rock slopes and must be explicitly accounted for when interpreting ground-based InSAR displacement fields or designing monitoring networks for thermally sensitive rock walls.

A key conclusion is that thermal fluctuations alone, even without additional triggers like rainfall or seismicity, can induce in-situ measurable displacements at the millimeter scale. These movements, characterized by seasonal rock-mass expansion and contraction, directly reflect the rock slope's response to thermal loading, and are highly sensitive to slope orientation, geometry, and boundary conditions. Specifically, the observed torsional displacement mode in pillars, localized amplification in convex walls, and differential movements between sun-exposed and shaded sectors underscore the critical influence of geometric and morphological factors in controlling the deformational response.

The approach proposed in this study operates at the slope scale, extending the numerical domain to encompass large portions of rock slopes. This enables the investigation of global deformation mechanisms and the assessment of the system's overall response, rather than isolated local behavior. This macro-scale perspective

facilitates the reconstruction of displacement maps comparable to those obtained by ground-based radar systems (e.g., GBInSAR), a capability often beyond the scope of small-scale fracture models. Our approach effectively bridges the gap between FEM modeling and large-scale monitoring techniques like GBInSAR, offering a robust framework for directly comparing numerical predictions with distributed displacement data. Hence, this work offers a novel perspective on integrating numerical simulation and remote sensing, opening new ways for using thermoelastic models as interpretative and predictive tools for slope-scale deformation in response to climatic forcing.

Overall, the results confirm the effectiveness of FEM-based thermo-mechanical modeling in capturing the elastic response of rock masses to temperature changes, particularly when realistic geometries and boundary conditions are implemented. While the presented simulations are simplified in nature, they successfully replicate the main kinematic response of the slopes under thermal forcing. This study reinforces the role of thermal forcing as a significant driver of slope deformation and highlights the value of numerical modeling as a crucial complement to long-term field monitoring. Furthermore, it demonstrates that FEM-based thermo-elastic modeling can serve not only as a diagnostic tool for interpreting long-term monitoring data but also as a predictive framework for understanding the evolution of slope deformation under current and future climatic conditions. This result can then be useful in the view of building digital twins of rocky cliff. Future developments could include the calibration of material parameters based on laboratory or in-situ data (displacements, rock surface temperature, sun radiation), and the incorporation of mechanical heterogeneities such as layering, joint sets, or thermal and mechanical anisotropy to further refine model accuracy, together with an elasto-plastic and fracture propagation modeling.

The idealized and real-geometry simulations presented in this chapter have treated rock slopes as purely thermo-elastic systems, deliberately excluding phase-change processes in order to isolate the geometric contribution to deformation. This controlled simplification, applied to two non-permafrost sites, establishes the baseline framework that Chapter 4 extends to a warm-permafrost setting. Crucially, the transition is not only thermal but also geometric: whereas here the pillar geometry was a simplified, idealized prism designed to isolate thermo-mechanical principles, Chapter 4 applies the same modelling logic to the Sas da Lech, a real dolomite pillar in the Italian Dolomites with a complex three-dimensional geometry reconstructed from high-resolution point-cloud

data. This progression from fictitious to natural geometry, and from thermo-elastic to phase-change-inclusive physics, defines the methodological step forward that the next chapter undertakes.

Chapter 4
THERMO-MECHANICAL AND KINEMATIC EVOLUTION OF A WARMING PERMAFROST ROCK PILLAR (SAS DA LECH, DOLOMITES)

4.1 **Aim**

This chapter investigates the thermo-mechanical evolution and residual stability of the Sas da Lech dolomite rock pillar, located in the Sella Group of the Italian Dolomites, which experienced a lateral collapse of approximately 3,500 m³ in September 2018. The site represents an ideal natural laboratory for addressing three of the five research questions formulated in Chapter 1. Research Question 2, concerning the modelling of subsurface temperature distributions in highly fractured rock walls accounting for both conductive and advective heat transport, is addressed through the development of an extended one-dimensional analytical heat-flow framework that explicitly incorporates localized fracture advection, latent-heat effects at the zero-curtain, and cold-air trapping. Research Question 3, identifying the factor that predisposes a rock mass to collapse and the mechanism that ultimately triggers it, is examined through a back-analysis of the 2018 failure, demonstrating that static gravitational loading alone cannot explain the observed detachment and that climate-driven degradation of ice-filled discontinuities acted as the long-term preconditioning mechanism. Research Question 4, concerning the simulation of high-altitude instability accounting for the progressive deterioration of physico-mechanical properties with temperature, is addressed through three-dimensional Strength Reduction Method analyses that systematically explore the role of temperature-dependent interface strength in governing both the pre-collapse stability and the post-collapse failure trajectory of the residual pillar.

Beyond these site-specific findings, the chapter introduces two methodological contributions of broader applicability. The first is a novel analytical thermal-compensation algorithm that isolates irreversible structural kinematics from the high-frequency thermoelastic noise and complex thermal snaking effects inherent to deep

inclino-extensometric chains, bypassing the limitations of physical dummy sensors. The second is an extended one-dimensional conduction model that efficiently integrates localized advective and latent-heat effects directly into the analytical heat-flow solution, capturing the non-conductive deep thermal dynamics of highly fractured rock masses without requiring a full three-dimensional coupled simulation. Together, these contributions provide a transferable methodological framework for monitoring and modelling complex, high-altitude rock pillars affected by permafrost one that is demonstrated here on the Sas da Lech but is designed to be applicable across the warming Alpine arc.

4.2 **Study area**

4.2.1 *Geological and Geomorphological setting*

The Sas da Lech rock pillar (46°32'09.43"N, 11°49'05.12"E) is located within the Sella Group, a prominent dolomitic massif at the orographic junction of the Gardena, Badia, Fassa, and Fodom valleys in the Italian Dolomites, at an elevation between 2,700 and 2,800 m a.s.l. (Figure 28). In September 2018, the northern portion of the structure was affected by a rockfall of approximately 3,500 m^3, which threatened the underlying hiking infrastructure and left the current residual rock tower structurally isolated from the main cliff. The remaining pillar stands approximately 80 m high, 25 m wide, and 15 m thick, and is intersected along its entire north face by a prominent vertical fracture with a present-day aperture of approximately 10–30 cm.

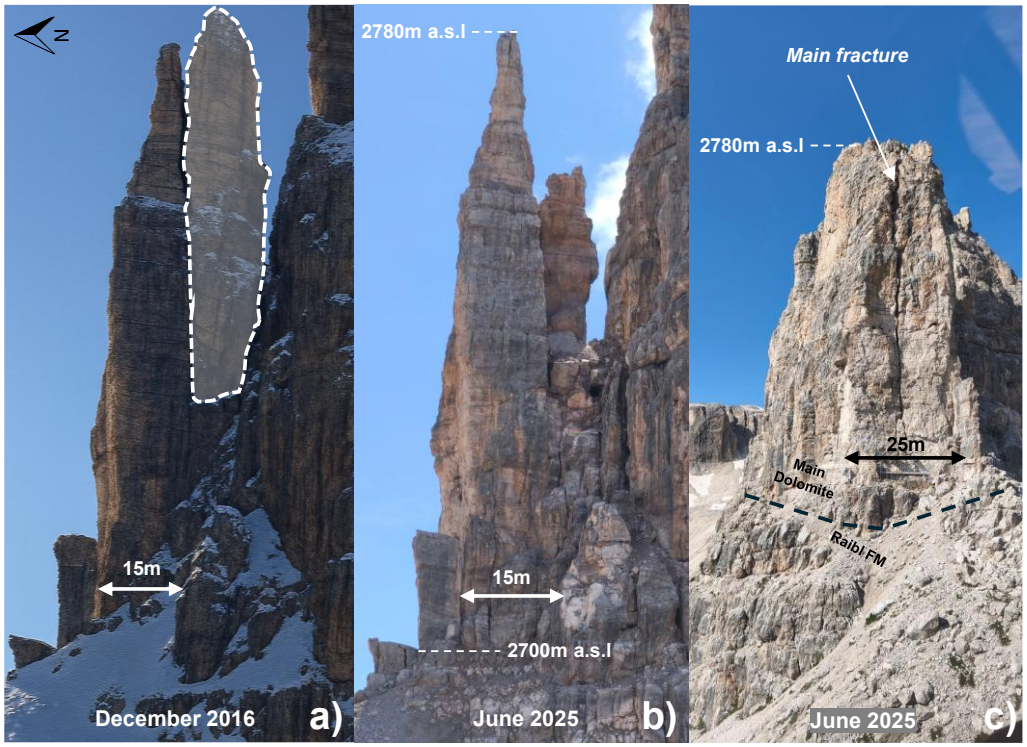


Figure 28 Lateral view (from the west) of the Sas da Lech pillar a) pre-event and b) post event of 2018 that involves up to 3500m^3 of rock represented by white dashed line on the pre-event photo. c) frontal view of the pillar after the failure event and showing the main central fracture cutting in half the pillar.

Stratigraphically, the Sella Group is dominated by thick successions of Dolomia Principale (Hauptdolomit) and Dolomia Dello Sciliar (Upper Triassic), which overlie the mechanically weaker Raibl Formation (Figure 29). The Raibl Formation forms the characteristic morphological terraces visible at mid-slope, acting as a preferential sliding horizon in many large-scale instability events documented in the Dolomites (Bosellini et al., 2003; Brondi et al., 1977). Although the Dolomia Principale is characterised by low primary porosity, it is pervasively intersected by strike-slip faults and joint systems that developed during the Alpine compressive phases, with structural offsets ranging from millimeters to hundreds of meters (Antonellini & Mollema, 2000; Mollema & Antonellini, 1998). These discontinuities strongly control both the subsurface permeability and the local geomorphological evolution, creating a highly anisotropic hydraulic and thermal medium that is fundamentally different from the homogeneous continuum assumed by standard conduction-only thermal models.

The Sella Group belongs to the Southern Alps tectonic domain, characterised by Permian–Triassic rifting phases, Meso–Cenozoic compression, and Neogene structuring into a south-vergent fold-and-thrust belt (Doglioni, 1987). The summit plateau, extending

between 2,750 and 2,950 m a.s.l., is dissected by karst depressions and cryonival landforms and is bounded by the vertical cliffs crowned by Piz Boè. The periglacial character of the area is clearly expressed by the presence of the nearby Murfreit rock glacier, a slow-moving ice-rich landform with surface velocities of 5–30 cm/yr (Krainer et al., 2020). The proximity of this active rock glacier, together with the elevation and north-facing aspect of the pillar's main fracture system, provides strong geomorphological evidence for the persistence of permafrost conditions within the fracture network of the Sas da Lech pillar itself.

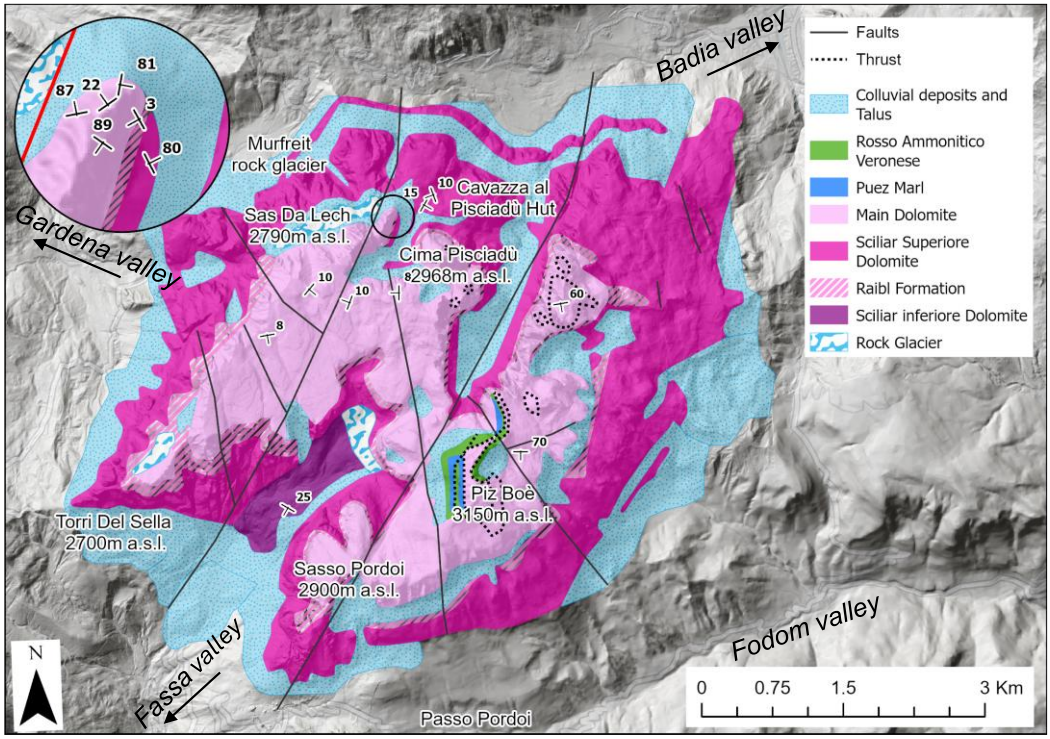


Figure 29 Geological Map of the Sella Group where the location of the Sas da Lech pillar and of the 2018 failure is marked inside a black circle (modified after 1:50.000 geological map n. 028 La Marmolada).

4.2.2 *Air Temperature and Climate Context*

The thermal forcing acting on the pillar was characterised using the meteorological dataset recorded at the Cima Pisciadù automatic weather station, located at approximately 3,000 m a.s.l. and approximately 700 m to the east of the study site. Temperature records spanning the period 2004–2024 were altitude-corrected using a standard environmental lapse rate of 0.6 °C per 100 m, applying a constant offset of +1.8 °C to account for the 300 m elevation difference between the station and the base of the pillar at approximately

2,700 m a.s.l. The resulting adjusted time series, shown in Figure 30 alongside the near-surface rock temperature recorded in situ at 0.23 m depth, demonstrates excellent temporal coherence between the two datasets, confirming the validity of the lapse-rate correction and the representativeness of the Pisciadù station as a thermal boundary condition for the study site.

The adjusted temperature record reveals a mean annual air temperature of approximately −1 to 0 °C at the pillar base, with summer maxima frequently exceeding +10 °C and winter minima regularly dropping below −10 °C. This thermal regime places the site firmly within the warm permafrost zone, where the mean annual temperature is close to but below 0 °C and the system is therefore highly sensitive to relatively small perturbations in climatic forcing. A discernible long-term warming trend is superimposed on the interannual variability, consistent with the broader pattern of accelerated permafrost warming documented across the European Alps over the early 21st century (Noetzli et al., 2024).

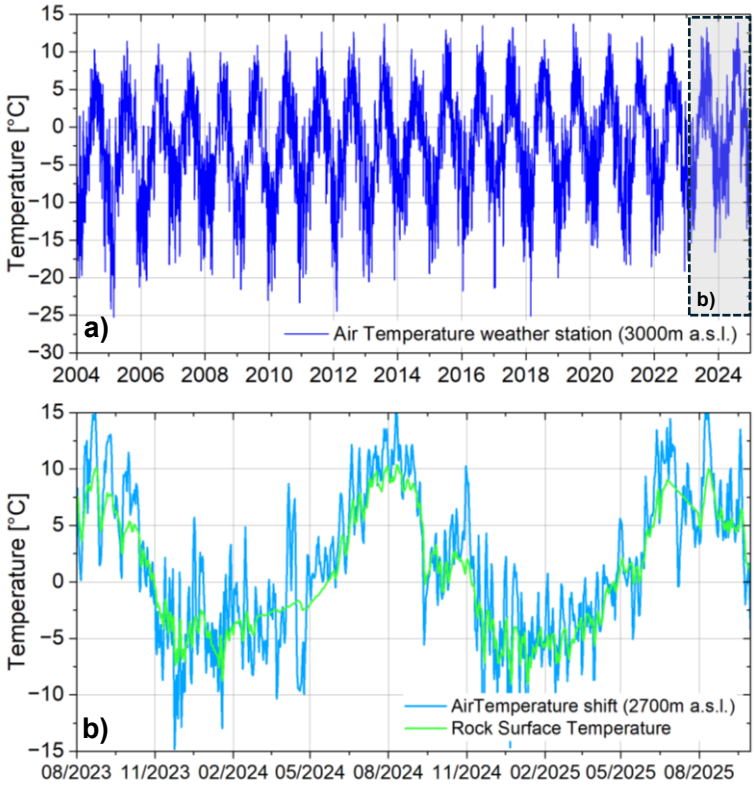


Figure 30 a) Air temperature time series registered at Cima Pisciadù (3000m a.s.l.) meteorological station; b) altitude-adjusted air temperature time series compared to rock surface temperatures registered at the base of the Sas da Lech pillar (2700m a.s.l.) at 0.23m depth.

The altitude-adjusted time series was used directly as the upper thermal boundary condition in the three-dimensional finite-element thermal simulations described in 4.3.8 and provided the historical forcing record from which the climate scenario projections were constructed.

4.2.3 *Pillar geometry and discontinuities analysis*

The investigated rock pillar has a height of approximately 80 m, a thickness (NS) of about 15 m, and a width (EW) of about 25 m (Figure 31). The current morphology resulting from the 2018 rockfall event was reconstructed from high-resolution 3D point-cloud data acquired through terrestrial laser scanning, UAV photogrammetry and UAV-borne LiDAR (79,509,117 points with a density of 300points/m^3) (Figure 31a-b). The point cloud was acquired with a DJI Zenmuse L2 equipped with DJI Matrice300 RTK drone. The acquisition was realized with a manual fly to adapt the scansion on the complex morphology, with a target distance between 20 and 50m. These datasets enabled the detailed measurement of the exposed surfaces and the identification of the principal discontinuity sets affecting the rock mass. The entire north face of the pillar is intersected by a major vertical fracture running through its central portion, with a present-day aperture of approximately 10-30 cm. Geo-mechanical analysis of the point cloud identified six main joint sets whose average orientations expressed as dip direction/dip are: S0 = 241°/03°, J1 = 215°/89°, J2 = 349°/87°, J3 = 063°/80°, and J4 = 100°/81° and J5 = 325°/22°(Figure 31c). In particular, set S0 refers to the sub-horizontal bedding, while the other sets reflect the vertical and subvertical fracture that affect the domain controlling the main morphological features.

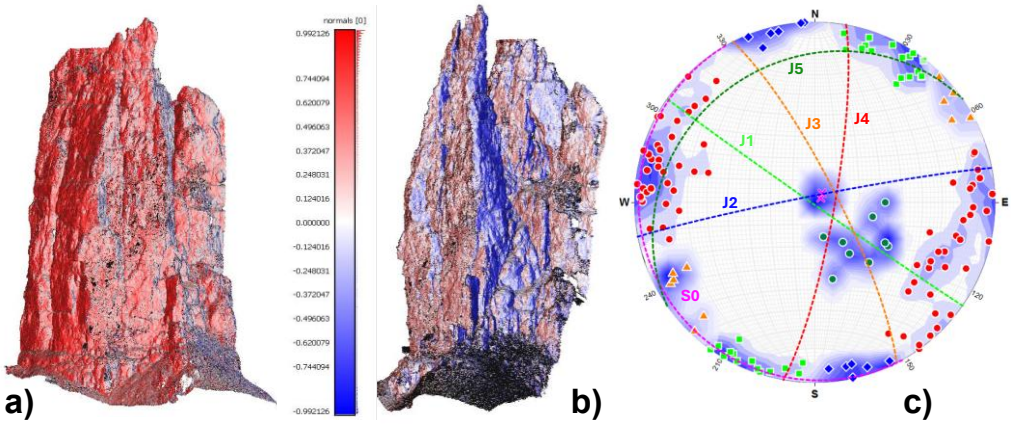


Figure 31 a-b) E-W component of normal vectors calculated on LiDAR point cloud observed from north-east (a) and northwest (b); c) Stereoplot with 138 poles of main joints measured on site and by Cloude Compare, and mean planes of the six main joint sets. S0 corresponds to the bedding.

In August 2023, three 21 m long boreholes (two horizontal and one inclined at 30°) were drilled to investigate and characterize the pillar. DMS02 was drilled through the eastern half of the pillar (to the left of the main fracture), while DMS01 and a third borehole were drilled through the western half (to the right of the main fracture). Optical and acoustic Borehole Televiewer (BHTV) logging was employed to reconstruct the borehole-wall features; the same boreholes were subsequently equipped with monitoring instrumentation to support continuous surveillance of the area. BHTV imagery enabled the identification of distinct features within the pillar. During the investigation of the DMS01 borehole, drilling-induced ice melting was observed at a depth of 11.75 m (Figure 32a). In the DMS02 borehole, a 0.6 m fracture was identified approximately 13.5 m from the collar. During drilling, this large fracture facilitated air circulation within the pillar's fracture network, evidenced by dust expelled from DMS02. This suggests that the temperature distribution (Figure 32b) within the pillar could be influenced by convective air movement within the fractures. The third horizontal borehole, situated between the other two, did not exhibit significant features.

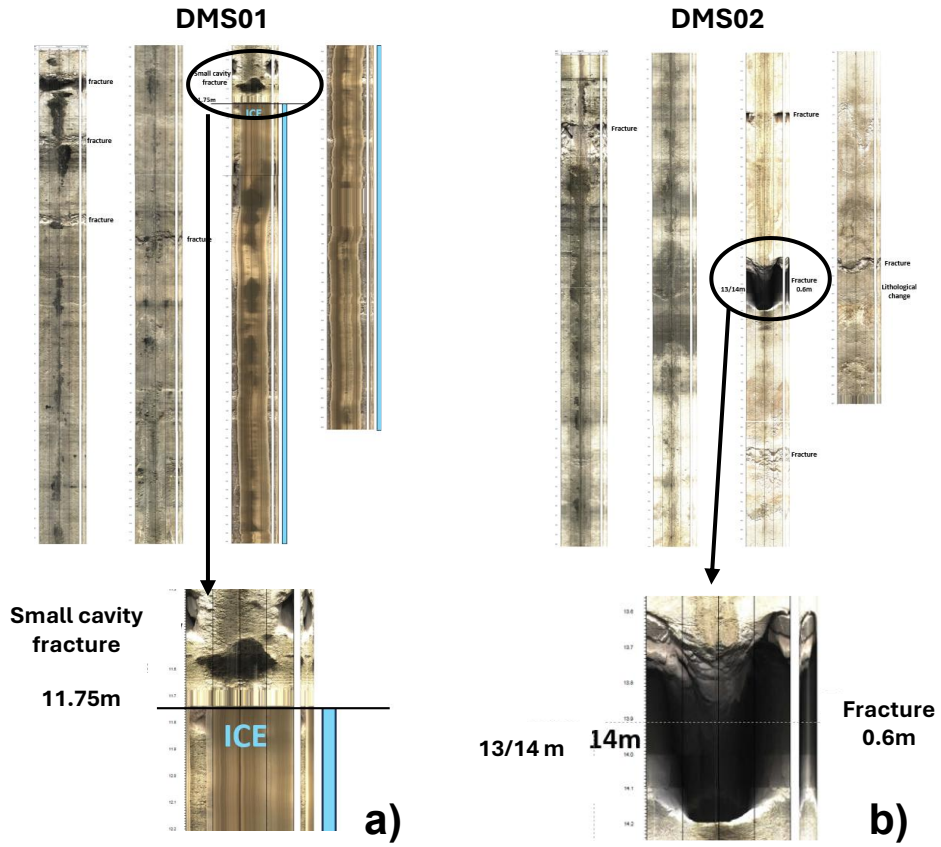


Figure 32 a) BHTV for borehole DMS01 in which a melted ice during the drilling started at 11.75m depth; b) BHTV for borehole DMS02 in which a large fracture of about 0.6m at 13/14m depth is observed. A third horizontal boreholes was drilled between the two DMS without interesting evidence during the BHTV investigation.

4.3 **Methodology and Theoretical Background**

4.3.1 *Monitoring layout*

A high-resolution multi-parametric monitoring network was installed in August 2023, immediately following the drilling campaign described in section 4.2.3. The monitoring strategy was designed to simultaneously constrain the subsurface thermal regime, the deep structural kinematics, and the surface fracture behaviour of the pillar, providing the multi-variable dataset required to test physically based models of permafrost-related instability. A schematic overview of the complete instrumentation layout is shown in Figure 33.



Figure 33 Monitoring approach adopted at the Sas da Lech pillar: a) ERT acquisition, b) 3 DMS extensometers (Ext21,22,23) for the superficial opening fractures, c) Aerial photogrammetry and LiDAR acquisition, d) 2 DMS multiparametric column (DMS1 and DMS2), e) Geoprecision temperature chain, and f) terrestrial laser scanner acquisition. The DMS columns and temperature chain are located inside three 21m long boreholes (2 horizontal and 1 inclined of 35°, long line red and blue).

The subsurface instrumentation is built around three boreholes drilled directly into the base of the rock pillar. Two 20-m boreholes specifically one horizontal (DMS01) and one inclined at approximately 35° below the horizontal (DMS02), are equipped with multiparametric Differential Monitoring of Stability columns (DMS, CSG s.r.l.). Each DMS column consists of 1-m spaced measuring modules equipped with inclinometers (repeatability ±0.002°), accelerometers (triggered by events exceeding a 10 mg threshold, ±2g range), and temperature sensors (0.1°C precision, sampling every 30 minutes). Each module is centered and fixed within the borehole via a series of spacers, ensuring mechanical coupling between the rigid sensor chain and the surrounding rock mass. This

coupling is particularly critical for DMS02, where three modules at depths of 2, 13, and 17 m are additionally equipped with axial extensometers (0.01 mm resolution) that directly measure column elongation and compression. To capture bidirectional axial kinematics, these extensometer modules were installed in a partially compressed state, enabling the accurate measurement of both subsequent elongation and shortening of the rock mass without ambiguity in sign. A third 19-m borehole, oriented horizontally between DMS01 and DMS02, accommodates a GeoPrecision thermometric chain (accuracy ±0.001°C) with non-uniform sensor spacing, specifically 0.23, 0.73, 0.98, 1.23, 1.48, 1.98, 2.48, 2.98, 3.48, 4.48, 5.48, 6.48, 8.48, 11.48, 14.48, and 18.48 m, deliberately designed to concentrate measurements where thermal gradients are steepest, that is in the shallowest meters of the rock wall, while still tracking the long-term thermal evolution at depth.

At the pillar surface, three DMS inclino-extensometers (Ext21, Ext22, and Ext23) were installed in August 2024 across the most prominent open fractures. These instruments continuously measure local air temperature, inclination change along two orthogonal planes, and fracture opening and closing. Ext21 is positioned across the main vertical fracture that bisects the pillar along its full height, while Ext22 and Ext23 monitor the secondary fractures delimiting a smaller adjacent pillar. Together, the surface and subsurface monitoring systems provide a spatially distributed, multi-depth kinematic and thermal dataset that spans from the rock surface to approximately 20 m depth

4.3.2 *Geomechanical Laboratory Characterization*

To parameterize the numerical models and provide a physically grounded interpretation of the field data, a comprehensive laboratory testing campaign was conducted on intact rock samples taken from the Sas da Lech site. The mechanical characterization included Uniaxial Compressive Strength (UCS) tests, Indirect Tensile Strength (ITT) tests, and Multistage Triaxial Compressive Strength (TCS) tests under varying confining pressures, all performed following ASTM standards. Tests were carried out on both the Dolomia Principale, the dominant lithology of the pillar and the Raibl Formation, which underlies the pillar. The results, summarized in Table 3, provide the baseline intact rock properties.

Table 3 Mean and standard deviation of each parameter measured with laboratory test for Dolomia Principale samples

Formation	Dolomia Principale		Raibl	
Parameter	**Mean**	**St. Deviation**	**Mean**	**St. Deviation**
Porosity [%]	*2.98*	*1.29*	*3.28*	*2.18*
UCS σc [MPa]	*127.5*	*33.43*	-	-
Et50 external [GPa]	*13.41*	*4.03*	*34.91*	*19.09*
Et50 local [GPa]	*11.74*	*0.39*	*21.41*	-
Poisson ratio [-]	*0.185*	*0.03*	*0.14*	-
Cohesion [MPa]	*3.33*	*5.77*	*36.25*	*1.06*
Friction angle [°]	*59.33*	*9.01*	*43.25*	*1.06*
σt [MPa]	*12.99*	*6.78*	*10.61*	*2.65*

The Dolomia Principale samples exhibit a mean UCS of 127.5 MPa with considerable variability (standard deviation 33.43 MPa), reflecting the heterogeneous fracturing and the presence of pre-existing microcracks in the core material. The mean tangent modulus Et50 is approximately 13.4 GPa externally measured and 11.7 GPa locally, with a Poisson's ratio of 0.185 and connected porosity ranging between 1.77% and 5.18% (mean 2.98%). Mean indirect tensile strength is 12.99 MPa, while the Mohr–Coulomb envelope derived from triaxial tests yields a mean cohesion of 3.33 MPa and a friction angle of 59.33°. The high variability in cohesion reflects the structural heterogeneity of the tested specimens, which include both intact and partially fractured material.

The Raibl Formation samples display a markedly different mechanical character. Although UCS tests were not performed on this formation due to sample quality constraints, the available data indicate a substantially higher stiffness — with Et50 external of 34.91 GPa and Et50 local of 21.41 GPa, combined with a higher cohesion of 36.25 MPa and a lower friction angle of 43.25°. The connected porosity is comparable to the Dolomia Principale at 3.28%, and the indirect tensile strength is 10.61 MPa. This combination of high stiffness and high cohesion with reduced friction angle is consistent with the carbonate-argillaceous composition of the Raibl Formation.

For the large-scale numerical models, the intact rock parameters of both formations were upscaled to equivalent rock-mass properties using the Geological Strength Index (GSI) approach, accounting for the pervasive jointing and structural heterogeneities observed in the field and documented by the BHTV logging.

4.3.3 *Theoretical background: 1D heat transfer and permafrost thermal regime*

Understanding the transient thermal regime of a high-altitude fractured rock pillar requires distinguishing between purely conductive heat transfer and the complex multiphysics processes such as air advection and phase changes, that locally overprint the conductive baseline. This distinction is not merely academic: it determines whether the temperature signal recorded at depth by a borehole sensor reflects the slow diffusion of surface forcing through intact rock, the rapid advection of cold or warm fluid through open fractures, or the thermal buffering of latent heat at a phase-change front. Each of these processes leaves a diagnostic signature in the spatio-temporal structure of the borehole temperature records and recognizing them is the prerequisite for any physically meaningful interpretation of the subsurface thermal regime.

According to the classical 1D Fourier analytical theory, surface temperature variations propagate into the rock mass as harmonic waves characterised by exponential amplitude attenuation and a progressive phase shift with depth. For a surface temperature oscillating sinusoidally around a mean value, the analytical solution for the subsurface temperature field in a semi-infinite half-space is (Carslaw & Jaeger, 1986):

$$T_{base}(z,t) = T_{mean} + A_0 e^{-z/d} \sin\left(\omega t - \frac{z}{d}\right) \quad [1]$$

where ω is the angular frequency (in rad/s), relating to the period of the cycle (P) by the formula $\omega = 2\pi/P$; T_{mean} is the mean surface temperature (°C) over the cycle; A_0 is the surface amplitude (°C) from the mean; $d = \sqrt{\frac{2\kappa}{\omega}} = \sqrt{\frac{\kappa P}{\pi}}$, is the damping depth (or skin depth, m). Here, κ is thermal diffusivity, defining the depth at which the amplitude is reduced to roughly 37% $(1/e)$ of the surface value. Low-frequency signals (e.g. annual) clearly penetrate much deeper than high-frequency signals (e.g. diurnal). By measuring the time lag between sensors at different depths, the actual thermal diffusivity of the rock mass can be back calculated (e.g., via the Ångström method). If the computed value aligns with standard ranges for the rock type, conduction is the main driver. If the value diverges significantly, it quantifies how much air advection is boosting the heat transfer. In the latter case, the lag Δt can be used to estimate the speed of the thermal front $v_{thermal} = \Delta z/\Delta t$). This could be related to the air velocity (v_{air}) if fracture porosity (n) is known, by using a retardation factor (R_f): $v_{thermal} = v_{air}/R_f$ where $R_f = 1 + c_{rock}/(n \cdot c_{air})$. The retardation depends on the ratio of the volumetric heat capacity of

the rock (c_{rock}) versus air (c_{air}), and n is the effective porosity. However, high-altitude environments (e.g., 2,700–3,000 m a.s.l.) strongly limits the advective thermal transport. While dolostone has a volumetric heat capacity of approximately 2.2 x 10^6 J/(m^3 K), the rarefied air at 3,000 m a.s.l. drops to roughly 0.9 x 10^3 /J/(m^3 K), and the thermal retardation factor becomes enormous. Even if air flows rapidly through a persistent fracture network (with an effective porosity n<1%), it carries negligible thermal energy compared to the massive thermal inertia of the surrounding rock, which instantly buffers the advective fluid. This process, known as retarded advection, confirms that the deep internal thermal field of the pillar remains strongly dominated by conduction. However, the presence of ice-bearing fractures introduces further non-linearity, the latent heat of fusion, that the purely conductive baseline cannot reproduce and that requires explicit treatment.

4.3.4 *Phase changes and zero-curtain effect*

Analyzing the thermal regime of subvertical rock walls requires addressing phase-change processes within ice-filled fractures. Assuming a dry continuum fundamentally fails to account for the latent heat of fusion. While intact rock has negligible primary porosity, fracture networks in periglacial environments act as concentrated latent heat reservoirs. The penetration of freezing or thawing fronts results in a moving boundary problem, known as the Stefan problem (Carslaw and Jaeger, 1959; Bird et al., 2002). Even a small effective fracture porosity (1–3%) saturated with ice creates a significant zero curtain effect, acting as a thermal brake that delays the deep active layer propagation. Classical analytical solutions (Nixon and McRoberts, 1973; Lunardini, 1981), like the analytical Neumann's solution which assume a sudden constant step-change in surface temperature, often fail to reproduce the sharp geometric knee characteristic of actual phase-change fronts because they ignore the memory effect of high-frequency daily fluctuations. A 1D Finite Difference Method (FDM) was implemented to simulate the transient heat flow step-by-step, driven by the exact chronological surface temperature history. This numerical approach utilizes the apparent heat capacity method to resolve the latent heat exchange. By defining a temperature-dependent specific heat capacity (c_p) that increases massively within a narrow temperature window around 0° C, the model accurately simulates the energy required to freeze or melt the pore water. This mathematical spike in c_p allows the simulated thermal wave to properly stall at the

freezing point, faithfully reproducing the exact sharp curves and the delayed zero-curtain effect measured in the boreholes.

Nevertheless, even if a 1D FDM can rigorously simulate this process, integrating such numerical solutions with high frequency multiparametric column data requires a more computationally efficient phenomenological approach.

To model this within a continuous sensor array framework, a latent heat dampening factor (τ) is applied exclusively to positive thermal anomalies in the localized fracture zone:

$$\boldsymbol{T_{mod}(z,t) = T_{base}(z,t) \cdot [1 - \tau \cdot W_{lat}(z)]} \quad [2]$$

where the dimensionless parameter τ represents the fractional intensity of the zero-curtain effect, and $W_{lat}(z)$ is a spatial latent heat weight expressed by a Gaussian function. This weight is cantered at the depth where the phase change (freezing/thawing) is occurring, describing how far up and down the rock mass the zero-curtain dampening effect spreads from the fracture. Physically, the term $\tau \cdot W_{lat}(z)$ quantifies the proportion of incoming thermal energy that is entirely consumed by the latent heat of fusion (e.g. melting the fracture ice) before the sensible heat of the rock can resume increasing. By establishing a defined cut-off threshold (e.g., τ=0.20), the model effectively truncates the amplitude of the summer warming wave. This mathematically stalls the thermal peak at the freezing point, reproducing the delayed zero-curtain effect measured in the boreholes without the computational overhead of fully coupled FDM matrices.

4.3.5 *Modeling localized thermo-hydro-mechanical anomalies*

The pure 1D conductive half-space model is often overprinted by localized processes. To quantitatively address these effects and interpret the inclino-extensometric sensor data (e.g., DMS02 column), we developed a coupled thermo-kinematic analytical model. To mathematically incorporate the localized advective phenomena (e.g. cold trapping and meltwater percolation) observed at the macroscopic back fracture, the purely conductive model was modified. These anomalies are superimposed onto the conductive background using a Gaussian spatial distribution $W(z)$ centered at the fracture depth z_f, with a standard deviation σ representing the physical thickness (or spatial radius of influence) of the damaged zone:

$$W(z) = \exp\left(-\frac{1}{2}\left(\frac{z-z_f}{\sigma}\right)^2\right) \quad [3]$$

To account for advective fluid flow and the asymmetric, fast-arriving thermal anomalies, a secondary depth-localized harmonic forcing term is superimposed:

$$T_{total}(z,t) = T_{mod}(z,t) - \beta \cdot W_{bias}(z) + A_{adv} \cdot W_{adv}(z) \cdot \sin\left[\frac{2\pi}{P}(t - t_{fase} - t_{adv})\right] \quad [4]$$

where A_{adv} represents the amplitude of the advective thermal shock, $W_{adv}(z)$ is the advection weight, centered at the depth of the active fracture/groundwater flow and controlling how far the thermal anomaly carried by the moving fluid penetrates into the surrounding rock. Because this phenomenological approach models the localized thermal effect rather than the explicit fluid dynamics, the formulation is fluid-agnostic. The specific nature of the acting fluid, whether water (high volumetric heat capacity, more concentrated and slower flow) or air (very low volumetric heat capacity, more dispersed and rapid flow), is captured by calibrating the amplitude (A_{adv}), the spatial standard deviation σ of $W_{adv}(z)$, and the temporal phase delay (t_{adv}) to reflect the distinct volumetric heat capacities and kinematic velocities of the respective fluids relative to the surface temperature.

Additionally, the chimney effect (cold air trapping) within the open fracture network is modeled by introducing a permanent negative thermal bias term ($-\beta \cdot W_{bias}(z)$). This local cold bias simulates the sinking and pooling of dense winter air. Thermodynamically, heavy, freezing air easily infiltrates gravity-driven convective pathways, but cannot be easily displaced by buoyant, warm summer air. By applying this negative bias to the specific spanning modules of the fracture zone via its spatial weight $W_{bias}(z)$, the model artificially shifts the mean annual ground temperature locally downward, replicating the asymmetric cooling efficiency of the open fracture.

4.3.6 *Thermo-mechanical coupling and kinematics of borehole snaking*

The primary objective of this methodological approach is to isolate and remove the seasonal thermal noise, in particular the lateral bending known as thermal snaking, to isolate the true underlying geotechnical residual displacement. Once the thermal field $T_{total}(z,t)$ is robustly calibrated, the model couples these temperature variations to the mechanical deformation of the column. The column is modeled as a discrete chain of

rigid segments (modules) of nominal length L_0, matching the spatial resolution of in situ sensors. The theoretical unconstrained axial thermal dilation ΔL for each module is calculated as:

$$\Delta L(z,t) = L_0 \cdot \Delta\alpha \cdot [T_{total}(z,t) - T_{mean}] \quad [5]$$

where $\Delta\alpha$ is the effective differential coefficient of thermal expansion between the sensor material and the surrounding medium. Because the column is confined by lithostatic pressure and friction within the borehole, this dilation cannot freely expand axially. The trapped strain energy forces the modules to buckle laterally (snaking). Assuming small displacements, the induced lateral tilt angle θ for each module is geometrically derived as:

$$\theta(z,t) = B \cdot sgn(\Delta L)\sqrt{\frac{2|\Delta L|}{L_0}} \quad [6]$$

where B is an empirical buckling amplification factor. While the square root term defines the pure geometric deflection, B (calibrated to 0.2 in our model) accounts for the real-world mechanical compliance of the column, including borehole clearance and spacer stiffness. This kinematic chain is interrupted by physical extensometer integrated within specific modules. Acting as mechanical expansion joints, they absorb the axial strain and locally suppress lateral buckling. The formulation applies an absorption function around these nodes, zeroing the effective ΔL available for buckling within a defined mechanical radius of influence.

Finally, real inclinometric systems derive global 2D horizontal displacement profiles by integrating local biaxial tilt measurements (pitch and roll) from the bottom up. assuming a stable anchor base. To isolate the geotechnical signal from the thermal noise, the true Cartesian displacement vectors (X_{real}, Y_{real}) must be projected onto the 2D azimuth (angle ψ) of maximum expected geotechnical movement:

$$Real_{Proj}(z_n,t) = X_{real}(z_n,t) \cdot \cos(\psi) + Y_{real}(z_n,t) \cdot \sin(\psi) \quad [7]$$

by subtracting the calculated theoretical radial thermal snaking profile from this projected real deformation, the seasonal structural artifacts are filtered out. The resulting time-series represents the pure geotechnical residual, completely decoupled from its thermodynamic environment.

4.3.7 *Thermal compensation algorithm of rock displacements*

The continuous kinematic monitoring of fractured rock cliffs using surface extensometers typically yields a composite displacement signal. This raw signal is heavily dominated by reversible thermo-elastic strains, that is the natural expansion and contraction of intact rock blocks and rock bridges in response to daily and seasonal thermal waves. To effectively use monitoring data for early warning and slope stability forecasting, it is mandatory to filter out this thermal noise to isolate any irreversible, damage-driven deformations. This compensation relies on the linear relationship between temperature variations and induced strain, governed by the thermal expansion coefficient of the material. However, in a jointed rock mass, the linear expansion coefficient of intact rock cannot be directly applied due to the complex interaction between rock blocks and void spaces.

Therefore, a thermal compensation methodology was developed by cross correlating the raw extensometric time series with the corresponding temperature data. By accounting for the thermal phase shift calculated from the 1D heat flow analysis, it is possible to derive an effective, site-specific thermal expansion coefficient for the fractured rock mass. Applying this empirical coefficient enables the subtraction of the reversible thermo-elastic component from the total measured displacement, thereby revealing the true geomechanical trend and identifying potential precursors to failure.

The objective of this methodology is to mathematically extract and eliminate the true thermal signature ($D_{thermal}(t)$) directly from the raw apparent strain signal ($D_{raw}(t)$), yielding the underlying net rock deformation ($D_{raw}(t)$). The algorithmic pipeline follows a five-step processing sequence. First, the sequence requires the raw measured displacement (apparent strain) and the local ambient air temperature high-resolution time series, both sampled at a fixed temporal interval (dt): $Inputs: D_{raw}(t), T_{air}(t)$.

To isolate the strictly diurnal thermo-elastic behaviour, which is the core subject of the correction, a high-pass filter is applied to both the strain and temperature datasets. This step removes slow geomechanical drifts and low-frequency seasonal trends by subtracting a moving average (MA) from the raw signals:

$$D_{HF}(t) = D_{raw}(t) - MA_W(D_{raw}(t)) \quad [8]$$

$$T_{HF}(t) = T_{air}(t) - MA_W(T_{air}(t)) \quad [9]$$

where $D_{HF}(t)$ and $T_{HF}(t)$ are the high-frequency strain and temperature time series, respectively, and W is the moving average window size (typically 24 hours). Raw data plotted against air temperature shows wide, fuzzy elliptical clouds associated with thermal hysteresis and the phase lag between the fast-acting ambient air temperature and the thermal mass of the sensor/resin. To resolve this commonly observed hysteretic cyclicity, the temporal phase lag between the atmospheric forcing and the thermal response of the rock-sensor system must be quantified. A cross-correlation (X-Corr) function is implemented between the derivative of the strain and the temperature to identify the time lag, Δt, that maximizes the correlation coefficient:

$$\Delta t = argmax_{\tau}(R_{D'T}(\tau)) \quad [10]$$

By applying this Δt, the temperature time series is mathematically shifted to realign the cause (temperature) and effect (strain) phases. This temporal shift forces the elliptical hysteresis cloud to collapse into a linear distribution. Following the phase alignment, a linear regression is performed on the high-frequency dataset. The calculated slope of the resulting best-fit line represents the equivalent coefficient of thermal expansion (α_{eq}) of the combined sensor, resin, and microclimate system under actual operational conditions:

$$D_{HF}(t) = \alpha_{eq}\, T_{Shifted}(t) + \epsilon \quad [11]$$

where $T_{Shifted}(t) = T_{HF}(t + \Delta t)$, and ϵ represents the residual noise. This empirical extraction is necessary because relying on a standard, theoretical thermal expansion coefficient (e.g., 1.20 x 10^{-5}/°C for steel instruments) is fundamentally inadequate for field applications. The data-driven α_{eq} captures the complex bulk response of the entire measurement setup, encompassing the expansion of the hardware, the behavior of the epoxy resin/grout, the deformation of the anchoring micro-fissures, and the specific solar exposure of that particular rock face. Furthermore, its calculated sign intrinsically accounts for the mechanical setup of the gauge (e.g., a negative slope indicating that instrument expansion is recorded as an apparent fracture closure). The goodness of fit is explicitly evaluated using the coefficient of determination (R^2) and the Root Mean Square Error (RMSE) to quantify measurement uncertainty. Finally, the α_{eq} parameter is utilized to calculate the absolute thermal noise across the entire raw temperature time series. This thermal component is then algebraically subtracted from the raw displacement data to yield the decoupled, net rock deformation:

$$D_{net}(t) = D_{raw}(t) - D_{thermal}(t) = \alpha_{eq}\, T_{air}(t) \quad [12].$$

By removing the combined seasonal drift and phase-lagged thermal hysteresis, this filtering method successfully isolates the pure daily breathing of the instrument. The resulting detrended kinematic signal perfectly preserves the sudden geomechanical jumps and irreversible damage events, while completely eliminating the high-frequency daily thermal static.

4.3.8 *3D transient thermal modelling setup*

To evaluate the spatial distribution of temperatures and the evolution of the permafrost active layer within the complex geometry of the pillar, a 3D transient thermal model was developed using the FEFLOW software (DHI). The unstructured 3D mesh (*supermesh*) of the pillar was generated from the available high-resolution point-cloud data to preserve the real topography. The hydro-thermal simulations were performed under fully saturated, no-flow conditions, ensuring that heat transport was purely conductive with surface convective transport (i.e., neglecting advective heat transport by groundwater). The material thermal parameters applied to the continuum are summarized in Table 4

Table 4 Parameters used in entire domain for thermal analysis.

PARAMETER	VALUE
Hydraulic Head [m]	2817
Porosity [-]	3%
Vol. Heat Capacity of fluid [MJ/m^3/K]	4.2
Vol. Heat Capacity of solid [MJ/m^3/K]	2.4
Thermal Conductivity of fluid [W/m/K]	0.65
Thermal Conductivity of solid [W/m/K]	2.5

To accurately simulate the progressive degradation of the permafrost, a three-step simulation strategy was implemented. First, a long-term initialization run (spin-up) was performed to minimize the influence of initial conditions and reach a quasi-periodic thermal state. This was achieved by imposing a 12-month cycle of monthly mean temperatures repeated for 90 years. Second, transient simulations were carried out using both the daily air temperature recorded at the Pisciadù weather station over the last 20 years, and the near-surface rock temperature from the shallowest GeoPrecision sensor (at a depth of 0.23 m) as boundary conditions, to explore the sensitivity of the thermal response. Finally, forward simulations were executed up to the year 2100, applying time-

varying temperature anomaly that increases linearly up to +1.8°C (RCP 4.5) and +4.3°C (RCP 8.5) by 2100 (IPCC, 2014). This approach shifts the long-term mean temperature while preserving the observed high-frequency daily variability of the reference period (Figure 34)

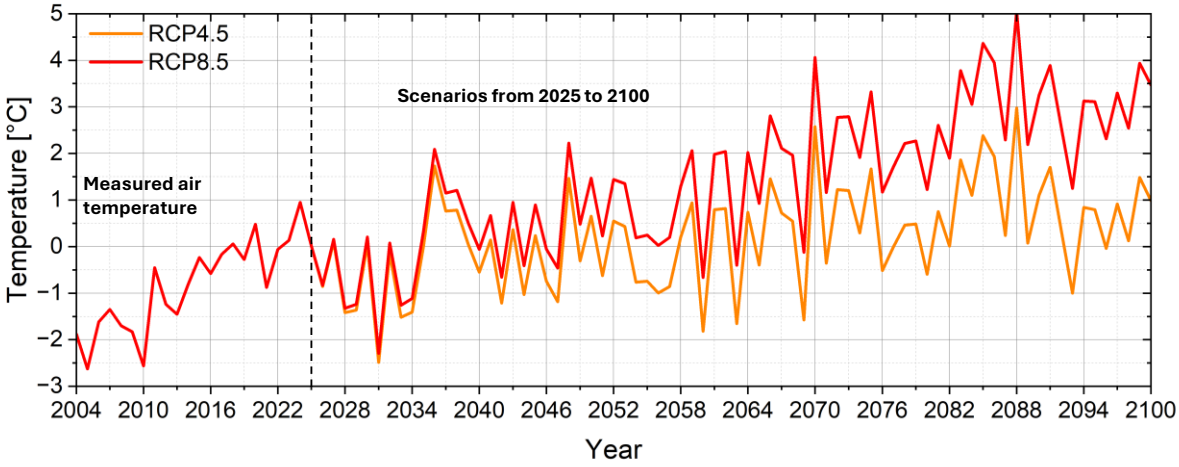


Figure 34 Annual air temperature time series for RCP4.5 and RCP8.5 climate scenarios up to 2100 used as input boundary conditions in thermal analysis. The 2004–2024-time interval includes the measurements acquired at the Pisciadù station whereas the future time series are built on global scenarios.

4.3.9 *3D mechanical stability analysis setup*

The mechanical response and the ultimate stability of the rock pillar was evaluated using the MIDAS FEA NX 3D finite-element software. The highly detailed geometry of the structural mesh was derived directly from the 79-million-point UAV LiDAR cloud. To ensure computational efficiency while preserving the structural features that control mechanical behavior, minor surface roughness was removed from the geometry. The major persistent discontinuities isolating the frontal sectors were explicitly modeled using interface elements. The final structural mesh consists of 202,759 elements and 107,774 nodes.

Appropriate boundary conditions were applied to restrain rigid-body motion: the basal surface was fixed in the vertical direction, while lateral boundaries were constrained horizontally. The continuous rock mass and the structural interfaces were modeled as elastoplastic materials governed by the Mohr–Coulomb failure criterion (Table 5). The equivalent continuum rock mass elastic properties were scaled from laboratory characterizations of the Dolomia Principale to represent the pillar scale. Because interface

strength is the primary source of uncertainty and controls the overall stability, five distinct parameter sets (Sets 1–5, Table 5) were defined. These sets span a realistic range of joint conditions, from relatively strong rock bridges to weakened, ice-filled discontinuities, supporting a systematic sensitivity analysis.

Table 5 Rock mass mechanical properties adopted in the MIDAS model for the SRM analyses and Interface mechanical properties adopted in the mechanical model for the SRM analyses. Five parameter sets (Set 1–Set 5) were defined including initial interface cohesion c and initial friction angle φ, normal and shear stiffness (k_n, k_s) and dilatancy angle. Cohesion and friction angle are bold since they are varied during the numerical simulations.

ROCK PARAMETER					**VALUE**
Young's module $[GPa]$					12
Poisson's ratio [-]					0.25
Unit weight $[kN/m^3]$					25.5
Cohesion $[KPa]$					1200
Friction Angle ϕ [°]					37
Dilatancy Angle [°]					8
INTERFACE PARAMETER	**Set 1**	**Set 2**	**Set 3**	**Set 4**	**Set 5**
Norm Stiffness $[N/m^3]$	2.58e+011	2.58e+011	2.58e+011	2.58e+011	2.58e+011
Shear Stiffness $[N/m^3]$	2.35e+010	2.35e+010	2.35e+010	2.35e+010	2.35e+010
Cohesion $[KPa]$	**840**	**840**	**300**	**100**	**100**
Friction Angle [°]	**28**	**35**	**35**	**35**	**28**
Dilatancy Angle [°]	0	0	0	0	0

The stability assessment was conducted through the Shear Strength Reduction Method (SRM), which progressively reduces the shear strength parameters until numerical non-convergence is reached, defining the Factor of Safety (FoS). The systematic modeling workflow considered two geometric states (pre- and post-2018 collapse) and three fracture configurations: (F1) back discontinuity only; (F2) back and central discontinuities; and (F3) central discontinuity only. First, a back-analysis of the 2018 rockfall was performed (Table 6, cases M1–M6) to verify that the critical strength parameters required to trigger the failure (FoS ≈ 1) correspond strictly to the degraded properties of a thawing permafrost rock mass. Following this validation, the calibrated parameters were applied to the current post-collapse geometry (case M7). The spatially distributed thermal fields extracted from the FEFLOW simulations were imported into

MIDAS as driving thermal loads, allowing for the calculation of the accumulated thermo-mechanical stresses and the future FoS evolution under the projected climate scenarios.

Table 6 Summary of SRM numerical simulations. The analysis considers two geometry states (pre-2018: back-analysis – BA2018, and post-2018 collapse: future failure scenario) and three fracture configurations: (F1) back discontinuity only; (F2) back and central discontinuities; and (F3) central discontinuity only. The interface strength parameters assigned to each case correspond to Sets 1–5 in Table 5.

Case ID	*Geometry*	*Fracture*	*Interf. Set*	*Aims*
M1	Pre collapse	F1	Set 1	BA2018: back fracture only, reference interface strength
M2		F2	Set 1	BA2018: two discontinuities, reference interface strength
M3		F2	Set 2	BA2018: increased interface friction angle (ϕ)
M4		F2	Set 3	BA2018: reduced interface cohesion (c)
M5		F2	Set 4	BA2018: low cohesion + high ϕ (ice-filled / weakened interface scenario)
M6		F2	Set 5	BA2018: low cohesion + lower ϕ (weaker/friction-reduced interface scenario)
M7	Post-collapse	F3	Set 4	Post-failure stability, ice-filled / weakened interface scenario

4.4 **Results**

4.4.1 *Subsurface Thermal Regime*

The subsurface temperature records from the three boreholes, DMS01, DMS02, and the GeoPrecision chain, provide a high-resolution, multi-depth characterization of the thermal regime of the rock mass. The geoprecision dataset is shown in Figure 35. In the shallowest sensors at approximately 1 m depth, temperatures exhibit high-frequency variability driven directly by atmospheric forcing, ranging from approximately −10 °C to +10 °C with peak-to-peak seasonal amplitudes of up to 20 °C. As the thermal wave propagates inward, both the amplitude and the rate of change progressively diminish,

while the timing of seasonal extrema is increasingly delayed relative to the surface forcing, a pattern entirely consistent with classical conductive heat diffusion through a homogeneous rock matrix. The synthesis of these multi-depth profiles allows the internal thermal architecture of the pillar to be partitioned into three physically distinct domains. The active layer, extending from the surface to approximately 8 m depth, is dominated by seasonal atmospheric forcing and experiences complete annual freeze-thaw cycles with significant penetration of the cold winter wave. The apparent thermal propagation velocities in this domain align closely with those predicted by the conductive model for intact dolomite, confirming that heat transport is predominantly diffusive in the shallow rock matrix. The marginal permafrost body, located between approximately 8 and 14 m depth, is characterised by temperatures that cluster persistently around 0 °C to −1 °C with markedly reduced seasonal variability and severely delayed extrema. This thermally buffered domain is fully consistent with warm, marginal permafrost conditions, and the persistent near-zero temperatures reflect a strong zero-curtain effect driven by the latent heat of fusion within ice-bearing discontinuities, a thermal signature that cannot be reproduced by purely conductive models and that provides direct evidence of interstitial ice at these depths. This interpretation is physically corroborated by the BHTV logging and drilling observations, which identified ice-filled fractures precisely within this horizon in both DMS01 and DMS02. The deep thaw zone, below approximately 14 m, exhibits a gradual temperature increase persistently above 0 °C, coupled with a near-absence of seasonal forcing. This deeper warming trend is attributed to a combination of basal geothermal heat flux; the complex three-dimensional topographic exposure of the pillar faces to differential solar radiation and localized deep air circulation within the major fracture network. The cross-comparison between the DMS columns and the GeoPrecision chain at overlapping depths reveals a highly consistent thermal behaviour, validating the spatial representativeness of each measurement system. The non-uniform spacing of the GeoPrecision chain resolves the steepest temperature gradients and rapid phase shifts in the upper few meters with higher resolution than the uniformly spaced DMS sensors, while the parallel DMS01 and DMS02 records capture small-scale lateral thermal heterogeneities between different sectors of the fractured pillar that would be invisible to a single borehole.

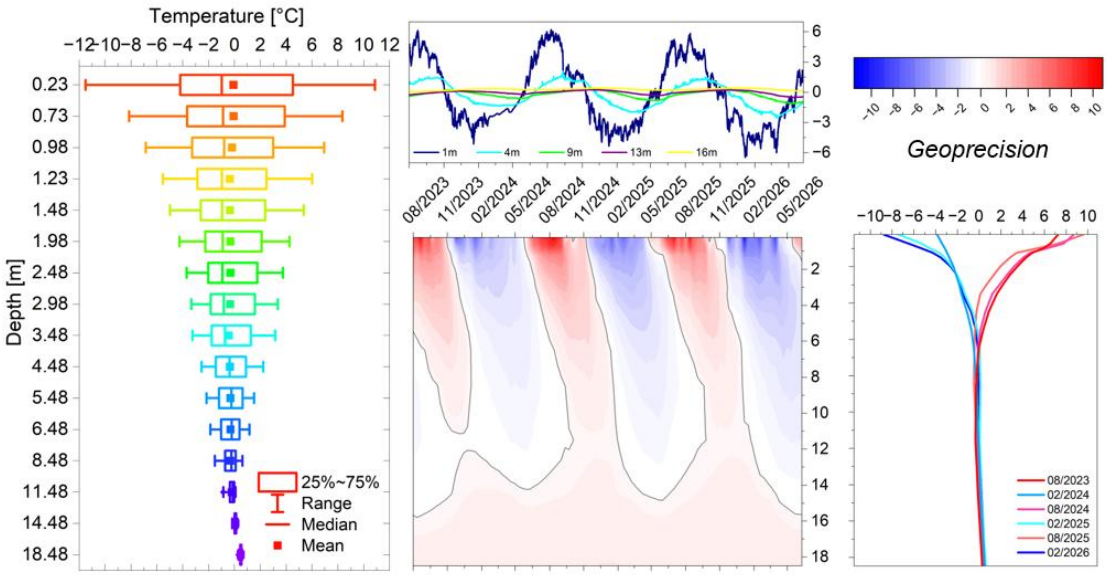


Figure 35 a) Boxplot showing the variability of temperature at each sensor along the Geoprecision thermal chain; b) Geoprecision temperature heat map with profiles at different days (d1) along the column and time series at different depths (d2).

4.4.2 *Conductive baseline and deep anomalies*

To establish a baseline for the thermal regime of the rock mass, the in-situ temperature time series were evaluated against the classical 1D analytical solution for transient heat diffusion in a semi-infinite solid. The spatio-temporal evolution of the measured temperatures was compared against theoretical heat maps and extreme trumpet plots (Figure 36) generated using two bounding thermal diffusivity values: a high diffusivity scenario $\kappa_{high} = 1.0 \times 10^{-6}$m²/s, representative of intact rock, and a low diffusivity scenario $\kappa_{low} = 0.5 \times 10^{-6}$m²/s. In the shallow domain (0 to ~12 m), the measured data exhibit excellent agreement with the analytical conductive model. The empirical heat maps clearly display the diagonal tilt characteristic of purely conductive heat transfer, where seasonal thermal waves propagate inward with progressive amplitude attenuation and a linear phase lag. The measured extremes perfectly plot within the theoretical trumpet envelopes defined by κ_{high}. The convergence of measurement points to a narrow range at approximately 12 m depth visually confirms the damping depth of the seasonal active layer, where the macroscopic thermal wave is effectively exhausted.

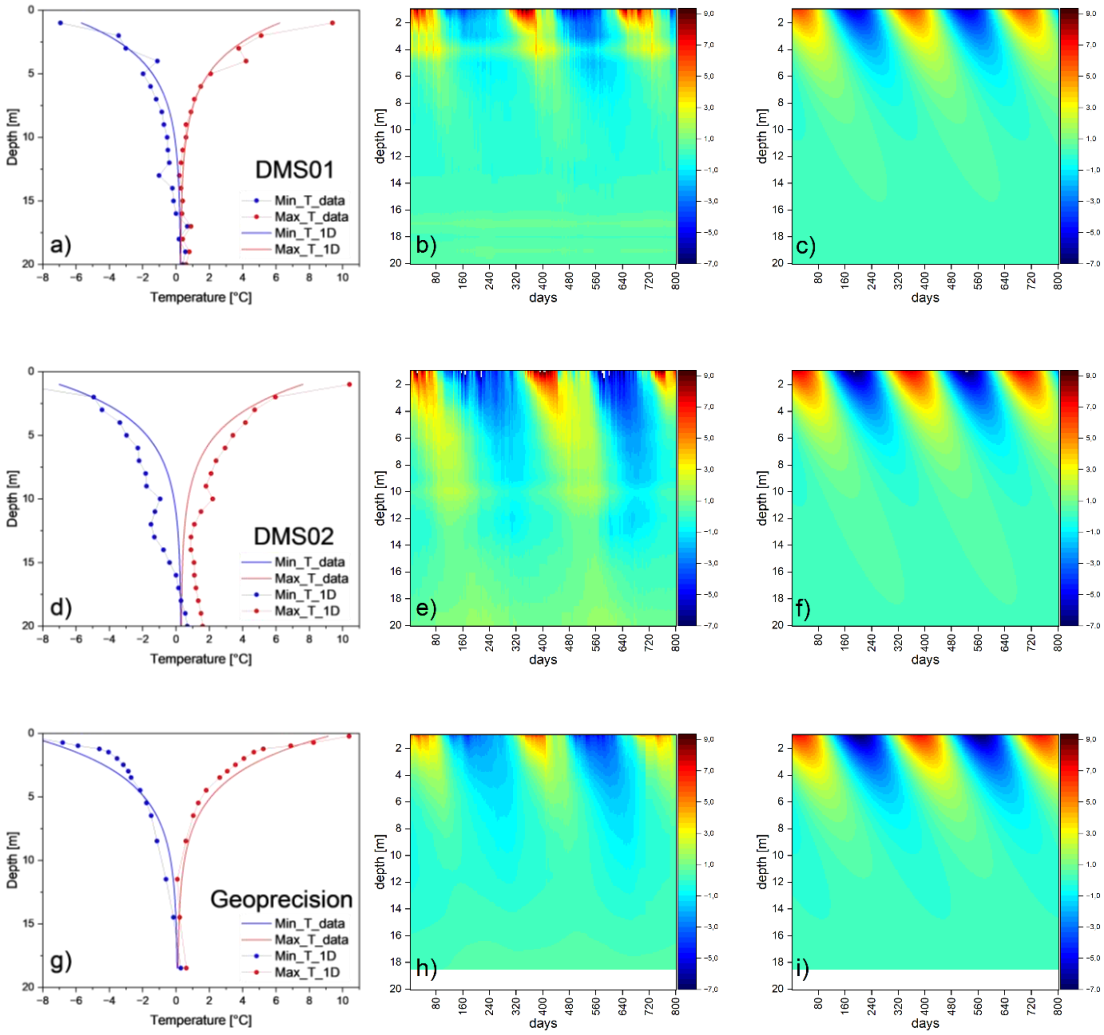


Figure 36 Comparison of measured thermal regimes against a purely conductive 1D heat transfer model for the DMS01 (a–c), DMS02 (d–f), and Geoprecision (g–i) boreholes. The left column (a, d, g) displays the thermal trumpet curves, plotting the minimum and maximum measured temperatures alongside the theoretical 1D conductive envelopes. The center column (b, e, h) shows the depth-time heatmaps of the in-situ measured temperatures. The right column (c, f, i) presents the corresponding theoretical heatmaps generated by the 1D diffusion model, highlighting the deviations between purely conductive predictions and the actual advection-influenced field data.

A rigorous sinusoidal fitting of the time series (Figure 37) further validates this conductive behaviour. In the upper 12 m, the amplitude attenuation follows a strict exponential decay, and the phase lag increases linearly with depth, strongly aligning with the theoretical curves for κ_{high}. This confirms that the bulk intact rock matrix acts as a homogeneous, consolidated conductive medium.

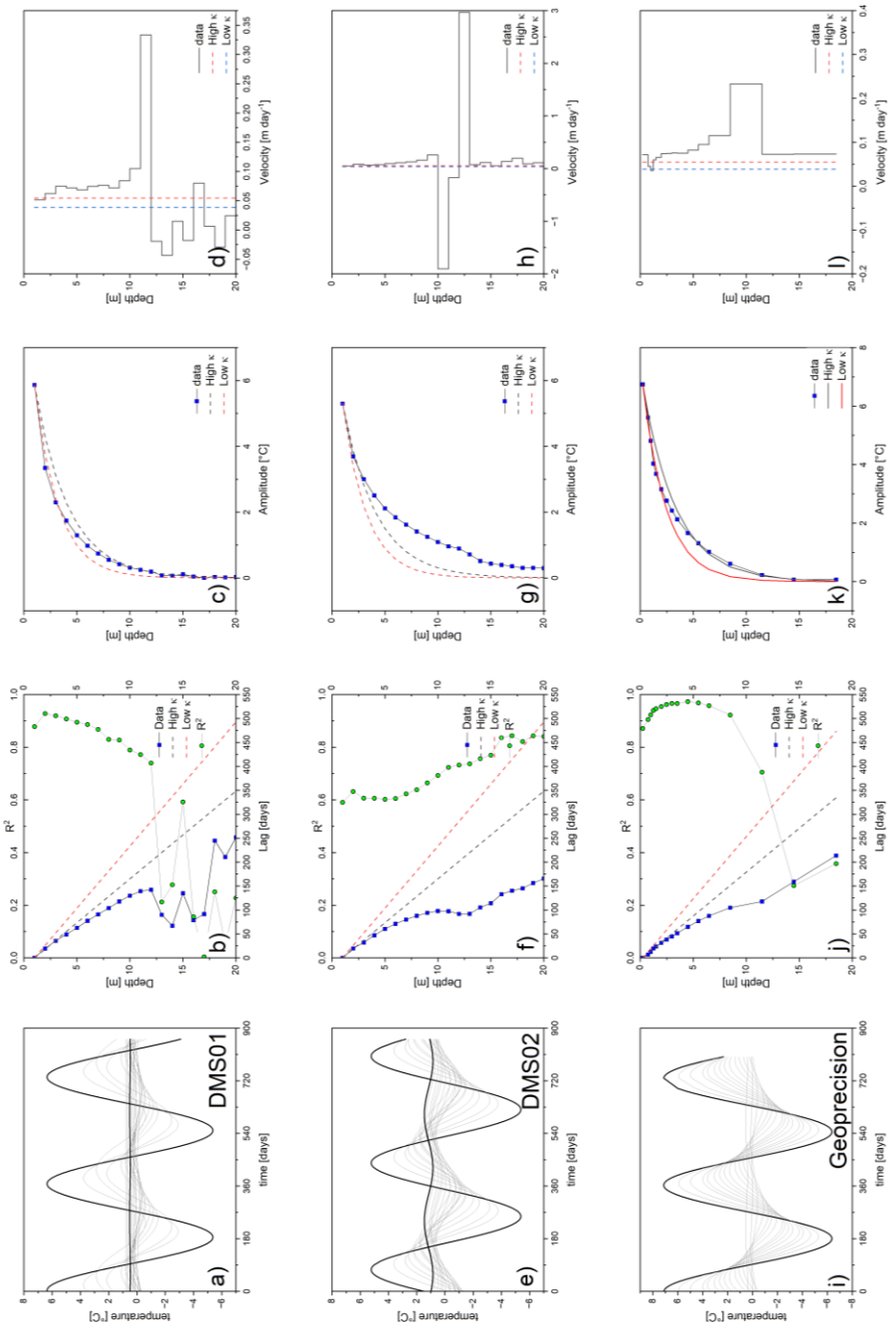


Figure 37 Depth-dependent thermal wave propagation and apparent velocity analysis for the DMS01 (a–d), DMS02 (e–h), and Geoprecision (i–l) boreholes. Panels (a, e, i) show the global sinusoidal fitting of the temperature time series at various depths. The phase lag (b, f, j) and amplitude attenuation (c, g, k) of the measured data (solid blue lines) are compared against theoretical limits calculated for low and high thermal diffusivity bounds (0.5 and 1.0 × 10^{-6} m^2/s, represented by red and blue dashed lines, respectively). Green dots in the phase lag panels indicate the R^2 value of the sinusoidal fit. Panels (d, h, l) display the computed apparent vertical thermal velocity from the measured data (solid black lines) compared to the constant theoretical velocities associated with the bounding diffusivity values.

2483 However, the analytical model breaks down in the deep zone (>12 m). By converting
2484 the phase lag of the thermal wave into an apparent vertical propagation velocity (v_T), a
2485 distinct bipartite vertical profile emerges. In the shallow zone, $v_T$is highly stable,
2486 averaging between 0.06 and 0.08 m/day. In stark contrast, below 12 m, a significant
2487 velocity anomaly is observed, with values either spiking above 0.3 m/day or becoming
2488 highly erratic.
2489 The deep analytical divergence can be attributed to two coupled factors. First, when
2490 the seasonal amplitude drops below the instrumental noise threshold (<0.1 °C), the
2491 mathematical reliability of the sinusoidal best-fit inherently degrades, as reflected by the
2492 dropping R^2 values, producing artificial velocity spikes. Second, and more critically from
2493 a physical standpoint, the pure 1D conductive half-space model is overprinted by
2494 localized advective processes. In a purely conductive regime, the temperature below the
2495 damping depth should remain stable or slowly increase according to the geothermal
2496 gradient. However, the data reveal a persistent negative thermal anomaly at depths
2497 between 12 and 13 m, where temperatures remain systematically lower than the
2498 theoretical conductive predictions. This systematic deviation strongly suggests that major
2499 discontinuities such as the macroscopic back-fracture identified at 13.5 m during drilling
2500 and BHTV logging, act as preferential thermal shortcuts. Because advective transport is
2501 orders of magnitude faster than conductive diffusion, open fractures introduce new
2502 internal boundary conditions, carrying the surface temperature signature deep into the
2503 rock mass with amplitude loss and a reduced time lag. To fully explain this localized
2504 thermal depression and the failure of the standard Fourier 1D solution at depth, three
2505 main, potentially concurrent thermo-mechanical hypotheses are proposed. The first
2506 mechanism is asymmetric air circulation, or cold trapping: driven by density, cold and
2507 heavy winter air descends into the open fractures via gravity-driven convective flows,
2508 rapidly cooling the deep rock mass, while during summer lighter warm air remains stably
2509 stratified near the surface and is unable to displace the trapped cold air. Acting in synergy
2510 with cold trapping is the second mechanism: latent heat buffering, or the zero-curtain
2511 effect, whereby the freezing and thawing of interstitial water within the fracture network
2512 pins the local temperature near 0 °C, actively resisting the downward propagation of the
2513 summer warming trend until all ice is completely melted. Finally, the advection of
2514 snowmelt constitutes the third contributing factor: the spring thaw generates significant
2515 volumes of meltwater at approximately 0 °C which, by percolating rapidly downward

through the open fracture system, prematurely cools the deeper sections of the rock mass, thereby dampening the arrival of the slower conductive summer heat wave. Together, these localized advective and latent bypasses dictate that more advanced modelling approaches are necessary to capture the full multiphysics behaviour of the fractured pillar.

4.4.3 *Deep Kinematics – Borehole Deformation*

The subsurface kinematic evolution of the pillar is characterised through the continuous integration of the inclinometric modules along the DMS01 and DMS02 columns. To correctly interpret the resulting displacement profiles, the specific mechanical architecture of the sensor chain must be understood. The discrete rigid modules are axially constrained along the column, with the exception of the three extensometric modules in DMS02, such that any localized axial shortening or elongation of the rock mass forces the adjacent constrained modules to react with angular deviations of similar magnitude but opposite sign. This kinematic compensation generates a characteristic saw-tooth pattern in the raw displacement profiles (Figure 38), which is particularly pronounced during the first year of monitoring and progressively diminishes as the column structurally settles and dynamically couples with the borehole walls. Once this initial transient dissipates, the displacement profiles reveal that deep deformation is not uniformly distributed along the borehole but is highly localized at discrete structural intercepts corresponding to the major fractures identified in the BHTV logs.

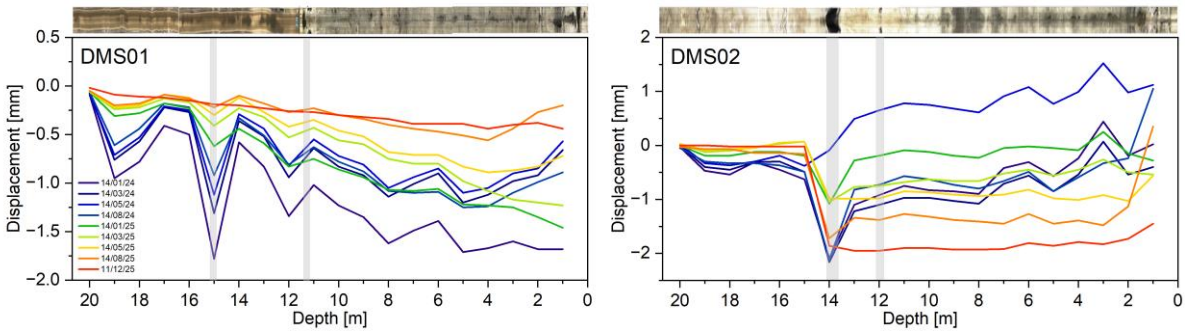


Figure 38 Displacement profile along the columns DMS01 (a) and DMS02 (b) at different dates. The BHTV images are shown at the top of each plot, to show the correspondence of displacement with the main fractures.

In DMS01, deformation concentrates at depths of 11.0–11.4 m, 14.9–15.1 m, and 19.0 m, with a cumulative surface displacement remaining below 2 mm. In DMS02, the emergence of the true kinematic signal after the initial settling period reveals a stark and

highly localized shear displacement at a depth of 13.5–14.0 m, precisely coinciding with the projection of the primary sub-vertical back-fracture that governed the 2018 instability and with the lower thermal boundary of the marginal permafrost body identified in Section 4.4.1. This spatial coincidence between the permafrost thaw boundary and the kinematic release surface establishes a direct, measurable coupling between the thermal and mechanical evolution of the pillar and represents one of the most significant observational results of the monitoring campaign.

The axial extensometers in DMS02 provide complementary information on the depth-dependent volumetric response of the rock mass (Figure 39). At 2 m depth, within the active layer, the axial displacement exhibits a clear seasonal cyclicity in anti-phase with the temperature signal, periods of warming correspond to contraction and cooling to extension, with an amplitude of ±0.25 mm superimposed on a net irreversible compression of approximately +0.021 mm over the monitoring period. This inverted phase relationship indicates that the near-surface deformation is not governed by simple local thermo-elastic expansion but by mechanical constraint effects within the rock mass. At 13 m depth, within the marginal permafrost zone, the displacement amplitude is strongly reduced, and the behaviour becomes episodic and in-phase with temperature, suggesting a direct coupling with the local thermal field rather than with remote surface forcing. At 17 m depth, in the deep thaw zone, the signal is characterised by near-neutral, low-amplitude conditions with no systematic relationship with temperature, marking the transition to the mechanically stable basal domain.

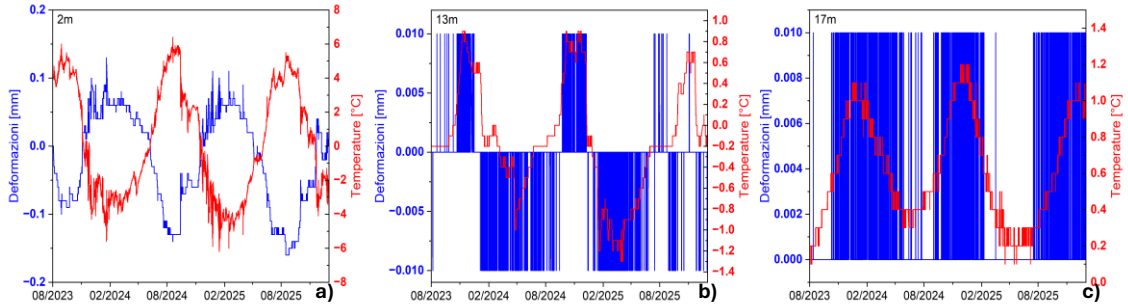


Figure 39 Time series of extensometer located at 2 m, 13 m, and 17 m from the surface along the DMS02. Deformation is expressed as compression (negative) and extension (positive) and plotted together with rock temperature measured in the same module.

4.4.4 *Isolation of the Geotechnical residual*

To bridge the gap between the observed raw borehole deformation and the underlying structural kinematics, a semi-empirical thermal-kinematic model was applied to the DMS02 dataset to separate the cyclic thermal snaking from the pure geotechnical residual displacement (Figure 40). Building upon the theoretical thermal diffusion model described in §4.3.3, the approach was calibrated using baseline thermophysical parameters representative of typical dolostones (thermal conductivity k = 4 W/m K and specific heat capacity c = 900 J/kg K) while explicitly integrating the fracture effects identified in section 4.4.2. The calibration defines a fractured zone of 1.7 m thickness centered at approximately 13 m depth, characterised by a local cold bias of 1.35 °C to account for the asymmetric cold trapping, and a zero-curtain latent heat dampening factor of 0.20 to capture the thermal buffering caused by phase changes within the fractured rock mass.

These localized additions allow the theoretical model to mirror the distinct non-linear thermal anomalies observed at depth in the real borehole temperature profiles. By feeding these refined, fracture-aware thermal variations into the kinematic model — amplified by a calibrated buckling factor of 0.2, baselines for the pure seasonal volumetric expansion and contraction were generated. Comparing this pure thermal prediction against the raw measured deformation highlights a deliberate and significant divergence: the measured signal contains a persistent structural drift that the thermal model cannot reproduce, confirming the presence of irreversible geotechnical displacement superimposed on the reversible thermal snaking. Subtracting the theoretical thermal model from the real projected deformation successfully isolates the purely geotechnical residual. This critical decoupling step filters out the cyclic noise induced by both shallow surface conduction and the deep, fracture-driven thermal anomalies, revealing the isolated trajectory of the underlying structural drift. Localized time-series analysis at specific depths confirms that absolute magnitudes differ due to the ongoing drift, the phase and frequency of the theoretical thermal strain align remarkably well with the cyclic components of the observed local extensometric displacements, validating the physical consistency of the compensation approach.

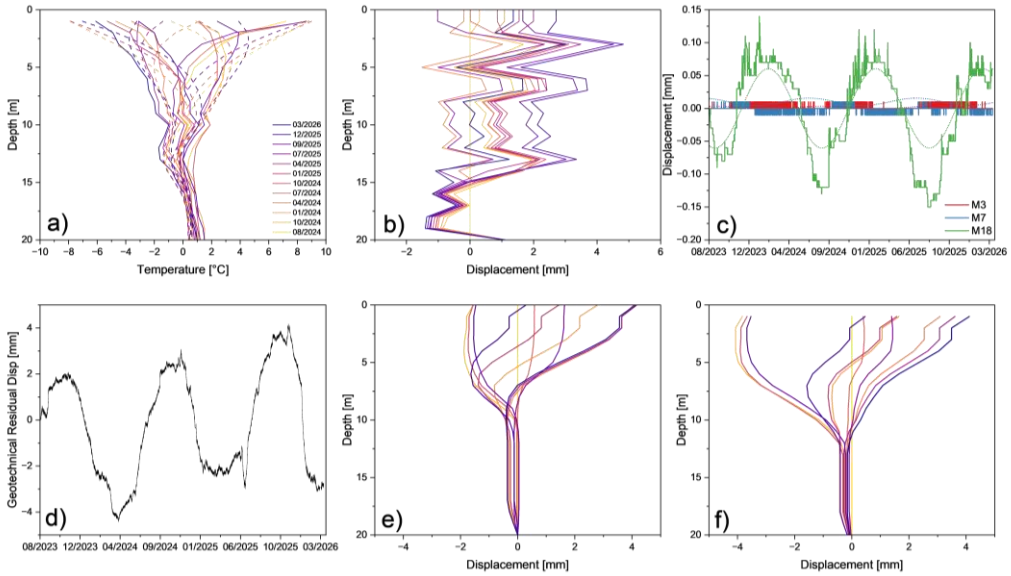


Figure 40 Application of the semi-empirical thermal-kinematic model to the DMS2 dataset to separate cyclic thermal snaking from underlying geotechnical displacement. a) Comparison between measured borehole temperatures (solid lines) and the calibrated theoretical thermal diffusion model (dashed lines) over depth. Colors indicate different months of the year. b) Measured cumulative deformation projected along the specified azimuth, containing both the seasonal thermal snaking and the long-term geotechnical drift. c) Time-series comparison at specific depths (M3, M7, M18) for extensometric deformation: local displacements (solid lines) against pure thermal-model predictions. d) Geotechnical residual displacement over time, obtained by subtracting the theoretical thermal model from the real projected deformation. e) Pure kinematic response generated by the semi-empirical model, predicting the seasonal expansion and contraction (snaking) based on theoretical temperature variations. f) Kinematic prediction using the actual measured temperature profiles as input for the theoretical snaking model, providing a baseline for expected thermal strain.

4.4.5 *Surface Fracture Kinematics and thermal decoupling*

The raw displacement measurements from the surface extensometers (Ext21, Ext22, and Ext23) show a clear thermo-mechanical response, characterised by a strong correlation between ambient air temperature fluctuations and recorded joint displacements (Figure 41). All sensors exhibit pronounced seasonal cycles, featuring progressive apparent contraction during winter cooling phases and expansion during summer warming periods. Furthermore, short-term displacement variations are highly synchronized with daily thermal oscillations, indicating that the thermo-elastic deformation of both the superficial rock mass and the steel instrumentation contribute significantly to the measured signal. Although long-term displacement trends suggesting cumulative opening or closing of the discontinuities are faintly visible in the raw time

series, their true magnitude and direction cannot be reliably quantified due to the masking effect of this dominant reversible thermo-elastic component.

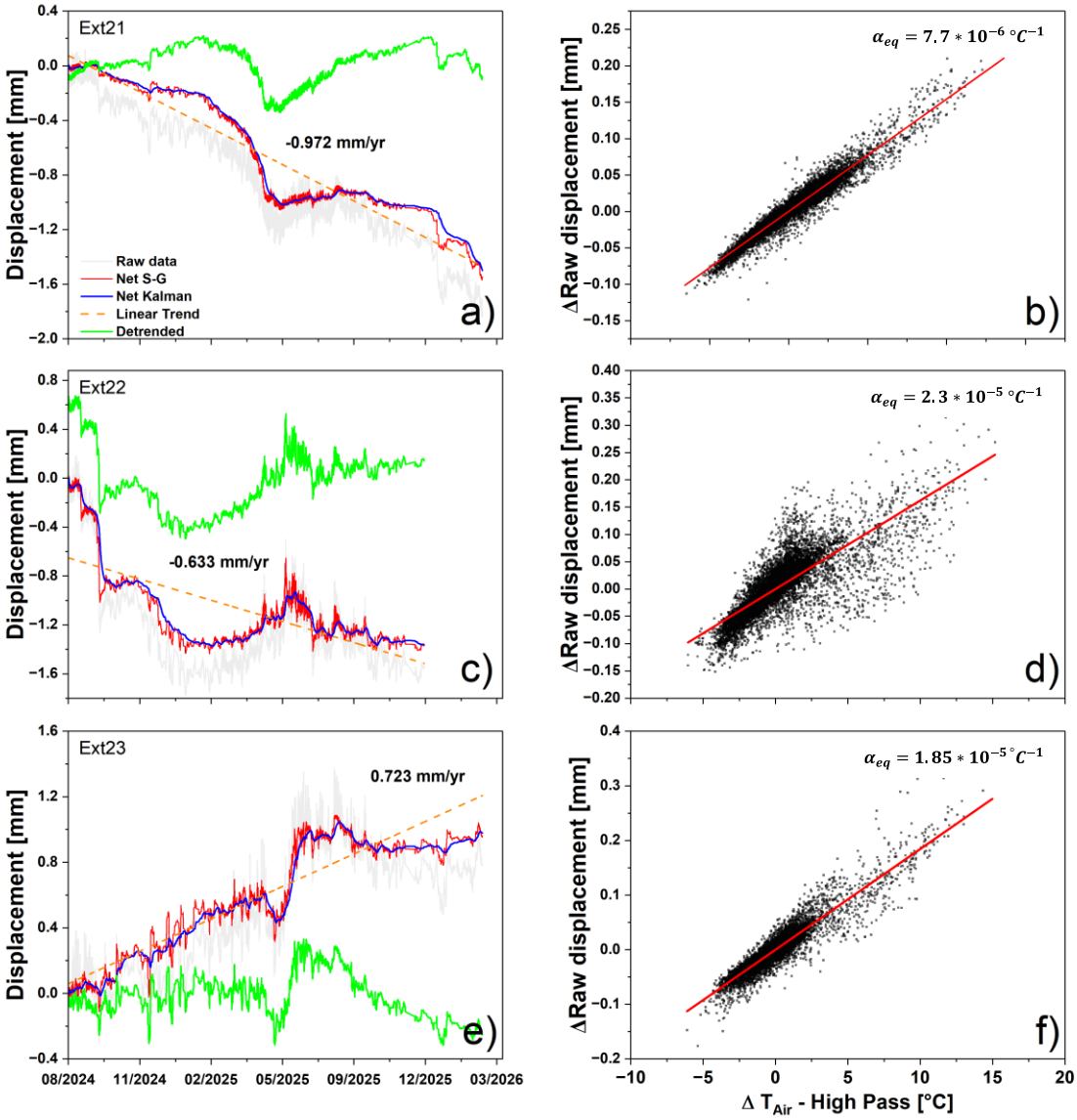


Figure 41 Surface extensometer records and thermal decoupling for Ext21 (a, b), Ext22 (c, d) and Ext23 (e, f), August 2024 – March 2026. Left column: cumulative displacement showing the raw signal, the thermally corrected net signal, the fitted long-term linear trend with its annual rate, and the detrended residual. Right column: high-pass filtered air temperature against raw displacement increment; the slope of the linear fit gives the equivalent coefficient of thermal expansion α_eq of each rock–sensor system. Applying the analytical decoupling procedure described in section 4.3.7 successfully filtered this thermal noise. The empirical equivalent coefficients of thermal expansion (α_{eq}) back calculated for the instrumented fractures were 7.7×10^{-6}°C⁻¹ for Ext21, 2.3×10^{-6}°C⁻¹ for Ext22, and 1.85×10^{-5}°C⁻¹ for Ext23. The significant deviation of these site-specific values from the nominal theoretical expansion coefficient of steel (1.20×10^{-5} °C⁻¹) confirms that field

measurements must account for the bulk response of the coupled rock-sensor system rather than relying on material-specific theoretical values.

Once thermally corrected, the extensometer records reveal clearly irreversible cumulative joint displacements affecting the monitored rock pillar (Figure 41). The largest cumulative displacement is observed at Ext21, which progressively contracted by approximately 1.5 mm. Ext22 and Ext23 recorded net displacements of approximately −1.3 mm and +1.1 mm respectively, indicating a progressive relative rotation of the monitored blocks. Linear trend analysis of the corrected signals yields annual displacement rates ranging between approximately 0.6 and 1.0 mm/yr. Ext21 exhibits the highest long-term rate while Ext22 shows the lowest, reflecting spatially variable kinematic behaviour within the highly fractured rock mass.

The removal of the thermo-elastic effects strongly attenuated the short-term signal variability, reducing the residual fluctuations to amplitudes of just ±0.2 to ±0.4 mm. This noise reduction allowed for the clear identification of transient deformation phases. Episodic displacement accelerations and localized step-like changes became particularly evident during the spring and early summer periods. Despite the differences in displacement magnitude and sign (opening versus closing), these accelerated movements are recorded nearly simultaneously across multiple sensors. This partially synchronous deformation pattern strongly suggests that the monitored discontinuities do not behave as independent structural elements but rather belong to a mechanically coupled block system responding to the evolving thermo-mechanical boundary conditions of the pillar.

4.4.6 *3D FEM thermal modeling: present-day validation and climate projections*

To overcome the geometric limitations of the 1D analytical approach and fully capture the complex three-dimensional topographic effects of the fractured pillar, transient thermal simulations were performed using the finite-element FEFLOW code. The numerical model was first rigorously validated against the in-situ GeoPrecision thermistor array at four representative depths (0.2, 1.5, 4.5, and 15 m). To quantify the sensitivity of the subsurface thermal field to the upper boundary conditions, two alternative forcing functions were tested (Figure 42): the daily air temperature (T_{air}) from the local weather station, and the near-surface rock temperature (T_{rock}) derived from the shallowest borehole sensor.

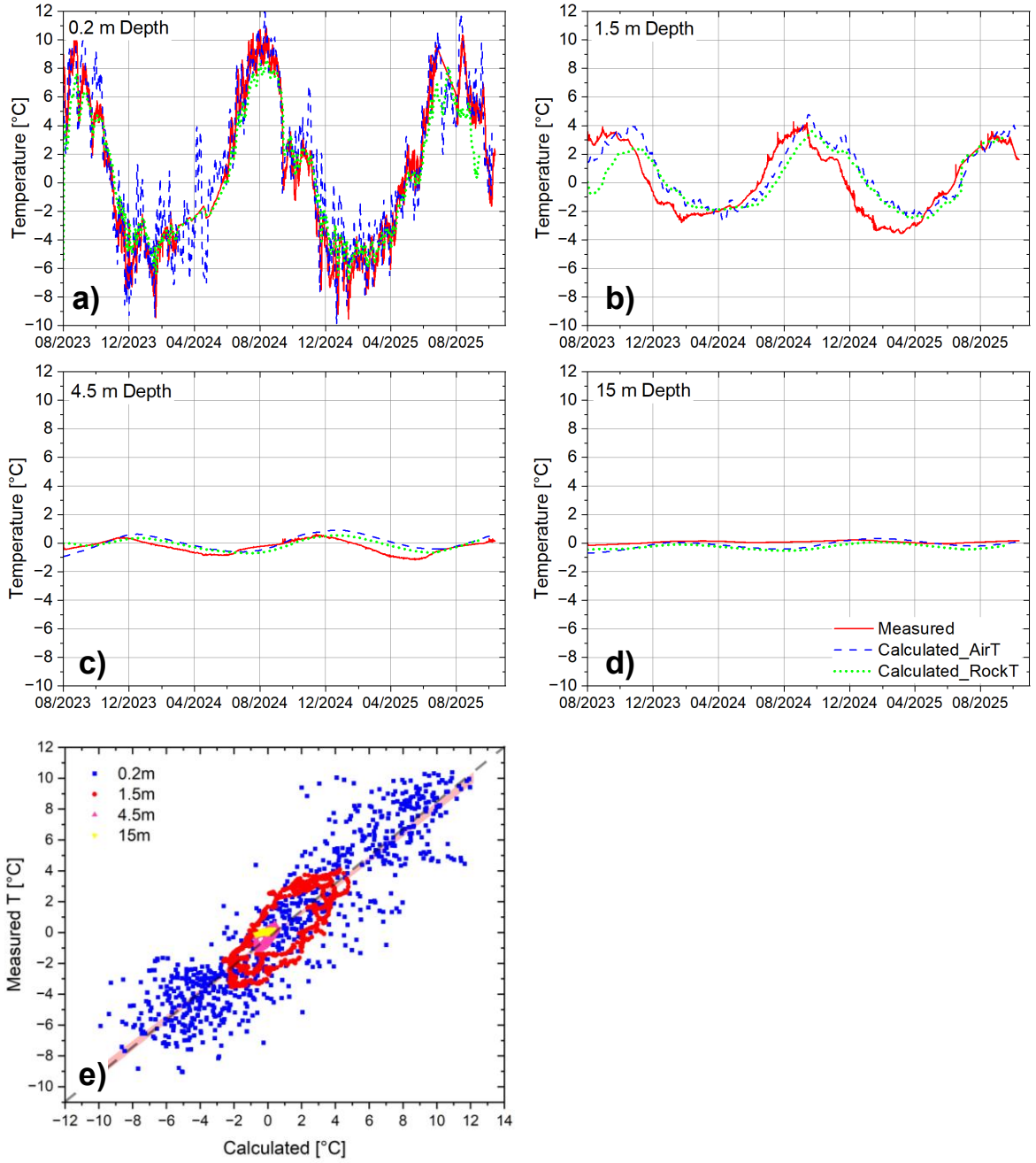


Figure 42 Validation of the thermal model against Geoprecision borehole temperatures at four depths: (a) 0.2 m, (b) 1.5 m, (c) 4.5 m and (d) 15 m. red lines show measured temperatures, while simulations are reported using two alternative surface boundary conditions: daily air temperature forcing (T_{air}; blue) and near-surface rock temperature forcing derived from the shallowest Geoprecision sensor (T_{rock}; green). e) Scatter plot of measured vs calculated temperatures at different depths.

In the shallow subsurface (0.2 to 1.5 m), the thermal record is dominated by high-frequency seasonal and diurnal fluctuations. At 0.2 m depth, measured temperatures range widely from −10 °C to +12 °C. While the T_{air} simulation adequately captures the seasonal envelope, it overestimates short-term high-frequency oscillations. Conversely, the T_{rock}-

forced simulation smoothly tracks the measured curve and successfully damps these spurious peaks. At 1.5 m depth, a systematic divergence occurs during the cold season: the T_{air}simulation underestimates winter cooling, bottoming at −3 °C while the actual rock temperature reaches −4 °C. The T_{rock}boundary condition resolves this mismatch, confirming that $T_{air}$is partially decoupled from the effective rock-surface temperature due to complex thermal boundary layer processes such as differential solar radiation across the three-dimensional rock faces.

In the deep subsurface (4.5 to 15 m), the model effectively captures the conductive filtering of the thermal signal. At 4.5 m depth, the seasonal oscillation is severely damped to 1–2 °C peak-to-peak, and the two simulations converge, showing excellent agreement with the measured phase lag. At 15 m depth, the simulated signal remains nearly constant at around 0 °C, with variations strictly confined within ±0.5 °C. At this depth, the discrepancy between the two boundary conditions disappears completely. This convergence validates the model's ability to reproduce the thermally buffered marginal permafrost body and confirms that the intact rock mass at 15 m, situated immediately below the active thermo-mechanical shear zone at 13.5–14.0 m, acts as a stable, structurally competent basal block under present-day thermal conditions.

Following this robust present-day validation, predictive forward simulations were carried out to the year 2100 using the RCP 4.5 and RCP 8.5 emission pathways (Figure 43). The resulting trajectories reveal a severe, depth-propagating degradation of the permafrost body. Under the moderate RCP 4.5 scenario, the deep marginal permafrost gradually warms, with temperatures at 15 m slowly rising by around +1 °C by 2100, marking the complete transition out of the zero-curtain phase. Under the severe RCP 8.5 scenario, the warming is drastic: by 2100, simulated temperatures at 15 m reach +3 °C, while the shallow levels (0.2–1.5 m) permanently shift into a mean envelope of +3 °C to +4 °C. The three-dimensional cross-sections illustrate a significant deepening of the active layer under both scenarios. By the end of the century under RCP 8.5, the 0 °C isotherm will be completely expelled from the structural core of the pillar, with direct implications for the mechanical integrity of the ice-bearing discontinuities that currently provide residual resistance along the central fracture system.

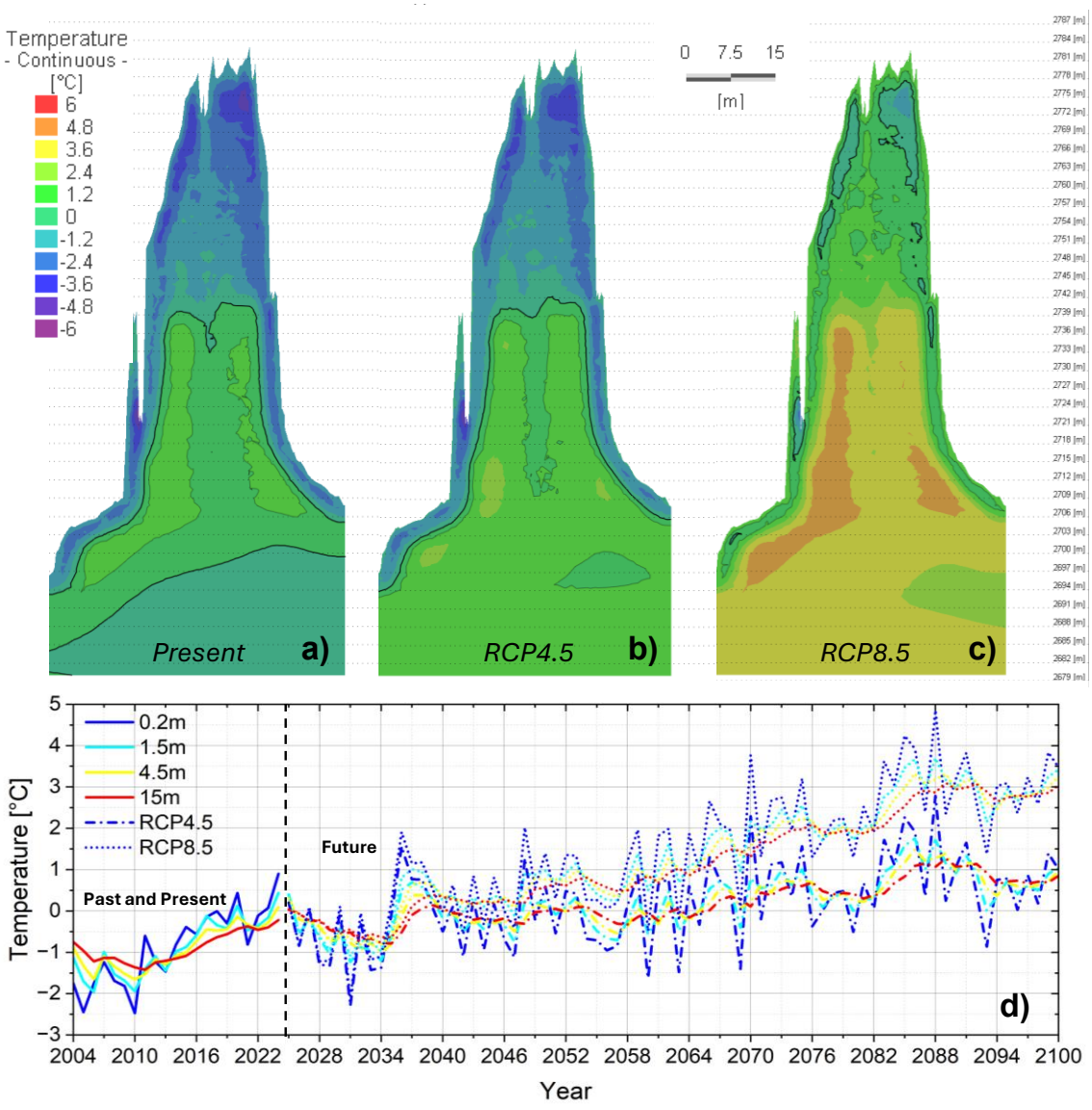


Figure 43 a) Temperature distribution from the 3D FEM simulation along an EW cross section of the pillar in January 2025; b-c) Temperature distribution for RCP4.5 and RCP8.5 climate scenarios at 2100 and d) Scenario-based evolution of simulated temperatures at 0.2, 1.5, 4.5 and 15 m depth under RCP4.5 and RCP8.5. The marked black line in a, b and c represent the 0°C isotherm, and the thick one the 1°C isotherm.

4.4.7 *3D mechanical stability and failure kinematics: pre- and post-2018 collapse*

To identify the specific structural causes of the 2018 event and to evaluate the controlling factors governing the current residual pillar mechanical stability, 3D Strength Reduction Method (SRM) analyses were performed. This model was applied to both the pre- and post-2018 detachment geometries. Rock-mass stiffness was strictly constrained by laboratory tests on the Dolomia Principale (Young's modulus E = 12 GPa, Poisson's ratio ν = 0.25, and unit weight = 25.5 kN m^{-3}), while equivalent strength parameters (c =

1.2 MPa and φ = 37°) were adopted to account for the pervasive macro-jointing and stress relief inherent to the 80 m high fractured pillar.

The pre-collapse scenario matrix (Cases M1–M6) yielded global Factor of Safety (FoS) values ranging from 3.13 to 3.69 under baseline quasi-static conditions. These static models predict a highly stable configuration (FoS > 3). This quantitatively demonstrates that gravitational loading and standard structural jointing alone were insufficient to trigger the 2018 collapse. Instead, it confirms the thermo-mechanical hypothesis that transient, uncompensated weakening processes, specifically the temperature-dependent degradation of the ice-filled joints identified in the FEFLOW thermal models, were the prerequisite mechanisms for the detachment, eventually supported by precipitation triggers.

Despite the high static FoS, the displacement fields at incipient numerical instability for the most critical pre-collapse run (Case M6, FoS = 3.13) capture the historical failure kinematics perfectly (Figure 44). The total displacement contours (Figure 44a) and plastic strain localization (Figure 44b) are dominated entirely by the rear discontinuity. This results in a localized, lateral (westward) detachment mechanism that precisely matches the actual 2018 failure, in which a rear rock slab collapsed without mobilizing the adjacent standing pillar. The interface relative normal displacements (Figure 44c) confirm that progressive opening and sliding along the back fracture governed the onset of instability.

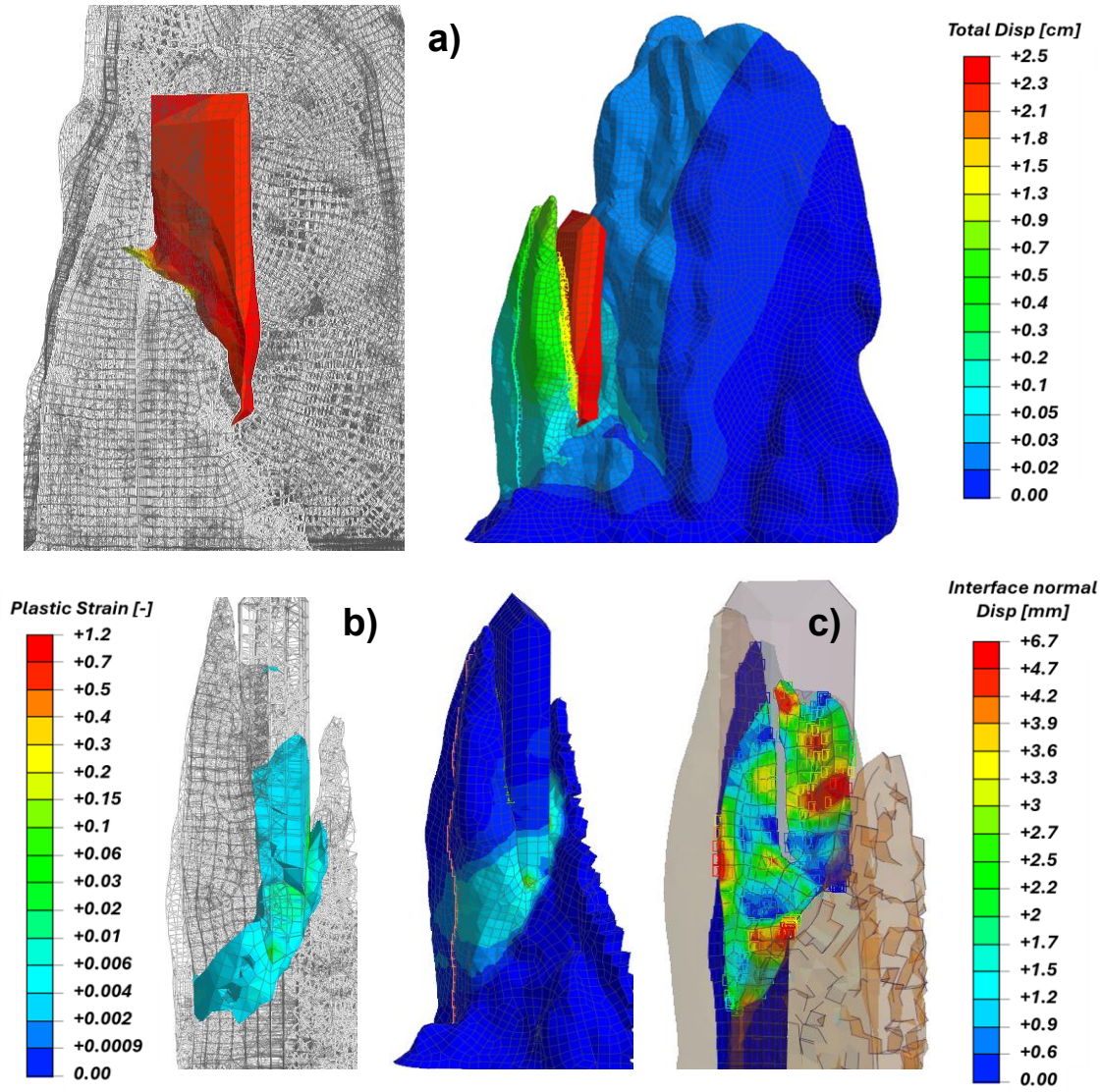


Figure 44 Pre-collapse SRM result (M6, FoS = 3.13): a) total displacement contours at incipient instability and illustrating a lateral detachment mechanism mainly controlled by the back discontinuity, b) equivalent plastic strain in the rock mass at incipient instability, showing localization adjacent to the back structural domain and c) back-interface relative displacement (normal component), highlighting deformation concentration along the controlling discontinuity.

Moving to the current post-collapse configuration (Case M7), the residual stability was evaluated using a weakened parameter set to represent post-2018 stress-relieved conditions. The results show a significant decrease in stability, with the global FoS dropping to 1.58. The SRM analysis reveals a fundamental shift in the expected failure kinematics. With the lateral confinement removed by the 2018 event, an unstable mechanism evolves. Deformation now begins within the previously activated structural domain and gradually spreads to the entire remaining pillar, shifting to a valley-facing (northward) frontal detachment mode (Figure 45a). The equivalent plastic strain (Figure

45b) indicates a much broader spatial mobilization of the standing rock mass. Meanwhile, the relative displacements now concentrate strictly along the central frontal discontinuity (Figure 45c).

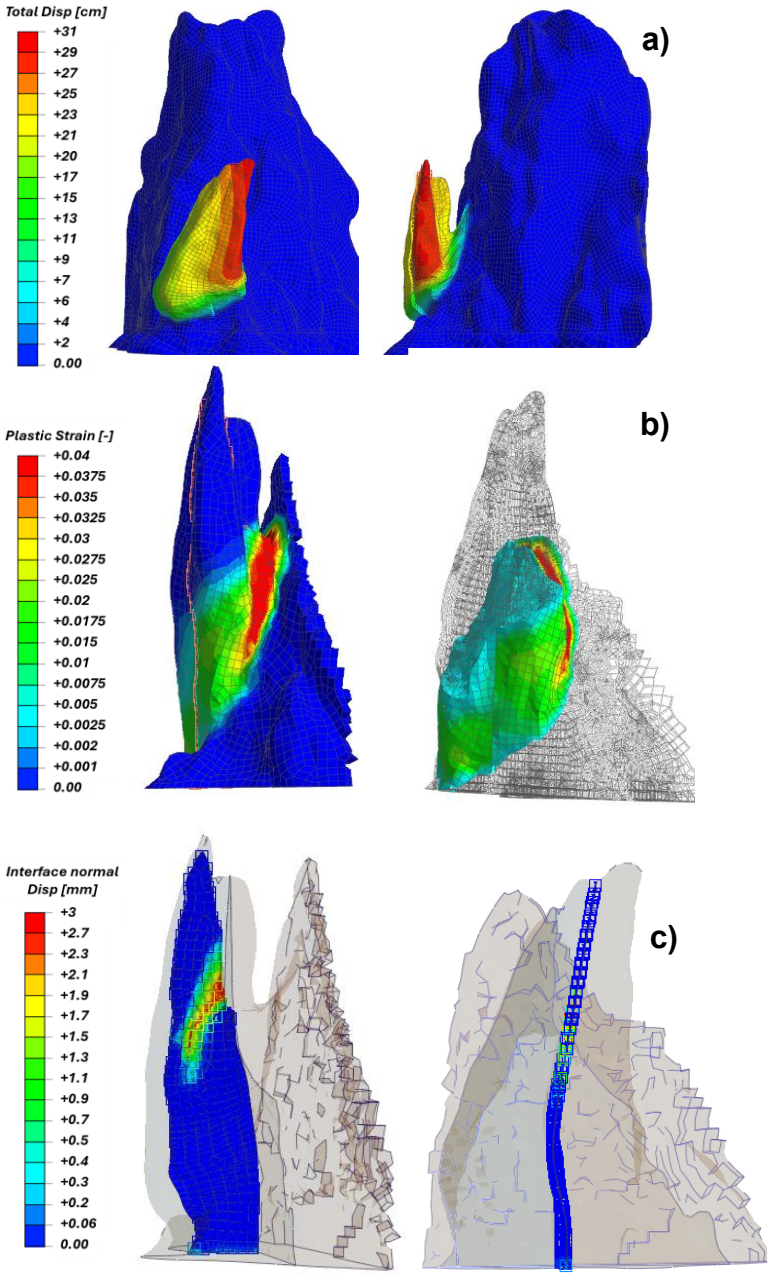


Figure 45 Post-collapse weakened SRM result (M7, FoS = 1.58): a) total displacement contours at incipient instability (left: frontal view from North; right: lateral view from West) indicating progressive mobilization of the standing pillar and a valley-facing (frontal) detachment mechanism; b) equivalent plastic strain in the rock mass at incipient instability, showing a broader inelastic zone compared to the pre-collapse case and c) frontal-interface relative displacement along the central fracture (normal component), showing a concentrated deformation band along the valley-facing discontinuity associated with the predicted forward failure mode.

To investigate the thermo-mechanical response of the rock mass, the displacement profiles derived from the 3D thermo-elasto-plastic model and their seasonal evolution were compared. The temporal evolution of XY-displacements at different depths (Figure 46a) highlights a strongly depth-dependent response. The largest displacement amplitudes are confined within the upper portion of the profile (up to 8–10 m), where a clear seasonal cyclicity is observed, with increasing displacements during warm periods and partial recovery during colder phases. The amplitude rapidly decreases with depth, and the signal becomes negligible below approximately 15 m, indicating an efficient attenuation of thermo-mechanical forcing. In the shallowest levels, a slight cumulative irreversible deformation is computed. The displacement profiles (Figure 46b) confirm the progressive near-surface concentration of deformation. The 3D model results show a peak at shallow to intermediate depths (around 4–8 m), followed by a rapid decay with depth. The comparison between warm (red) and cold (blue) seasons indicates larger displacements during warm conditions, consistent with thermally induced expansion and associated stress redistribution within the rock mass. The 1D FDM results reproduce the general increase in displacement toward the surface and provide values representative of the overall magnitude of deformation. However, it should be noted that these results are not directly comparable with the 3D thermo-elasto-plastic outputs, as the latter isolate the pure thermal displacement component. The two approaches are therefore complementary: the 3D results emphasized the spatial variability of the thermo-mechanical response, while the 1D FDM provides a bulk estimate of displacement magnitude that includes the behaviour of the sensor column and extensometric modules.

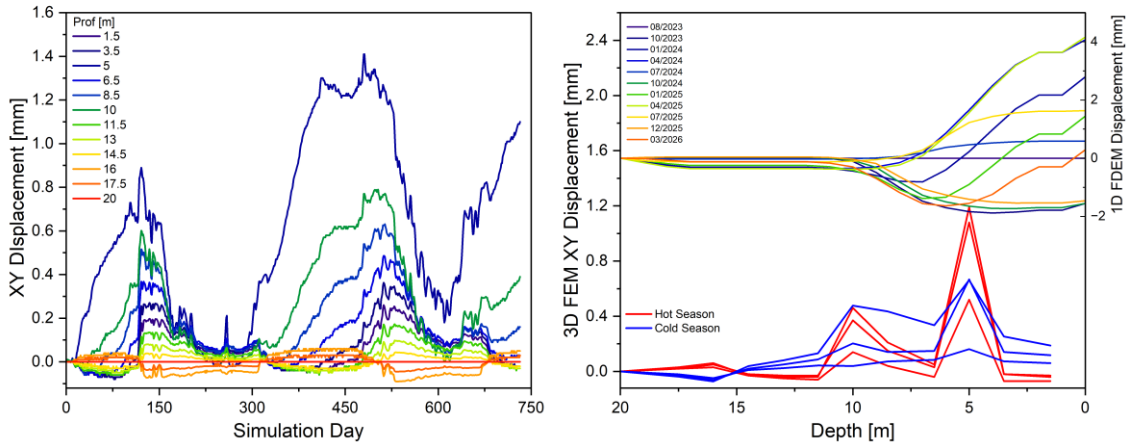


Figure 46 Thermo-mechanical displacement response derived from numerical modelling. Left panel: temporal evolution of XY displacement at different depths obtained from the 3D thermo-elasto-plastic model over the simulation period, showing a marked seasonal cyclicity and strong attenuation

of amplitude with depth. Right panel: depth profiles of XY displacement for representative warm (red) and cold (blue) seasons from the 3D model, compared with the corresponding 1D FDM results (upper curves), which include the effect of column snaking and extensometric modules. The 3D results highlight the thermo-induced displacement component and its localization within the shallow domain, whereas the 1D FDM outputs provide a bulk estimate of displacement magnitude.

4.5 **Discussion**

4.5.1 *Thermo-mechanical Preconditioning vs. Hydro-meteorological Triggering*

Comprehensive modelling of the pre-2018 pillar configuration highlights a fundamental mechanism in high-alpine rockfall mechanics: the decoupling of preconditioning factors from ultimate triggers. Baseline static SRM analysis clearly demonstrated that gravitational and structural forcing alone yielded a highly stable configuration (FoS > 3). Progressive, climate-driven degradation of the permafrost body, specifically the melting of interstitial ice and the consequent loss of cohesive rock-ice interlocking, was therefore fundamental, long-term thermo-mechanical preconditioning. This slow exhaustion of shear strength brought the rock mass to a state of marginal stability, dynamically dilating the primary sub-vertical back-fracture. However, the timing of the detachment, which occurred between 1 and 9 September 2018, points to an acute hydro-meteorological trigger. Local records from the week before the collapse show a severe precipitation event totaling around 120 mm (Figure 47). During this time, air temperatures fluctuated between −0.2 °C and +22 °C, causing the heavy precipitation to fall almost entirely as liquid water or rapidly melting snow. Because the long-term thermal preconditioning had already opened the rear structural discontinuities, the rock mass was highly receptive to deep fluid infiltration. The rapid advective influx of meteoric water into the deep sub-vertical back fracture generated a massive transient spike in localized water pressure which lowered the remaining frictional resistance along the failure plane. This cascade mechanism aligns well with recent conceptual models of high-alpine rock slope failures (Gruber & Haeberli, 2007; Krautblatter et al., 2013; Walter et al., 2020), where newly available structural porosity renders the rock mass susceptible to deep fluid infiltration and transient hydrostatic thrusts.

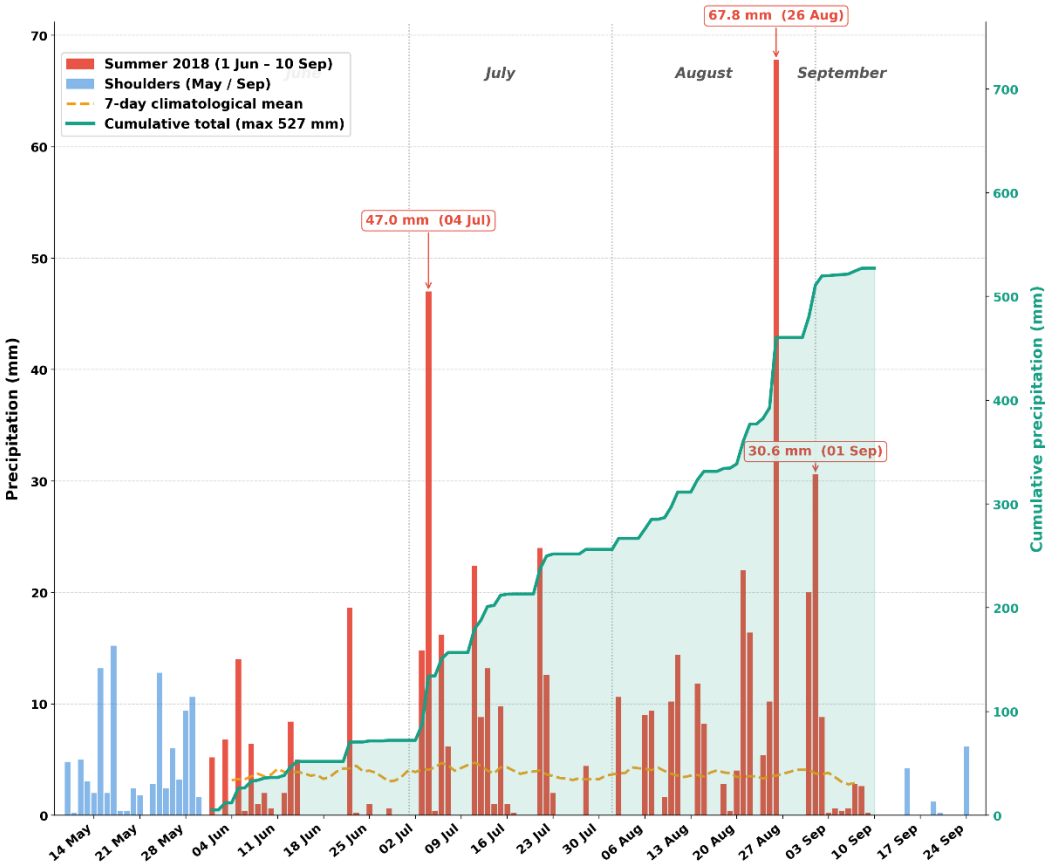


Figure 47 Cumulative precipitation from May to September with the important event the week before the 2018 collapse in which 120mm of rain fell in the Sas da Lech area.

4.5.2 *Localized Advective Heat Transport and Thermo-mechanical Feedback*

The integrated dataset collected at the Sas da Lech pillar offers a detailed view of the thermo-mechanical evolution of a steep, fractured rock mass operating at the critical permafrost boundary. In the shallow subsurface (0 to approximately 12 m), the strong exponential attenuation and linear phase shift of the seasonal temperature signal align perfectly with classical one-dimensional analytical models of conductive heat transfer in solid rock (Noetzli & Gruber, 2009). Here, the rock matrix effectively acts as a low-pass thermal filter. However, the significant divergence of the thermal wave velocity v_T observed below 12 m reveals the limitations of purely conductive models in highly disjointed rock masses. Between 12 and 15 m, the thermal regime is characterised by a persistent near-isothermal plateau hovering precisely around 0 °C. Rather than indicating deep conductive equilibrium, this damping is a classic manifestation of the zero-curtain effect, dominated by the latent heat of fusion during the continuous phase transition of interstitial ice (Hasler et al., 2012). This is directly corroborated by field evidence: during

the DMS01 drilling operations, localized interstitial ice and active meltwater percolation were observed within deep structural discontinuities beyond 13 m. Furthermore, neither the 1D FDM nor the 3D conductive FEM models can reproduce the erratic thermal velocities and localized warming spikes at depths exceeding 13.5 m without the presence of advective heat transfer. As documented in similar Alpine settings (Hasler et al., 2011; Draebing et al., 2017; Aumer et al., 2025), macroscopic open fractures alter the bulk thermal diffusivity. At Sas da Lech, the main sub-vertical back fractures act as highly efficient thermal shortcuts. The persistent millimeters-scale opening facilitates deep convective air circulation (the chimney effect) and the rapid downward advective percolation of surface meltwater and rainfall. This advective bypass delivers sensible heat directly to the deep interior of the pillar, driving temperatures persistently above 0 °C. A critical positive feedback loop is thereby established: the initial structural opening enhances heat transport by advection, which accelerates basal permafrost thaw, which in turn weakens or nullifies joint cohesion and interlocking, promoting kinematic release and further fracture dilation.

4.5.3 *Permafrost Rock Mechanics at the Melting Point*

The specific thermal regime of the Sas da Lech pillar dictates its mechanical failure mode. While the broader frost-weathering literature suggests that volumetric damage, such as ice segregation, peaks within a frost-cracking window between −3 °C and −8 °C (Hales & Roering, 2007; Anderson et al., 2013), the thermal monitoring presented here shows that the critical basal sliding plane at 13.5–14.0 m operates persistently at or slightly above the melting point. The pillar's mechanical sensitivity is therefore not governed by frost-cracking expansion but rather by the progressive, temperature-dependent reduction of interface shear strength (Davies et al., 2001; Krautblatter et al., 2013). This deep strength degradation is physically manifested in the in-situ kinematic data. The high-resolution DMS monitoring reveals that deformation is not homogeneous volumetric strain but a structurally controlled rigid-block adjustment. Superimposed on the shallow, reversible thermo-elastic breathing cycles, the deepest extensometers record an irreversible, positive accumulation of tensile displacement. As the 2018 event removed lateral geometric confinement, the residual pillar is currently undergoing a slow kinematic re-orientation driven by subcritical crack growth along the main valley-facing discontinuity (Gischig et al., 2011). As projected by the RCP 8.5 thermal scenarios and

corroborated by the post-collapse SRM analysis (residual FoS = 1.58 and decreasing), the total exhaustion of the deep zero-curtain zone could ultimately sever the last remaining ice-rock bridges, setting the stage for a catastrophic frontal failure.

4.5.4 *The Analytical Thermal-Compensation Approach*

Robust kinematic interpretation of the Sas da Lech pillar depends on successfully isolating true geomechanical strain from parasitic thermo-elastic noise. Traditionally, this decoupling relies on physical dummy sensors (Collins et al., 2016). However, the analysis reveals critical vulnerabilities in this empirical hardware-based approach due to micro-climatic misalignment and time-scale decoupling. An active sensor crossing an open discontinuity experiences convective and conductive heat flow, whereas a dummy sensor experiences predominantly convective heat transfer. This thermodynamic mismatch creates phase shifts and hysteretic cyclicity that cannot be resolved by simple algebraic subtraction, risking the introduction of analytical artefacts into deep geological records. To overcome these physical limitations, the analytical thermal compensation method implemented in this study proves to be a critical advancement. By directly extracting the equivalent, site-specific thermal expansion coefficient (α_{eq}) from the phase-aligned hysteretic loop of the active sensor itself, the method entirely bypasses the need for redundant hardware. Its universal applicability is strongly supported by retrospective validation against two independent, high-noise benchmark datasets. When applied to the Alpine permafrost crackmeter data of Draebing et al. (2017), the algorithm successfully collapsed the raw hysteretic cloud into a linear trend, removing high-frequency diurnal noise while perfectly preserving the long-term fracture kinematics. Similarly, when tested against the high-temperature granitic exfoliation dataset of Collins et al. (2016) which included an actual physical dummy sensor, the analytically derived α_{eq}matched the empirical control value with extraordinary precision (Figure 48). This dual validation demonstrates that the proposed analytical approach resolves in-situ physical parameters without microclimatic bias, providing a mathematically rigorous standard for filtering complex thermo-mechanical time series in warming permafrost environments. Under these conditions, assuming a single, fully linear thermo-elastic response across wide temperature ranges crossing the freezing point may oversimplify the rock-mass behaviour, as phase changes and ice mechanics naturally introduce non-linearities.

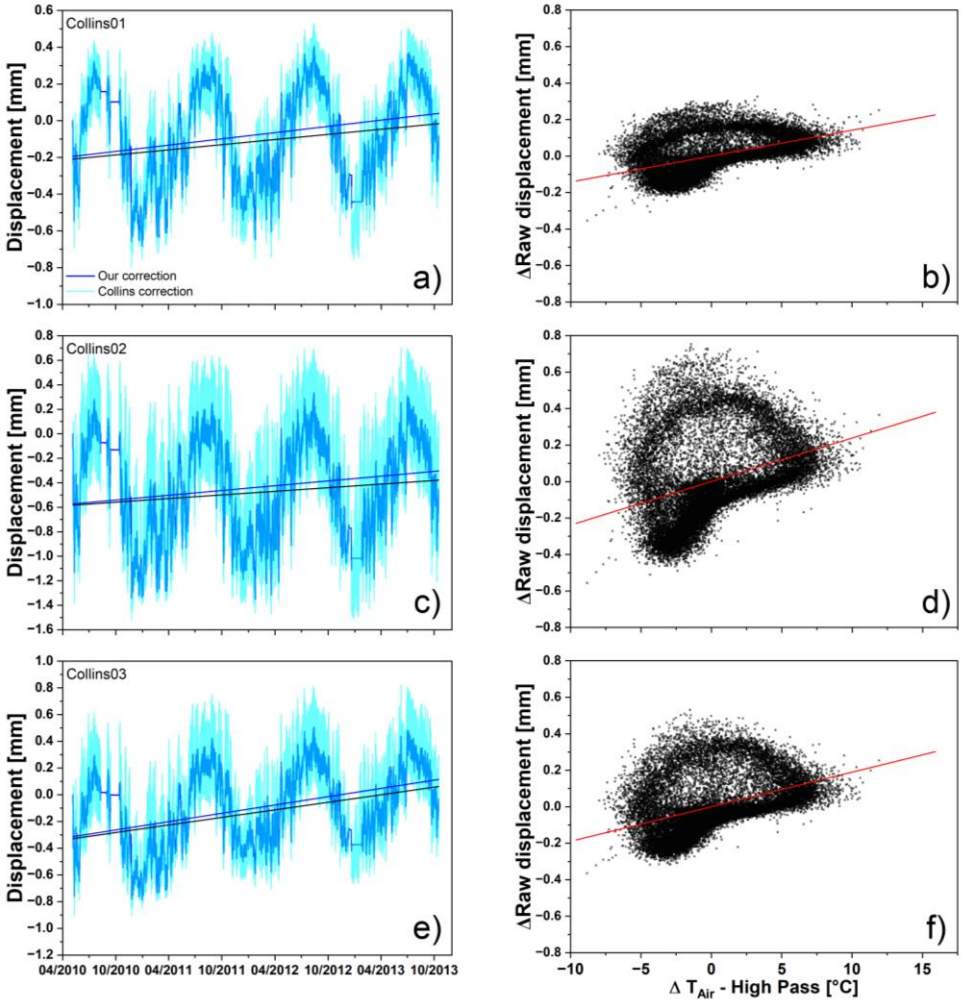


Figure 48 Validation of the analytical thermal-compensation method using an independent monitoring dataset for a thermally forced exfoliation monitoring system (after Collins et al 2016) (a, c, e) corrected by dummy sensor data (cyan) and corrected by the filtering approach (light blue). Best linear fitting of Collins corrected data (black line) and of the analytical compensated series (blue); (b, d, f): High-frequency displacement–temperature relationship for the same dataset, illustrating the hysteretic cloud following phase alignment and enabling derivation of an equivalent thermal expansion coefficient (α_{eq}).

4.6 **Case Study Conclusion**

The integrated thermo-mechanical monitoring and three-dimensional numerical modelling of the Sas da Lech rock pillar provide a comprehensive framework for understanding the destabilization of steep, fractured carbonate slopes in the context of warming Alpine permafrost environments. Moving beyond site-specific observations, this chapter yields several methodological advances and general conclusions directly addressing Research Questions 2, 3, and 4.

In response to Research Question 2, the results demonstrate that while one-dimensional analytical models successfully predict the conductive attenuation of seasonal thermal waves in the shallow intact rock matrix, they systematically fail to capture the deep thermal dynamics of highly disjointed rock masses with complex three-dimensional geometries. At Sas da Lech, macroscopic structural discontinuities act as advective thermal shortcuts, delivering meteoric water and atmospheric ventilation deep into the pillar. This fracture-driven advection causes rapid, localized basal thawing of the marginal permafrost body beyond 13.5–14.0 m depth, operating significantly faster than purely conductive processes. The extended one-dimensional analytical framework, incorporating a Gaussian spatial distribution centered at the discrete fracture depth, a dimensionless latent heat dampening factor, and a permanent negative thermal bias to simulate cold-air trapping, proves effective in capturing this multiphysics behaviour without the computational overhead of fully coupled three-dimensional simulations.

In response to Research Question 3, the analysis establishes a clear and quantitative distinction between long-term thermo-mechanical preconditioning and discrete hydro-meteorological triggering. Baseline static SRM analyses yielded a Factor of Safety consistently exceeding 3 for all pre-collapse configurations, demonstrating that gravitational and structural forcing alone were insufficient to trigger the 2018 failure. Climate-driven degradation of interstitial ice at the zero-curtain phase acted as the critical long-term preconditioning, progressively exhausting shear strength and dilating primary fractures over decades. The final detachment was triggered by a severe 120 mm precipitation event in the days immediately preceding the collapse, which generated a transient hydrostatic overpressure within the structurally prepared discontinuity network. This compound cascade mechanism, whereby progressive climatic weakening unconditionally primes the rock mass, making it susceptible to catastrophic failure under short-term hydrostatic impulses, represents a general pattern of high-alpine rockfall mechanics with broad applicability across the warming Alpine arc.

In response to Research Question 4, the three-dimensional SRM analyses demonstrate that the progressive, temperature-dependent degradation of ice-filled discontinuities, operating persistently in the zero-curtain regime near 0 °C rather than in the classical frost-cracking window of −3 °C to −8 °C, is the dominant mechanical control on pillar stability. The 2018 structural release fundamentally altered the boundary conditions of the residual rock mass, transitioning the failure kinematics from a localized lateral

detachment to a broad valley-facing instability. With a current post-collapse FoS of 1.58 and long-term kinematic data showing irreversible rigid-block rotation, the residual pillar is operating on a critical trajectory toward frontal failure, the timing of which will be strictly governed by future warming pathways. Under the RCP 8.5 scenario, the complete exhaustion of the deep zero-curtain zone by 2100 would sever the last remaining ice-rock bridges, eliminating the residual cohesive resistance along the central frontal discontinuity.

A further methodological contribution of this chapter concerns the isolation of geotechnical kinematics from thermo-elastic noise in monitoring data. Traditional approaches relying on physical dummy sensors are vulnerable to micro-climatic misalignment and time-scale decoupling. The analytical thermal-compensation algorithm developed here, which extracts the site-specific equivalent thermal expansion coefficient α_{eq}directly from the phase-aligned hysteretic loop of the active sensor, bypasses this limitation entirely, providing a hardware-independent, mathematically rigorous standard for filtering complex thermo-mechanical time series. Its validation against independent datasets from Alpine permafrost crackmeters and granitic exfoliation monitoring systems confirms its transferability beyond the specific instrumentation and lithology of the Sas da Lech site.

The Sas da Lech case ultimately illustrates a critical shift in perspective for permafrost rock mechanics: peak rockfall hazard in degrading Alpine permafrost is not governed by extreme low-temperature processes but by prolonged operation near the melting point. In this zero-curtain regime, the loss of rock-ice cohesive interlocking, combined with extreme sensitivity to liquid water infiltration, shifts the rock mass into a critical state where structurally localized weakening drives the system toward unavoidable failure. This insight, demonstrated here on a well-instrumented dolomite pillar of intermediate scale, provides the conceptual and methodological foundation for Chapter 5, where the same thermo-hydromechanical framework is transferred to the larger and less instrumented Cima Falkner rock avalanche. That case introduces a further challenge, the absence of subsurface monitoring data, and demands a more general, probabilistic treatment of the triggering mechanism, motivating the episodic framework developed in the following chapter.

Chapter 5
THERMAL PRECONDITIONING UNLOCKS EPISODIC HYDROLOGICAL TRIGGERS IN PERMAFROST ROCKWALL COLLAPSE

5.1 **Aims**

This chapter investigates the August 2025 Cima Falkner rock avalanche, a 5.7×10^5 m^3 collapse in the Brenta Dolomites, Italian Alps, as a large-scale natural laboratory for formalizing the physical mechanisms governing catastrophic permafrost rockwall failure. The case directly addresses Research Questions 3 and 4 formulated in Chapter 1.

Research Question 3, identifying the factor that predisposes a rock mass to collapse and the mechanism that ultimately triggers it, is examined through a back-analysis of the failure sequence, demonstrating that decades of climate-driven thermal preconditioning progressively degraded the shear resistance of ice-filled discontinuities, creating a vulnerability window that a discrete hydromechanical trigger exploited to initiate the final collapse. Research Question 4, concerning the simulation of high-altitude instability accounting for the progressive deterioration of physico-mechanical properties with temperature, is addressed through a novel episodic thermo-hydromechanical framework that explicitly decouples long-term conductive heat transfer from episodic hydrological shocks, and through three-dimensional finite-element simulations that constrain the pre-failure thermal envelope and reproduce the spontaneous emergence of the observed failure plane.

Beyond the site-specific reconstruction, this chapter identifies and resolves a structural limitation affecting the entire existing class of permafrost rockwall models. Standard modelling approaches apply continuous atmospheric forcing, distributing thermal and hydrological energy linearly over time and imposing a monotonic decline in simulated stability. This forces modelers into a calibration trap: to match observed failure chronologies, basal friction parameters must be inflated well beyond physically plausible limits, obscuring the true underlying physics. The episodic framework developed here

resolves this paradox by preserving the discrete nature of fluid pressurization and the subsequent poro-elastic recovery of effective stress, successfully reproducing the exact timing of the 2025 collapse using strictly uncalibrated, laboratory-constrained parameters and without requiring complete volumetric ice ablation as a prerequisite for failure.

5.2 **Study Area**

5.2.1 *Regional Instability context*

The Trentino–Alto Adige region includes some of the steepest and highest-elevation rock walls of the Eastern Alps, where rockfall processes represent a recurrent geomorphic activity and a significant natural hazard for trails, climbing routes, infrastructure, and transport corridors. Rockfall magnitude spans several orders of magnitude, from frequent small detachments to rare cliff failures reaching $10^6\ m^3$. These thermo-mechanical processes manifest regionally as a documented increase in rockfall activity across the Eastern and Central Alps, with evidence from Austria, Germany, and northern Italy (Sass & Oberlechner, 2012; Rupp & Damm, 2020; Messenzehl et al., 2018; De Blasio et al., 2018; Nigrelli et al., 2024; Bonometti et al., 2026).

Regarding the specific climatic controls in the UNESCO Dolomites massifs, Bonometti et al. (2026) compiled an inventory of 5,503 rockfalls, of which 2,971 have documented dates of occurrence (Figure 49). Their analysis reveals distinct spatial trends: 70% of events below 1,000 m a.s.l. occurred on south-facing slopes, contrasting with 50% of events above 2,000 m located on north-northwest facing slopes, the latter being preferential aspects for permafrost occurrence. Although the altitudinal distribution shows a historical concentration of events below 1,500 m, an increasing frequency has been observed above this elevation over recent decades. By analyzing mean air temperature, temperature variations, and precipitation, the authors determined that 50% of rockfalls were associated with at least one climatic anomaly (significance level $\alpha = 0.2$). Positive temperature anomalies were found to be more frequent triggers than precipitation anomalies. A notable temporal dichotomy emerged: daily and weekly temperature anomalies were predominantly negative, short-term cold spells promoting freeze–thaw cycling, whereas monthly and quarterly anomalies were more frequently positive, reflecting sustained warming driving permafrost degradation. Large-magnitude events were notably more frequent in conjunction with positive anomalies, and rockfalls

within permafrost boundaries were strongly controlled by permafrost-favorable conditions rather than other climatic factors.

The spatio-temporal distribution of Figure 49 provides a striking visual synthesis of these trends. The record is nearly empty prior to the 1990s, reflecting a combination of underreporting bias in historical inventories and a genuine low-frequency background state. A marked increase in both event frequency and volume is evident from the early 2000s onward, consistent with the accelerating warming documented for the Eastern Alps (Bonometti et al., 2026; Crespi et al., 2021). Most critically, the largest events (>10^5–10^6 m³) appear almost exclusively after 2015 and at elevations above 2,900–3,100 m a.s.l. — a band that falls squarely within the continuous permafrost zone mapped by Boeckli et al. (2012). This upward migration of large-volume failures toward elevations that were historically frozen and mechanically competent represents a physically coherent signal of permafrost boundary retreat and directly contextualizes the 2025 Cima Falkner event within a broader regional destabilization trend.

This trend becomes even more significant when considered in light of the hypsometric structure of Alpine terrain. In mountain ranges, available rock wall surface area decreases markedly with elevation. Consequently, raw event counts underestimate the true increase in failure density at high elevation: when normalized per unit of exposed rock wall area, the relative surge in large-volume events above 2,900 m is considerably more dramatic than it appears in absolute terms. This area-frequency imbalance reinforces the interpretation that high-elevation permafrost rock walls are entering a qualitatively new instability regime, reflecting a genuine increase in the susceptibility of previously stable, frozen terrain.

Well-documented reference cases in the Dolomites include the October 2007 collapse at Cima Undici (3,092 m a.s.l., ~60,000 m³; Viero et al., 2013) and, at the upper end of the magnitude spectrum, the 2016 collapse on the north slope of Piccola Croda Rossa (~700,000 m³). Numerous other events affected Dolomitic rock walls between 2,300 and 3,300 m a.s.l. in the past two decades. The 2025 Cima Falkner event provides a recent and well-constrained case study of a large cliff failure in an Alpine permafrost environment, combining independent observational and modelling constraints that allow quantitative reconstruction of the failure mechanism.

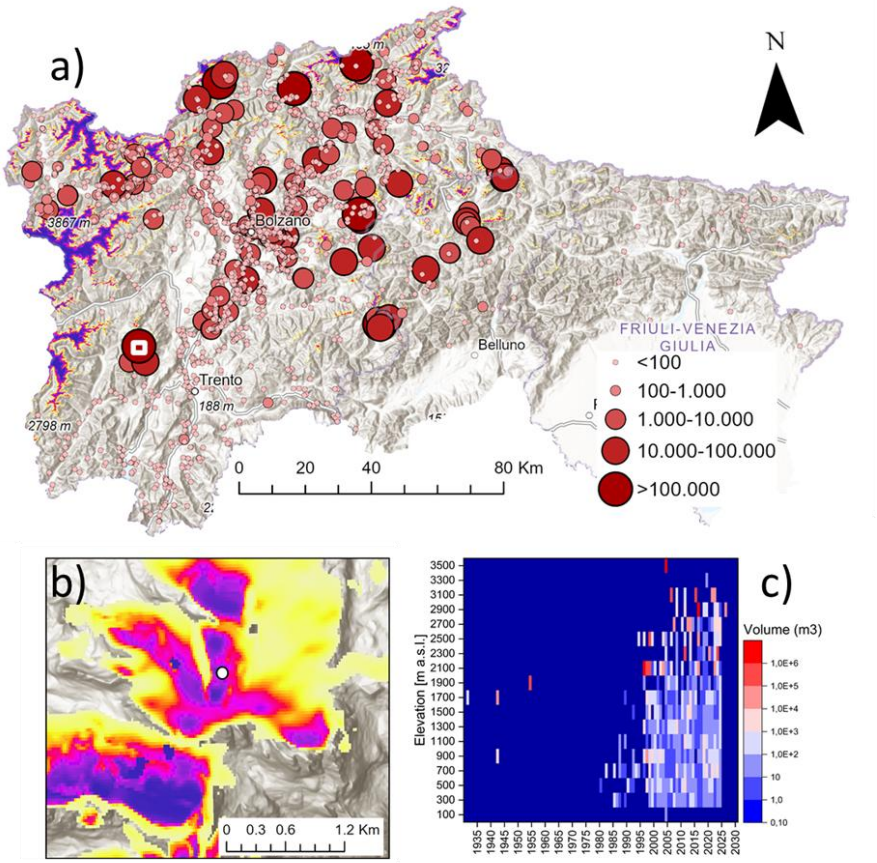


Figure 49 Large volume rockfalls in the Dolomites are migrating to higher elevations in response to permafrost degradation. (a) Regional distribution and volume of rockfalls in Trentino–Alto Adige and Veneto (symbol size proportional to event volume). The white square indicates the Cima Falkner study site. (b) Site location overlaid on the Alpine Permafrost Index Map. The 2025 collapse (white dot) occurred within the continuous permafrost zone. (c) Spatio-temporal distribution of rockfall events. Event frequency increases post-2000, with a distinct upward migration of large-volume events (>10^5 m^3) above 3,000 m a.s.l. during the last decade.

5.2.2 *Geological and Geomorphological Setting*

Cima Falkner (2,999 m a.s.l.) is located in the central sector of the Brenta Dolomites, a massif forming part of the Dolomites UNESCO World Heritage site (nine distinct massifs, covering 1,420 km²). The peak lies on a N–S-trending ridge connecting Passo del Grostè to Bocca di Brenta, within terrain exceeding 3,000 m a.s.l. The site belongs to a typical high-alpine setting where steep rock walls coexist with small glacial bodies and late-glacial deposits. The western flank forms the headwall of the Vallesinella Valley, hosting two small glaciers: the Vedretta di Vallesinella Superiore (2,600–2,850 m a.s.l.) and Inferiore (2,400–2,600 m a.s.l.), alongside Little Ice Age glacial deposits. The steep eastern face overlooks the gently north-dipping Grostedì surface and is traversed at mid-

height by the Benini via ferrata. The marked aspect contrast between the two main faces creates different radiative and snow-cover conditions, influencing both weathering processes and the thermal regime of the rock mass.

Geologically, the Brenta Dolomites belong to the South Alpine domain. At the local scale, Cima Falkner consists primarily of the Triassic Dolomia Principale formation (Castellarin et al., 2005), a massive, fine-crystalline dolomite characterised by sub-vertical jointing intersecting bedding planes dipping NW at 10°–30° (Figure 50). In steep carbonate cliffs, this persistent stratification controls: (i) overall cliff morphology; (ii) the formation of release surfaces and ledges; and (iii) the kinematics of larger detachments, particularly when combined with sub-vertical joint sets. Two independent lines of evidence support the permafrost classification of the site. First, the Alpine Permafrost Index Map (Boeckli et al., 2012) classifies the highest ridges in this sector as lying within the continuous permafrost zone. Second, field observations following the 2025 failures directly confirmed the presence of massive permafrost within the structural network. Post-event surveys of the freshly stripped scarp surfaces documented massive intact ice candles, 30/40 m high and approximately 1.4–1.6 m thick, preserved at a depth of 8–10 m below the original summit surface. These observations are treated not merely as proof of spatially continuous permafrost, but as critical empirical validation that a significant ice volume persisted inside the discontinuities, structurally interacting with the rock mass up to the exact moment of the final rain-triggered collapse.

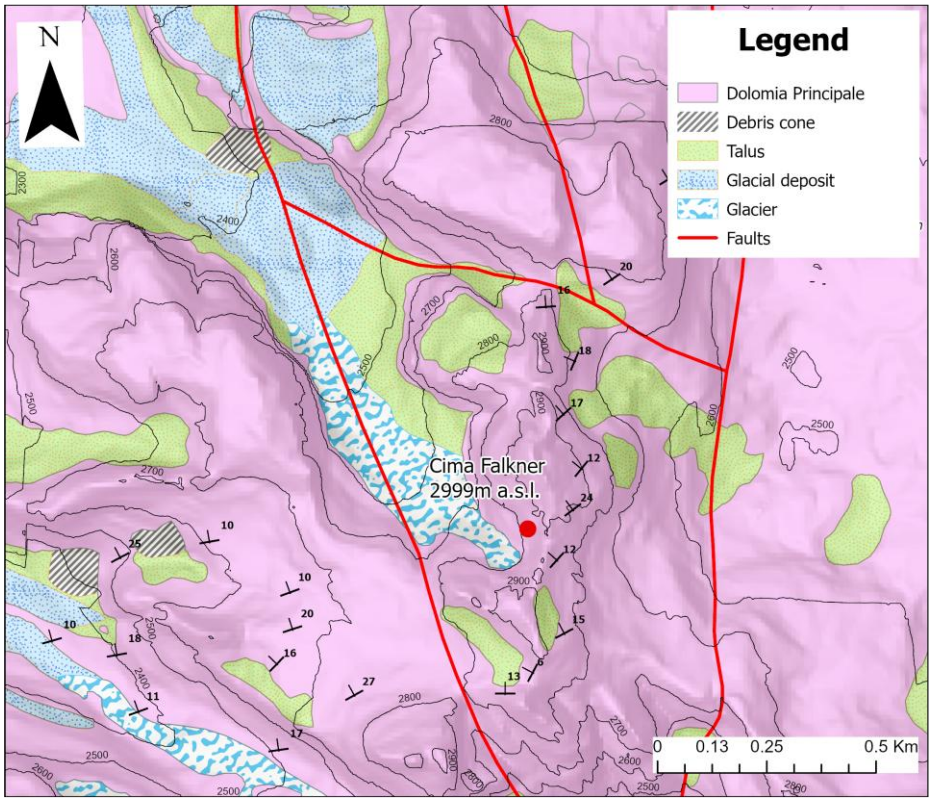


Figure 50 Geological Map of the Cima Falkner (red circle) area (Modified from the CARG Geological MAP 059 Tione di Trento Castellarin, Dal Piaz, et al., 2005).

5.2.3 *Regional Climatic Setting and Hydrological Anomaly*

The climate of Trentino–Alto Adige is predominantly Alpine, characterised by cold, snowy winters and cool-to-temperate summers with marked diurnal and altitudinal temperature variations. Complex orography produces significant climatic heterogeneity. Above 1,700–2,000 m a.s.l., conditions become strictly Alpine-continental, colder and more humid. Regional variability defines two climatic zones: the northern Bolzano province presents a continental climate subject to cold northern air masses, whereas the southern Province of Trento exhibits an intermediate temperate climate locally mitigated by the thermal inertia of Lake Garda.

A recent analysis of meteorological data spanning 1961–2020 documents a significant warming trend of 0.3–0.5 °C per decade, which accelerated between the 1981–2010 and 1991–2020 climatological normals (Bonometti et al., 2026; Crespi et al., 2021; Bongiovanni et al., 2025). Comparing the most recent 30-year period (1991–2020) with the 1961–1990 baseline, net increases were observed in mean daily temperatures (~1.1 °C), daily minima (~0.5 °C), and daily maxima (~1.7 °C). Nine of the hottest years since 1921 in the Southern and North-Eastern Alps occurred between 2011 and 2023. Focusing

on the Dolomites specifically, Bonometti et al. (2026) report an average increase in mean annual temperature of approximately 0.37–0.5 °C per decade above 2,000 m a.s.l. since 1980. Mean temperatures are projected to rise by approximately 1 °C by 2030 relative to the 1981–2010 baseline, with the most intense warming expected in winter and summer.

While average regional annual precipitation is approximately 891 mm (Crespi et al., 2021; Bongiovanni et al., 2025), local orographic forcing at Cima Falkner elevates the historical expected baseline to approximately 1,200–1,500 mm yr^{-1}. However, local cumulative precipitation data spanning the last three decades reveal massive interannual variability that plays a critical role in the rockwall's failure kinematics. The years immediately preceding the collapse were characterised by a stark hydrological deficit, followed by an extremely wet anomaly, as summarized in Table 7.

The specific sequence of this hydrological forcing has direct mechanical implications. During the dry biennium of 2022–2023, the rock mass experienced intense atmospheric thermal forcing without the concomitant advective heat and hydrostatic pressure usually delivered by infiltrating water a period of pure thermal preconditioning during which ice softening and adhesive strength loss proceeded without hydrostatic loading. Following a return to near-average conditions in 2024 (1,437.8 mm), the year of the collapse (2025) registered an extraordinary cumulative precipitation of 2,037.0 mm in the seven months to 1 August, the date of the collapse. This specific sequence, prolonged dry period driving pure thermal degradation, directly followed by an extreme hydrological wet anomaly delivering abrupt hydrostatic shocks and advective latent heat fluxes, provides the exact climatological boundary conditions that the episodic 1D model described in Section 5.4.2 identifies as the terminal trigger for the August 2025 event.

Table 7 Recent annual cumulative precipitation (2020–2025) highlighting the severe dry biennium (2022–2023) preceding the 2025 anomalous peak. The 2025 value is cumulative from 1 January to 1 August 2025 (date of collapse), not a full calendar-year total.

Year	Annual Cumulative Precipitation (mm)
2020	1598.80
2021	1457.80
2022	977.00
2023	839.40
2024	1437.80
2025	2037.00

5.3 **Kinematic Evolution and Failure Reconstruction**

5.3.1 *Multi-temporal Aerial Imagery and Fracture Aperture Evolution*

A time series of aerial and satellite imagery spanning 2011 to July 2025 documents the progressive opening of summit tension fractures at Cima Falkner to apertures of 2.0–2.5 m by the time of the main collapse (Figure 51a–a‴). Images were collected from the Trentino Autonomous Province Geodatabase (2011, 2014, 2015, 2020, 2023) and from Google Earth (2021 and 2025). The record shows that the main fracture opening of approximately 2,500 mm occurred predominantly between 2023 and 2025, at a mean rate of 3.5 mm d^{-1}, the highest recorded throughout the entire observational period.

This kinematic acceleration physically manifests the severe late-stage preconditioning phase of the rock mass. The wet summer of 2023, followed by the exceptionally wet spring and summer of 2025 within an annual total of 2,037 mm, degraded the remaining ice anchor via advective heat transport, progressively widening the rear tension fracture and reducing the effective contact area of the ice-rock interface. On 27 July 2025, a precursory event mobilized approximately 36,000 m^3 from the summit immediately following the pronounced July 2025 rainfall pulse, eliminating the kinematic toe buttress and redistributing stress onto the remaining thermally degraded ice bridges. This accelerated the final approach to brittle-like failure, which occurred on 1 August 2025.

Post-event field surveys of the freshly stripped scarp surfaces provided direct physical confirmation of the pre-collapse structural state. Massive intact ice candles, 30/40 m high and approximately 1.4–1.6 m thick, were documented at a depth of 8–10 m below the original summit surface (Figure 51b–c). These surviving ice structures demonstrate that significant ice volume persisted structurally within the discontinuities up to the exact moment of the final collapse, directly contradicting the assumption that complete volumetric ice ablation is a prerequisite for failure, a result of central importance for the modelling framework developed in Section 5.4.

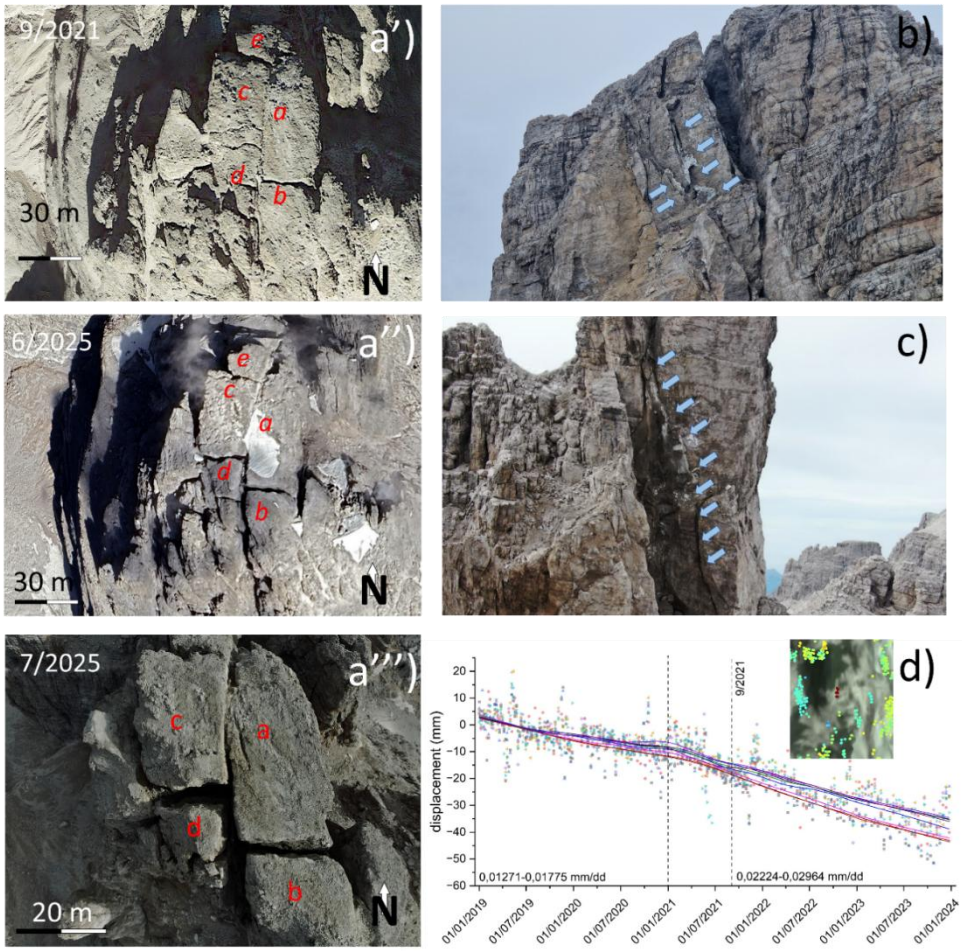


Figure 51 pre-collapse kinematic acceleration and surviving basal ice confirm failure occurred prior to complete volumetric ablation. (a′, a″) pre-event aerial imagery (September 2021 and June 2025) documenting progressive pre-failure creep, with rear fracture apertures reaching 2.0–2.5 m prior to the main collapse. (a‴) High-resolution UAV orthophoto of the highly dilated crest following the July 27, 2025, precursory event. (b, c) post-collapse field photographs (July and August) highlighting massive surviving ice candles (blue arrows) preserved within deep tension fractures and exposed basal scarps. (d) European Ground Motion Service (EGMS) displacement time series (2019–2023) for seven Persistent Scatterers (PS) on the Cima Falkner peak block (descending orbit; inset shows PS locations). Continuous lines represent Lowess-smoothed datasets, revealing a distinct kinematic acceleration initiating in December 2020 (dashed vertical line).

5.3.2 *EGMS Satellite InSAR Kinematics*

Pre-failure displacement time series were derived from the European Ground Motion Service (EGMS, Copernicus), utilizing descending geometry acquisitions spanning 2019 to 2023 (Figure 51d). Seven Persistent Scatterers identified on the Cima Falkner peak block were analyzed. To isolate the macroscopic kinematic acceleration from high-frequency seasonal noise, primarily the reversible thermo-elastic displacement cycles

characteristic of permafrost-affected rock walls, a Lowess regression with a span of 0.3 was applied to the scatter data, retaining the nearest 30% of data points for each smoothed estimate.

The EGMS dataset reveals a background displacement rate of 7.5–9.3 mm yr^{-1} along the satellite line of sight, independently corroborating the slope-scale creep documented in the aerial imagery. Most significantly, the Lowess-smoothed time series resolves a distinct kinematic acceleration initiating in December 2020, the geodetic signature of the transition point at which cumulative thermal damage and kinematic fracture widening began to outpace the winter refreeze capacity of the cold-trapping system. This InSAR-detected acceleration predates the final catastrophic failure by approximately five years, demonstrating that continuous satellite monitoring can detect the onset of the critical precursory phase in thermally sensitive rock walls lacking in-situ instrumentation a finding of direct relevance for early-warning system design across the warming Alpine arc.

5.3.3 *Point Cloud Change Detection and Volumetric Budget*

Three high-resolution point clouds were acquired using a DJI Matrice 300 RTK drone equipped with a DJI Zenmuse L2 LiDAR sensor, flown in manual mode maintaining a target standoff distance of 20–50 m from the rock face. The acquisitions correspond to the post-precursory event survey (27 July 2025; 86,775,626 points), the post-main collapse survey (1 August 2025; 159,676,599 points), and a stabilization follow-up (October 2025; 296,856,262 points). A regional 2014 airborne LiDAR survey served as the pre-collapse baseline. Processing and alignment were performed in CloudCompare.

Three-dimensional surface-change mapping was executed using the Multiscale Model to Model Cloud Comparison (M3C2) algorithm (Lague et al., 2013), which computes precise cliff retreat by comparing point cloud surfaces along locally oriented normal vectors (Figure 52). The post-first-event point cloud (27 July 2025) was set as reference and compared against the post-main-event cloud (1 August 2025). M3C2 distances are interpreted through the spatial coherence of anomalies rather than isolated values at cloud margins, with no-data sectors explicitly distinguished from areas of near-zero change reflecting stable bedrock. The distance maps reveal a highly localized change domain coinciding with the detachment niche, dominated by negative distances marking locations

where the post-event surface is systematically set back relative to the pre-event reference, consistent with a maximum vertical cliff retreat of approximately 50 m.

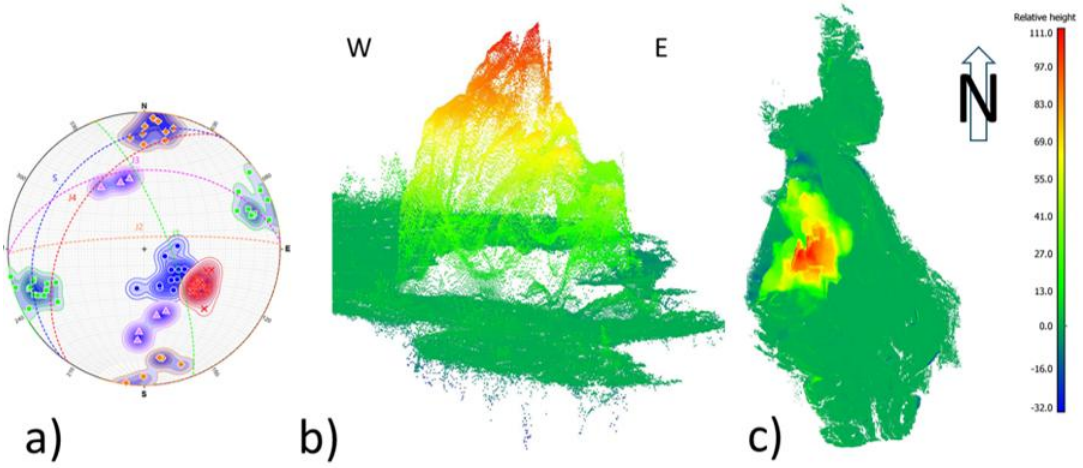


Figure 52 Point cloud analysis. a) Stereoplot of main joint sets; b) and c) 2.5D Volume difference computed from the pre- and post-failure DEMs results and showing the volume involved during the main collapse event of August 2025.

Longitudinal and transversal cross-sections were extracted to quantify topographic changes at the top scar and along the deposition path (Figure 53). The 2.5D volume differencing over the selected region of interest (80,604 m²) yields a removed volume of 577,883 m³ and an added volume of 38,195 m³, resulting in a net balance of −539,689 m³ and a mean net lowering of approximately 6.70 m. The computation reports 71% matching cells, expected in steep terrain with frequent occlusions; derived volumes should therefore be treated as conservative estimates in non-overlapping sectors. The deposit volume along the Vallesinella valley was estimated at approximately 660,000 m³, yielding a bulking factor of approximately 15%. The reconstructed failure geometry, combined with the identified sliding surface orientation of 290–310°/45–55°, constitutes the geometric and volumetric input for the thermo-mechanical stability analysis described in Section 5.4.

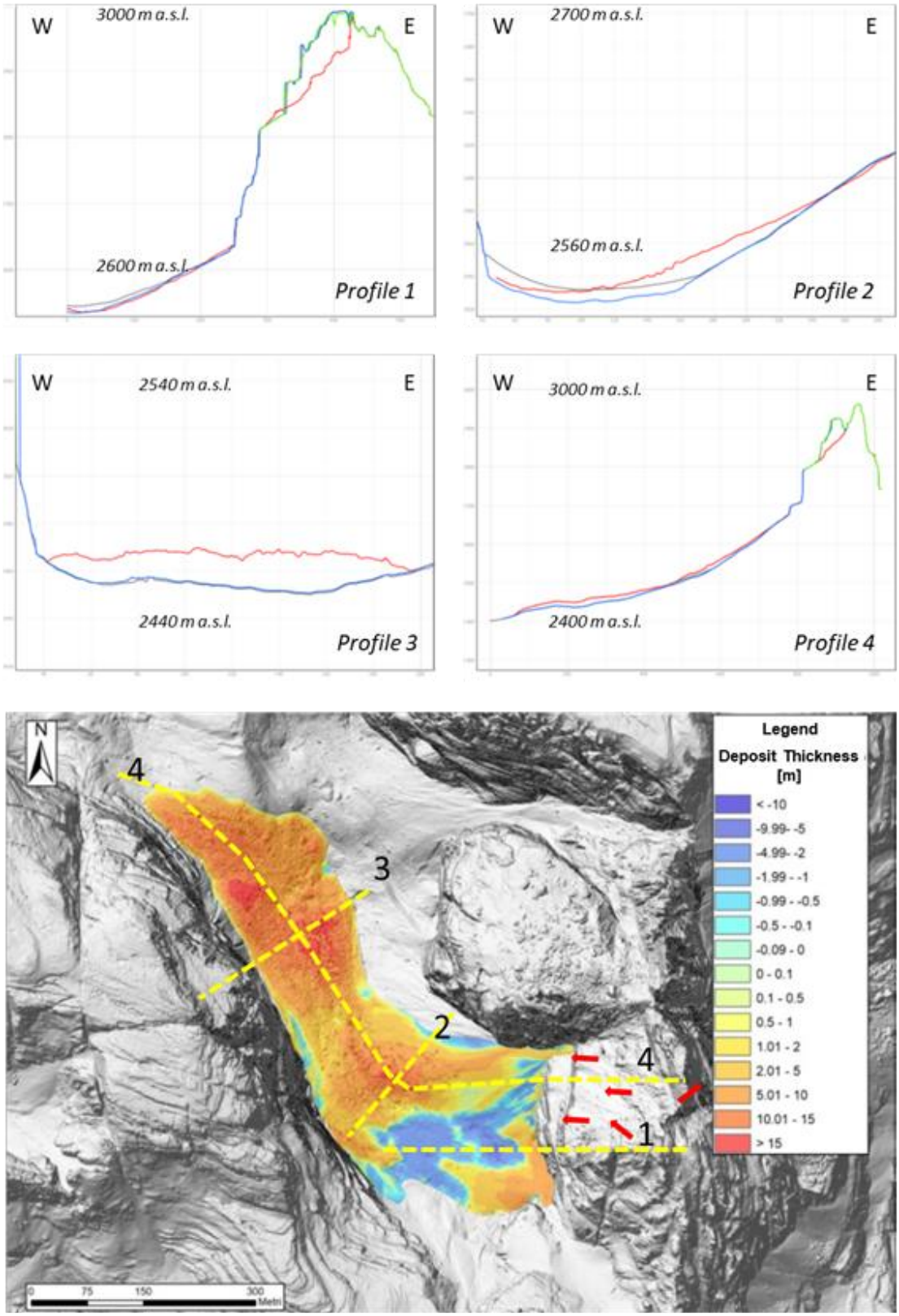


Figure 53 DEM cross-section comparison. Red lines: 4 August 2025 (post-main collapse); green: 27 July 2025 (post-first collapse); blue: 2022 baseline; grey: 2014 baseline. Lower panel: deposit extent and thickness from DoDs (LiDAR 2025 vs. 2022). Red arrows indicate main displacement directions from the source zone.

A follow-up UAV LiDAR survey in October 2025 documents limited post-collapse scarp evolution, with detachment of a 700 m³ rock pillar and minor debris erosion, confirming progressive stabilization of the detachment niche following the main August 2025 event (Figure 54).

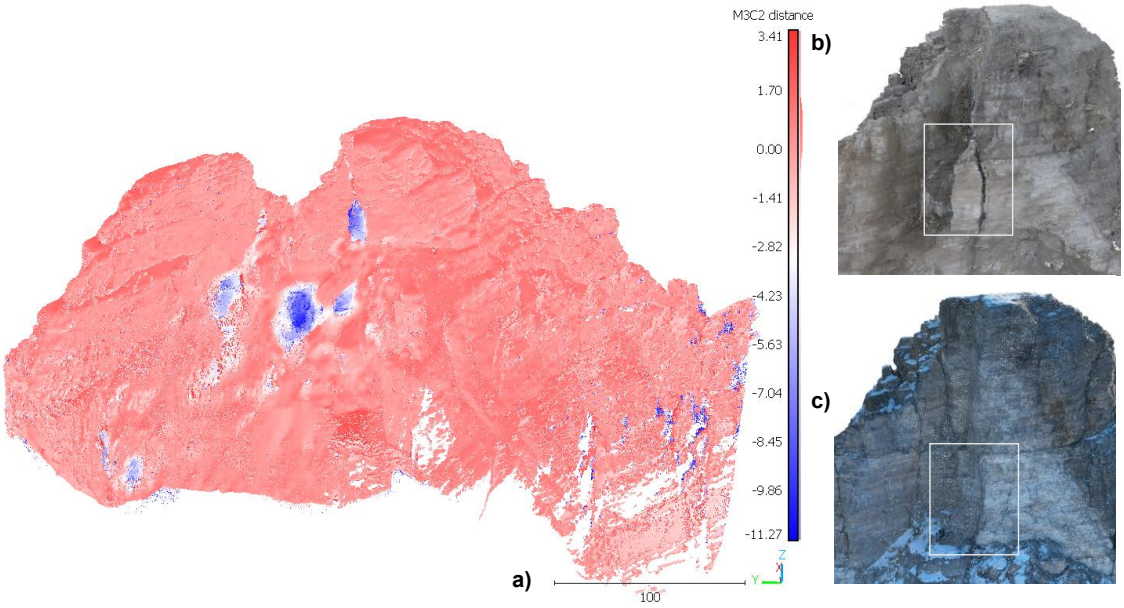


Figure 54 Short term headscarp evolution. (a) M3C2 distance between August 2025 and January 2026 point clouds; (b-c) Detailed view of the 700 m³ detached block.

5.4 **Methodology and Theoretical Background**

5.4.1 *The Calibration Trap: Structural Limitations of Existing Models*

The existing class of permafrost rockwall stability models shares a common structural limitation that has remained largely unaddressed in literature. Standard approaches apply continuous atmospheric forcing, coupling rockfall occurrence directly to mean air temperature anomalies or to time-averaged thermal and hydrological energy inputs (Gruber & Haeberli, 2007; Krautblatter et al., 2013; Mamot et al., 2021). By distributing climatic energy uniformly over time, these models impose a constant, uninterrupted downward trend in baseline stability. As the simulated ice-rock interface weakens monotonically under sustained warming, the model inevitably reaches criticality at some point, but that point is systematically earlier than the observed failure date when physically grounded, laboratory-constrained parameters are used.

To reconcile simulated and observed failure chronologies, modellers are therefore forced to artificially inflate basal friction angles or cohesion values beyond any

experimentally documented range for the relevant rock-ice interface conditions. This is the calibration trap: the model produces the right answer for the wrong physical reason, at the cost of obscuring the true underlying mechanics. The trap is not a consequence of poor parameterization but of a structural conceptual error, the conflation of two physically distinct processes that operate on fundamentally different timescales.

In nature, these two processes are decoupled. Long-term thermal preconditioning, the progressive warming of interstitial ice toward 0 °C under secular climate change, acts over decades, exponentially reducing ice-rock adhesive strength and creating a slowly growing window of vulnerability (Krautblatter et al., 2013; Mamot et al., 2021; Weber et al., 2025). The proximate trigger, by contrast, is a discrete, episodic hydromechanical event: a transient hydrostatic overpressure generated by infiltrating water bypassing the remaining ice anchor via marginal flow during an intense rainstorm (Hasler et al., 2011; Leinauer et al., 2024). Because the latent heat of fusion required to ablate the ice column is thermodynamically far larger than the sensible heat delivered by infiltrating water, the deep structural ice anchor is preserved until the very moment of collapse, as directly validated by the post-event documentation of surviving ice candles at Cima Falkner. The failure is not caused by the ice melting away; it is caused by the ice being progressively weakened to the point where it cannot resist the non-linear, quadratic hydrostatic forces generated by ordinary but intense infiltration events.

Resolving the calibration trap therefore requires a model that simultaneously (i) preserves the discrete nature of fluid pressurization and the subsequent poro-elastic recovery of effective stress between events, (ii) explicitly represents the latent heat budget governing ice candle dynamics, and (iii) derives a time-continuous Factor of Safety trajectory from an uncalibrated, laboratory-constrained parameter set. The episodic thermo-hydromechanical framework described in section 5.4.2 provides this formulation.

5.4.2 *Episodic Thermo-hydromechanical Framework*

The core physical framework is implemented as a custom one-dimensional process-based model simulating the coupled evolution of rock temperature, fracture ice dynamics, and limit-equilibrium stability over the period 1940–2036 (Figure 55). The block geometry is idealized as a rigid wedge sliding on a planar basal surface inclined at α= 42°, with a rear release surface constituted by a vertical tension crack of depth H_{crack}= 42 m, consistent with both the fracture apertures documented in field and UAV

observations and with the thermal penetration depth predicted by the three-dimensional FEFLOW and MIDAS simulations described in Section 5.4.3 and Section 5.4.4.

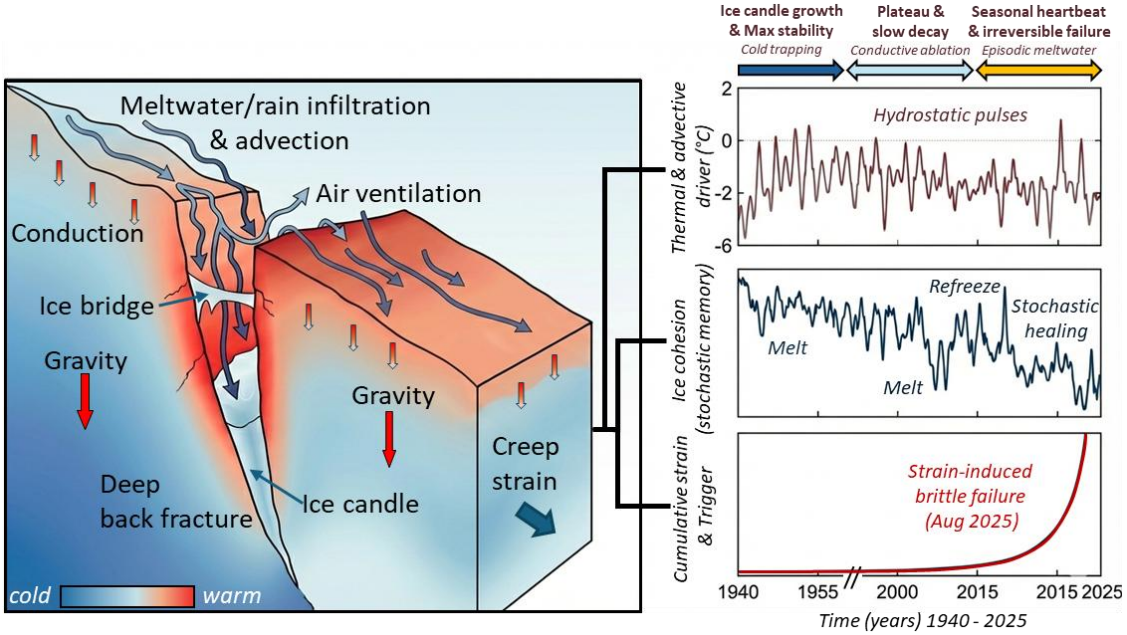


Figure 55 Catastrophic failure is driven by the decoupling of long-term thermal preconditioning and transient hydromechanical shocks. Left: Schematic of the structural block geometry. Progressive secular warming drives conductive heat into the rock mass, exponentially reducing the shear strength of the deep ice candle. As the rock-ice interface approaches 0°C, extreme precipitation bypasses the remaining ice anchor via marginal flow, generating transient hydrostatic overpressures. Right: Three-phase stability evolution (1940–2025). Phase 1 (Cold-trapping): Infiltrating water refreezes, growing the ice candle and maximizing the Factor of Safety (FoS). Phase 2 (Plateau & slow decay): Long-term conductive ablation degrades baseline ice cohesion. Phase 3 (Seasonal heartbeat): Episodic rainstorms generate acute hydro-mechanical shocks (transient FoS drops). Subsequent drainage and refreezing allow episodic effective stress recovery, maintaining marginal stability through 2024 and into the extreme wet conditions of 2025.

Temperature evolution. Rock temperature $T(z,t)$within the block is governed by a one-dimensional analytical solution that explicitly separates secular warming from seasonal oscillation through two distinct damping depths:

$$T(z,t) = T_{mean} + \Delta T_{warming}(t) \cdot e^{-z/d_1} + T_{seas} \cdot e^{-z/d_2} \cdot \cos(\omega t - \varphi_z)$$

where $d_1$and $d_2$are the thermal damping depths for the long-term warming trend and seasonal forcing respectively, $\omega$is the annual angular frequency, and $\varphi_z$is the depth-dependent phase lag. This dual-depth formulation separates the two governing timescales: $d_1$controls secular warming signal penetration over metres to tens of metres, while $d_2$governs the shallower seasonal active layer dynamics. The non-linear acceleration of

$\Delta T_{warming}(t)$after 1980 is prescribed to reproduce the observed rate increases documented for the Eastern Alps (Bonometti et al., 2026; Crespi et al., 2021). Rock mass thermal diffusivity is set to κ= 1.1 × 10^{-6} m^2 s^{-1}, representative of dolomite. As demonstrated by inspection of the simulated temperature fields across all three FEFLOW scenarios in Section 5.5.3, isotherms are consistently oriented sub-parallel to the fracture walls away from topographic singularities, with the dominant thermal gradient directed perpendicularly to the fracture plane, confirming that the one-dimensional diffusive formulation provides a physically consistent approximation of heat transport in the rock mass surrounding individual fractures.

Ice candle dynamics. The ice column height $h_{ice}(t)$within the rear fracture evolves through a balance between accumulation by cold trapping and ablation dominated by conductive heat transfer:

$$\frac{dh_{ice}}{dt} = +\dot{h}_{acc} \text{if } T_{air} > 0 \text{ and } T_{rock} < 0 \text{[Cold Trapping]}$$

$$\frac{dh_{ice}}{dt} = -\dot{h}_{abl} \text{if } T_{air} > 0 \text{ and } T_{rock} \approx 0 \text{[Conductive/Advective Erosion]}$$

Water infiltration is triggered by snowmelt (0 °C < T_{air}< 5 °C) or rainfall (T_{air} > 5 °C). Refreezing occurs only when local rock temperature $T_{rock}$is sufficiently negative to absorb the latent heat of fusion (L = 334 kJ kg^{-1}) through cold trapping. This physically explains the persistence of fracture ice even as the surrounding rock warms: since the sensible heat of infiltrating water is thermodynamically dwarfed by the massive latent heat buffer, the ice anchor is preserved for decades of progressive surface warming, a key emergent result directly validated by the post-event ice candle observations. This $h_{ice}(t)$behaviour, in which fracture filling persists for decades despite progressive surface warming and degrades top-downward as the cold trap capacity is exhausted, is a central emergent result of the model.

Marginal bypass flow and transient hydrostatic forcing. A critical limitation of conventional permafrost rockwall models is the paradoxical treatment of water pressure: if a fracture is entirely plugged by ice, hydrostatic pressure cannot develop; if the ice melts completely, the fracture drains freely. The episodic framework resolves this paradox through the marginal bypass flow mechanism, which conceptually represents the differential thermal erosion and permeability at the rock-ice interface. As the baseline permafrost temperature warms into the transitional regime (−5 °C to −1 °C), cold-trapping

capacity is irreversibly exhausted and infiltrating water transitions from a stabilizing agent, winter refreeze, to a destructive mechanical force. During episodic extreme precipitation events, water bypasses the structural core of the ice candle via the marginal rock-ice interface and transiently pressures up to 60% of the total fracture height, generating a horizontal driving force $V(t)$on the tension crack and an uplift force $U(t)$on the basal plane. The maximum allowable water height during a storm is bounded by a fractional fill parameter $h_{w,max,frac}$= 0.6, representing the maximum transient saturation before outward drainage occurs, yielding:

$$V(t) = \frac{1}{2}\rho_w g z_w^2$$

$$U(t) = \frac{1}{2}\rho_w g z_w L_{base} U_{drain}$$

where $z_w = h_{w,max,frac} \cdot H_{crack}$is the transient water column height and U_{drain}= 0.5 represents a standard triangular pressure dissipation along the sliding surface. Because lateral hydrostatic thrust scales quadratically with z_w, this generates massive, non-linear mechanical shocks acting upon a thermally preconditioned ice anchor.

Factor of Safety formulation. The transient Factor of Safety is computed daily as:

$$FoS(t) = \frac{(W\cos\alpha - U(t))\tan\varphi_{res} + R_{therm}(T)}{W\sin\alpha + V(t)}$$

where $W$is block weight, α= 42° is the basal inclination, $U(t)$and $V(t)$are the time-dependent transient hydrostatic forces defined above, $\varphi_{res}$is the residual basal friction angle, and $R_{therm}(T)$is the temperature-dependent thermal resistance of the ice-rock interface following the empirical exponential constitutive law of Krautblatter et al. (2013). To strictly avoid the calibration trap, the residual friction angle is explicitly uncalibrated at φ_{res}= 41.0°, independently constrained by laboratory testing on cold, polished dolomitic joints, with zero cohesive interlocking assumed on the pre-existing sliding plane (c = 0 kPa).

Temperature-dependent strength and tensile reduction factor. Ice shear strength $\tau_{ice}(T)$follows the empirical exponential relationship of Krautblatter et al. (2013):

$$\tau_{ice}(T) = \tau_{max} \cdot [1 - \exp(\lambda T)] \text{for } T < 0\ °C$$

where τ_{max}= 600 kPa and $\lambda$is a shape parameter calibrated on experimental data. Since the rear fracture opens in tension, the relevant failure mode is adhesive debonding rather

than shear sliding. A tensile reduction factor $k_{tensile}$= 0.15 is applied to convert shear strength to effective tensile adhesive strength:

$$\sigma_{tensile} = k_{tensile} \cdot \tau_{ice}(T)$$

The value $k_{tensile}$= 0.15 is grounded in three independent experimental sources (Raraty & Tabor, 1958; Hawkes & Mellor, 1972; Davies et al., 2001; Schulson & Duval, 2009; Kodama et al., 2013) and represents the conservative lower bound of the experimentally documented range of 0.15–0.30. This choice is physically appropriate for a partially open, rough natural fracture where ice-rock adhesive contact is imperfect. A higher $k_{tensile}$would further increase the $FoS$and extend the simulated slope lifetime, making this choice conservative: the episodic model resolves the correct failure date even with the minimum experimentally supported adhesive strength.

Continuous versus episodic forcing. To demonstrate why conventional models fail to capture the failure timing, two distinct hydrological boundary conditions are implemented with identical annual water budgets targeting 1,200 mm yr^{-1}. In the continuous model, water flux is parameterized as a constant daily rate equal to mean annual precipitation divided by the number of days with positive air temperature T_{air}. No cold-trapping mechanism is implemented, not as a simplification but as the defining characteristic of the continuous formulation, resulting in a monotonic decline in baseline stability without transient hydrostatic pressurisation. In the episodic model, daily precipitation events occur with probability p= 0.20 conditional on positive T_{air}, with event magnitude drawn from an exponential distribution. Concentrating the same annual flux into approximately 36 episodic events leaves the interface sub-zero and available for cold trapping between events. This is not a parameter choice but a process representation choice, and it determines whether the model is physically capable of reproducing $h_{ice}(t)$accumulation in a warming climate.

The Seasonal Heartbeat The thermo-rheological formulation explicitly demonstrates that rockwall preconditioning does not require the complete volumetric ablation of the ice candle. Instead, the mere penetration of the summer heatwave raises the ambient ice temperature from its deep-winter baseline to near 0 °C. Due to the exponential nature of the constitutive law $\tau_{ice}(T)$, this slight warming drastically lowers the adhesive strength, creating a transient window of vulnerability. While winter refreeze temporarily restores this structural rigidity, the progressive decadal warming of the permafrost baseline ensures that each successive summer's stability drop is deeper than the last. This thermal

fatigue generates the characteristic seasonal heartbeat of the $FoS(t)$trajectory, a pattern of transient exceedances of the critical threshold during extreme precipitation years, followed by episodic effective-stress recovery via drainage and refreezing, ultimately driving the slope to irreversible failure even before advective erosion has completely destroyed the structural ice core.

The 0-mm Precipitation Control Run To definitively validate the hypothesis that long-term climatic warming acts as a preconditioning agent while episodic precipitation acts as the proximate trigger, a targeted numerical control experiment was implemented. In this scenario, annual precipitation forcing was artificially set to 0 mm, effectively neutralizing all marginal bypass flow and transient hydrostatic forces ($U(t) = 0, V(t) = 0$). Under this pure conductive-rheological trajectory, the model slope is subjected solely to long-term atmospheric warming and seasonal thermal diffusion. As established in the energy partitioning analysis, while advective heat transport is thermodynamically negligible compared to the massive latent heat buffer, the complete removal of water eliminates the critical mechanical trigger. Consequently, volumetric ice loss proceeds smoothly rather than in discrete advective steps, and $FoS(t)$declines monotonically without the high-frequency hydrostatic spikes characteristic of the episodic model. In the 0-mm control run, theoretical geomechanical collapse is delayed by several years relative to the observed August 2025 event, proving that while progressive conductive warming strictly governs the underlying trajectory toward instability, the mountain does not fail due to thermal exhaustion alone. The observed catastrophic failure requires the precise temporal intersection of a thermally degraded, rheologically softened rock mass with the transient hydrostatic pressurization delivered by an intense episodic summer rainstorm (Figure 55).

5.4.3 *3D Thermal Modelling Setup*

Transient three-dimensional thermal simulations were conducted using the FEFLOW finite-element software (DHI) on an unstructured mesh derived from a 1 m × 1 m DEM of the pre-event topography. Surface temperature at each of the 51,185 mesh superficial nodes was parameterized as:

$$T_{surf}(node,t) = [T_{air}(t) + \Delta T_{mean}] + \alpha_T \cdot \frac{[R(node,m) - R_{mean}(m)]}{R_{mean}(m)} + lapse\ rate \cdot \frac{(z_{max} - z)}{100}$$

where $T_{air}(t)$ is the air temperature recorded at the Grostè meteorological station (ca. 2,250 m a.s.l.), $\Delta T_{mean} = 1.5\,°C$ is a domain-wide thermal offset, calibrated on the measured surface offset (MAGST − MAAT) of +1.5 °C recorded by a 16-level thermistor chain at a comparable N-facing permafrost site (Pisciadù, ~2,750 m; see Section 5.6.5), $\alpha_T = 3\,°C$ (Gruber & Haeberli, 2007) scales the radiative anomaly term derived from monthly solar radiation fields $R(node,m)$ computed from the same DEM using the Raster Solar Radiation tool (ArcGIS Pro, ESRI), accounting for slope, aspect and topographic cast shadows. (Fu & Rich, 2002; Gruber et al., 2004; Noetzli et al., 2007; Magnin et al., 2015) (Figure 56), and the third term applies a local elevation-dependent lapse-rate correction of 0.48 °C per 100 m, within the range independently measured between two Brenta Dolomites stations (0.43–0.53 °C per 100 m; see Section 5.6.5) — referenced to the maximum mesh elevation (3044 m), so that lower-elevation nodes receive proportionally greater warming. The main limitations of this approach, neglect of snow cover and fracture-ventilation effects, may introduce local deviations of 1–3 °C (Hasler et al., 2011; Magnin et al., 2015).

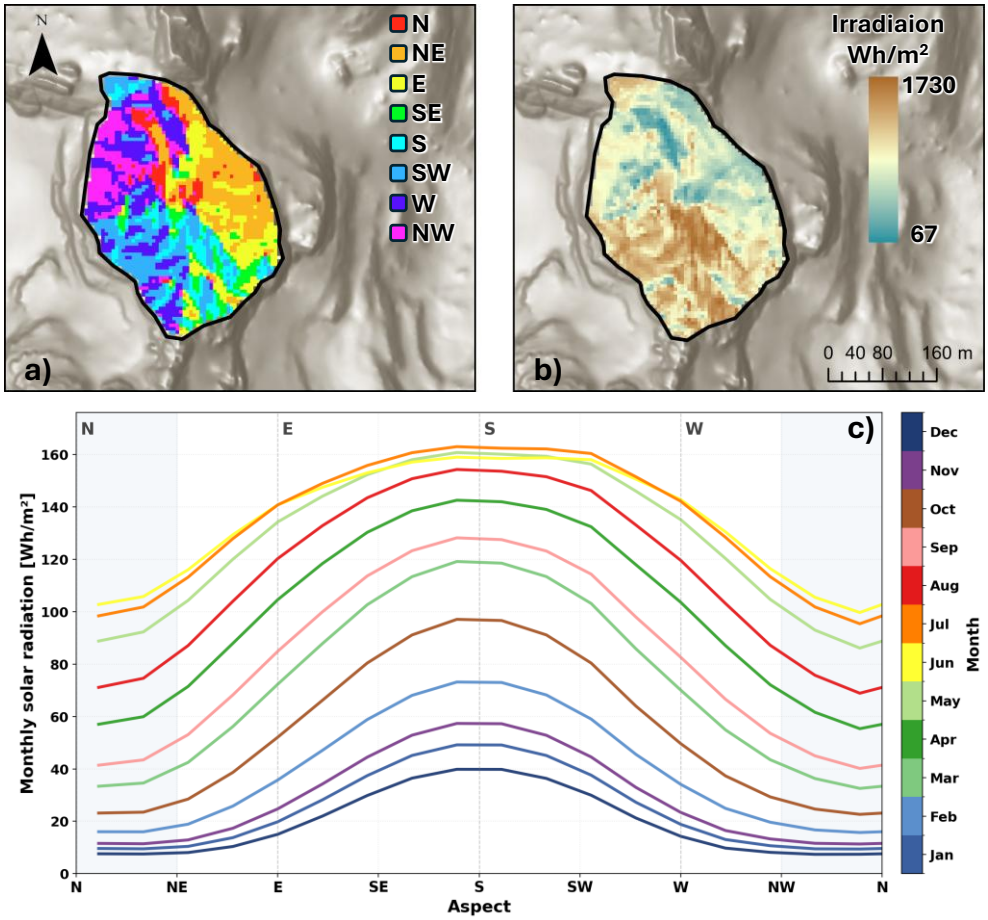


Figure 56 a) Aspect Map from ArcGIS Pro; b) Solar radiation calculated from DEM, Slope and Aspect and c) Solar radiation distribution during every month for each aspect position.

To reproduce the ice thickness observed at the detachment surface (~8 m), the conductive baseline (Scenario A) was extended by incorporating latent-heat effects through a freezing-point depression scheme (piFreeze module). Because this scheme requires a variably saturated flow formulation as a numerical prerequisite, the governing Richards' flow equation was used; the domain was nonetheless kept fully saturated by construction (uniform hydraulic head fixed above the maximum surface elevation, no active flow boundary condition), so that the rock mass remains physically fully saturated throughout the simulation, consistent with the hydrothermal formulation adopted elsewhere in this chapter. A linear freezing function was adopted, with a transition interval of ±1 °C around 0 °C and a residual liquid-water fraction of 10^{-4}; outside this interval, constant ice or water thermal properties apply. Rock porosity was set to 3%, consistent with a low-porosity, densely fractured dolomitic rock mass. Material and phase-change parameters are summarized in Table 8.

Table 8 Material properties used for the FEFLOW FEM thermal analysis.

Parameter	Value	Units
Porosity (n)	3%	—
Solid thermal conductivity (λ)	2.5	W m^{-1} K^{-1}
Thermal diffusivity (α)	1.1×10^{-6}	m^2 s^{-1}
Latent heat of fusion (L)	334	kJ kg^{-1}
Rock density (ρ)	2,700	kg m^{-3}
Geothermal heat flux	65	mW m^{-2}
Liquid density	1000	kg m^{-3}
Ice Density	917.5	kg m^{-3}
Ice volumetric heat capacity	1.86×10^6	J m^{-3} K^{-1}
Ice thermal conductivity	≈ 2.2	W m^{-1} K^{-1}
Residual liquid fraction	1×10^{-4}	—

A three-stage initialization strategy was adopted to minimise boundary errors: (i) a spin-up step using an annual temperature cycle constructed from monthly means, repeated until quasi-periodic equilibrium was achieved; (ii) historical monthly mean forcing applied up to 2021, to reproduce the long-term thermal inertia and deep permafrost evolution; and (iii) a high-resolution simulation with daily mean temperatures from January 2022 to 1 August 2025, to capture the short-term thermal anomalies immediately preceding the collapse.

In the absence of deep borehole temperature measurements, the model cannot be formally calibrated against in-situ data. The analysis instead aims to constrain a physically plausible thermal state at the time of failure, using the post-event observation of massive ice exposed in the detachment niche as a qualitative benchmark validating the simulated sub-zero temperatures.

Three boundary-condition scenarios were evaluated to isolate the contributions of topographic exposure and advective heat transport to the pre-failure thermal regime: Scenario A: conduction only, with the spatially variable, aspect-dependent surface-temperature correction described above; Scenario B: conduction plus convection applied to deep fractures penetrating the full thickness of the summit structure; and Scenario C: conduction plus convection limited to mid-depth fractures representative of the observed tension crack network. Convection was implemented via Newton's law boundary conditions at the fracture surfaces, with imposed temperature equal to T_{air}. While Scenario A was simulated using FEFLOW under the hydrothermal formulation described above, Scenarios B and C were implemented in MIDAS FEA, where convective boundary conditions were applied directly at the fracture surfaces within the three-dimensional

mechanical mesh, enabling a consistent evaluation of advective heat transport effects within the same geometric framework used for the stability analysis.

5.4.4 *3D Mechanical Stability Analysis Setup*

Three-dimensional finite-element geomechanical analyses were conducted using MIDAS FEA NX on the pre-event topographic geometry discretized into 745,362 elements and 137,751 nodes. The rock mass was modelled using an elasto-plastic Mohr–Coulomb criterion with parameters characteristic of fractured Dolomia Principale (E = 10 GPa; ν= 0.25; cohesion = 800 kPa; friction angle = 30°; unit weight = 27 kN m^{-3}). Gravitational loading activated the in-situ lithostatic stress state. Boundary conditions prevented rigid-body motion: fully constrained base; outward-normal restraint on lateral faces; traction-free upper surface.

Major discontinuities and the potential sliding surface were implemented as Mohr–Coulomb interface elements with normal stiffness K_n= 158 GPa m^{-1} and shear stiffness K_s= 14.4 GPa m^{-1}. A strength reduction factor of 0.7 was pre-applied to all interface parameters to account for the weakening effects of ice-bearing discontinuities and reduced effective interlocking along frozen and open fractures, consistent with the field observations of massive ice, the thermal results from the FEFLOW simulations of Section 5.4.3, and published values for ice-filled rock discontinuities in the transitional thermal regime (Davies et al., 2001; Mamot et al., 2021; Arenson & Springman, 2005). Constitutive parameters are summarized in Table 9.

Table 9 Constitutive parameters for the 3D FEM mechanical analysis (MIDAS FEA).

Parameter	Rock mass	Interface	Reduced interface (×0.7)	Units
E (Young's modulus)	10	—	—	GPa
ν (Poisson's ratio)	0.25	—	—	—
c′ (cohesion)	800	300	210	kPa
φ′ (friction angle)	30	28	20	°
γ (unit weight)	27	—	—	kN m^{-3}
K_n (normal stiffness)	—	158	—	GPa m^{-1}
K_s (shear stiffness)	—	14.4	—	GPa m^{-1}

Four end-member scenarios were analyzed to assess sensitivity to the localization of plastic deformation and the presence of a kinematic constraint. Case 1 (mixed elasto-plastic) assigns elastic response to stable bedrock and plastic behaviour to potentially unstable blocks. Case 2 (fully plastic with predefined sliding surface) assumes fully plastic Mohr–Coulomb behaviour for the entire domain with the mapped sliding surface active. Case 3 (fully plastic, no predefined sliding surface) maintains the fully plastic domain of Case 2 but removes the explicit sliding surface, testing whether the observed failure plane emerges naturally from stress redistribution and structural anisotropy alone. Case 4 (elastic rock mass, plastic interfaces only) restricts plasticity to interfaces, testing purely structure-dominated behaviour. Across all cases, stability was assessed through the Shear Strength Reduction Method, which progressively reduces shear strength parameters $c$and $\tan\varphi$simultaneously until numerical non-convergence, yielding the global FoS.

5.5 **Results**

5.5.1 *Resolving the Calibration Trap*

Direct model comparison using physically grounded, laboratory-constrained parameters, residual rock friction angle φ_{res}= 41° and realistic mean annual precipitation of 1,200 mm yr^{-1}, demonstrates the structural limitations of continuous forcing and the ability of the episodic framework to resolve them (Figure 57).

Thermal evolution and ice candle dynamics. The spatio-temporal thermal evolution map (Figure 57e) reveals one of the most counterintuitive results of the entire simulation: the trajectory of the top ice depth, that is the progressive downward retreat of the upper ice candle boundary, is virtually identical under continuous and episodic forcing throughout the entire 1940–2040 period. Both approaches show the 0 °C isotherm descending from approximately 5 m depth in 1940 to approximately 15 m depth by 2025, driven primarily by long-term conductive warming. This convergence directly demonstrates that the macroscopic morphological evolution of $h_{ice}(t)$is governed by latent heat dynamics rather than by hydrological forcing: the sensible heat advected by infiltrating water is thermodynamically dwarfed by L= 334 kJ kg^{-1}, the latent heat required to ablate the structural ice candle. The deep ice anchor is therefore preserved in both models up to the moment of collapse, a result directly validated by post-event field

surveys documenting a surviving ice candle 30/40m high and 1.4–1.6 m thick, exposed at 8–10 m depth within the freshly stripped detachment niche. The decadal depth profiles of rock temperature (Figure 57f) reveal a progressive deepening of the permafrost warming front. In the early decades (1955–1985), sub-zero temperatures extend to the full fracture depth of 42 m. By 2020–2025, the warmest annual profiles, corresponding to the hottest day of each year, show temperatures approaching 0 °C at depths of 8–12 m, while the deeper sections remain persistently frozen. The corresponding temperature-dependent ice shear strength profiles (Figure 57g) translate this thermal evolution into mechanical terms: as temperatures rise toward 0 °C in the upper portion of the fracture, $\tau_{ice}(T)$collapses exponentially from values exceeding 400 kPa in the 1950s to values approaching 50–100 kPa by 2020–2025. This exponential strength collapse, concentrated in the −2 °C to 0 °C transitional window, is the physical mechanism by which decades of modest warming translate into a sudden, catastrophic loss of structural resistance.

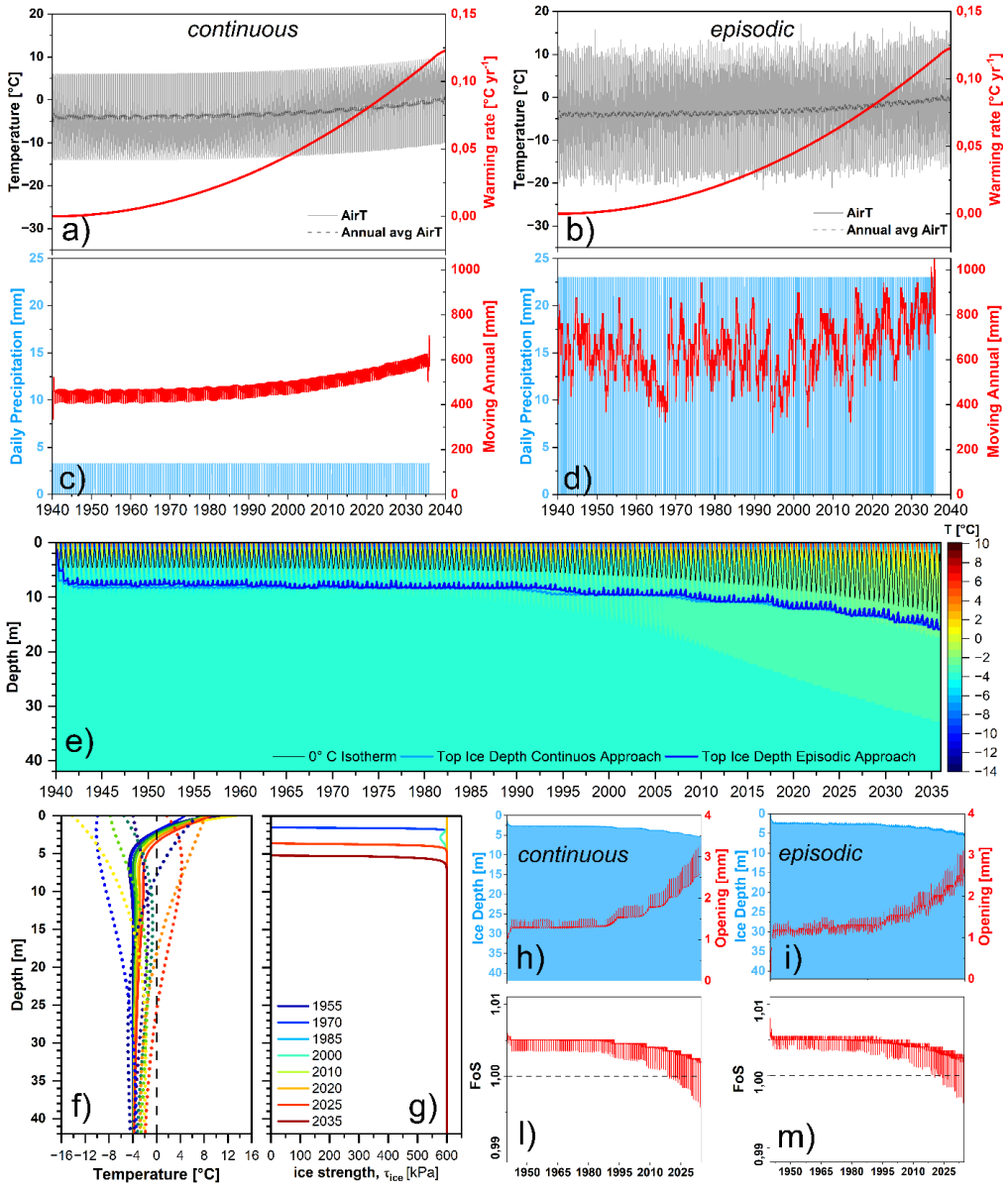


Figure 57 Episodic hydromechanical forcing resolves the premature failure paradox while preserving deep basal ice. (a–d) Comparison of continuous (a, c) and episodic (b, d) atmospheric forcing models for daily air temperature and precipitation. (e) Spatio-temporal thermal evolution map (1940–2040). The overarching top ice depth trajectory is virtually identical under continuous (light blue line) and episodic (dark blue line) forcing, governed predominantly by latent heat. (f, g) Decadal depth profiles of rock temperature (f) and the corresponding temperature-dependent ice shear strength (g). In (f), continuous lines represent the hottest day of the respective year, while dotted lines represent August 1st. (h–m) Long-term evolution of ice depth, fracture opening (red lines; h, i), and Factor of Safety (FoS; l, m). The grey vertical band highlights the critical failure divergence: continuous forcing (l) imposes an artificial downward trend, driving the FoS below unity (dashed line) prematurely. Conversely, the episodic framework (m) captures episodic poro-elastic recovery, delaying the definitive FoS drop below unity until the exact timing of the 2025 collapse.

Long-term evolution of fracture opening and ice depth. The long-term evolution of $h_{ice}(t)$and fracture opening (Figure 57h, i) highlights the divergence between the two hydrological forcing regimes. In the continuous model Figure 57h), $h_{ice}(t)$decreases monotonically throughout the simulation as the uninterrupted daily water flux progressively ablates the ice candle at a rate proportional to the excess temperature above −0.5 °C. Fracture opening accumulates smoothly and continuously, reflecting the monotonic rheological decay of the ice-rock interface. In the episodic model (Figure 57i), by contrast, $h_{ice}(t)$exhibits the characteristic episodic behaviour described in Section 5.4.2: during the early cold-trapping phase (1940–1990), infiltrating water encounters deeply supercooled rock and refreezes, episodically augmenting the ice column. As the baseline permafrost temperature warms into the transitional regime, cold-trapping capacity is gradually exhausted and ablation progressively dominates, but the deep structural anchor persists far longer than in the continuous model, consistent with the surviving ice candle observation.

Factor of Safety trajectory. The $FoS(t)$trajectories (Figure 57l, m) represent the central diagnostic result of the entire framework. In the continuous model (Figure 57l), $FoS(t)$declines in a smooth, monotonic downward trend from values around 1.08 in 1940 to a definitive and irreversible drop below unity in 2018, seven years before the observed event. Aligning this premature failure with the observed 2025 event would require inflating φ_{res}well beyond physically documented values, the essence of the calibration trap. In the episodic model (Figure 57m), the $FoS(t)$trajectory is fundamentally different. During the early cold-trapping phase, the baseline $FoS(t)$is maintained at or slightly above the continuous model level, with no significant seasonal oscillations because infiltrating water refreezes rather than pressurising the fracture. As the system enters the transitional thermal regime from approximately 2010 onward, discrete episodic infiltration events begin generating transient hydrostatic spikes, sudden drops of $FoS(t)$toward or below unity, followed by rapid rebounds via poro-elastic recovery as pore pressures dissipate between events. This seasonal heartbeat intensifies progressively through the wet years of 2024 and 2025, when the record annual rainfall of 2,037 mm (2025) generates the most severe fatigue cycles in the entire simulation. The $FoS(t)$transiently approaches but does not irreversibly cross unity during these years, as winter drainage and partial refreezing restore effective stress. Following July 2025 sub-maximal rainfall pulse, corresponding to the fourth wettest July in the 35-year

meteorological record, the $FoS(t)$drops definitively and irreversibly below unity, perfectly capturing the onset of the August 2025 collapse without any site-specific parameter tuning.

5.5.2 *Isolating the Trigger: The 0-mm Precipitation Control*

To isolate the role of discrete hydromechanical shocks from long-term thermal preconditioning, a control simulation was performed with annual precipitation artificially set to 0 mm, effectively neutralizing all marginal bypass flow and transient hydrostatic forces ($U(t) = 0, V(t) = 0$). The results are shown in Figure 58.

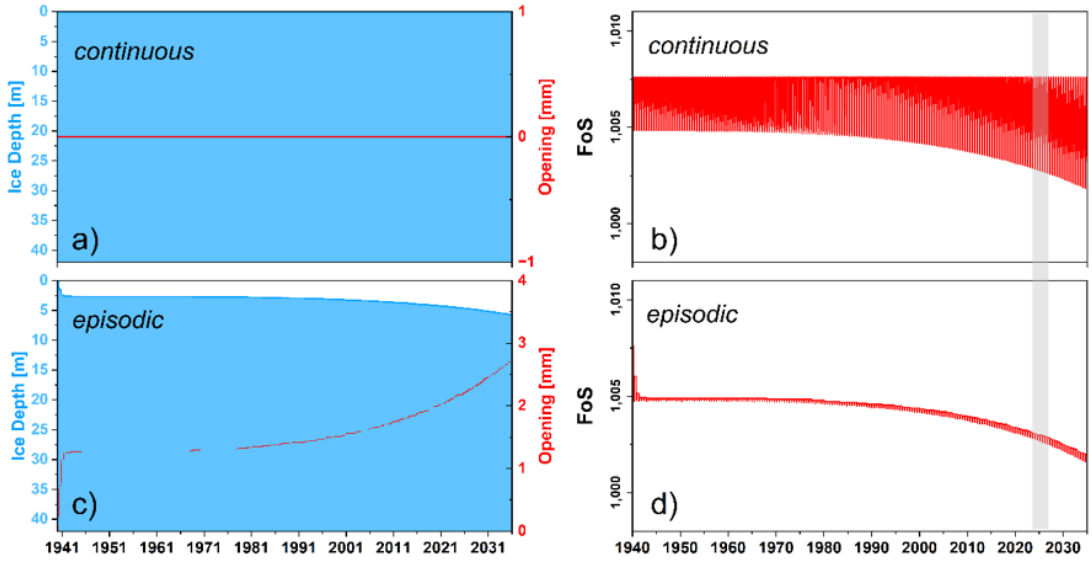


Figure 58 0-mm precipitation control simulation isolates thermal preconditioning and confirms the necessity of hydromechanical triggers. (a, b) Evolution of ice depth, fracture opening (a), and Factor of Safety (FoS) (b) under continuous thermal forcing with zero precipitation. (c, d) Corresponding outputs under episodic thermal forcing with zero precipitation. The grey vertical band indicates the timing of the August 2025 collapse. In the complete absence of infiltration and subsequent hydrostatic shocks, thermal degradation alone causes a progressive, decadal decline in baseline stability. However, the FoS consistently remains above unity (>1.0) across the entire simulated period in both modelling approaches. This control run mechanically validates that while secular warming acts as a critical preconditioning factor by degrading ice shear strength, extreme transient hydrostatic forcing is strictly required to induce the final catastrophic failure.

Under purely thermal forcing, $FoS(t)$declines smoothly without the high-amplitude seasonal oscillations characteristic of the episodic model. In the complete absence of episodic cold-trapping events, $h_{ice}(t)$evolves monotonically under conductive ablation alone, without the discrete accumulation–depletion cycles that govern the full episodic

simulation. Crucially, both the continuous and episodic zero-precipitation runs yield a $FoS(t)$that consistently remains above unity across the entire simulated period from 1940 to 2036. Theoretical geomechanical collapse is delayed several years beyond the observed August 2025 event in both cases.

This result has a precise physical interpretation rooted in the energy partitioning analysis of Section 5.4.2. While advective heat transport is thermodynamically negligible compared to the massive latent heat buffer (L = 334 kJ kg^{-1}), the complete removal of water eliminates the critical mechanical trigger entirely. Without episodic infiltration events, no marginal bypass flow develops, no transient hydrostatic overpressures are generated, and the quadratic amplification of $V(t)$and $U(t)$with water column height $z_w$never occurs. The rock mass is thus subjected to pure conductive thermal fatigue, which progressively degrades $\tau_{ice}(T)$and $\sigma_{tensile}(T)$toward zero, but this degradation alone is insufficient to drive $FoS(t)$below unity within the observed timeframe.

The 0-mm control run therefore provides a mathematically rigorous, independently validated proof that the August 2025 Cima Falkner collapse was not the result of thermal exhaustion alone. The precise temporal intersection of a thermally degraded, rheologically softened rock mass, whose baseline $FoS(t)$had been progressively lowered by decades of conductive preconditioning, with the transient hydrostatic pressurization delivered by the July 2025 rainfall pulse is the necessary and sufficient condition for the observed failure chronology. A mountain does not collapse because its ice slowly melts away; it collapses because accumulated thermal degradation leaves it defenceless against the non-linear, quadratic hydrostatic forces generated by ordinary but intense fluid infiltration.

5.5.3 *3D Thermal Regime*

Transient three-dimensional FEFLOW and MIDAS simulations across the three boundary-condition scenarios constrain the pre-failure thermal envelope of the Cima Falkner rock mass. The primary objective of thermal modelling is not formal calibration which is precluded by the absence of deep borehole temperature measurements at this site but rather the establishment of a physically plausible thermal state at the time of failure that is internally consistent across scenarios and coherent with the post-event field observations of massive ice preservation.

Scenario A — Conduction only consider solar radiation In the piFreeze conductive scenario, incorporating the spatially variable, aspect-dependent surface-temperature correction described above, temperature time series were extracted at fifteen points systematically distributed across the inferred sliding surface (P1-P15; Figure 59c replacing the smaller set of manually positioned monitoring locations used in earlier iterations of this model. Over the simulated record, most points remain within a narrow band of approximately −2 °C to −4 °C, while one point (P4) shows markedly larger seasonal amplitude, approaching 0 °C during summer months and dropping below −4 °C in winter, indicating the greatest sensitivity to atmospheric forcing among the sampled locations; another point maintains a comparatively warmer and more stable regime, closer to −1 °C throughout the record (Figure 59d). The spatial distribution of long-term trends across the fifteen points reveals a systematic gradient rather than random scatter, ranging from approximately +0.09 °C yr^{-1} on one side of the rupture surface to −0.05 °C yr^{-1} on the opposite side (Figure 59c), consistent with variable aspect and exposure across the concave detachment surface rather than a numerical artefact.

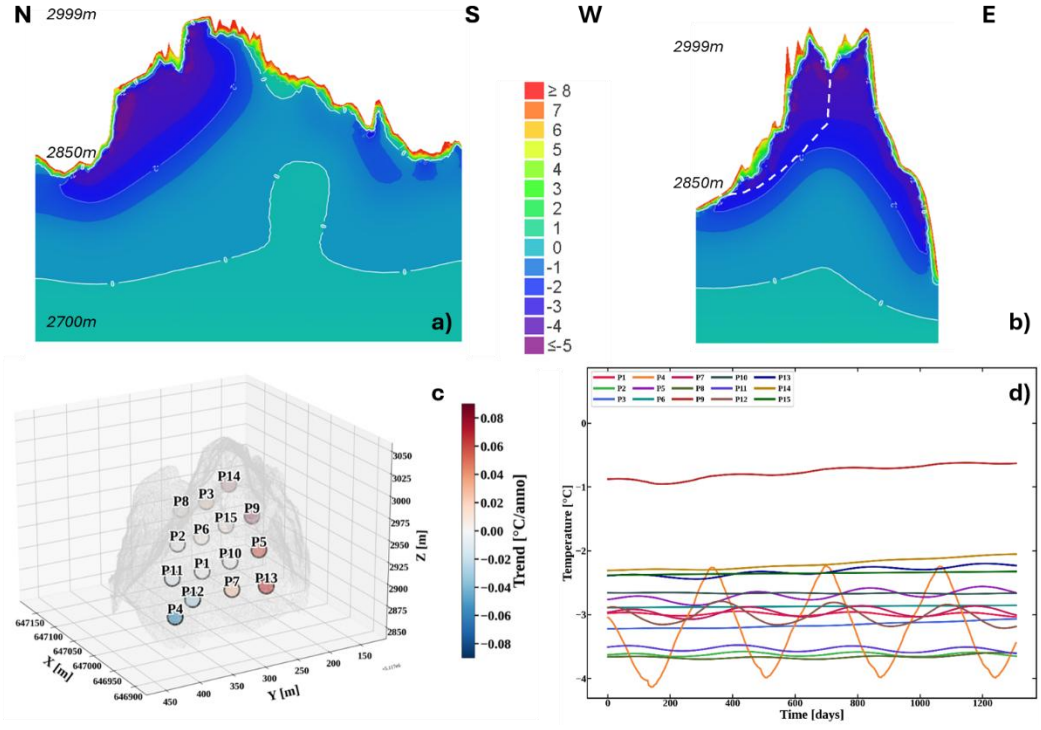


Figure 59 Cross-sections of the FEFLOW conductive-plus-latent-heat (piFreeze) temperature field: (a) North–South and (b) West–East vertical sections at the date of collapse (1 August 2025); colors represent temperature distribution (°C), with the white contour marking sliding surface. c) Location of the fifteen systematically distributed monitoring points (P1–P15) across the inferred rupture surface, colored by long-term temperature trend (°C yr^{-1}); the gradient from warming to cooling values across the surface reflects variable aspect and exposure. d) Modelled temperature evolution at the fifteen points over the simulated record; most locations remain within a narrow sub-

zero band, while point P4 shows the largest seasonal amplitude, indicating the greatest sensitivity to atmospheric forcing.

Cross sections of the temperature field (Figure 59a-b). reveal a thermally stratified domain: a warm active layer develops at the surface, transitioning to cold, sub-zero conditions at depth, with the 0 °C isotherm marking the boundary between the seasonally thawed layer and the underlying permafrost. The active layer thickness, determined from the depth at which the envelope of monthly temperature-depth profiles (August 2024–July 2025) and the profile at the time of collapse converge to 0 °C, is ALT = 9.8 m (Figure 60 — markedly closer to the ~8 m ice thickness documented in the field than would be obtained from a purely conductive formulation, providing quantitative support for the latent-heat (piFreeze) formulation adopted in this scenario.)

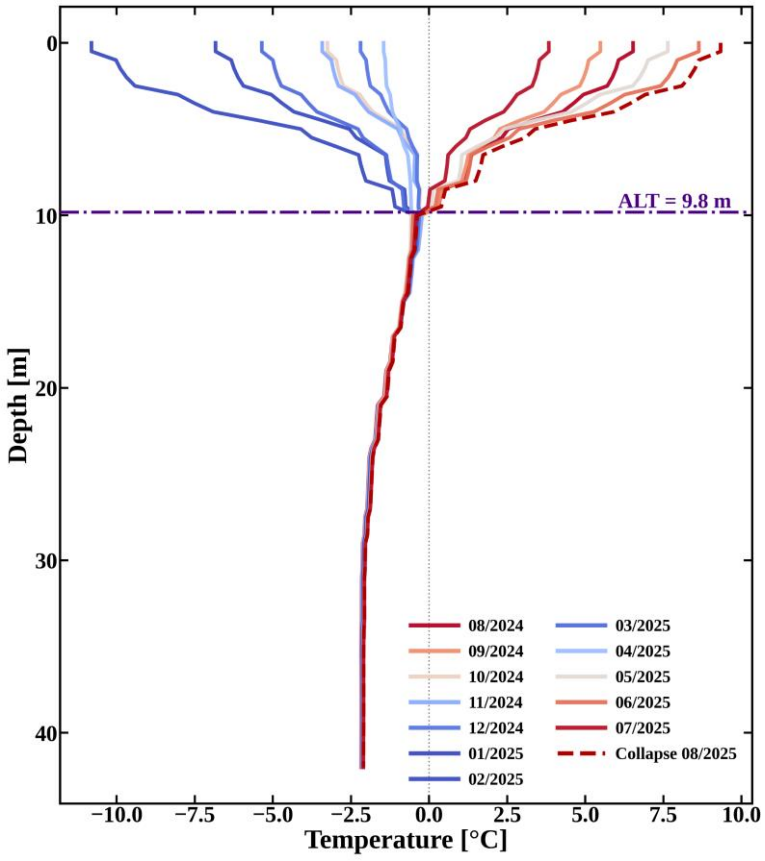


Figure 60 Vertical temperature-depth profiles at the location of maximum ice thickness along the rupture surface, showing monthly profiles from August 2024 to July 2025 (color gradient, blue to red) and the profile at the time of collapse (August 2025, dashed line). The active layer thickness (ALT), defined as the depth at which the envelope of monthly profiles converges to 0 °C, is 9.8 m (dash-dot line).

The temperature field calculated on the day of the collapse, mapped onto the post-failure point cloud (Figure 61), shows a cold rupture surface (down to approximately −4

°C) sharply contrasting with the surrounding, sun-exposed rock surface (up to approximately +10 °C). This radiation- and latent-heat-corrected baseline is consistent with the post-event field observation of surviving massive ice, providing quantitative confirmation that the failure surface was frozen at the time of collapse and ruling out bulk ice melting as the primary failure mechanism. The vertical fracture plane stands at about -2.2 °C, representing the critical window where the cohesion of the rock-ice interface decreases significantly. This radiation-corrected baseline is therefore consistent with the post-event field observation of surviving massive ice, providing quantitative confirmation that the failure surface was frozen at the time of collapse and ruling out bulk ice melting as the primary failure mechanism. The model's inherent limitation, its assumption of a continuous rock mass without preferential flow paths for air or water, means that it likely underestimates the true thermal state of the most exposed and fractured sectors of the rock wall, where advective processes become increasingly influential as fracture apertures widen (Hasler et al., 2011).

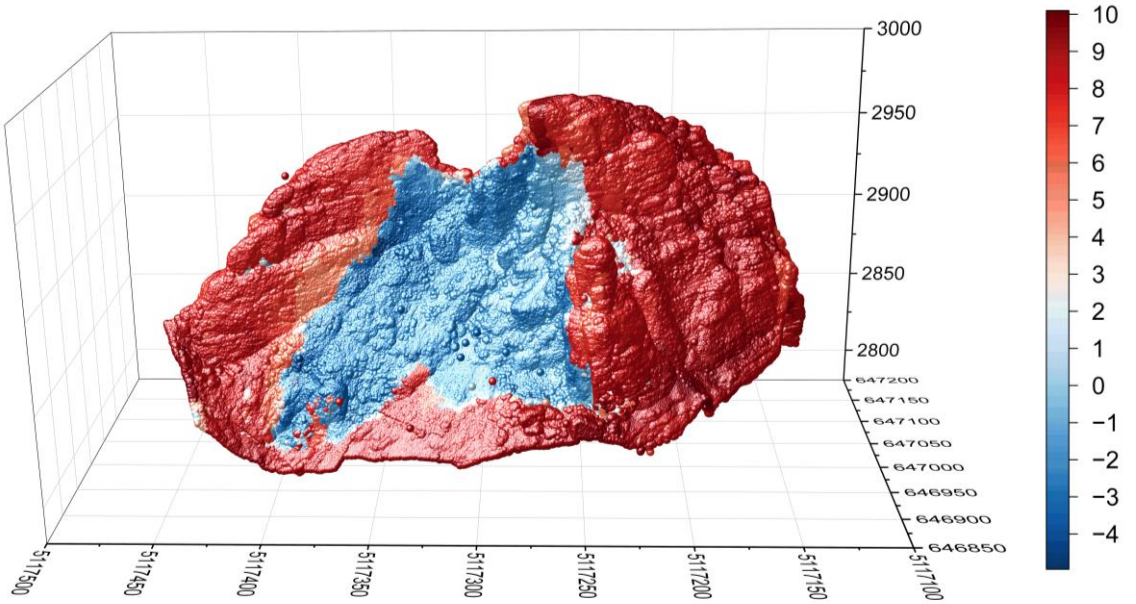


Figure 61 FEFLOW conductive-plus-latent-heat (piFreeze) temperature field mapped on the post-collapse point cloud, showing a cold rupture surface (blue tones) contrasting with the surrounding, sun-exposed rockmass surface (red tones, computed considering solar radiation) at the date of the collapse event.

Scenarios B and C — Convective regimes. To account for the progressive widening of the fracture network, documented by the aerial imagery and InSAR kinematic acceleration from late 2020, two additional scenarios were implemented with convective

Newton's law boundary conditions applied at the main fracture surfaces. In Scenario B, convection is applied along deep fractures penetrating the full thickness of the summit structure, while in Scenario C the same convective forcing is limited to fractures of intermediate depth, representative of the observed tension crack network. The internal thermal response of the slope across all three scenarios is shown in Figure 62. Scenario B produces a dramatically different thermal pattern from the conductive baseline. Deep fractures act as preferential conduits for warm air and water advection, distorting isotherms and driving heat penetration far beyond what purely conductive predictions would produce. The temperature time series at the monitored points along the sliding surface show that several locations approach or transiently exceed 0 °C during the extreme summers of 2023 and 2024, placing the rock-ice interface within the melting regime, the critical thermal window where $\tau_{ice}(T)$collapses most rapidly (Krautblatter et al., 2013; Mamot et al., 2021). The transient temperature-depth profiles spanning from January 2024 to the failure date of 1 August 2025 show significant thermal anomalies propagating deep into the rock mass in Scenario B, actively driving basal temperatures into the critical transitional regime (−5 °C to 0 °C) compared to the heavily damped, purely conductive baseline. Scenario C produces an intermediate response, with temperatures approaching but not systematically exceeding 0 °C at depth, and enhanced seasonal variability in the uppermost fractures, a physically plausible regime for a site where fracture connectivity is partial and spatially heterogeneous. Taken together, the three scenarios define a physically plausible thermal envelope for the pre-failure rock mass state. The conductive baseline confirms sub-zero conditions at depth and provides a conservative lower bound on the degree of thermal degradation. The convective scenarios demonstrate that even moderate air and water advection, increasingly enabled by the kinematic widening of the fracture network documented from 2020 onward, was sufficient to drive rock-ice interface temperatures within the transitional (−5 °C to −1 °C) and potentially melting (>−1 °C) regimes identified as critical for ice-filled joint failure. The progressive thermal weakening concentrated along the pre-existing discontinuity network provides the physical mechanism linking the observed InSAR kinematic acceleration to the ultimate collapse and constitutes the essential thermal preconditioning context within which the episodic hydrological trigger of Section 5.5.1 operated. Furthermore, inspection of the simulated temperature fields across all three scenarios confirms that, away from topographic singularities, isotherms are consistently oriented

sub-parallel to the fracture walls providing direct physical support for the one-dimensional diffusive formulation adopted in the 1D process-based model of Section 5.4.2.

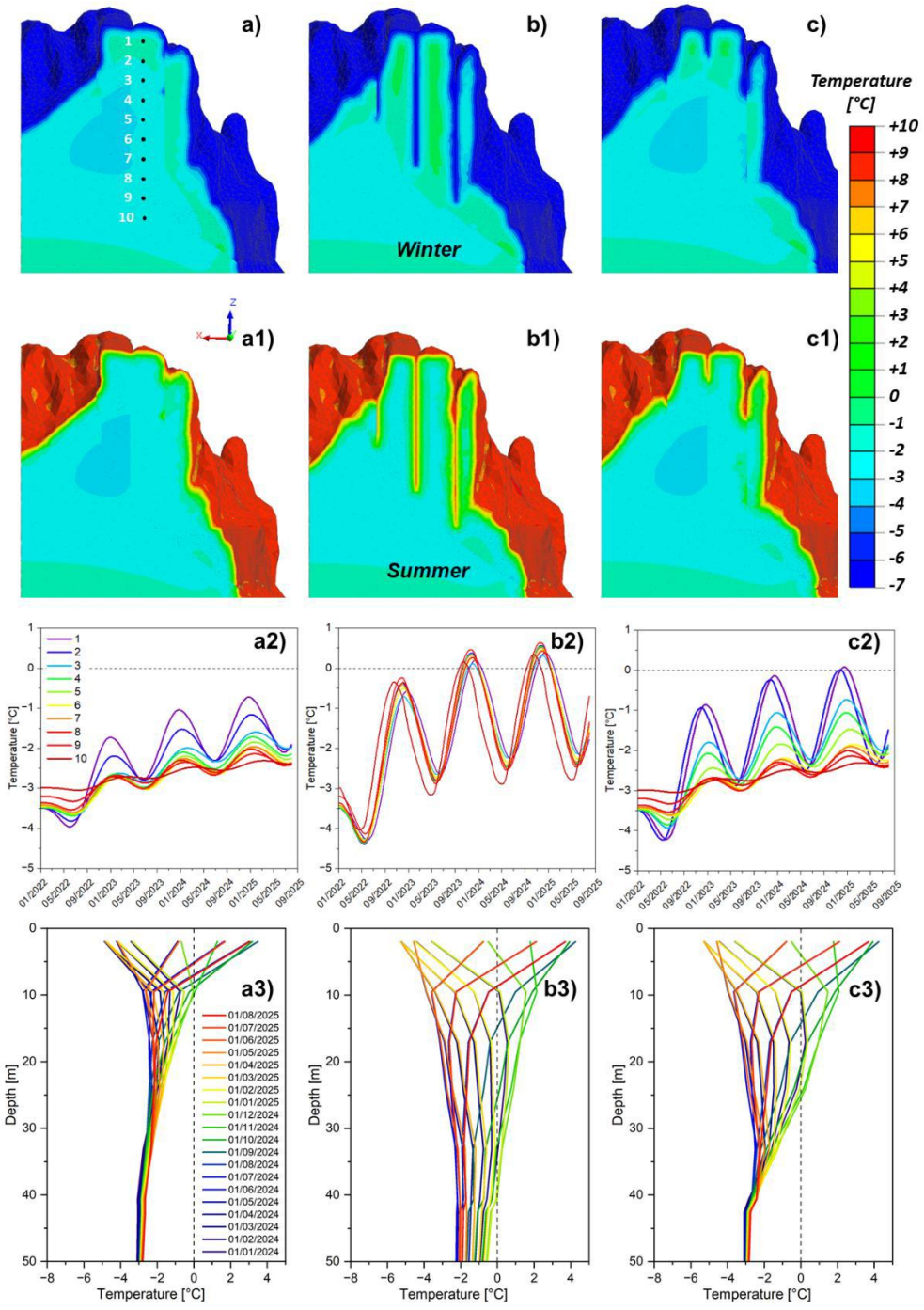


Figure 62 Internal thermal response of the slope across three 3D FEM modelling scenarios. Left column (a, a1, a2, a3): conduction only (Scenario A). Centre column (b, b1, b2, b3): conduction plus fluid convection/advection in deep fractures (Scenario B). Right column (c, c1, c2, c3): conduction plus convection/advection in mid-depth fractures (Scenario C). Top row (a–c): winter temperature cross-sections. Second row (a1–c1): summer temperature cross-sections (see nodal thermal

temperature color scale). Third row (a2–c2): temperature time series (January 2022 – August 2025) at ten monitored points distributed along the back-fracture sliding surface (locations indicated in panel a). Bottom row (a3–c3): transient temperature-depth profiles spanning from January 2024 to the failure date (August 1, 2025). Note how the depth profiles in the convective scenarios (b3, c3) demonstrate significant thermal anomalies propagating deep into the rock mass, actively driving basal temperatures into the critical transitional regime (–5°C to 0°C) compared to the heavily damped, purely conductive baseline (a3).

5.5.4 *3D Mechanical Stability and Emergent Failure Plane*

Three-dimensional FEM-SRM analysis across the four geomechanical scenarios provides an independent structural validation of the failure mechanism proposed by the one-dimensional episodic framework (Figure 63). The SRM analysis was not intended to force collapse by prescribing a pre-degraded geomechanical state, but to identify the critical strength reduction required to induce failure and to evaluate whether plastic strain localization is consistent with the independently mapped post-event detachment geometry.

The four scenarios yield markedly different FoSvalues that illuminate the relative contributions of bulk rock mass yielding and interface plasticity to the instability mechanism. Cases 1–3, which all include some form of bulk elasto-plastic rock mass behaviour, cluster tightly around $FoS \approx$ 2.1–2.2: specifically, Case 1 (mixed elasto-plastic, active sliding surface) yields FoS= 2.24, Case 2 (fully plastic, active sliding surface) yields FoS= 2.06, and Case 3 (fully plastic, no predefined sliding surface) yields FoS= 2.17–2.21. Case 4, in which the rock mass remains elastic and plasticity is restricted exclusively to the interface elements, yields FoS= 4.50, an order of magnitude increase in stability relative to Cases 1–3, with no continuous failure band developing across the domain. This sharp contrast between Case 4 and Cases 1–3 confirms that interface plasticity alone is insufficient to drive instability and that bulk yielding of the rock continuum is an essential component of the failure mechanism.

For Cases 1 and 2, displacement contours highlight a strongly localized deforming domain bounded by the structural network, with displacement vectors indicating a translational movement direction geometrically compatible with the observed release. Plastic strain concentrates along a narrow band coinciding with the imposed sliding surface, connecting the back-fracture release region to the slope toe. The most diagnostically significant result emerges from Case 3, in which no predefined sliding

surface is specified. Without any kinematic constraint imposed, plastic strain spontaneously localizes along the exact structural band observed in post-event LiDAR data, a band whose orientation (290–310°/45–55°) was independently mapped from point-cloud analysis and was not used as input to the mechanical model.

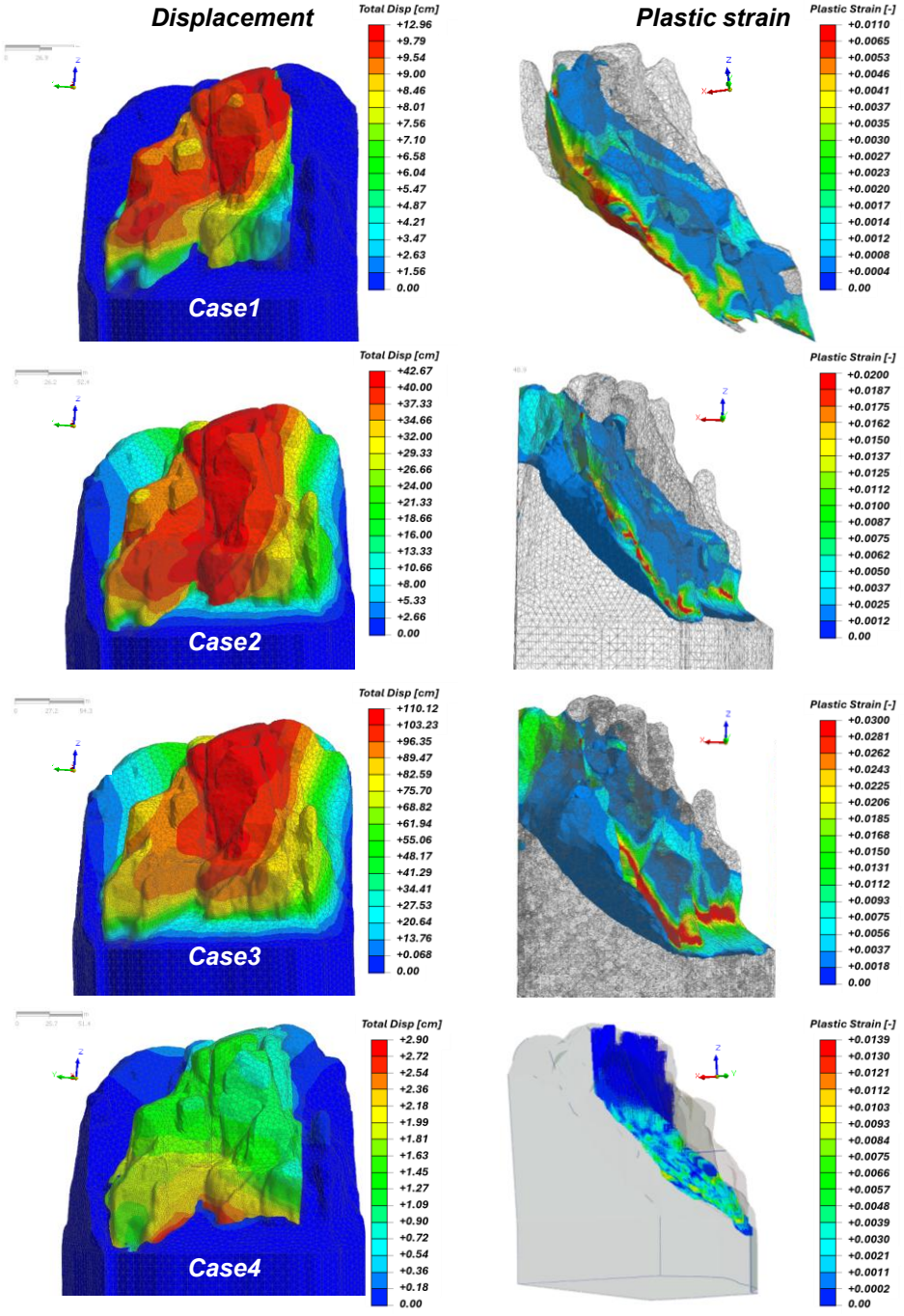


Figure 63 FEM-SRM results for the four geomechanical scenarios. Left column: total displacement magnitude (m); right column: equivalent plastic strain for Cases 1–3 and interface normal relative displacement for Case 4. Case 1 (mixed elasto-plastic, active sliding surface; FoS = 2.24): displacements localized in the summit block, plastic strain confined to the imposed sliding

surface. Case 2 (fully plastic, active sliding surface; FoS = 2.06): broader displacement field with distributed yielding geometrically consistent with the observed failure plane. Case 3 (fully plastic, no sliding surface; FoS = 2.17–2.21): plastic strain localizes spontaneously along the same band as Cases 1–2, confirming that the failure plane is an emergent structural feature independent of any predefined kinematic constraint. Case 4 (elastic rock mass, plastic interfaces only; FoS = 4.50): displacements reduced by an order of magnitude with no continuous failure band, demonstrating that bulk yielding is essential to drive instability; interface slip alone is insufficient.

This emergent failure plane, arising purely from the internal stress-strain response of the massif under plausible ice-bearing interface conditions, confirms that the detachment niche was an inherent structural weakness of the rock mass geometry. Case 4 produces displacements reduced by an order of magnitude with no continuous failure band, reinforcing the conclusion that bulk yielding is essential to reproduce the observed instability. Applying the SRM reduction factor of approximately 2.1 to the interface parameters pre-reduced by 0.7 for ice-bearing conditions yields effective operational strengths at failure of $c_{eff} \approx$ 143 kPa and $\varphi_{eff} \approx$ 14°.

Kinematic interpretation and emergent failure plane. The kinematic analysis across scenarios provides the most diagnostically significant result of the mechanical modelling. For Case 2 (fully plastic with predefined sliding surface), displacement contours highlight a strongly localized deforming domain bounded by the structural network. Displacement vectors indicate a translational movement direction fully compatible with the observed release geometry, and plastic strain concentrates along a narrow band coinciding with the imposed sliding surface, connecting the back-fracture release region to the slope toe.

The decisive validation emerges from Case 3, in which no predefined sliding surface is specified, and the rock mass deforms freely under the combined effect of gravity, structural anisotropy, and progressive shear strength reduction. Without any kinematic constraint imposed, plastic strain spontaneously localizes along the exact structural band observed in post-event LiDAR data, a band whose orientation (290–310°/45–55°) was independently mapped from point-cloud analysis and not used as input to the mechanical model. The near-identical spatial distributions of plastic strain in Cases 2 and 3 confirm that the mapped post-event sliding surface is mechanically consistent with the true internal stress-strain response of the massif under plausible ice-bearing conditions. This emergent failure plane demonstrates that the detachment niche was an inherent structural weakness governed by the real geometry and structural fabric of the rock mass, not by

modelling assumptions. The real-world geometry of the ice-rock contact along this surface is highly irregular, unlike the simplified planar joints of laboratory specimens, the natural interface is subjected to complex mixed-mode stresses (shear and tension) depending on local roughness and fracture aperture variability. This structural complexity implies that strength loss is spatially patchy and progressive, consistent with the observation that the July precursory event eliminated the kinematic toe buttress and redistributed stress onto the remaining thermally degraded ice bridges in the upper slope before the main August collapse.

5.6 **Discussion**

5.6.1 *Mechanics of Thermal Preconditioning and Hydrological Triggering*

The central result of this chapter is not merely the reconstruction of the Cima Falkner collapse, but the identification and resolution of a fundamental structural limitation in permafrost rockwall modelling. By isolating the precipitation variable through the 0-mm control run, it has been demonstrated that while long-term climatic warming is the ultimate cause of instability, it acts primarily as an invisible preconditioning agent. Continuous models capture this preconditioning as pure conductive thermal fatigue: the warming of interstitial ice toward 0 °C drastically reduces its shear strength, creating a seasonal window of vulnerability even without significant volumetric ice loss. However, these models fail to predict failure timing because they structurally exclude the proximate trigger. In nature, the final collapse is dictated by episodic hydromechanical shocks, transient hydrostatic overpressures delivered via marginal flow during extreme summer rainstorms. Resolving the calibration trap requires explicitly modelling this interplay. A mountain does not collapse because its ice slowly melts away, but because accumulated thermal degradation leaves it defenseless against the non-linear, quadratic hydrostatic forces generated by ordinary fluid infiltration extremes.

This dynamic perfectly explains the observed failure chronology. The rock mass withstood the 30-year maximum rainfall events of 2012 and 2014 because the deep ice anchor retained sufficient thermal resilience and shear strength to resist extreme hydrostatic loading. A decade later, however, the system mechanical threshold had been so severely degraded that a sub-maximal hydrostatic pulse, during the fourth wettest July in the 35-year meteorological record, was sufficient to trigger the final collapse. The

episodic, event-driven hydrological generator avoids the calibration trap by capturing the true episodic nature of fluid infiltration and drainage. Between discrete events, the fracture is allowed to drain, temporarily restoring effective stress and allowing the system to survive the transient hydrostatic shocks of 2023 and 2024. The model accurately simulates this hydromechanical load partitioning alongside the constitutive decay laws governing ice-rock interface strength (Krautblatter et al., 2013; Mamot et al., 2018; Mamot et al., 2021), successfully reproducing the August 2025 failure using strictly conservative, uncalibrated geotechnical parameters, the pure residual friction angle of cold dolomitic rock joints (φ_{res} = 41.0°) with zero cohesion. This demonstrates that failure emerges from the thermodynamic and poro-elastic physics of the system rather than from parameter overturning.

The required strength reduction identified by the 3D FEM analysis, yielding a pre-collapse $FoS$of approximately 2.1 in Cases 1–3, is not evidence of baseline model inaccuracy. Rather, it quantifies the state of thermal degradation that must have been reached by the time of collapse: the operative in-situ shear strength was approximately 45–50% of standard deeply frozen values. This is fully consistent with experimental evidence showing that ice-rock adhesive strength does not decrease linearly but drops precipitously by 50–60% as temperatures rise into the critical −2 °C to −0.5 °C window (Davies et al., 2001; Krautblatter et al., 2013; Mamot et al., 2018). The effective interface parameters at failure (c_{eff}≈ 143 kPa and φ_{eff}≈ 14°) fall squarely within the experimentally documented range for rock-ice interfaces in the transitional thermal regime, as detailed in Table 10.

Table 10 Comparison of SRM-reduced interface parameters at failure with literature values for ice-filled rock discontinuities.

Source / regime	c (kPa)	φ (°)	Notes
This study — SRM failure (Cases 1–3)	143	14	$c_{eff}$and φ_{eff}after double reduction (0.7 pre-factor × FoS≈ 2.1)
transitional regime (−5°C to −1°C)	100–400	10–20	Direct shear tests on ice-filled rock joints (Davies et al., 2001; Krautblatter et al., 2013)
transitional regime	100–400	10–20	Rock-ice-mechanical model validated against laboratory data

			(Mamot et al., 2018; Mamot et al., 2021)
dirty/partially thawed ice	50–200	12–25	Ice-rich frozen soils near 0 °C (Arenson & Springman, 2005)
melting regime (> −1°C)	0–50	5–10	Lubricated sliding; polycrystalline ice approaching 0 °C (Schulson & Duval, 2009)
temperature- and stress-controlled	Varies	Varies	Failure criterion combining thermal and mechanical controls (Mamot et al., 2018; Mamot et al., 2021)

Furthermore, the real-world geometry of ice-rock contact is highly irregular. Unlike simplified planar joints, the natural interface is subjected to complex mixed-mode stresses (shear and tension) depending on local roughness and fracture aperture variability. This structural complexity implies that strength loss is spatially patchy and progressive. The July 27 precursory event, which mobilized approximately 36,000 m³ from the summit immediately following the pronounced July 2025 rainfall pulse, likely eliminated the kinematic toe buttress, instantly redistributing stress onto the remaining thermally degraded ice bridges in the upper slope. The loss of this first block was therefore not merely a warning sign, but an active mechanical preparatory factor for the main August collapse.

5.6.2 *From Cold-trapping to Advective Bypass*

A highly counterintuitive result of the simulation is that the morphological evolution of $h_{ice}(t)$is nearly independent of the hydrological forcing regime. Contrary to previous assumptions, the advective sensible heat delivered by infiltrating water is thermodynamically dwarfed by the massive latent heat of fusion (L = 334 kJ kg^{-1}) required to ablate the ice column. The geometry of $h_{ice}(t)$is therefore governed almost exclusively by long-term conductive rock warming in both continuous and episodic models. This explains why the deep ice anchor is preserved up to the moment of collapse, a result directly validated by the post-event documentation of the surviving ice candle at 8–10 m depth. However, while the ice candle morphology converges between the two models, they diverge radically in their mechanical response to water.

Early in the simulation (1940–1990), the fracture is thermally isolated: infiltrating meltwater encounters deeply supercooled rock and refreezes. This episodic cold-trapping is a self-amplifying feedback that sustains the structural ice candle and shields the basal plane from fluid pressures. As the baseline permafrost temperature warms into the transitional regime (−5 °C to −1 °C), however, this cold-trapping capacity is irreversibly exhausted. The episodic model reveals that water then transitions from a stabilizing agent, winter refreeze, to a highly destructive mechanical force. Instead of melting the anchor, extreme wet years, culminating in the record-breaking annual rainfall of 2025 (2,037 mm), drive massive volumes of water through progressively widening fractures. This bypass flow rapidly pressurizes the deep fracture, generating the fatal hydrostatic spikes ($U(t)$and $V(t)$forces) responsible for the collapse. This two-phase hydrological evolution, from cold-trapping stabilizer to advective bypass destabilizer, represents a fundamental regime shift in the behaviour of the fractured rock mass that continuous models are structurally incapable of representing.

5.6.3 *The Seasonal Heartbeat and Precursory Kinematics*

The transient nature of the failure mechanism has profound implications for hazard monitoring. In the final approach to failure (2015–2025), the system enters a seasonal heartbeat regime where $FoS(t)$oscillates across the critical threshold. While the continuous model experiences a premature and definitive FoSdrop below unity in 2018 due to uninterrupted thermal degradation of ice strength, the episodic model survives until 2024–2025. This survival is dictated by the rapid dissipation of transient pore-pressures: after each discrete hydromechanical shock, the drainage or refreezing of the marginal water instantly restores effective stress, allowing stability to temporarily recover. The InSAR-derived kinematic acceleration from late 2020 is the geodetic signature of this critical transition, the exact point at which cumulative thermal damage and kinematic fracture widening began to outpace the winter refreeze capacity. As strain rates accelerated, reaching 3.5 mm day^{-1} and culminating in 2.0–2.5 m of pre-failure fracture aperture, the record precipitation of 2024 acted as a severe late-stage fatigue cycle. Consequently, the August 2025 rainstorm triggered a brittle-like catastrophic rupture.

This highlights a critical monitoring blind-spot: snapshot observations and static stability analyses cannot detect a system oscillating close to failure. The episodic $FoS(t)$trajectory transiently approaches but does not irreversibly cross unity during 2023

and 2024, meaning that any static stability assessment performed during these years would have incorrectly concluded that the system was safe. Early warning requires time-continuous frameworks capable of tracking the exhaustion of winter recovery capacity and the progressive shortening of the stable recovery window between successive hydromechanical shocks

5.6.4 *FEM vs. 1D: Complementary Roles and the Decoupling of Forcings*

When comparing the one-dimensional analytical and three-dimensional FEM results, key methodological distinctions and complementarities emerge. The FEM models provide highly detailed spatial visualization of internal stress distribution and strain localization, enabling the spontaneous emergence of the failure plane and the quantification of the required strength reduction. The one-dimensional analytical approach offers the computational efficiency required to directly couple complex thermal-decay functions with episodic hydrological transients over nearly a century, a combination that would be computationally prohibitive in a three-dimensional framework.

A critical thermal discrepancy emerges when comparing the depth profiles of the two approaches. In the one-dimensional model, deep permafrost temperatures stabilize around a minimum of approximately −4 °C, whereas the three-dimensional FEFLOW model records warmer basal temperatures near −2.5 °C. This difference is a direct consequence of geometry: the one-dimensional model assumes an infinite half-space dominated by purely vertical conduction, whereas the three-dimensional model captures multi-directional heat ingress from the exposed rockwalls, reflecting the lateral warming typical of complex ridge morphologies such as Cima Falkner (Noetzli & Gruber, 2009; Noetzli et al., 2007).

Far from invalidating the coupled analysis, this geometric limitation renders the one-dimensional model highly conservative. Ice at −4 °C possesses significantly higher shear and tensile strength than ice at −2.5 °C, which sits closer to the phase transition (Krautblatter et al., 2013; Mamot et al., 2021). Furthermore, a colder modelled rock substrate maximizes the thermal potential for winter cold-trapping, promoting faster and more voluminous refreezing of infiltrating water than would occur in three-dimensional reality. The one-dimensional model also neglects the substantial latent heat released into the surrounding rock mass when infiltrating water freezes, a feedback that would

progressively warm the fracture walls and accelerate thermal degradation of the ice anchor in reality. The one-dimensional framework therefore systematically overestimates both the baseline cohesion of the residual ice anchor and its capacity for seasonal self-healing. The fact that $FoS(t)$drops definitively below unity in August 2025 due to transient hydrostatic pulses, despite these artificially resilient baseline conditions, provides robust and unequivocal evidence of marginal bypass flow as the primary triggering mechanism.

5.6.5 *Regional Validation of the Thermal Regime: Independent Air- and Ground-Temperature Evidence*

The FEFLOW thermal model presented in section 5.4.3 and section 5.5.3 indicates a rupture surface persistently confined within a narrow sub-zero window in the years preceding collapse. Because this result underpins the interpretation of a frozen, ice-bonded failure plane at the time of collapse, it is worth testing independently against measured, rather than modelled, thermal data from comparable high-elevation sites in the same geological and climatic setting.

Two long-term air-temperature stations in the Brenta Dolomites, the same massif as Cima Falkner, provide a first independent constraint: Grostè (2,258 m) and Rifugio Alimonta (2,577 m), with daily records spanning 2007–2024. Their climatological mean annual air temperatures (MAAT) are +2.1 °C and +0.7 °C respectively; the Alimonta record required correction for a pronounced winter-biased data gap (17.6 % missing days overall, concentrated in December–January), which a naive daily average would otherwise render anomalously warm. The two co-located stations also provide a direct measurement of the local lapse rate, 0.43–0.53 °C per 100 m, already adopted in the surface boundary condition of section 5.4.3 in place of a coarser regional value. Extrapolating the Alimonta MAAT to the elevation of the Cima Falkner failure zone (2,850–2,999 m) with this local lapse rate yields a warm-bound estimate of −1.1 to −1.5 °C. A second, fully independent station, the Piz Pisciadù automatic weather station (2,985 m, Sella Dolomites), sits at almost exactly the failure elevation and records a measured MAAT of −2.8 °C, providing a cold-bound estimate. Cima Falkner, a ridge combining sheltered and exposed faces, is expected to fall between these two bounds. Set against four confirmed-permafrost boreholes reported in the regional literature, Zugspitze (−4.5 °C, 2,962 m; Weber et al., 2016), Stelvio (−3.7 °C, 3,000 m; GTN-P), Piz Pisciadù (−2.8

°C, 2,985 m) and Piz Boè (≈−1.5 °C, 2,905 m, the same Dolomia Principale lithology as Cima Falkner), the estimated Cima Falkner MAAT falls within the envelope of every one of these sites, at the warm end alongside the lithologically identical Piz Boè record (Figure 64).

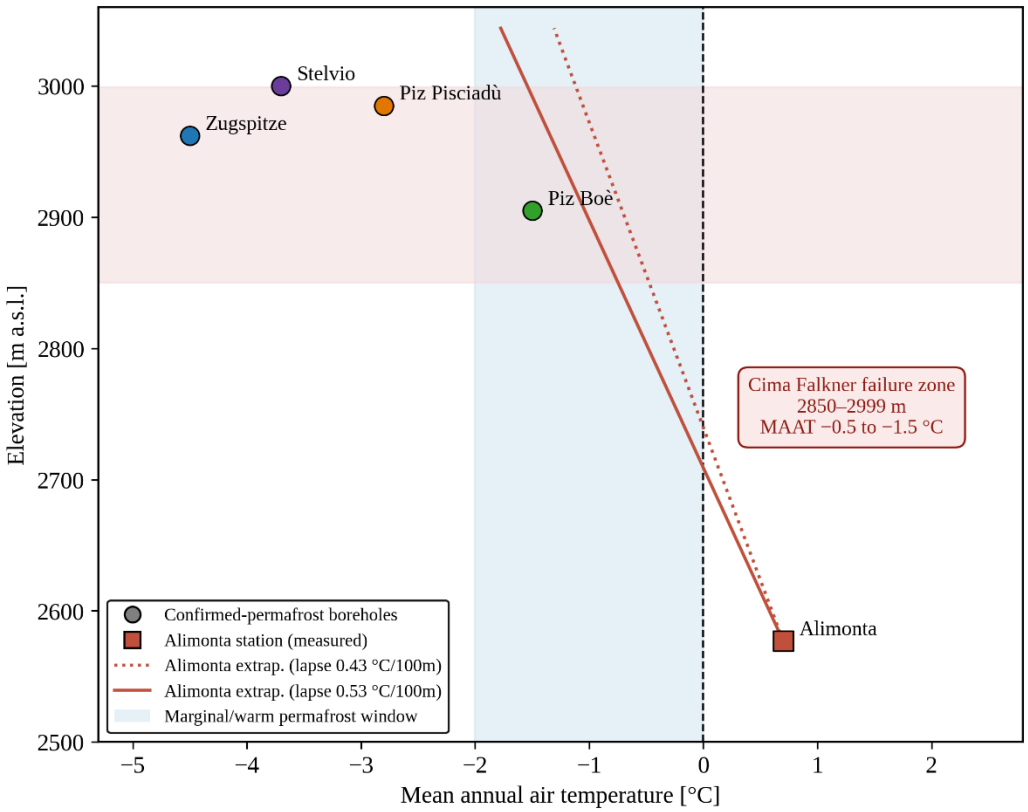


Figure 64 Mean annual air temperature (MAAT) of four confirmed-permafrost Alpine boreholes (Zugspitze, Stelvio, Piz Pisciadù, Piz Boè) plotted against elevation, together with the two Brenta Dolomites stations (Grostè massif) used for extrapolation to the Cima Falkner failure zone. The solid and dotted red lines show the Alimonta MAAT projected upward using the locally measured lapse-rate range (0.43–0.53 °C per 100 m); the shaded blue band marks the marginal/warm-permafrost window (MAAT between −2 and 0 °C). The Cima Falkner failure zone (2,850–2,999 m) falls within the MAAT envelope of all four boreholes, at the warm end alongside the lithologically identical Piz Boè record.

This regional comparison is reinforced by the borehole network of Noetzli et al., 2024, which reports deep ground temperatures close to the depth of zero annual amplitude, and therefore closely approximating the true permafrost state, at all four sites over 12–24-year records. All four boreholes remain sub-zero at depth, with a modest warming trend of 0.2–0.45 °C per decade. Normalised to the Cima Falkner summit elevation using the locally measured lapse rate, the deep ground temperatures of these analogue sites bracket −0.5 to −1.5 °C at approximately 20 m depth, again with the same-lithology Piz Boè

record at the warm end. A further point emerges from the Zugspitze north–south borehole pair: despite a marked contrast in surface aspect, the two boreholes differ by only ~0.2 °C at 20 m depth, indicating that at failure-relevant depths the deep thermal state, rather than the surface insolation contrast, is the governing factor, and that both aspects remain firmly sub-zero.

The strongest single line of independent evidence comes from direct field measurement rather than regional extrapolation. A 16-level thermistor chain, recording hourly since August 2023 at depths of 0.23–18.48 m, is installed at a north-facing site at Pisciadù (~2,750 m, below the Cima Falkner failure elevation but within the same lithology and fracture system also intersected by the site instrumentation referenced in section 5.5.3). This chain provides a complete, measured permafrost thermal profile: rock temperature remains continuously sub-zero from the surface to approximately 12–13 m, with a coldest mean annual ground temperature of −0.43 °C recorded at 3.5 m depth and a zero-annual-amplitude depth of approximately 14 m; the inferred permafrost base coincides with ice encountered during drilling at this depth (Figure 35 in Chapter 4). Below approximately 11 m, the profile is diagnostically non-monotonic, warming with depth from −0.19 °C at 11.5 m to +0.08 °C at 14.5 m and +0.49 °C at 18.5 m, a reversal that pure conduction cannot reproduce and that is instead consistent with advective heat input through fractures, independently supporting the role attributed to fracture-hosted advection in the conceptual framework of section 5.4.2. Combining the measured near-surface temperature (−0.06 °C at 0.23 m) with the screened local MAAT (≈−1.6 °C, from the Piz Pisciadù record lapsed to the Pisciadù site elevation) yields a measured surface offset of approximately +1.5 °C, directly supporting the domain-wide thermal offset ΔT_{mean} adopted in the FEFLOW surface boundary condition (section 5.4.3).

An additional, independent physical constraint is provided by the post-collapse persistence of massive ice within the rupture surface itself. The most prominent surviving ice mass, in the rear tension crack, has remained intact through at least the full 2025–2026 annual cycle. A simple surface energy balance shows that even a modest, shaded summer melt rate would be sufficient to remove a body of this thickness within two to three years; its multi-year survival is therefore incompatible with a seasonally melting, near-0 °C crack, and instead requires sublimation-dominated ablation under a permanently sub-zero thermal regime, consistent with the −1 to −1.5 °C mean annual ground temperature independently derived above.

Taken together, these four independent lines of evidence, regional air-temperature extrapolation, comparison with published permafrost boreholes of comparable elevation and lithology, a directly measured ground-temperature profile at a nearby site, and the physical constraint imposed by the surviving ice itself, converge on a consistent interpretation: the Cima Falkner failure zone occupied a marginal, warm-permafrost thermal regime in the years preceding collapse. This independent, measurement-based validation is consistent with, and lends external support to, the thermal state reproduced by the FEFLOW model in section 5.5.

This measured thermal range has a direct mechanical implication. Applying the same temperature-dependent adhesion law introduced in section 5.4.2, $\tau(T) = \tau_{max}\,(1 - e^{(kT)})$, to the block geometry established in section 5.4.4 (basal plane at 42°, residual friction angle 41°), the dry factor of safety on friction alone is 0.965, marginally unstable, so that limit equilibrium requires the ice bond across the rear tension crack to supply a mean resistance of approximately 172–241 kPa. Resolving this resistance into its kinematic components (approximately 53 % opening, Mode I, and 47 % shear, Mode II, consistent with the crack geometry) and evaluating the constitutive law over the measured temperature range of section 5.6.5 yields a mixed-mode bond capacity of approximately 190 kPa at −2.8 °C, 120 kPa at −1.5 °C, and 90 kPa at −1.1 °C. The required resistance is therefore met only at the cold end of the measured bracket and falls below the stability threshold as the interface warms across the −1.5 to −1.1 °C window, precisely the mean annual temperature range independently established for the failure zone above. This convergence, obtained without parameter tuning, indicates that the thermal state reconstructed from independent regional and borehole evidence coincides closely with the threshold at which the ice-rock interface ceases to mechanically stabilize the block.

5.6.6 *Regional Implications in a Warming Cryosphere*

The failure mechanism described here, slow thermal preconditioning unlocking episodic hydromechanical failure, is not unique to Cima Falkner. It is physically expected wherever ice-filled discontinuities occupy the transitional thermal regime (−5 °C to −1 °C). However, the timing of this critical transition is heavily modulated by topographic factors, primarily slope aspect. Because ice ablation in the model is dominated by conduction rather than fluid advection, the survival of the ice anchor is strictly tied to the surface energy balance. South- and west-facing rockwalls, subjected to intense daily

insolation, accumulate conductive heat and exhaust deep fracture ice far faster than shaded north-facing faces. Consequently, highly sun-exposed slopes will cross the marginal-flow threshold decades earlier than shaded counterparts, precisely the zone that Alpine permafrost rockwalls are entering as atmospheric warming drives the 0 °C isotherm progressively deeper (Magnin et al., 2015; Noetzli et al., 2024).

The regional inventory context underscores the urgency of this reframing (Figure 48). Large-volume failures (>10^5 m³) in the Dolomites have appeared almost exclusively above 2,900–3,100 m a.s.l. since 2015 (Bonometti et al., 2026). Under the RCP 4.5, 6.5 and 8.5 emission scenarios, the continuous permafrost belt of the Eastern Alps, currently spanning approximately 2,400–3,500 m a.s.l., will experience progressive warming throughout this century, systematically driving vast rockwall areas across the geomechanical threshold identified here. The strength of the episodic thermo-hydromechanical framework lies in its ability to explicitly couple these long-term conductive trajectories with short-term poro-elastic shocks, completely bypassing the empirical calibration trap. The Cima Falkner event is therefore not a local anomaly but an early signal of a regime shift in Alpine mass waste that demands the adoption of coupled episodic thermo-mechanical paradigms to anticipate future catastrophic collapses. Effective hazard management in the warming cryosphere requires a paradigm shift: snapshot stability analyses must be replaced by time-continuous frameworks capable of tracking the exhaustion of the rock mass thermal memory and its vulnerability to ordinary meteorological extremes.

5.6.7 *Model Limitations and position in literature*

The episodic thermo-hydromechanical framework presented in this chapter couples four processes that have typically been addressed separately in the literature: (i) seasonal ice formation controlled by latent heat exchange and cold trapping; (ii) long-term conductive ice ablation driven by a physically realistic secular warming trend; (iii) fracture aperture evolution linked to kinematic pre-failure widening; and (iv) a time-continuous $FoS(t)$trajectory derived from a temperature-dependent constitutive law subjected to episodic hydrostatic shocks. The mathematical formalization of the marginal bypass flow mechanism, demonstrating that extreme precipitation acts as a transient, non-linear mechanical force rather than a thermal agent, is what distinguishes this framework from previous approaches and allows the identification of a specific failure window that

emerges organically from uncalibrated physics rather than being prescribed. It also successfully captures the seasonal heartbeat of $FoS(t)$, featuring transient threshold exceedances in 2023–2024 followed by effective-stress winter recovery, a critical precursory dynamic entirely unobtainable from steady-state or snapshot analyses.

Despite these strengths, four limitations must be acknowledged. First, the one-dimensional geometry neglects lateral heat flow and three-dimensional fracture network connectivity, resulting in colder basal rock temperatures (~−4 °C) compared to the three-dimensional FEFLOW model (~−2 °C). As discussed in Section 5.6.4, this limitation renders the findings intrinsically conservative, as the colder one-dimensional permafrost implies artificially higher baseline ice strength and maximized winter cold-trapping capacity, meaning the episodic model resolves the correct failure date even under these artificially resilient conditions. Second, the cubic aperture growth law ($W \propto t^3$) is a kinematic prescription rather than a rheologically grounded relationship; calibration against the most recent InSAR displacement rates would strengthen this assumption. Third, pore pressure is applied only within the fracture, neglecting matrix suction and pressure diffusion into the surrounding rock mass. Fourth, spatial variability of ice thickness along the fracture plane and irregular fracture geometry are not accounted for. Despite these simplifications, the model reproduces the observed failure timing and is fully consistent with the independent thermal and mechanical constraints provided by the FEFLOW and MIDAS FEA three-dimensional simulations.

Positioning the present framework within the existing literature is useful along four points of contact: the constitutive foundations for ice-rock interface strength, the role of advective heat transport, the qualitative precedents available from comparable Alpine case studies, and direct field evidence for the proposed pressurization mechanism.

Constitutive foundations: Krautblatter et al. (2013) and Mamot et al. (2021). Krautblatter et al. (2013) established the temperature-dependent failure criterion underlying this study: the adhesive shear strength of ice-filled rock joints decays exponentially as temperatures rise from about −10 °C toward 0 °C, with reductions of roughly 60–78% across the critical −2 °C to −0.5 °C window. Mamot et al. (2018, 2021) extended this relationship to slope scale through three-dimensional back-analyses, showing that the resulting effective mechanical parameters are consistent with documented Alpine rockslide factors of safety. The present framework builds on this constitutive basis in three respects. First, the temperature-dependent rheology is coupled

here to a time-evolving ice volume governed by an explicit latent-heat budget, so that cold-trapping sustains the structural ice anchor and avoids the premature exhaustion of ice strength that affects continuous-forcing implementations of the same constitutive law. Second, the marginal bypass flow mechanism separates two physically distinct roles that infiltrating water can play, a stabilizing thermal role while the rock remains well below 0 °C, and a destabilizing hydrostatic role once cold-trapping capacity is exhausted, roles that earlier formulations left conflated or unmodelled. Third, because the August 2025 failure timing is reproduced here using strictly uncalibrated, laboratory-derived parameters, the calibration trap emerges not as an unavoidable property of the underlying physics but as a structural artefact of conflating processes that operate on fundamentally different timescales. In this sense, the Cima Falkner case confirms at the event and decadal simulation scale what Krautblatter et al. (2013) and Mamot et al. (2021) established at the material and cross-sectional scale: it is the brittle adhesive failure of ice-rock interfaces, rather than bulk ice ablation or creep, that governs catastrophic permafrost rockwall collapse. A further distinction concerns the representation of temperature itself: whereas Mamot et al. (2021) imposed discrete thermal zones within a UDEC mechanical framework, the one-dimensional formulation adopted here computes rock-mass temperature as a continuous analytical function of depth and time over an 85-year trajectory, allowing the progressive deepening of the critical thermal regime to be captured rather than evaluated only at a small number of predefined states.

Advective heat transport: Hasler et al. (2011) showed experimentally that advective heat transport through open clefts can warm fracture surfaces considerably faster than conduction alone. The thermal scenarios B and C developed in this chapter operationalize this process at slope scale: convective boundary conditions at deep and mid-depth fractures drive sliding-surface temperatures transiently into the −5 °C to −1 °C regime during the anomalously wet summers of 2023 and 2024, a response that is entirely absent from the conductive baseline. Where Hasler et al. (2011) characterised advective transport mainly in terms of time-averaged throughput, the precipitation record analyzed here highlights its episodic character instead: the dominant advective events occur as discrete, high-intensity storms during which large volumes of comparatively warm water briefly penetrate the partially ice-obstructed fracture network. The latent-heat budget underlying the one-dimensional model (Section 5.5.1) shows that even during these events the sensible heat carried by infiltrating water remains thermodynamically

negligible relative to the latent heat required to ablate the ice anchor: water does not melt the anchor away, it pressurizes the fracture instead, a distinction that no continuous-forcing formulation is able to capture.

From qualitative analogy to a quantitative process model: the Piz Cengalo and Matterhorn precedents. Walter et al. (2020) documented the 2017 Piz Cengalo rock-ice avalanche, identifying a multi-year kinematic precursory phase and post-event structural ice within the detachment niche, and attributing the collapse qualitatively to long-term thermal priming followed by a late-summer meteorological trigger. Weber et al. (2025) similarly tracked the progressive destabilization of a Matterhorn rock pillar over a decade of continuous monitoring under secular warming. Both studies provide valuable observational precedents, but neither formalizes a quantitative process model linking the decadal thermal trajectory to an episodic precipitation trigger, nor explicitly resolves the calibration trap. The physical scenario they invoke qualitatively, a thermally preconditioned rock mass whose seasonal recovery of effective stress is progressively exhausted until a sub-maximal hydrological pulse delivers the decisive hydrostatic shock is precisely what the framework developed in this chapter reproduces quantitatively for Cima Falkner, narrowing the gap between qualitative inference and transferable predictive modelling.

Field evidence for pressurized fracture flow. The central physical assumption underlying the marginal bypass flow mechanism, that transient hydrostatic overpressures can develop within partially ice-filled fractures during intense precipitation events, because partial ice fill obstructs drainage enough to sustain elevated hydraulic heads on storm timescales, has received direct field validation in comparable permafrost rock-slope settings. Offer et al. (2025) documented pressurized water flow in fractured permafrost at the Zugspitze using simultaneous borehole temperature, electrical resistivity tomography and piezometric records, showing that hydraulic heads in partially ice-filled fractures can transiently approach values consistent with near-complete fracture filling during rainfall events, closely matching the maximum transient fill fraction (0.60) and triangular basal pressure distribution adopted in the present model. Scandroglio et al. (2024) extended this through a decade-long hydraulic head record at the same site, showing that water storage and outflow in degrading permafrost rock slopes are fundamentally episodic and become progressively amplified as ice content decreases: as hydraulic connectivity increases but instantaneous storage capacity falls, peak hydraulic heads during individual storms grow

correspondingly, an exact hydraulic analogue of the amplification mechanism formalized in this chapter. Taken together, these independent observations indicate that the hydraulic parameters adopted here represent conservative lower bounds relative to measured field values, and that pressurized fracture flow in degrading Alpine permafrost is a documented, rather than merely postulated, physical process. The present framework bridges these gaps by formalizing these conceptual elements into a quantitative, time-continuous simulation, providing what was previously missing in the literature: a strict mathematical decoupling of thermal and hydrological forcings that avoids the calibration trap and delivers a physically grounded explanation for the timing of catastrophic permafrost rockwall collapses.

5.7 **Case study conclusion**

This chapter presented the 2025 Cima Falkner rock avalanche as a large-scale natural laboratory for formalizing the physical mechanisms governing catastrophic permafrost rockwall failure, addressing Research Questions 3 and 4 through an integrated observational and modelling framework.

In response to Research Question 3, the analysis establishes that catastrophic permafrost rockwall failure is governed by the critical decoupling of slow thermal preconditioning and episodic hydromechanical shocks. Climate-driven thermal fatigue acts over decades as an invisible preconditioning agent, progressively degrading the shear resistance of ice-filled discontinuities and creating a slowly growing window of structural vulnerability, without, however, constituting the direct cause of failure. The proximate trigger is a discrete, episodic hydromechanical event: transient hydrostatic overpressures delivered via marginal bypass flow during intense rainstorms, which exploit the accumulated mechanical weakness to initiate the final collapse. The 0-mm precipitation control run provides mathematical proof of this decoupling: under purely thermal forcing, the simulated $FoS(t)$remains above unity throughout the entire simulation period, and theoretical failure is delayed by several years beyond the observed August 2025 event. The distinction between preconditioning and triggering is therefore not merely conceptual but quantitatively demonstrable, and its formal recognition resolves the calibration trap that has systematically affected back-analyses of permafrost rockwall failures in the existing literature.

In response to Research Question 4, the episodic one-dimensional limit-equilibrium framework demonstrates that physically realistic simulation of high-altitude instability requires the explicit representation of two coupled but temporally separated processes: the long-term conductive trajectory of ice-rock adhesive strength degradation, and the episodic poro-elastic recovery of effective stress between discrete hydrological shocks. Conventional continuous-forcing models, by conflating these processes, artificially impose a monotonic decline in baseline stability and force modellers into an empirical calibration trap. The episodic framework, by formalizing the marginal bypass flow mechanism and preserving the discrete nature of fluid pressurization, reproduces the exact timing of the 2025 collapse using strictly uncalibrated, laboratory-constrained parameters, without site-specific tuning. The three-dimensional FEM-SRM analysis provides independent structural corroboration: the spontaneous localization of plastic strain along the exact post-event failure band in Case 3, without any predefined sliding surface, confirms that the failure plane was an inherent structural weakness governed by the true stress-strain response of the rock mass under ice-bearing interface conditions.

Two results of broader scientific significance emerge from this chapter. First, complete volumetric ice ablation is not a prerequisite for collapse. Progressive heat penetration exponentially degrades ice-rock adhesion, creating a critical vulnerability window long before the structural ice anchor is destroyed, directly validated by the post-event documentation of a surviving ice candle 30/40 m high and 1.4–1.6 m thick at 8–10 m depth. Second, the seasonal heartbeat of $FoS(t)$, characterised by transient threshold crossings during the precipitation years of 2023–2024, followed by episodic effective-stress recovery and irreversible failure under a sub-maximal hydrostatic pulse in July 2025, is a detectable mechanical signature of the final approach to collapse. These dynamic highlights a critical monitoring blind-spot: snapshot observations and static stability analyses cannot detect a system oscillating close to failure. Time-continuous frameworks capable of tracking the exhaustion of winter recovery capacity are required for effective early warning.

The Cima Falkner event is not a local anomaly but an early signal of a regime shift in Alpine mass wasting. As atmospheric warming drives the 0 °C isotherm progressively deeper, vast rockwall areas across the Eastern Alps will systematically cross the geomechanical threshold identified here. The transferable episodic framework developed in this chapter provides the methodological foundation for this broader challenge. Its

application has been demonstrated here on a large, poorly instrumented rock avalanche, in deliberate contrast to the well-instrumented Sas da Lech pillar of Chapter 4, demonstrating that the approach does not depend on subsurface monitoring data and can be applied wherever independent geometric, thermal, and kinematic constraints are available. Chapter 6 broadens the scope of the thesis from natural rock-slope instability to the interaction between the thermal environment and engineered infrastructure, examining how human-made structures at high altitude modify the local permafrost regime.

Chapter 6
A Persistent Anthropogenic Heat Source In Cold Bedrocks: The Punta Helbronner Cable-Car Shaft

6.1 **Aim and case study**

This chapter investigates the Punta Helbronner cable-car station (Skyway), on the Mont Blanc massif at 3,488 m a.s.l., where a lined structural shaft and its foundation are excavated directly into permafrost-affected granite (Figure 65). The case broadens the scope of the thesis from the natural rock-slope instabilities examined in Chapters 3 to 5 to the interaction between engineered high-altitude infrastructure and the surrounding thermal regime, and it directly addresses Research Question 5 formulated in Chapter 1.

Research Question 5, concerning the influence and interaction between permafrost degradation and the presence of high-altitude infrastructure, is examined through a combination of multi-year rock- and shaft-temperature monitoring at different aspects, depths and distances from the structure, a regional permafrost-probability map used to frame the site within its broader cryospheric context, and two- and three-dimensional finite-element thermal simulations. Taken together, these approaches show that the shaft and foundation act as a persistent, non-negligible heat source, superimposed on and locally overwhelming the natural aspect-controlled thermal regime, and producing a positive-temperature anomaly that persists year-round in the rock mass immediately surrounding the infrastructure.



Figure 65 View from Est of Punta Helbronner with a cable car arrive at 3488m a.s.l.

6.2 **Study Area**

6.2.1 *Geological and geomorphological setting*

The investigated area belongs to the broader Helvetic–Ultra Helvetic domain of the External Alps, which reaches the Italian sector only marginally and is represented here by the Mont Blanc Massif. In the Aosta Valley, this domain comprises four distinct tectonic elements arranged from SE to NW and, structurally, from higher to lower position: the Ultra Helvetic cover nappes, the Mont Chétif Ultra Helvetic listric wedge, the Mont Fréty Nappe (Ultra Helvetic or Helvetic affinity), and the Helvetic basement unit of the Mont Blanc Massif (Gianotti et al., 2011). The upper Ultra Helvetic cover is formed by at least two detachment nappes, separated by the Mont Chétif wedge, and consists mainly of Middle–Upper Triassic and Lower Jurassic (Lower Lias) to Upper Jurassic (Malm) successions. The Mont Chétif listric wedge is composed predominantly of gneisses and mica-schists derived from granitic and rhyolitic protoliths, locally preserving magmatic parageneses and textures, with subordinate calcitic marbles that are better preserved toward the roof (southern sector) of the gneissic body (metaporphyroids). The wedge is also associated with a Liassic calcareous–arenaceous cover and is bounded at both base and top by Helvetic–Ultra Helvetic units including dark-grey schists, graphitic phyllites, calcschists, phyllitic calcschists, and marbles. The Mont Fréty Nappe, of Middle–Upper Jurassic age, overlies the Mont Blanc Massif in an overturned succession and is characterized by a calcareous–argillaceous series (Gianotti et al., 2011). The Mont Blanc basement unit consists chiefly of migmatitic gneisses, which crop out mainly in the western sector of the massif, and of metagranites intruded into the older gneissic complex; an Alpine metamorphic overprint is locally observed. Surficial deposits include recent alluvium on the valley floor, undifferentiated glacial deposits related to valley glaciers, active talus/scree accumulations, and regolithic or eluvio-glacial covers on the surrounding slopes (Von Raumer & Bussy, 2004). Structurally, the upper Aosta Valley intersects the regional tectonic grain at a high angle and terminates against the Mont Blanc Massif near Entrèves. From Entrèves, Val Veny and Val Ferret diverge with a NE–SW trend, broadly parallel to the SE margin of the Mont Blanc crystalline basement. This structural setting is mirrored by mylonitic and cataclastic belts along the southern flank of the Mont Blanc Massif, reflecting heterogeneous Alpine deformation within and along the margins of the crystalline rocks (Guermani & Pennacchioni, 1998;

Leloup et al., 2005). The morphology of Val Ferret and Val Veny (left and right tributaries of the Valdigne) is strongly conditioned by Late Pleistocene glacial evolution. In strict terms, the Last Glacial Maximum (LGM) is commonly placed at ~26.5–19 ka BP, followed by a sequence of Late-glacial readvances and stillstands up to the onset of the Holocene (~11.7 ka BP). At least four glacial pulses of decreasing magnitude have been recognized in the area, each associated with erosional deepening of variable intensity; field evidence suggests that the last two pulses played a major role in shaping the present valley trough. Ice-surface topography during peak glacial conditions in Val Veny and Val Ferret was reconstructed by Porter & Orombelli, (1982), who inferred an ice cover reaching maximum elevations of approximately 2600–2900 m a.s.l.

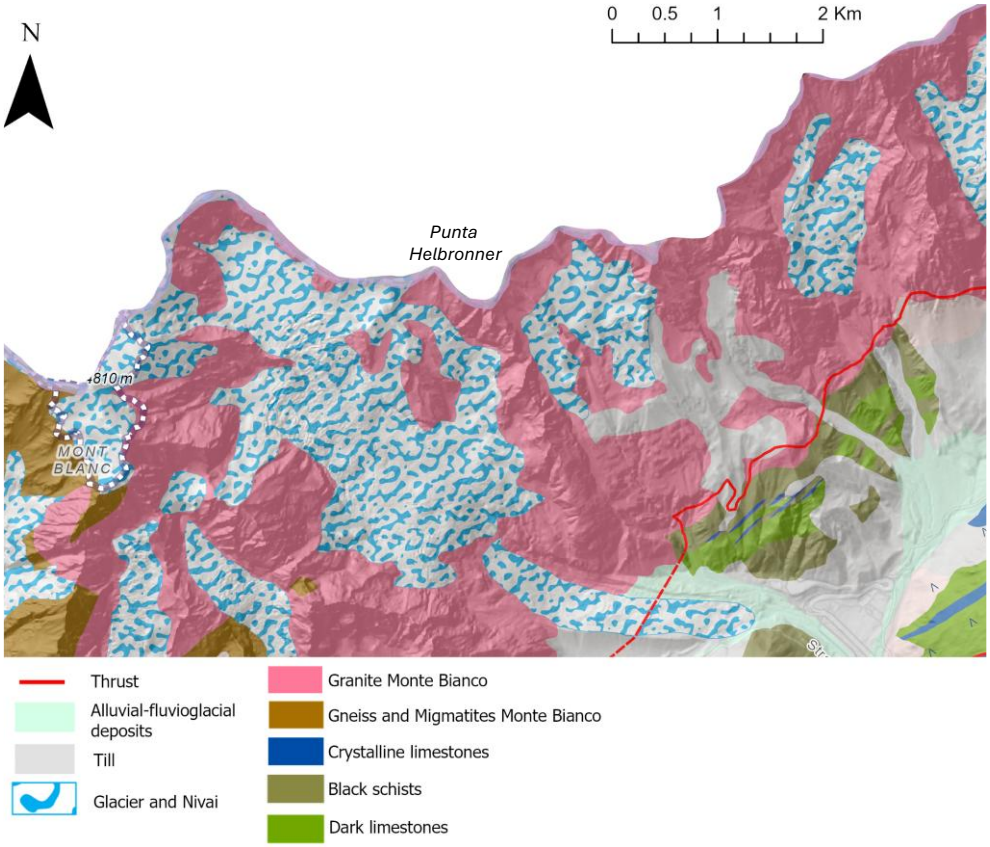


Figure 66 Geological Map of Monte Bianco area in which Punta Helbronner is located.

6.2.2 *Air Temperature and climate context*

The thermal forcing acting on the Punta Helbronner site was characterised using a daily air-temperature record from an automatic weather station located in the immediate vicinity of the monitoring borehole. The dataset spans 1 January 2008 to 7 March 2023, with a continuous, gap-free daily series retained for the period January 2008 to December 2022 (15 nearly years complete). This record provided both the climatological forcing (a repeated mean annual cycle) and the monthly forcing (real monthly means) used in the spin-up of the numerical simulations described in section 6.3.4.

Over the 15-year period, the mean annual air temperature was −5.18 °C, with a marked seasonal cycle: January is the coldest month on average (−11.9 °C), while August is the warmest (+2.9 °C). The coldest daily value on record was −27.4 °C (27 February 2018) and the warmest was +13.4 °C (26 June 2019); on average, 273 days per year (range 246–306) recorded sub-zero air temperatures (Figure 67).

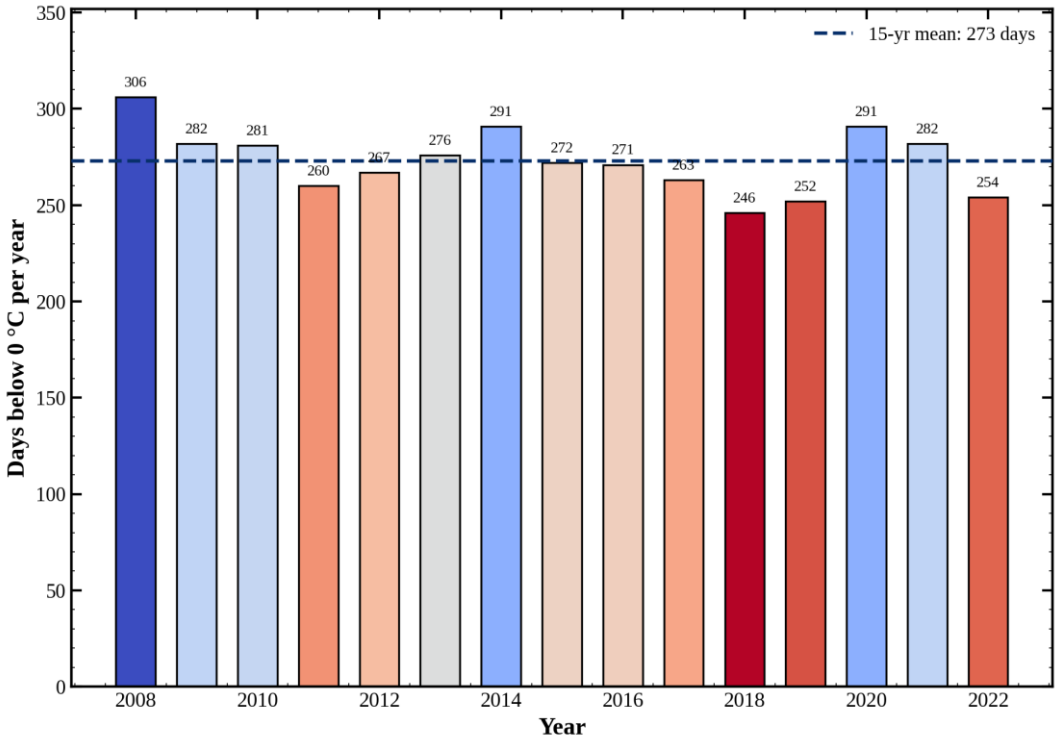


Figure 67 Number of days per year with sub-zero daily air temperature at Punta Helbronner (2008–2023), colour-graded relative to the 15-year reference mean (273 days/year).

This thermal regime places the site well within a cold, permafrost-favorable climatic envelope, markedly colder and less marginal than warm-permafrost sites such as the Sas da Lech pillar discussed in Chapter 4.

A linear regression on the annual mean air temperature over the full record indicates a warming trend of +0.68 °C/decade, but this trend is not statistically significant ($R^2 = 0.17$, $p = 0.13$); the number of sub-zero days per year decreases by 16.2 days/decade over the same period, also not significant ($p = 0.10$). Splitting the record into three consecutive five-year periods shows a similar picture: the annual mean rises from −5.58 °C (2008–2012) to −4.94 °C (2013–2017) but then remains essentially stable at −5.01 °C (2018–2022) rather than continuing to increase (Figure 68). A one-way ANOVA across the three periods ($F = 1.16$, $p = 0.35$) and a direct t-test between the first and last periods ($\Delta = +0.58$ °C, $p = 0.27$) both confirm that these differences are not statistically significant.

The magnitude of the trend is nonetheless consistent with regional estimates for the Aosta Valley and the wider Alps: air-temperature records from weather stations between 1500 and 3500 m a.s.l. show warming rates of 0.3–0.9 °C/decade (Nigrelli & Chiarle, 2023, in Pogliotti et al., 2023), and the on-site automatic weather station at Cime Bianche (3,100 m a.s.l., about 30 km from Punta Helbronner) records a trend of 1 °C/decade over 2007–2022 (Pogliotti et al., 2023). The same regional dataset shows that, even with continuous records of comparable or greater length, warming trends on more exposed, higher-variability rock-surface series can fail to reach statistical significance ($p > 0.05$) once interannual fluctuations are accounted for Pogliotti et al. (2023), the same behaviour observed here. The 15-year length of the local series at Punta Helbronner is therefore too short to statistically confirm a trend whose direction is nonetheless consistent with the broader Alpine warming signal (Noetzli et al., 2024; Pogliotti et al., 2023): the interannual variability in annual means (standard deviation of 0.6–0.9 °C) is by itself sufficient to account for the differences observed between periods. This should be read as a limitation of the available record length, not as evidence against a real underlying warming trend.

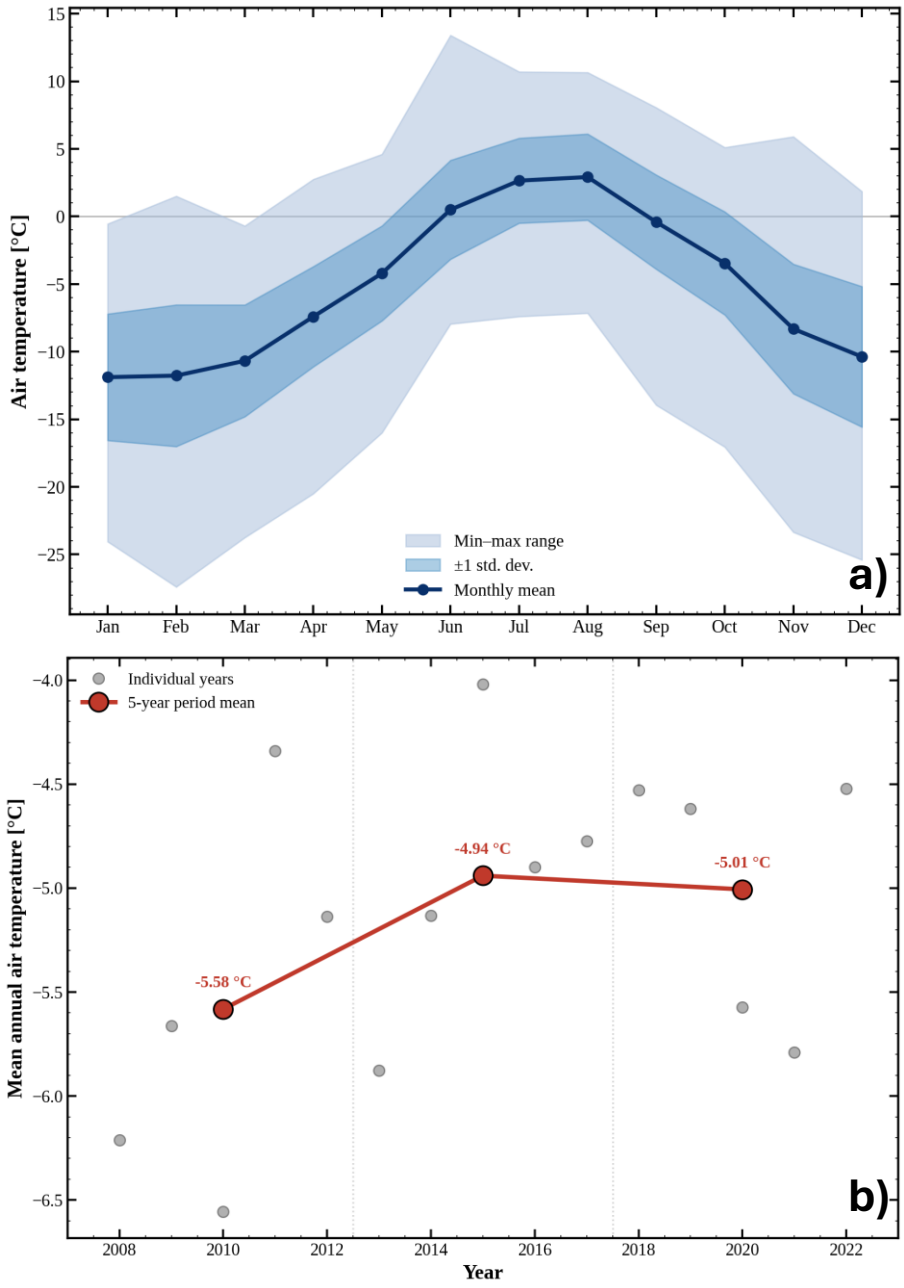


Figure 68 a) Mean seasonal cycle of daily air temperature at Punta Helbronner (2008–2023), showing the monthly mean, the minimum–maximum range and ±1 standard deviation; b) Annual mean air temperature over three consecutive five-year periods (2008–2012, 2013–2017, 2018–2022), with individual annual values shown in the background and period means highlighted.

6.2.3 *Infrastructure: Skyway cable car*

The Skyway cable car was inaugurated in 2015 after construction began in 2011 and is organized into three stations: valley (Pontal), intermediate or interchange (Pavillon), and mountain (Punta Helbronner, PH). The system has a total length of 4,500 m and covers a difference in altitude of 2,137 m. It replaced the previous three-section system,

which had a different departure station in La Palud. The first section covers a difference in altitude of approximately 866 m with a linear length of approximately 1,750 m. The second section covers a vertical distance of approximately 1276 m over a length of approximately 2600 m. Both sections use a double-cable ropeway system, anchored at both the valley and mountain stations, with traction cables suspended between them by means of line brackets (Dimensione Ingenierie s.r.l., 2009). The tensioning station for the haul and rescue cables is located upstream, while the drive station is located downstream.

The valley station of the lift is located on a slight slope at an altitude of approximately 1315 m above sea level. This site has a gradual slope towards the south, and the station structure interacts with soils of varying composition, with abundant organic material and a shallow water table. The intermediate station of Pavillon (2165 m above sea level) is located on a moderately sloping (20°-25°) slope exposed to the SSW. The second section, Pavillon - Punta Helbronner, runs exclusively on the Granites of Mont Blanc. The first pylon of this section (3040 m above sea level) is about 100 m high and located on the left side of the ridge that extends from NW to SE from the Torino refuge. The second pylon is located near the Torino Vecchio refuge (approx. 3310 m above sea level) on a small ridge-oriented NNE - SSW. This ridge was affected by minor surface instability and the movement of a large rock block during construction. The Punta Helbronner Mountain station and the surrounding areas, including the Col de Saussure and the ridge with the old intermediate station and the Torino Refuge, are completely within the granite-granodiorite pluton of Mont Blanc (Upper Carboniferous). The arrival station is located at approximately 3466 m above sea level and includes the horizontal tunnel (approximately 154 m long, section 3.6 m x 3.9 m) and the structural shaft (approximately 80 m deep, diameter: 5 m), both excavated in the Mont Blanc Granites. The shaft (Figure 69) is characterized by structural lining thicknesses that vary with depth: 1 m up to approx. -35 m and then 0.5 m thick down to the bottom of the shaft. On the northwest side, there are the old French station connected with the Skyway station, that allowed to reach Chamonix from Punta Helbronner

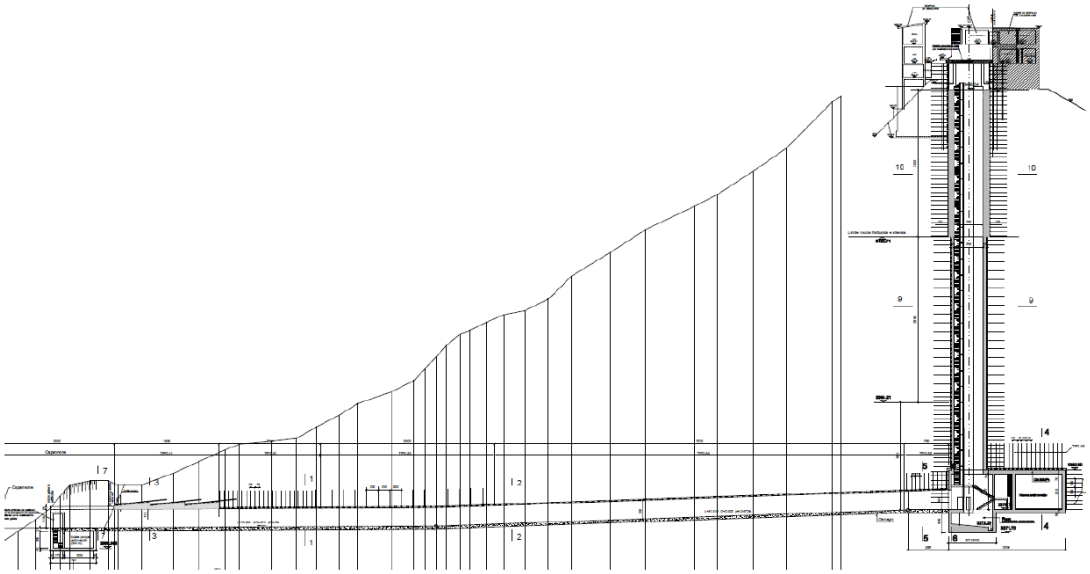


Figure 69 Section of concrete shaft with elevator and visitor gallery (Dimensione Ingenierie s.r.l., 2009).

6.3 Methodology and Theoretical Background

6.3.1 *Regional Permafrost probability map*

To frame the Punta Helbronner case study within its regional cryospheric setting, a permafrost probability map of the Aosta Valley was produced following the step-by-step workflow of Magnin et al. (2019). Mean Annual Air Temperature (MAAT) was first computed for the period 2012–2022 and spatialized by interpolating mean values from meteorological stations distributed across Valle d'Aosta, including a limited number of stations located just outside the regional boundaries to reduce edge artefacts and obtain a more stable temperature field across the whole domain. Because MAAT decreases with elevation, this step provides the dominant, elevation-controlled thermal baseline of the predicted rock-surface temperature field. In parallel, Potential Incoming Solar Radiation (PISR) was derived from a 10 × 10 m DEM to represent the potential solar forcing controlled by terrain geometry (slope, aspect and topographic shading).

Following Magnin et al. (2019), MAAT and PISR were then combined into the predicted Mean Annual Rock Surface Temperature ($MARST_{pred}$) by adding to the MAAT baseline a radiative correction term derived from PISR normalized to its domain minimum. By construction, this correction is zero for the most persistently shaded cells (where local PISR equals its domain minimum) and increases with increasing PISR, so

that it can only warm, never cool, the elevation-controlled baseline. As a result, the aspect-driven correction modulates the thermal regime locally, colder on shaded, north-facing terrain; warmer on sun-exposed, south-facing terrain, but cannot invert the first-order control exerted by elevation through MAAT: higher, colder sites remain systematically colder than lower, warmer sites at comparable exposure. Because the method targets steep bedrock, only terrain cells with slope > 40° were retained for the subsequent steps.

Permafrost occurrence was finally expressed as the probability that the predicted rock-surface thermal regime corresponds to $MARST_{pred} \leq 0\,°C$. In accordance with Magnin et al. (2019), $MARST_{pred}$ was standardized over the steep-slope domain as

$$MARST_{norm} = \frac{-(MARST_{pred} - \mu_{pred})}{\sigma_{pred}}$$

where μ_{pred} and σ_{pred} are the mean and standard deviation of $MARST_{pred}$ computed only for cells with slope > 40. The leading minus sign means that colder-than-average cells ($MARST_{pred} < \mu_{pred}$) yield a positive $MARST_{norm}$, while warmer-than-average cells yield a negative one; the probability was then obtained using the logistic approximation of Magnin et al. (2019):

$$P(p) = \frac{1}{1 + e^{-(0.076056 \times MARST_{norm}{}^3 + 1.5976 \times MARST_{norm})}}$$

so that increasingly positive $MARST_{norm}$ (i.e., increasingly cold sites) is mapped onto increasing permafrost probability. For cartographic readability, the resulting probability field was grouped into the permafrost condition classes shown in the legend (isolated, sporadic, discontinuous and continuous). The Mont Blanc sector is outlined by the red box in the regional map, and the corresponding zoomed inset provides the spatial reference where Punta Helbronner is located (Figure 70)

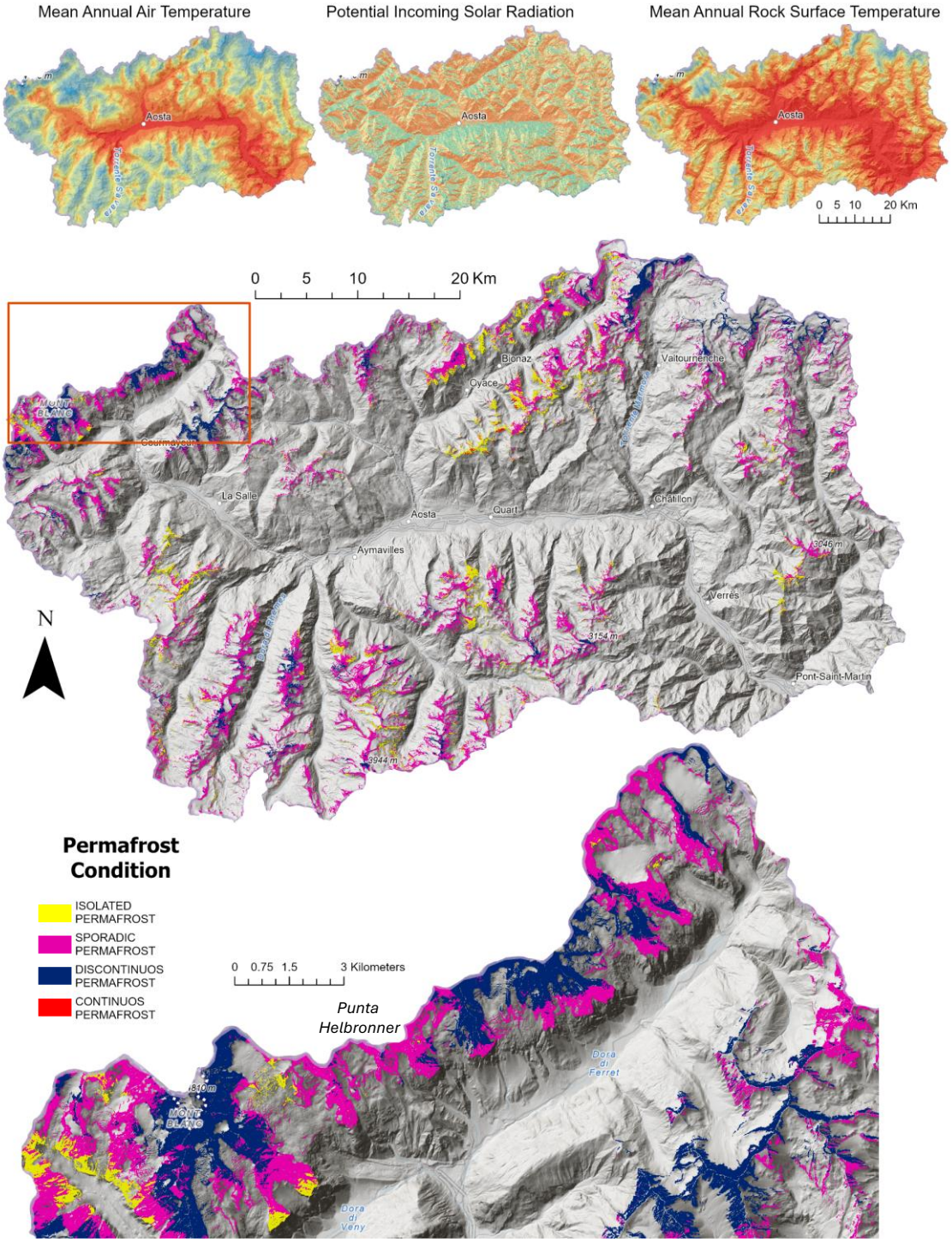


Figure 70 Raster maps of MAAT, PISR and MARST used to calculate the probability of permafrost occurrence map, according to Magnin et al., 2019) with a zoom on the Mont Blanc Massif, where Punta Helbronner is located.

6.3.2 *Monitoring Layout*

The Punta Helbronner site is instrumented with a multi-parametric network designed to characterise the thermal regime of the surrounding bedrock at different distances from,

and depths relative to, the shaft, spanning from centimetre-scale near-surface conditions to the deep rock mass. The network combines six boreholes installed and operated by ARPA Valle d'Aosta with a deep external borehole and the shaft itself, both instrumented with Differential Monitoring of Stability (DMS) columns (Figure 71).

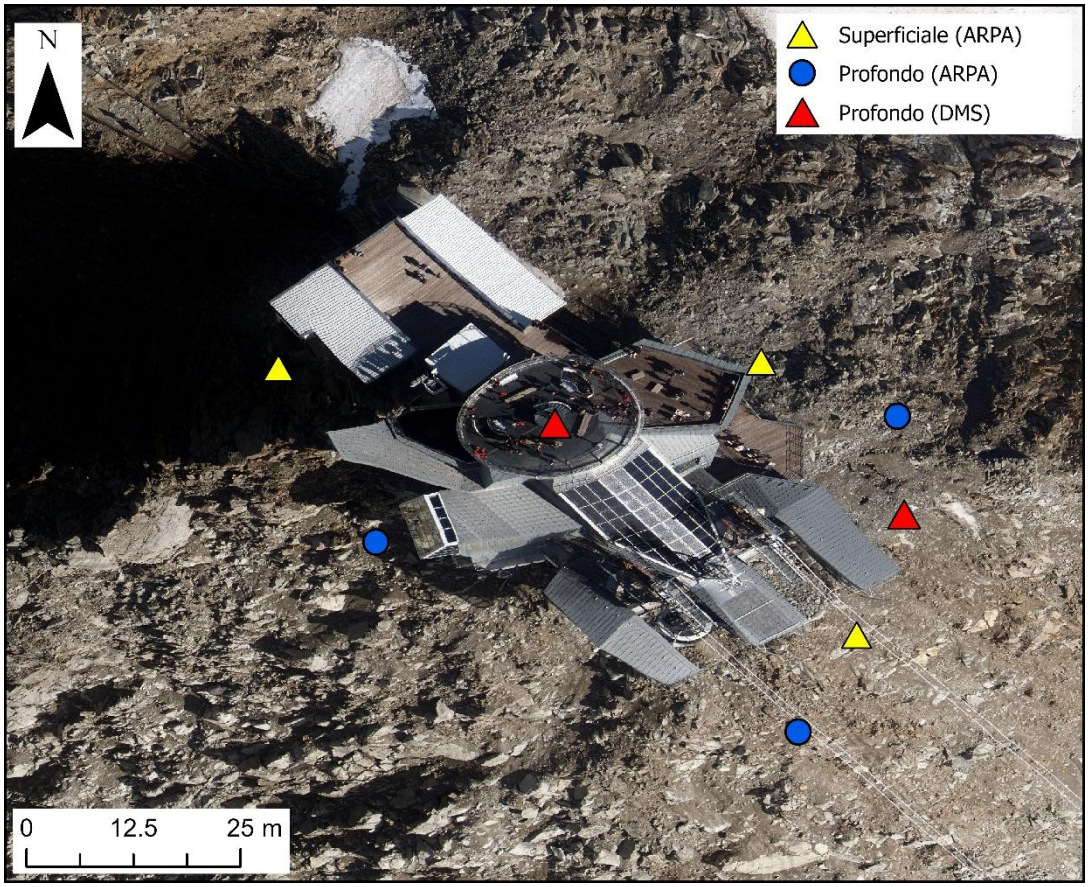


Figure 71 Orthophoto of the Punta Helbronner site showing the location of the monitoring boreholes: shallow ARPA boreholes (yellow triangles), deep ARPA boreholes (blue circles), and deep DMS-instrumented points (red triangles), the shaft itself (center) and the external validation borehole (~37.8 m to the SE).

Three shallow boreholes, 0.55 m deep, were completed by ARPA Valle d'Aosta in summer 2023 on slopes of different aspect (East, West and South) around the infrastructure. Each borehole was equipped with temperature sensors at 0.10, 0.30 and 0.55 m depth, providing a point-scale record of near-surface rock temperature (RST) within the active layer. On the same three slopes, three deeper boreholes were instrumented with thermistor chains reaching maximum depths of approximately 11.7 m (East), 9.6 m (South) and 6.8 m (West), extending the thermal record from the active layer into the underlying rock mass.

In addition to the ARPA network, an external deep borehole located approximately 37.8 m from the shaft was equipped with a DMS multiparametric column, providing an independent thermal record used later in this chapter as an out-of-model validation point for the three-dimensional thermal simulation (section 6.4.6).

Within the shaft itself, two complementary DMS-based instruments were installed. A vertical multiparametric column with 24 sensors spaced 2.5 m apart runs the length of the concrete shaft, recording the air temperature inside it. Radially, small boreholes drilled into the shaft concrete ring and the surrounding bedrock, oriented South-East and South-West, were equipped with sensors at three fixed distances from the shaft wall (0.1, 0.6 and 1.1 m), at multiple elevations along the shaft; the shallowest of these radial sensors is positioned 21 m below the shaft head, where the thermal influence of the infrastructure is expected to be strongest.

6.3.3 *2D Thermal FEM setup*

The first step of the numerical work, performed to study the possible interaction between rock mass, slope geometry and structural elements, consisted of a two-dimensional finite-element thermal analysis aimed at quantifying the thermal disturbance induced by the completion of the shaft concrete lining and by the air circulation inside the shaft. This phase was designed to reproduce and verify the modelling approach previously proposed by Bertoncelli (2016), providing a consistency check against earlier results, confirming values for controlling variables and establishing a robust starting point for the subsequent 3D simulation.

The model represents a cross-section of a 5 m diameter circular shaft embedded within a 50 m × 50 m square rock domain. The shaft is surrounded by a 1 m thick concrete ring, while the external medium is a homogeneous granitic rock mass. The mesh was refined in the concrete lining (element size ~0.2 m) to correctly capture the steep thermal gradients expected close to the shaft, whereas a coarser discretization was adopted in the rock domain (element size ~1 m). Overall, the 2D model includes 7,405 elements and 7,531 nodes, balancing numerical accuracy and computational cost (Figure 72).

Heat transfer was modelled as conduction in the solid media, while the interaction between the shaft air and the inner concrete wall was represented through a convective boundary condition, imposed with a constant heat-transfer coefficient ($h = 20$ W m^{-2} K^{-1}) and a prescribed air temperature inside the shaft. At the external boundary of the rock

domain, a uniform and time-invariant temperature was imposed to represent the far-field thermal condition of the rock mass. A set of parametric runs explored the sensitivity to both (i) the far-field boundary temperature (tested at −3, −6 and −10 °C) and (ii) the air temperature within the shaft, varied over representative values from a few degrees above 0 °C up to approximately 10 °C.

Two analysis types were carried out on the same geometry: steady-state and transient. For the extraction of radial profiles, distance from the shaft was measured along a transect oriented at 45°, which reduces the influence of the square external boundary on the radial trend.

For the transient analysis, the early-age thermal effect of concrete casting was additionally included to account for the exothermic nature of cement hydration. Since the numerical formulation adopted here does not explicitly compute hydration heat production, the phenomenon was introduced using the same pragmatic approach proposed by Bertoncelli (2016): a high initial temperature was assigned to the concrete lining (50 °C), reproducing the short-lived heat pulse immediately after casting.

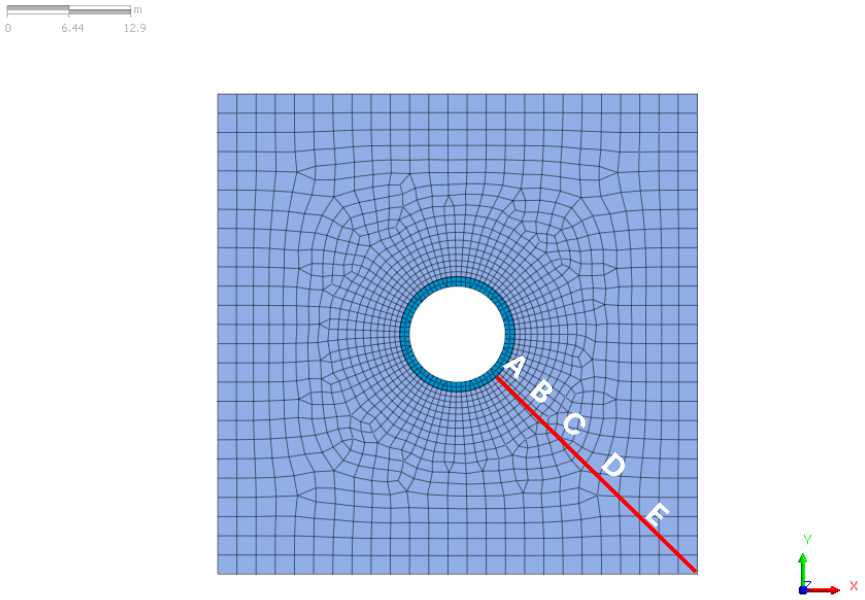


Figure 72 2D mesh represents a section of concrete shaft. The red line indicates the line in which results are extracted.

6.3.4 *3D Thermal FEM setup*

To capture the real three-dimensional geometry of the shaft and quantify its thermal influence on the surrounding permafrost, a transient thermal model was developed using the FEFLOW software (DHI). The approach builds on the same radiative boundary

condition and spin-up strategy previously applied to the Cima Falkner case study (Chapter 5), extended here with a snow-season correction that represents a methodological advancement over the original application. The model domain is an irregular polygon of approximately 220 × 220 m centered on the shaft, discretized into an unstructured mesh of 393,120 nodes and 741,750 elements. The shaft, approximately 80 m deep with an outer radius of 2.5 m, is represented explicitly within the mesh. Thermal properties were assigned to two material domains, rock and shaft concrete, summarized in

Table 11 Thermal parameters used for the rock and shaft-concrete domains in the 3D FEFLOW model.

Material	k (W/m*T)	P [kg/ m^3]	C [J/(kg*T)]	*Vol. Heat Capacity [J/(m^3*T)]*
Granite	2.8	2700	800	2.16×10^6
Concrete	2.2	2549	900	2.294×10^6

The surface thermal boundary condition combines three terms: a spatially uniform air-temperature forcing, a constant offset, an elevation-dependent lapse-rate correction, and a radiative correction controlled by local terrain geometry:

$$T_{surf}(node,t) = [T_{air}(t) + \Delta T_{mean}] + \alpha_T \cdot \frac{[R(node,m) - R_{mean}(m)]}{R_{mean}(m)} + lapse\ rate \cdot \frac{(z_{max} - z)}{100}$$

Where $\alpha_T = 3°C$ (Gruber & Haeberli, 2007), $\Delta T_{mean} = 1.5°C$, lapse rate 0.48°C/100m and z_{max} is the maximum elevation of the model domain, computed from the site DEM. This formulation follows the same approach adopted at Cima Falkner (Chapter 5).

$R(node,m)$ is obtained from a set of twelve-monthly potential-radiation rasters computed on the site DEM to capture local slope and aspect (Figure 73).

The resulting radiative correction to air temperature ranges between approximately −2.1 °C and +2.5 °C across the domain. Because local exposure is controlled by the real, complex micro-topography around the shaft rather than by nominal compass direction, points with the same labelled aspect can receive different radiative forcing if their local slope geometry differs, a behaviour that is physically expected in complex terrain rather than indicative of an error.

The lapse-rate term was carried over unchanged from the Cima Falkner implementation, since no independent multi-elevation dataset is available at Punta Helbronner to calibrate an elevation gradient locally. The offset term, was instead checked directly against the ARPA ground-surface temperature record introduced in section 6.4.1: comparing the East- and West-facing stations at 0.55 m against the air-temperature climatology for the snow-free summer months (July–September) yields an observed offset of +1.66 to +1.98 °C, of the same order of magnitude as, though somewhat smaller than, the assumed value of 1.5 °C. This value was therefore retained as a reasonably conservative estimate rather than being independently re-calibrated. The South-facing station was excluded from this comparison: its much larger apparent offset (+5.03 °C) reflects the strong radiative anomaly associated with the persistent winter zero-curtain plateau documented at that station (section 6.4.1), which is already accounted for separately by the radiative correction term, rather than by the mean offset.

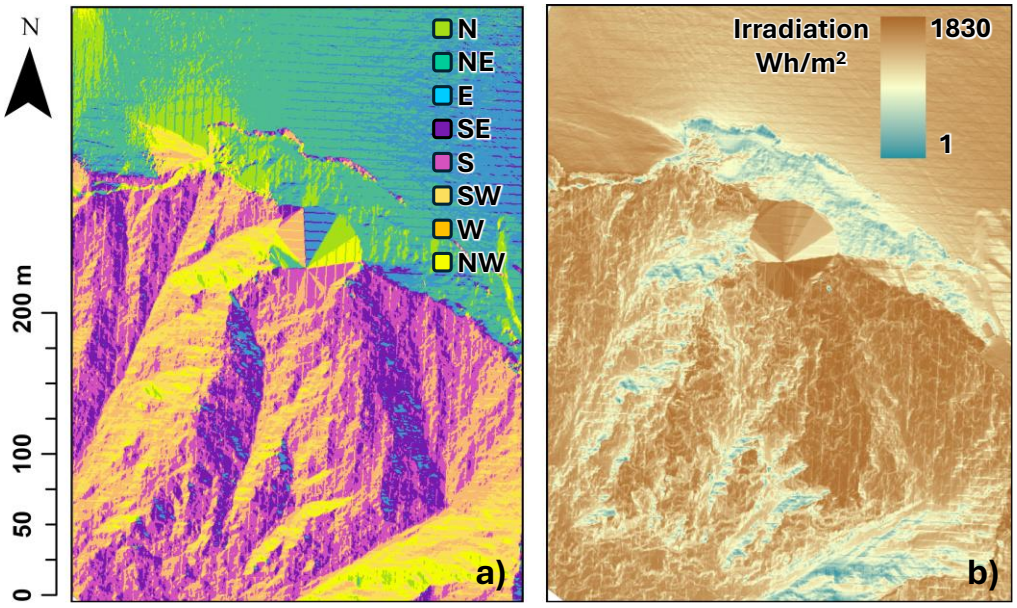


Figure 73 a) Eight-class aspect map (N, NE, E, SE, S, SW, W, NW) derived from the site's high-resolution DEM, used to construct the radiative boundary condition of the 3D FEFLOW model; b) Corresponding potential incoming solar radiation (Wh/m²) derived from the same DEM.

The choice of spin-up duration was verified against an independent estimate of the characteristic diffusion timescale, $\tau = L^2/(\pi^2\alpha)$, where L is the relevant vertical length scale and α is the thermal diffusivity of rock (0.112 m² per day). For the full 332 m depth of the model domain, τ is approximately 273 years, implying only about 31% convergence toward equilibrium after 100 years; for the shallower 100 m zone most relevant to the shaft, however, τ is approximately 25 years, corresponding to

approximately 98% convergence over the same 100-year period. The climatological spin-up was therefore considered adequate for the near-surface and shaft-proximal thermal regime that is the focus of this chapter, even though the full model domain remains far from equilibrium at greater depth. Reaching this level of convergence within a practical spin-up duration required initializing the climatological phase from a linear temperature gradient with depth, rather than from a spatially uniform temperature: since the characteristic timescale itself does not depend on the initial condition, but the magnitude of the initial disequilibrium does, starting from a profile already close to the expected equilibrium shape substantially reduced the transient adjustment that the spin-up needed to resolve.

The simulation followed a three-phase spin-up strategy analogous to that used in Chapters 4 and 5, designed to bring the model to a physically consistent thermal state before activating the shaft. In the first phase, the fifteen-year air-temperature climatology described in section 6.2.3 was reduced to a twelve-value mean seasonal cycle and repeated for 100 years to reach a quasi-periodic natural regime.

In the second phase, sixteen years of real, chronologically ordered monthly mean air temperatures were applied, with the initial condition transferred from the end of the climatological phase. In the third and final phase, the shaft concrete material and its associated boundary condition were activated, and the same fifteen-year, chronologically ordered monthly air-temperature sequence used in the second phase was applied again, with the initial condition transferred from the end of that phase; the shaft's thermal influence is therefore simulated as a fifteen-year transient response superimposed on an already-equilibrated natural regime. A phase-change formulation was additionally activated to represent latent-heat effects during freeze–thaw transitions, using porosity values of 3% for rock and 12% for shaft concrete (within the 11–18% range reported for ordinary structural concrete), following the same implementation used for the Cima Falkner model (Chapter 5); because the shaft boundary condition remains above 0 °C throughout, this formulation has a negligible effect immediately around the shaft itself and mainly refines the representation of the colder rock mass further away. At the base of the model domain, a fixed temperature of +1.7 °C was imposed as the lower boundary condition, calculated from an assumed geothermal heat flux and the rock thermal conductivity (yielding a gradient of approximately 20.67 °C/km); a fixed-temperature

condition was adopted, rather than a free-flux condition, because the latter did not converge within a practical computation time.

A preliminary comparison against field temperature data indicated that, without any correction for snow cover, the model substantially overestimated winter cooling. A snow-season correction was therefore introduced: during the snow-covered months, the surface boundary condition at a given node is overwritten with a fixed "zero-curtain" temperature, decoupling the ground thermal regime from winter air-temperature oscillations; outside this period, the radiative boundary condition described above applies. The correction is applied only to nodes with a local slope at or below a threshold value, since on steeper terrain snow does not persist and the rock surface remains coupled to air temperature year-round. Three parameters define the correction, each calibrated against independent evidence: a slope threshold of 50°, raised from an initial value of 40° following photographic verification that snow cover is widespread at the site even on comparatively steep slopes; a snow season extending from October to July, extended from an initial end-date of June because the shallow borehole record shows no sign of thaw as late as mid-June; and a zero-curtain temperature of +0.6 °C, taken directly as the observed mean near-surface temperature at the validation borehole over the winter period, in preference to a value back-calculated to close the model–observation gap, which would have lacked independent observational support.

6.4 **Results**

6.4.1 *Near-surface and borehole rock temperature*

To characterise the thermal regime of the near-surface rock, ARPA Valle d'Aosta instrumented three shallow boreholes (0.55 m deep) and three deeper boreholes on slopes of different aspect (East, West and South) around the Punta Helbronner infrastructure This network provides a robust point-scale proxy of near-surface rock temperature (GST) within the active layer and is therefore useful for quantifying aspect-controlled thermal contrasts (Figure 74).

At the shallow boreholes, the time series show a clear seasonal signal, with the largest amplitudes at 0.10 m and progressively damped and phase-lagged at 0.30 m and 0.55 m, consistent with heat diffusion in bedrock. The East-facing site follows a regular seasonal cycle at 0.10 m, ranging from −10.75 °C (29 November 2023) to +17.43 °C (10 August

2024), with the range narrowing to −10.00/+9.06 °C at 0.55 m. The West-facing site records the coldest conditions among the three over the shorter period for which continuous data are available (23 August – 10 December 2023), reaching −16.50 °C at 0.10 m and still −13.18 °C at 0.55 m. The South-facing site reaches by far the highest summer peaks (+28.37 °C at 0.10 m, 7 September 2023) but comparatively mild winter minima (no lower than −2.50 °C at 0.10 m, and only −0.31 °C at 0.55 m over the whole record), reflecting a fundamentally different thermal regime rather than simply a warmer version of the other two aspects.

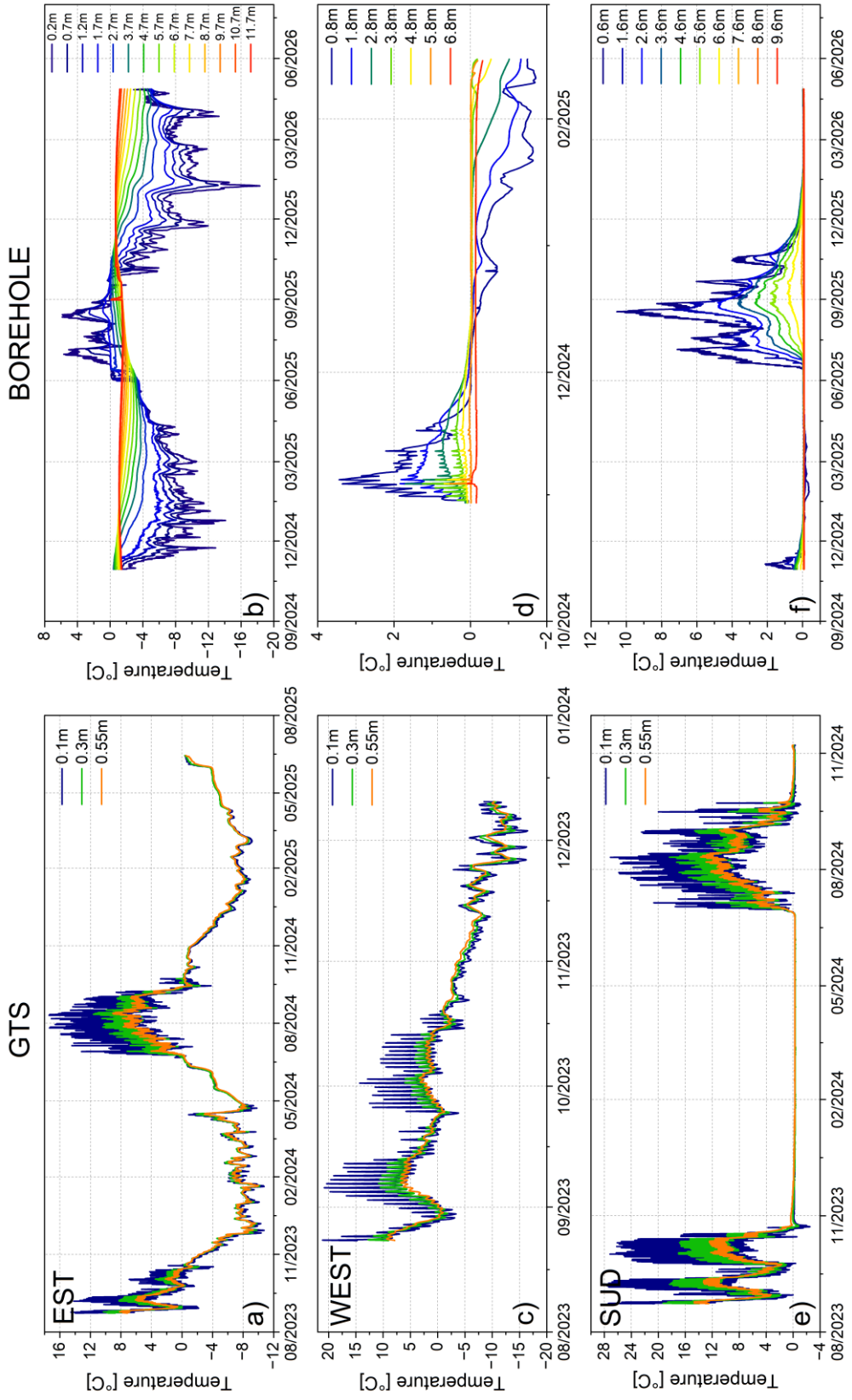


Figure 74 Ground surface temperature (GST, left panels, sensors at 0.10, 0.30 and 0.55 m) and borehole temperature (right panels, thermistor chains to maximum depths of 11.7 m East, 6.8 m West and 9.6 m South) at a-b) East, c-d) West and e-f) South aspects.

This difference is made explicit by the South-facing borehole's most distinctive feature: at 0.55 m, temperature remains continuously within ±1 °C of 0 °C for 251 consecutive days, from 23 October 2023 to 29 June 2024, against a longest comparable spell of only 20 days at East and 6 days at West over the same period. This is consistent with a "zero-curtain" behaviour, a near-isothermal period around the freezing point associated with the latent heat of phase change of water in pores and fractures, here plausibly reinforced by a persistent, locally redistributed snow cover on this aspect.

The deeper boreholes extend the thermal record from the active layer into the underlying rock mass, reaching maximum depths that differ between sites (East to approximately 11.7 m, South to approximately 9.6 m, West to approximately 6.8 m). Across all sites, the amplitude of the annual signal decreases with depth and the seasonal extrema become progressively phase-lagged downward, reflecting attenuation and delayed propagation of the thermal wave. At the East site, shallow sensors show large seasonal excursions while the deepest sensors remain comparatively stable and predominantly below 0 °C throughout the observation period; this persistence of sub-zero temperatures at depth is consistent with cold, potentially perennially frozen bedrock conditions, although the monitoring period remains limited in time. At the South site, the shallowest sensors show strong summer warming with pronounced short-lived peaks, while temperatures at greater depth remain close to 0 °C and vary only weakly through the year; such near-isothermal behaviour at depth can reflect the combined effect of conductive damping and latent-heat buffering in water- and ice-bearing fractures, but because near-zero plateaus can also be influenced by local hydrological conditions or sensor–contact effects, this interpretation should be supported by ancillary evidence before being treated as established. The West site provides a markedly shorter record, limited to part of the cold season; within this period, temperatures remain close to 0 °C with smaller depth-dependent contrasts than at the East site, suggesting either a reduced winter cooling signal or stronger insulation of the rock surface (for instance by persistent snow cover); because the record does not span a full annual cycle, seasonal metrics and inter-aspect comparisons for the West site should be regarded as preliminary.

Beyond the ARPA network, an external borehole located approximately 37.8 m from the shaft and instrumented with a DMS multiparametric column extends the depth range of direct observation well beyond the deepest ARPA sensor, down to 70 m (Figure 75). The available record spans 2 December 2025 to 22 June 2026, under seven months,

covering winter through early summer but not yet a full annual cycle, so the profiles discussed here should be regarded as an early snapshot rather than a definitive characterisation of the borehole's thermal regime. Within this record, the near-surface layer (uppermost few metres) is the coldest and most variable part of the borehole, reflecting direct exposure to winter air temperature; temperature increases with depth and stabilises at approximately −1 to −0.5 °C from roughly 10–20 m down to about 50 m. This stabilisation depth and temperature range are broadly consistent with the sub-zero conditions recorded at the base of the deepest ARPA borehole (East, to 11.7 m), providing independent, deeper confirmation of the cold, potentially perennially frozen bedrock conditions inferred from the ARPA network. Between approximately 55 and 65 m depth, the earliest profiles in the record (from December 2025) show a localised warm anomaly, with temperature rising above 0 °C to approximately +1 °C before returning to near 0/−0.5 °C by 70 m; this anomaly is markedly attenuated, or absent, by the most recent profiles (June 2026). Given the short record and the absence of independent hydrogeological data at this depth, the anomaly cannot be attributed with confidence: transient water circulation within a fracture zone is a plausible hypothesis, but it remains to be evaluated rather than an established interpretation, and it will be worth revisiting once a longer record is available.

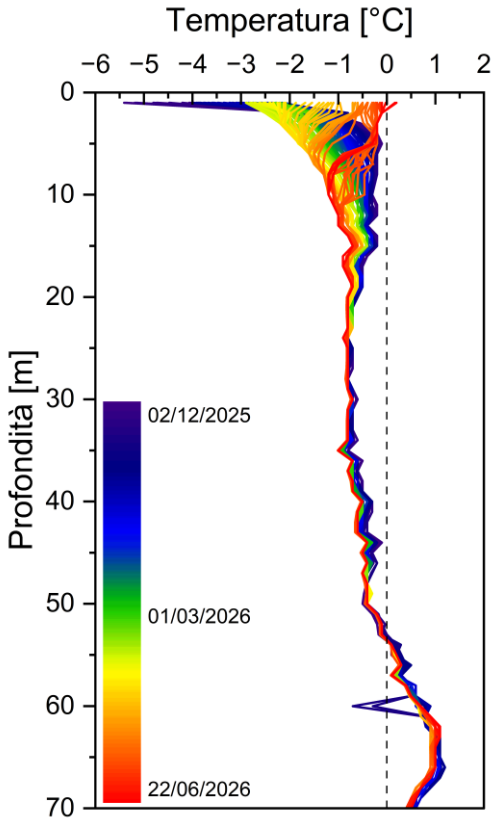


Figure 75 Vertical temperature profile at the external DMS borehole (0–70 m depth, ~37.8 m from the shaft), colored by acquisition date from 2 December 2025 (dark blue/purple) to 22 June 2026 (red).

6.4.2 *Shaft internal temperature*

The air temperature inside the shaft was recorded by a vertical multiparametric column of 24 sensors spaced 2.5 m apart, from the shaft base (Module 0, at depth) to its head near the surface infrastructure (Module 24) (Figure 76). The single most important feature of this dataset is that, over the entire monitoring period and at every module along the full length of the shaft, the recorded air temperature never drops below approximately +3 °C, even at the base, its coldest and most stable section, the observed minimum remains positive. Since the surrounding bedrock at this elevation is expected to be in permafrost conditions (section 6.4.1), this means the shaft does not simply perturb the local thermal regime seasonally near the surface: its interior constitutes a permanent, year-round heat source along its entire length, continuously conducting heat into the rock mass around it.

Superimposed on this permanently positive baseline, both the central tendency and the spread between extremes increase markedly from base to head. At the base, the maximum recorded temperature is approximately 5–6 °C and the minimum approximately 3 °C, a

comparatively narrow and stable range. Near the head, the maximum reaches approximately 18–19 °C while the minimum is itself elevated to approximately 7–8 °C, a much wider range dominated by episodic warm extremes. This pattern is consistent with strong, direct thermal influence from the surface infrastructure at the shaft head (solar gain, door openings, occupancy), superimposed on a more moderate, seasonally driven background trend that persists down the full length of the shaft. A secondary, smaller feature is visible at the very base (Module 0), where all four statistics are slightly higher than at the modules immediately above (Module 2–4) before increasing again toward the head, a subtle "C-shaped" pattern consistent with an additional, localised heat source at the shaft base, distinct from the dominant head-driven warming.

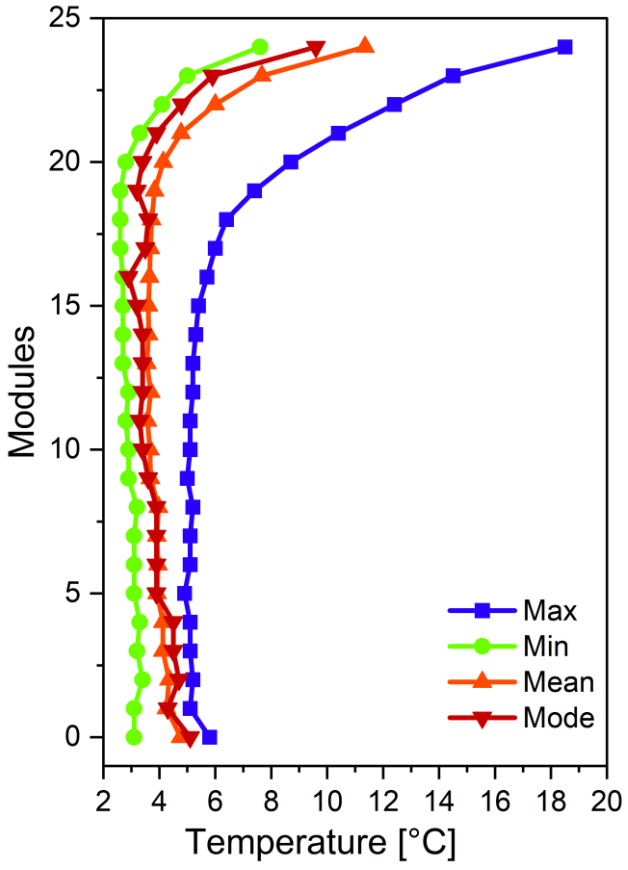


Figure 76 Maximum, minimum, mean and mode of the air temperature recorded inside the shaft by each module of the vertical multiparametric column (2.5 m spacing), over the full monitoring period, from the shaft base (Module 0) to the shaft head near the surface infrastructure (Module 24).

6.4.3 *Shaft radial temperature*

Having established that the shaft interior acts as a permanent, year-round heat source (section 6.4.2), radial sensors installed at three fixed distances from the shaft wall (0.1, 0.6 and 1.1 m), drilled through the concrete ring and into the surrounding bedrock, at two orientations (South-East and South-West) and at multiple elevations along the shaft, provide a direct observation of how that heat source is transmitted outward into the rock (Figure 77). A clear seasonal signal is visible, especially at the shallowest sensors (0.1 m), confirming that the internal shaft signal propagates outward through the lining rather than being fully damped within it. At equivalent distance, the South-West orientation consistently records higher temperatures than the South-East, with the seasonal peak lagging by approximately two months, an aspect control analogous to that observed in the free-field ARPA boreholes (section 6.4.1), but here superimposed on the shaft's own heat signal rather than acting alone.

The shallowest available set of radial sensors is positioned 21 m below the shaft head. Given the strong head-driven warming and the more moderate, stable regime found deeper in the shaft (section 6.4.2), these sensors sample a section of the shaft already past the zone of strongest infrastructure influence, closer to the stable background regime; the slight secondary warming toward the very base identified from the internal air column is consistent with, and provides an independent check on, the small "C-shaped" feature attributed there to the technical facility at the shaft base. The geometry of the concrete lining itself also shapes the radial signal: the shaft ring is approximately 1 m thick in its upper half and 0.5 m thick in its lower half, so the sensor at 0.1 m from the wall is always recording within the concrete itself, regardless of elevation, while the sensors at 0.6 and 1.1 m sample either concrete or the fractured rock beyond it depending on elevation, a zone where the local presence of air or water in fractures can additionally modulate the signal beyond simple conduction from the shaft.

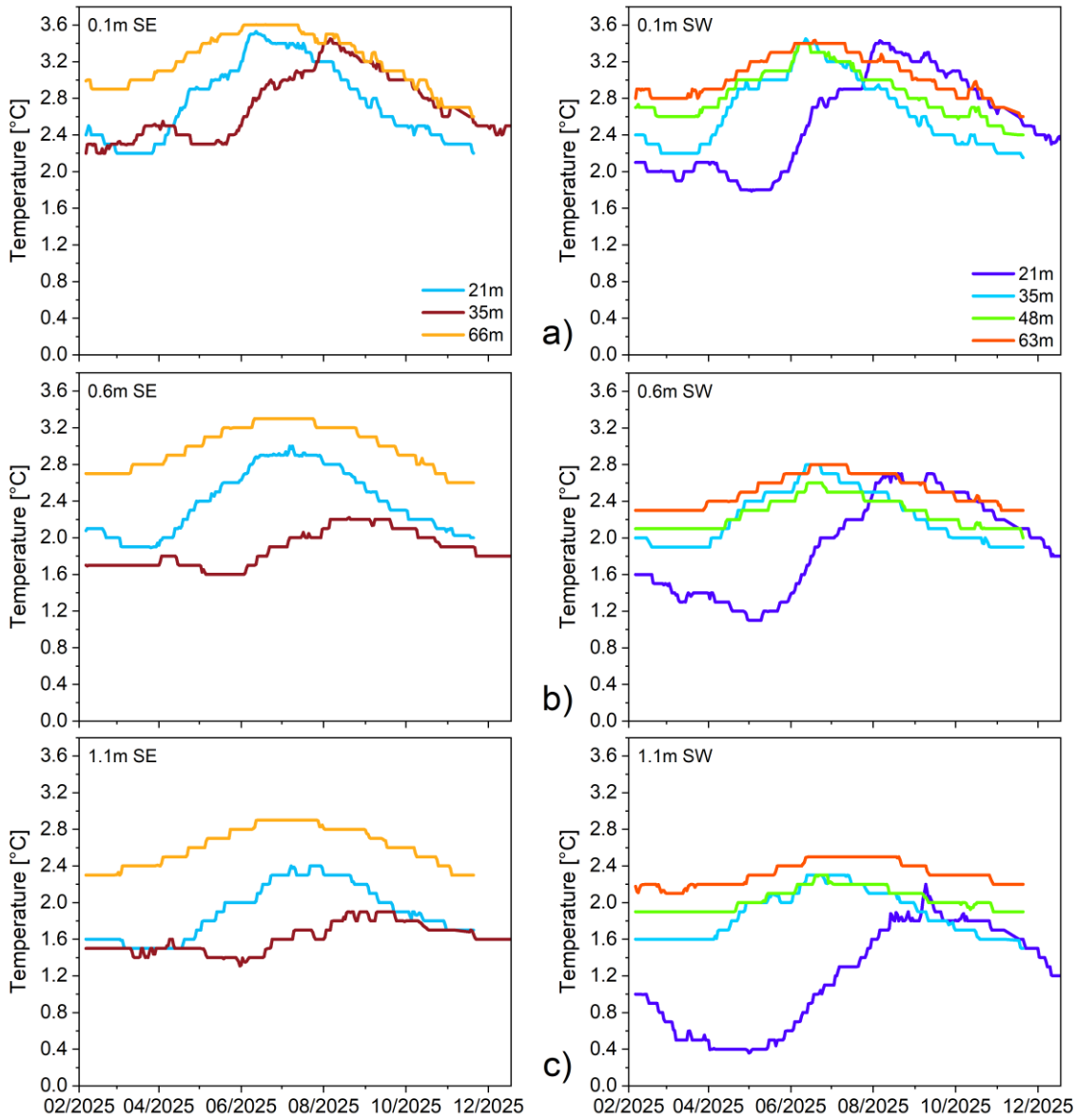


Figure 77 Time series of temperature around the shaft registered at different vertical depth and at different distance from shaft in two different orientation (SE -SW) in which a) 0.1m b) 0.6m and c) 1.1m distance from shaft.

6.4.4 *2D thermal analysis results*

The steady-state simulations were run for all nine combinations of far-field boundary temperature (−3, −6, −10 °C) and shaft-air temperature (3, 6, 10 °C), organized in Figure 78 in two complementary ways to isolate each control in turn.

In Figure 78a–c, the far-field boundary temperature is held fixed within each panel (a: −3 °C, b: −6 °C, c: −10 °C) while the three curves show the effect of shaft-air temperature. Near the shaft wall, the three curves are clearly separated, spanning approximately 7–7.5

°C regardless of which far-field condition is applied (from approximately 2.5–3 °C for the coldest shaft air to approximately 10 °C for the warmest, closely tracking the imposed air temperature itself, consistent with the moderate convective coupling at the shaft wall). This spread narrows progressively with distance and the three curves converge onto the imposed far-field value by approximately 20–23 m; only in the coldest far-field case Figure 78c) does a small residual separation persist to the edge of the domain, indicating that the near-field influence of a strong shaft-air anomaly can outlast the others under the most contrasting boundary condition tested. In Figure 78d–f, the shaft-air temperature is instead held fixed within each panel (d: 3 °C, e: 6 °C, f: 10 °C) while the three curves show the effect of the far-field boundary temperature. Here the pattern is reversed: the curves start close together near the shaft, reflecting the shared air-temperature condition, and progressively diverge with distance, ending up separated by the full 7 °C spanned by the three tested far-field values (−3, −6 and −10 °C) at the domain edge. Taken together, Figure 78a–f confirms that the shaft-air temperature dominates the thermal state in the near field (within a few meters of the shaft), while the far-field boundary condition dominates at greater distance, with the two influences of comparable magnitude (on the order of 7 °C) but operating over different, only partly overlapping ranges of distance from the shaft.

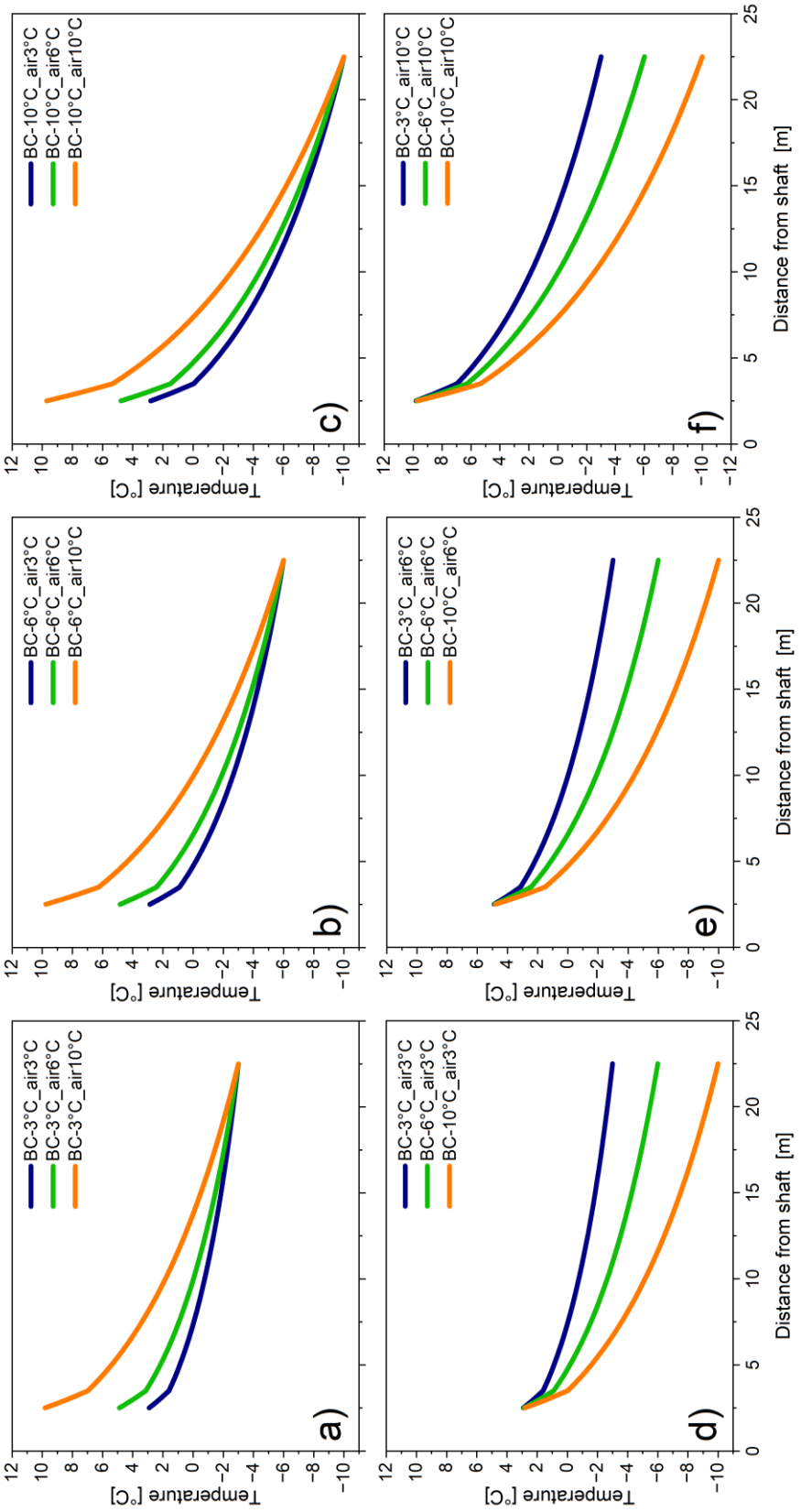


Figure 78 Results from 2D steady analysis in terms of temperature in function of distance from shaft for all case.

The transient analysis, which reproduces the short-lived heat pulse released by the exothermic hydration of the concrete lining immediately after casting, is summarized in Figure 79, where the radial profile is tracked from the inner shaft wall (point A, 2.5 m) through the concrete ring (up to point C, 3.55 m, matching the 1 m ring thickness) and into the surrounding rock (points D and E). At 6 hours, the profile already shows a sharp internal peak of approximately 50°C at point B (approximately 3.1–3.15 m, within the ring rather than at either boundary), decaying to approximately 32 °C at the outer ring boundary (C) and to near-zero values by point D (approximately 4.0 m); by 24 hours, this peak has fallen to approximately 43–44 °C. This apparent cooling of the peak with time is accompanied by an opposite trend farther out: at point D, the 24-hour profile is warmer than the 6-hour profile, since the thermal pulse has had more time to diffuse outward even as it dissipates near its source — a behaviour characteristic of transient conduction, where the near-field amplitude and the far-field penetration evolve in opposite directions over the same 24-hour window. Beyond point D, all four curves converge toward the same low value (approximately −1 to −2 °C) by point E (approximately 5.2 m), confirming that even this large, short-lived hydration pulse remains confined to the shaft lining and its immediate vicinity, and does not measurably perturb the rock mass beyond a few tens of centimeters from the ring within the first day.

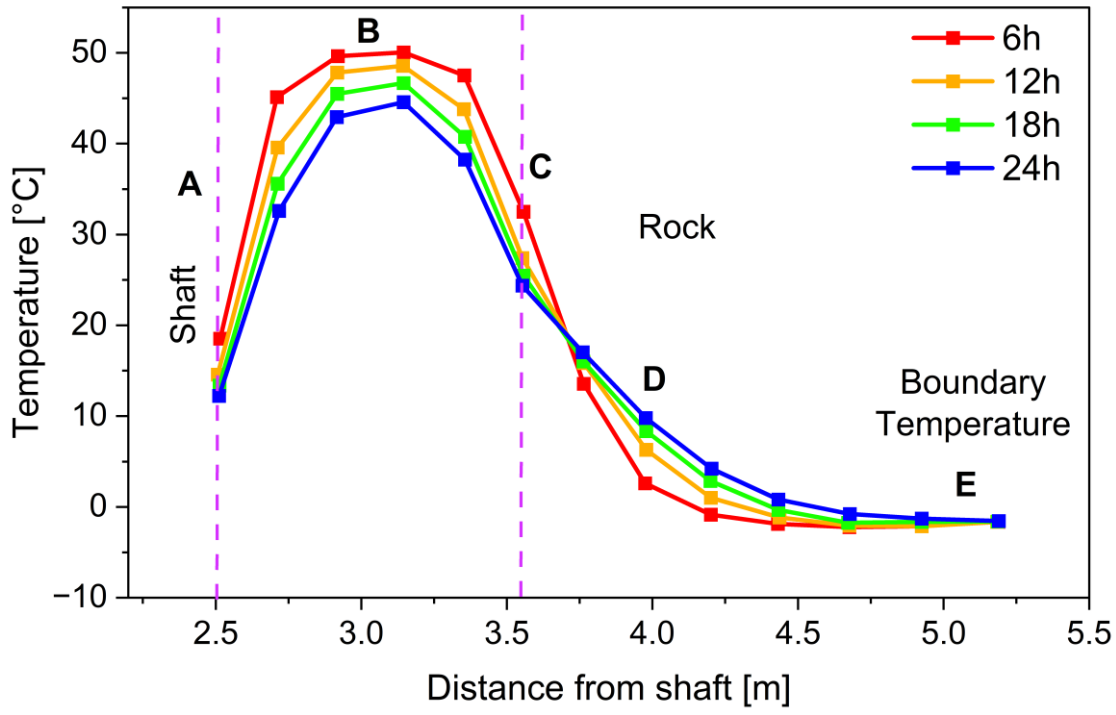


Figure 79 Temperature evolution in the first 24h after concrete hydration exothermic reaction.

6.4.5 *3D thermal analysis results*

The three-dimensional simulation was queried at eight compass directions and six fixed distances from the shaft wall (0.5, 1, 2, 5, 10 and 15 m), at three characteristic depths (shaft top, mid-depth and shaft base), and against a reference point 50 m from the shaft, assumed to lie outside the zone of infrastructure influence (Figure 80).

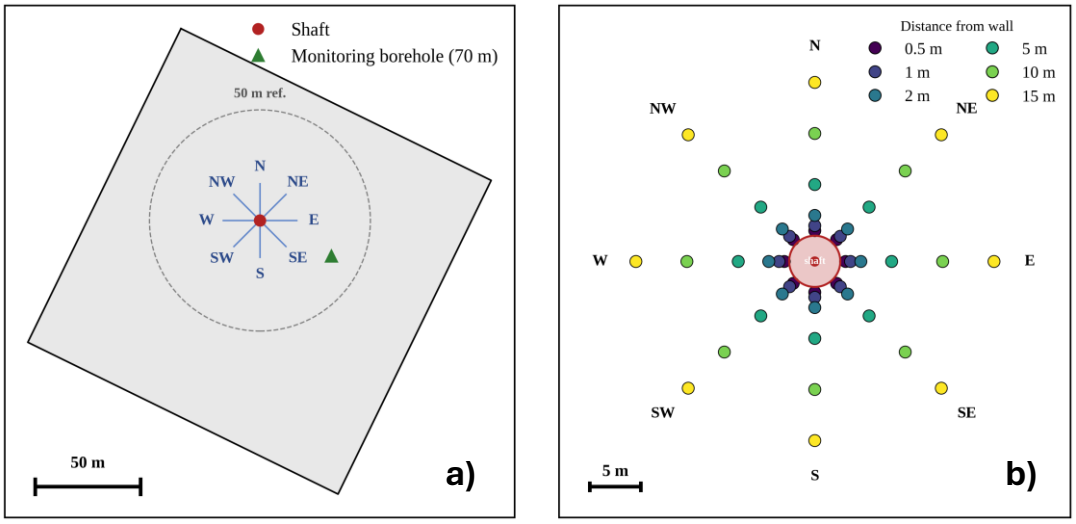


Figure 80 Extraction geometry for the 3D FEFLOW model results. a) Plan view of the model domain (~220 × 220 m), showing the shaft, the eight compass directions used for extraction, the 50 m reference point (dashed circle) and the position of the external monitoring borehole (70 m); b) detail of the extraction grid around the shaft, showing the eight directions at six fixed distances from the shaft wall (0.5, 1, 2, 5, 10 and 15 m).

The overall spatial expression of the resulting thermal anomaly is evident in vertical cross-sections through the model: the shaft appears as a sharply bounded, warm vertical column, locally exceeding 10 °C near the surface and remaining above approximately 3–4 °C down to near its base, embedded within a much colder rock mass that remains close to, or below, 0 °C away from the shaft, consistent with permafrost conditions at this elevation (Figure 81). Away from the shaft, the same cross-sections also show the ground surface responding to aspect, with warmer near-surface temperatures on the more sun-exposed slope than on the shaded one, providing an internal, three-dimensional confirmation of the aspect control already established from the regional permafrost map (section 6.3.1) and from the ARPA monitoring network (section 6.4.1). These results indicate that the shaft acts as a spatially confined heat source within an otherwise cold, aspect-controlled rock mass, rather than producing a broad regional warming.

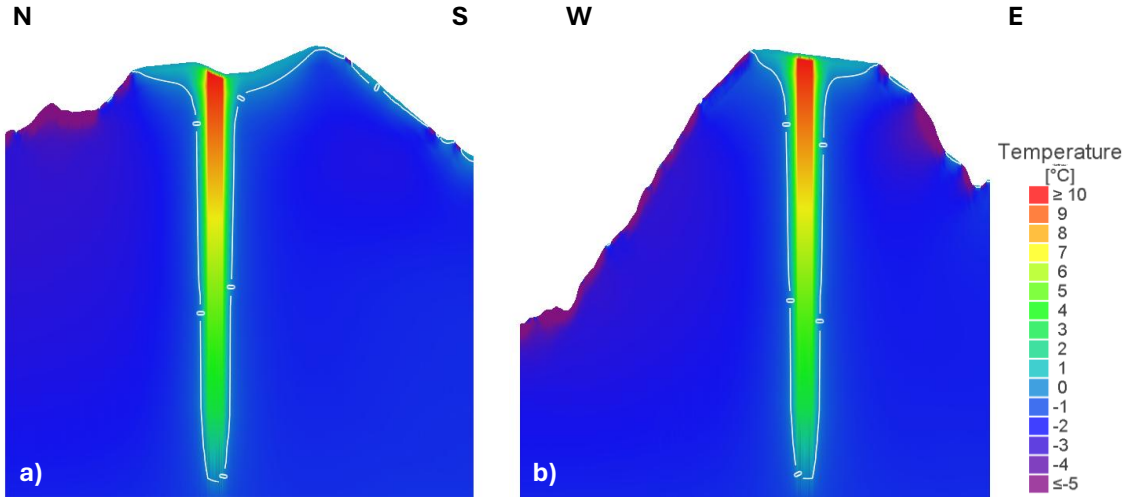


Figure 81 Modelled temperature field in vertical cross-section through the shaft: a) North–South section; b) West–East section. Contour lines mark isotherms; note the sharply bounded warm column corresponding to the shaft, embedded in colder, permafrost-consistent rock, and the aspect-related warming of the ground surface on the more sun-exposed side of each section.

The radial extent of the shaft-driven anomaly, extended in this analysis out to 15 m, shows a substantial reduction with distance but not yet a complete return to background conditions within the simulated period. Near the shaft top, the temperature anomaly decreases from approximately 5–8 °C at 0.5 m from the shaft wall to approximately 1–2 °C at 5 m and to under 1 °C by 10–15 m (Figure 82).

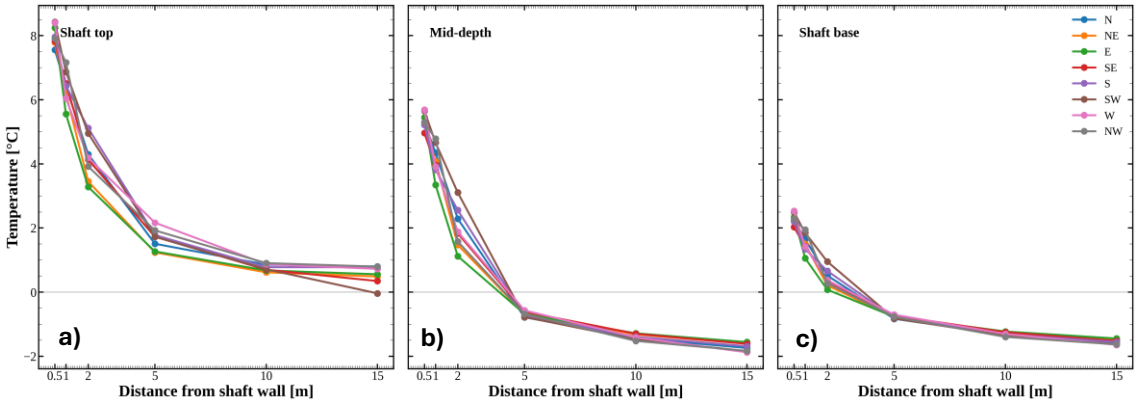


Figure 82 Horizontal temperature profiles as a function of distance from the shaft wall (0.5, 1, 2, 5, 10 and 15 m), for the eight compass directions, at three characteristic depths: shaft top, mid-depth and shaft base.

At mid-depth and at the shacompletely anomaly decreases from approximately 4–5.5 °C and 2–2.5 °C respectively at 0.5 m to values in the range of approximately −0.7 to −1.5 °C by 5–15 m; because the corresponding undisturbed reference at these depths lies at approximately −1.8 to −2.2 °C (section 6.4.5, time series), a residual difference of the order of 0.7–0.9 °C persists even at 15 m, indicating that the shaft's thermal footprint is

substantially, but not yet completely, exhausted at this distance. This vertical contrast, a much larger anomaly near the top than at depth, at every distance tested, mirrors the internal air-temperature pattern already established for the shaft itself (section 6.4.2), confirming that the head-driven warming documented there propagates outward into the surrounding rock rather than remaining confined to the shaft lining (Figure 83).

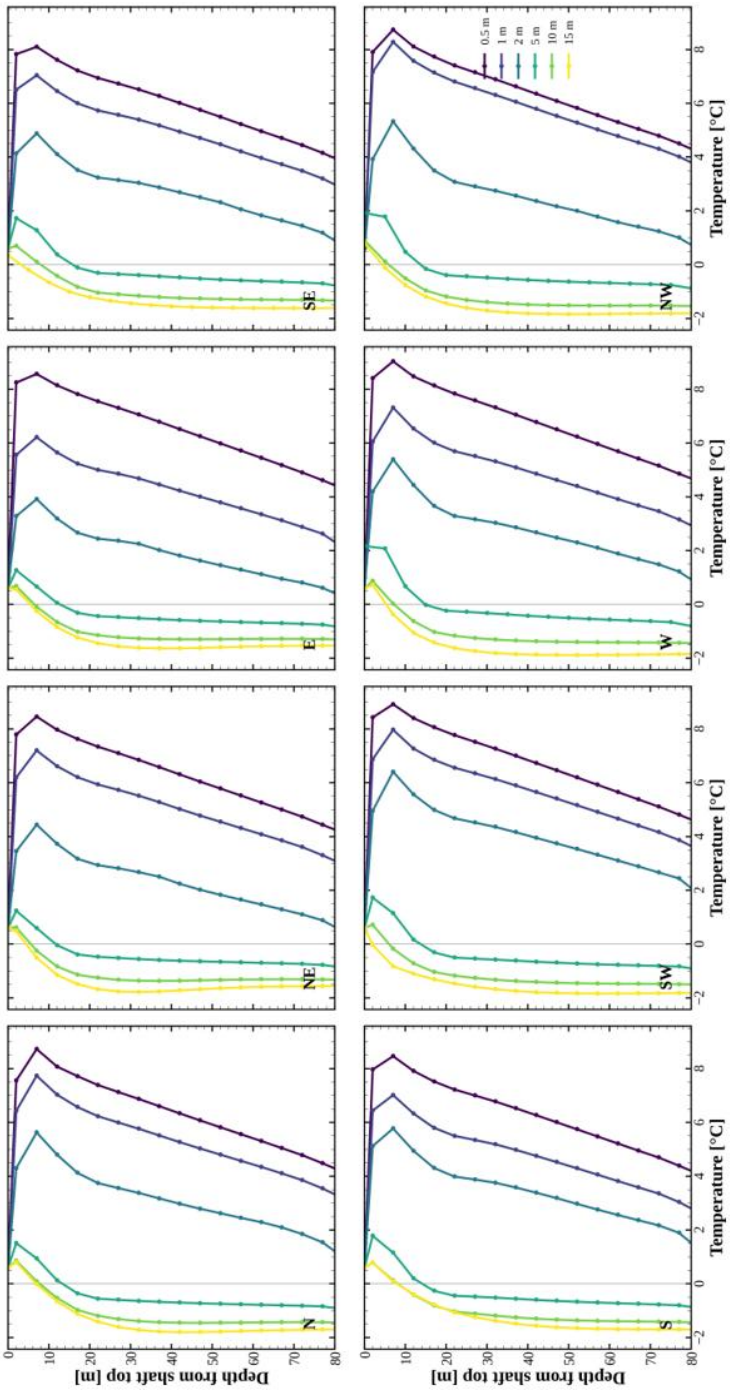


Figure 83 Vertical temperature profiles from the shaft top to its base, at six fixed distances from the shaft wall (0.5, 1, 2, 5,10 and 15 m), for each of the eight compass directions (N, NE, E, SE, S, SW, W, NW).

The eight directions behave similarly close to the shaft: at 0.5 m, they differ by no more than approximately 1–2 °C on an anomaly of 5–8 °C at the shaft top, indicating that the shaft's thermal signal dominates over the natural, aspect-driven differences documented in section 6.4.1. This directional agreement decreases somewhat with distance, though the eight curves remain broadly clustered even at the largest distances tested.

Extending the simulated period to fifteen years, using a chronologically repeated monthly air-temperature forcing rather than the two-year daily record used in an earlier, superseded version of this model, provides a substantially more robust basis for assessing how close the system comes to a steady state (Figure 84). At 1 m, the anomaly at mid-depth and at the shaft base is still rising steadily after fifteen years, with no clear flattening. At 5 m, by contrast, the equivalent time series show a marked deceleration, bending visibly toward a plateau over the final years of the simulation, consistent with the characteristic equilibration time estimated for this distance (on the order of years to a decade, section 6.3.4). At 10 m, the mid-depth and base time series also show a comparable, though less pronounced, flattening trend, while the corresponding curve near the shaft top remains essentially flat throughout the fifteen years, reflecting the dominance of the surface boundary condition rather than of the shaft itself at this combination of depth and distance. Taken together, these results show that the shaft-driven anomaly is converging toward a steady state at distances of 5–10 m within a fifteen-year timeframe, substantially more consistent with equilibrium than could be established from the two-year simulation used in an earlier stage of this work, even though full equilibrium at these distances had not yet been reached by the end of the simulated period.

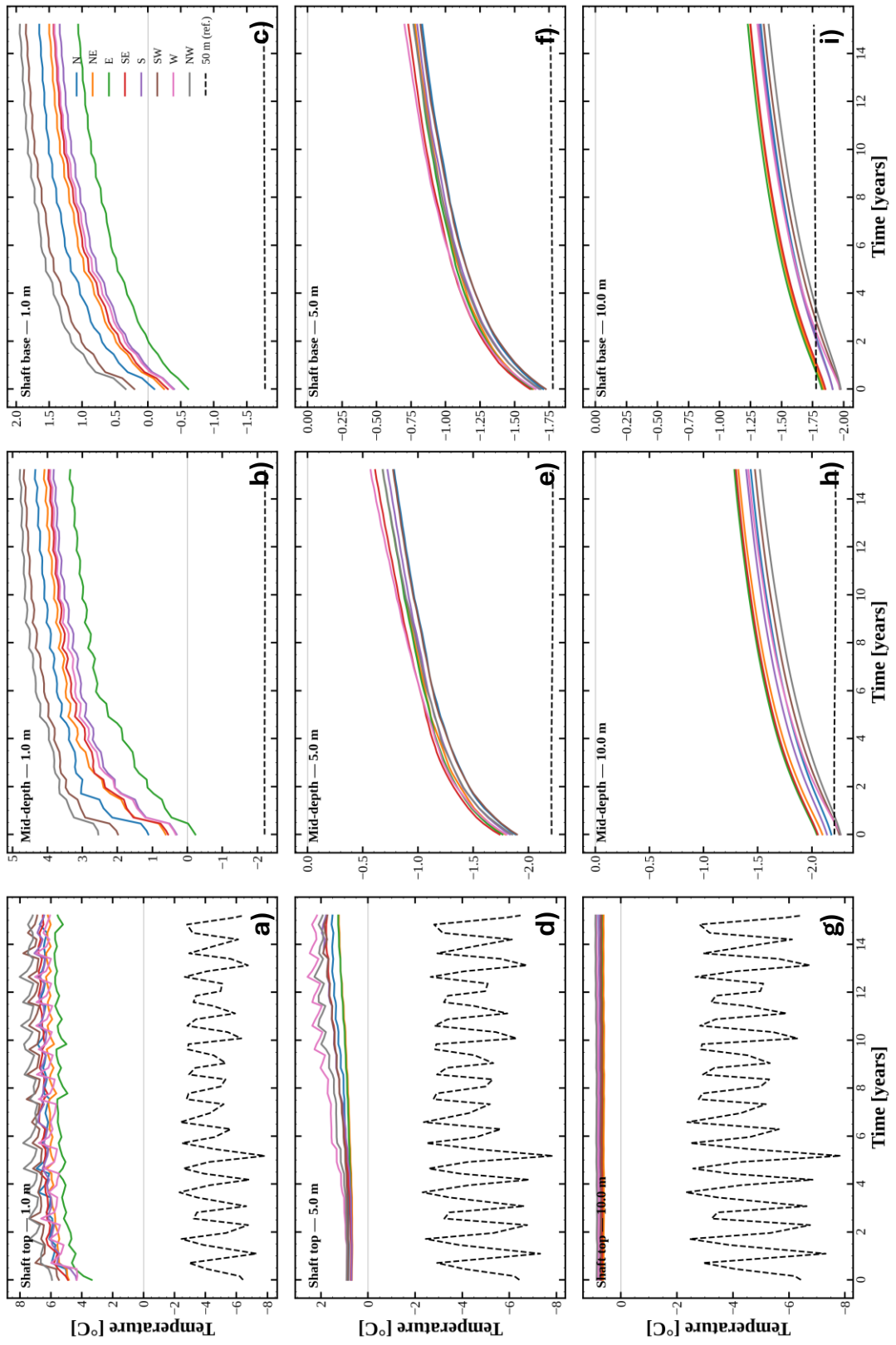


Figure 84 Simulated temperature time series over the fifteen-year period during which the shaft was thermally active, at 1 m, 5 m and 10 m from the shaft wall (rows), at shaft top, mid-depth and shaft base (columns), for the eight compass directions, compared against the 50 m reference point (dashed line).

6.5 **Discussion**

6.5.1 *A coupled Natural-Anthropogenic thermal regime*

The results presented in this chapter show two thermal controls operating simultaneously at Punta Helbronner: a natural, aspect-driven regime governing the free-field rock mass, and a persistent, infrastructure-driven heat source confined to the immediate vicinity of the shaft. Neither control alone is sufficient to characterise the site's thermal state, and their combination is the central finding of this chapter in response to Research Question 5.

The mechanism identified here, a shaft acting as a sustained heat source that measurably warms the surrounding permafrost, is not unique to Punta Helbronner. The closest documented analogue is the Sphinx observatory elevator shaft at Jungfraujoch (Wegmann & Keusen, 1998), where deep borehole monitoring during construction similarly linked shaft-induced warming to fracture-ice melting, and where thermal modelling incorporating geothermal flux and radiative forcing was used, much as in this chapter, to reconstruct the thermal perturbation induced by the shaft. The short-lived, hydration-driven heat pulse captured by the two-dimensional analysis also has a documented real-world counterpart: at the Grächen chairlift, the heat released during concrete curing was shown to locally melt fracture ice in the surrounding permafrost (Phillips et al., 2007), confirming that this transient thermal mechanism operates beyond the idealised setting of a numerical model. A further parallel comes from the Zugspitze, where excavations for cable-car infrastructure directly intersected fractures filled with decametre-thick ice lenses and year-round frozen loam (Ulrich & King, 1993), illustrating how construction activity in permafrost terrain routinely encounters the same cold, ice-bearing rock mass characterised here through monitoring and modelling.

The natural, aspect-driven component of the thermal regime documented at Punta Helbronner, pronounced differences in near-surface temperature between East, West and South exposures, and a persistent winter zero-curtain plateau restricted to the South-facing borehole, closely parallels findings from the Aiguille du Midi, the cable-car station at the opposite end of the same Panoramic Mont-Blanc line connecting to Punta Helbronner. Working on comparable steep granite rock walls in the same massif, Magnin et al. (2015) similarly found that micro-meteorology and aspect are the primary controls on near-surface rock temperature and identified a comparable thermal-insulation effect of

snow cover, delaying both winter refreezing and summer thaw of the active layer on shaded aspects. The convergence between an independent site in the same massif and the present study strengthens confidence that the aspect and snow-cover controls identified here reflect a genuine regional pattern rather than a site-specific artefact.

Taken together, these comparisons place the thermal mechanism identified at Punta Helbronner within a well-established pattern of infrastructure–permafrost thermal interaction across the Alps (Duvillard et al., 2021), while also showing that this chapter's continuous, multi-year monitoring combined with numerical modelling offers a more complete thermal characterisation than most of the earlier, largely retrospective observations this comparison draws on.

6.5.2 *Model validation and the direction of the residual bias*

The three-dimensional model was validated against an independent borehole located 37.8 m from the shaft and instrumented to 70 m depth, with a continuous daily record spanning December 2025 to June 2026 (203 days). Because the climatological component of the model forcing repeats an identical annual cycle, the comparison was performed by day-of-year rather than by calendar date, allowing the full available observation period to be used despite the mismatch between the simulated and observed years. Across all compared depths (2–67 m), the model shows a systematic residual offset of approximately −1.18 °C relative to the observed record (range approximately −0.32 to −1.64 °C), with the model consistently colder than the measured temperature at every depth. This offset represents a modest but genuine improvement over an earlier, superseded implementation of the surface boundary condition, which showed a larger mean offset of approximately −1.50 °C (range −0.66 to −1.74 °C); critically, the direction and systematic character of the bias are unchanged, and the refinement of the boundary condition alone was not sufficient to close the gap.

Independent support for the cold, permafrost-consistent conditions found at the validation borehole comes from the ARPA monitoring network described in section 6.4.1: the deepest sensors of the East-facing borehole remain predominantly below 0 °C throughout the observation period, and comparable near-zero stabilisation is observed at depth in the other ARPA boreholes. Although these instruments were not used to extract or compare model output at their specific locations, and therefore do not constitute a second quantitative validation point, the consistency between the stabilisation

temperatures they record and those observed at the external DMS borehole strengthens confidence that the cold thermal regime characterised at the validation point is representative of the wider rock mass, rather than a localised or anomalous condition specific to that single borehole.

The sign and persistence of the residual offset, even after refining the surface boundary condition, are physically informative. The model represents heat transfer as conduction only, and does not include the advective mechanisms that operate in real fractured permafrost bedrock, principally the infiltration of meltwater and the release of latent heat upon its refreezing at depth, and air circulation within open fractures. Both mechanisms act to warm the rock mass relative to a purely conductive regime, and their absence from the model is consistent with a bias in a single, unchanging direction that a refinement of the surface forcing alone cannot fully correct. This interpretation is supported by independent evidence on permafrost infrastructure elsewhere: in a nine-year monitoring study of a permafrost road embankment, Chen et al. (2020) showed that heat advection driven by subsurface water flow produced warming rates up to two orders of magnitude greater than those attributable to conduction alone, demonstrating that even limited water circulation in otherwise cold ground can dominate the local thermal balance.

This systematic, one-directional bias has a direct implication for the interpretation of the results presented in section 6.4.5: rather than undermining the modelled shaft-driven anomaly, it indicates that the true magnitude of the thermal disturbance around the shaft is more likely to be underestimated than overestimated by the present model. The radial and vertical extent of the anomaly quantified in this chapter should therefore be read as a conservative, lower-bound characterisation of the shaft's thermal influence on the surrounding permafrost, consistent with full equilibrium not yet being reached at 5–15 m within the simulated period (section 6.4.5).

6.5.3 *Model limitations and position in literature*

Beyond the conduction-only bias discussed above, four further methodological choices constrain how the results of this chapter should be read. First, the 50° slope threshold used to delimit the snow-season correction (section 6.3.4) was calibrated by raising an initial, less conservative estimate after photographic verification of widespread snow cover on comparatively steep terrain, but it could not be independently validated against a second borehole record at a comparably steep slope; the only validation borehole

available lies at approximately 21°, too gentle to constrain the upper bound of the threshold with confidence. Second, the same correction extends the snow season from October to July on the basis that the shallow record shows no sign of thaw as late as mid-June; because observations spanning August and September are not available, the exact onset and end of the protected period remain only partly constrained. Third, the fixed-temperature lower boundary condition (+1.7 °C, derived from an assumed rather than directly measured geothermal gradient) was adopted in place of a free-flux condition because the latter did not converge within a practical computation time; this pragmatic choice trades a small, difficult-to-quantify uncertainty at the base of the domain for numerical tractability, with an effect expected to be minor at the shallow-to-intermediate depths where the shaft-driven anomaly is characterised, though it has not been separately tested. Fourth, two parameters of the surface boundary condition, the offset term and the elevation lapse rate, were both carried over from the Cima Falkner implementation rather than calibrated independently at Punta Helbronner; was subsequently checked against local ARPA temperature data and found consistent (section 6.3.4), but lapse rate could not be verified in the same way, since no dataset spanning a sufficient elevation range is available at this site, and its transfer from Cima Falkner assumes broadly comparable near-surface elevation gradients.

Taken together with the limited duration of the external validation record (203 days, spanning December 2025 to June 2026 rather than a complete annual cycle; section 6.4.1) and the fact that, even after extending the simulated period to fifteen years, a residual difference from the undisturbed reference of the order of 0.7–0.9 °C persisted at 5–15 m from the shaft (section 6.4.5), these limitations place the quantitative results of this chapter closer to a first, conservative characterisation of the shaft's thermal influence than to a definitive one. None of them is expected to reverse the sign of the systematic bias identified in section 6.5.2: a more tightly bounded snow correction, a measured rather than assumed basal gradient, a locally calibrated lapse rate, or a longer validation record would refine the magnitude of the offset, not its direction.

This directionally consistent, conduction-only bias is not specific to Punta Helbronner. The same sign of disagreement, model colder than observation, emerges independently at Sas da Lech (Chapter 4), where deep borehole records below approximately 13.5 m are only reproduced once fracture-driven advection is added to an otherwise conductive framework, and is consistent with experimental evidence that advective heat transport

through open clefts and infiltrating water can warm fractured rock considerably faster than conduction alone (Hasler et al., 2011; Draebing et al., 2017; Aumer et al., 2025). The convergence of this pattern across a natural dolomite pillar and an engineered granite shaft, two different lithologies and two independently built models, suggests that the bias identified here reflects a general property of conduction-only formulations in fractured permafrost bedrock rather than a site-specific artefact, a point developed further in the cross-chapter synthesis of Chapter 7.

6.5.4 *Implication for High-Altitude Infrastructure on Permafrost*

The findings of this chapter carry two implications that extend beyond the specific case of Punta Helbronner. The first concerns the timescale over which infrastructure-driven thermal disturbance develops. Existing vulnerability assessments for Alpine infrastructure on permafrost, such as the classification framework proposed by Duvillard et al. (2021) for the French Alps, are generally informed by observed damage records or by regional climatic exposure. The results in section 6.4.5 suggest an additional, largely independent dimension: even with climatic forcing held constant, a structure's own thermal footprint can continue to grow for years after construction, since the shaft-driven anomaly modelled here was still substantially, though not yet completely, converging toward equilibrium after fifteen years of simulated activity. This self-driven, multi-year transient is conceptually distinct from, and could in principle compound with, the climatically driven warming documented for the region (section 6.2.3), and is not, to the authors' knowledge, routinely considered in existing infrastructure risk frameworks.

The second implication concerns how such disturbances are typically documented. With the partial exception of Jungfraujoch, where monitoring accompanied construction itself (section 6.5.1), most of the comparable cases discussed in this chapter such as Grächen, the Zugspitze excavations, the Val Thorens funitel pylon (Duvillard et al., 2021), were investigated only after damage or displacement had already occurred. The approach adopted here, combining multi-year monitoring with a validated numerical model prior to any observed structural response, offers a proactive alternative: a quantified, mechanistic baseline against which future changes in the thermal or mechanical behaviour of the infrastructure could be assessed, rather than a reconstruction undertaken retrospectively once damage has already occurred.

These implications also point to a practical direction not explored within the present work. Active thermal-stabilization techniques for infrastructure on permafrost, such as shallow cooling-pipe systems intended to counteract heat penetration into the ground, are currently under development for Alpine cable-car and mountain-hut foundations. Although evaluating such a mitigation strategy at Punta Helbronner falls outside the scope of this thesis, the validated three-dimensional model developed here provides a physically grounded basis on which the potential effect of such measures could be assessed in future work.

6.6 **Case study Conclusion**

This chapter has presented the Punta Helbronner cable-car station as a fully monitored and numerically modelled case of engineered infrastructure founded in permafrost-affected bedrock, addressing Research Question 5 through an integrated observational and modelling framework combining multi-year borehole monitoring, two- and three-dimensional finite-element thermal simulation, and direct validation against independent field data.

In response to Research Question 5, concerning the influence and interaction between permafrost degradation and the presence of high-altitude infrastructure, the analysis establishes that the shaft functions as a permanent, non-seasonal heat source rather than a passive structure embedded in an otherwise undisturbed thermal environment. Air temperature within the shaft never drops below approximately 3 °C at any point along its full 80 m length, even where the surrounding bedrock is independently shown to be cold enough to sustain permafrost. This heat is transmitted measurably into the surrounding rock mass, producing a thermal anomaly that decreases substantially with distance from the shaft, from several degrees within the first metre to under 1 °C beyond approximately 10 m, but that locally is superimposed on, and in places exceeds, the natural, aspect-controlled thermal regime that otherwise dominates the site. The interaction between infrastructure and permafrost at Punta Helbronner is therefore not adequately described by either control in isolation, but by their coupling: a natural cryospheric background modulated by a persistent, spatially confined anthropogenic perturbation. Critically, even after extending the simulated period to fifteen years of shaft activity, a residual difference of 0.7–0.9 °C from undisturbed conditions still persisted at 5–15 m, and independent

validation against field data indicates that the model itself is more likely to underestimate than to overestimate the true magnitude of the disturbance. The shaft's thermal influence on the surrounding permafrost should therefore be regarded as a substantially, but not yet completely, equilibrated process rather than a fixed or fully realised condition.

Two results of broader significance emerge from this chapter. First, the modelling workflow developed for the Cima Falkner rock avalanche in Chapter 5 has been successfully generalised to a structurally engineered feature absent from its original application, extending it with a snow-season correction calibrated against independent field observations; this demonstrates that the same validated numerical approach can characterise both a natural, catastrophic mass-wasting event and a slow, anthropogenic thermal perturbation within a single, internally consistent methodological framework. Second, the systematic, one-directional bias identified during validation, attributable to the absence of advective heat transport in an otherwise carefully calibrated conductive model, converges with the same sign of disagreement independently identified at Sas da Lech in Chapter 4; this convergence across two different lithologies, a natural dolomite pillar and an engineered granite shaft, and two independently built models, indicates that conduction-only thermal models applied to fractured Alpine permafrost bedrock should generally be expected to underestimate, rather than overestimate, the true thermal disturbance, a methodological caveat with relevance well beyond the present case.

The quantitative characterisation developed here constitutes a proactive baseline: a physically validated thermal reference for the site, established through continuous monitoring and independently validated modelling rather than through retrospective reconstruction, against which future changes in the site's thermal regime, or the effectiveness of any mitigation measures, could be assessed. Chapter 7 draws together the findings of all four case studies presented in this thesis, returning to the five research questions formulated in Chapter 1 to address the broader questions of methodological transferability and significance for Alpine permafrost research that motivated this work.

Chapter 7
CONCLUSION

7.1 **Summary of the thesis**

This thesis set out to investigate how warming conditions and thermo-cryogenic processes interact with rock mass structure to control instability in high-elevation, permafrost-affected rock walls, and how the same processes affect engineered infrastructure founded on permafrost bedrock. The work was organised as a progression of four case studies, each adding a layer of physical complexity to a single, internally consistent monitoring–modelling framework: idealised and real, non-permafrost geometries at Scaiùn and Monte Colodri (Chapter 3); a well-instrumented, warm-permafrost dolomite pillar with a known 2018 failure at Sas da Lech (Chapter 4); a large, poorly instrumented catastrophic rock avalanche at Cima Falkner in 2025 (Chapter 5); and an engineered cable-car shaft at Punta Helbronner, where the same thermal processes act on and are altered by human infrastructure (Chapter 6).

Read together, these four chapters do not simply juxtapose independent case studies: they trace a deliberate methodological arc. Chapter 3 isolates the purely geometric and thermo-elastic component of rock-slope deformation, deliberately excluding phase change, to build a validated baseline. Chapter 4 introduces phase-change physics and fracture-driven advection on a real, permafrost-affected geometry with known failure history, extending the one-dimensional analytical approach and cross-validating it against three-dimensional Strength Reduction Method (SRM) analysis. Chapter 5 removes the assumption of a well-instrumented site and formalises, through an episodic hydro-mechanical limit-equilibrium framework, the decoupling between slow thermal preconditioning and discrete hydrological triggering that Chapter 4 had already identified qualitatively. Chapter 6 finally transfers the entire validated approach to an anthropogenic setting, showing that a permanent, non-seasonal heat source embedded in cold bedrock can be characterised with the same rigour as a natural instability. This closes the thesis on a coherent note: the same physically grounded, validated modelling logic can describe

natural catastrophic failure and slow, human-induced thermal perturbation within a single framework.

The remainder of this chapter returns explicitly to the five research questions formulated in Chapter 1 (Section 7.2), synthesises the original contributions and methodological advances of the thesis (Section 7.3), acknowledges its limitations (Section 7.4), discusses the practical and management implications of the findings (Section 7.5), and outlines directions for future research (Section 7.6).

7.2 **Answers to the Research Questions**

Before addressing each question in turn, it is useful to recall, in one place, the key quantitative results that the following synthesis draws on: a static pre-collapse Factor of Safety consistently above 3 and a current post-collapse Factor of Safety of 1.58 at Sas da Lech; a 120 mm precipitation trigger for the 2018 Sas da Lech failure and a 0-mm-precipitation control run at Cima Falkner under which failure is delayed by several years beyond the observed August 2025 event; a systematic, depth-independent conduction-only bias of approximately −1.18 °C at Punta Helbronner; and a shaft-driven thermal anomaly there that decreases substantially within 10–15 m of the shaft, though a residual difference of 0.7–0.9 °C from undisturbed conditions still persisted at that distance after fifteen simulated years. These figures anchor the discussion that follows.

7.2.1 *RQ1 - Geometric controls on thermo-mechanical response*

RQ1: In thermally sensitive high-mountain environments, and separating geometric controls from geomechanical responses, what are the thermo-mechanical effects directly attributable to the geometry of potentially unstable rock elements?

Chapter 3 answers this question directly through parametric FEM simulations on idealized geometries and real geometries at Scaiùn and Monte Colodri, validated against GBInSAR displacement fields. The results establish that geometry is not a secondary modulator but a primary, systematic control on thermally induced deformation: isolated pillars with high vertical aspect ratios develop torsional displacement modes under asymmetric thermal forcing; convex rock walls localize thermal stress at their apex, amplifying displacement relative to planar surfaces of equal extent; and slope aspect imposes a spatial hierarchy of deformation, with sun-exposed sectors expanding earlier

and more than shaded ones. These effects were obtained under a purely thermo-elastic assumption, deliberately excluding phase change, which makes them a clean geometric signature rather than an artefact of permafrost-specific processes. This distinction matters for the rest of the thesis: it means that when torsional or asymmetric kinematics are later observed at Sas da Lech (Chapter 4) or inferred from the structural geometry of the Cima Falkner failure plane (Chapter 5), part of that signal can be attributed to geometry alone, separate from ice-related weakening.

7.2.2 *RQ2 - Modelling conductive and advective heat transport in fractured rock*

RQ2: Given the local temperature distribution in a high-altitude rock wall, how can the subsurface thermal regime be modelled in a way that accounts for both conductive and advective heat transport?

This question is addressed primarily in Chapter 4, and receives independent, convergent confirmation in Chapter 6. At Sas da Lech, standard one-dimensional conductive models correctly reproduce the attenuation of the seasonal thermal wave in the shallow, intact rock matrix, but systematically fail at depth, where structural discontinuities act as advective shortcuts for meteoric water and air, driving basal thawing beyond 13.5–14.0 m at a rate conduction alone cannot explain. The extended one-dimensional analytical framework developed in this chapter, incorporating a Gaussian spatial distribution of advective heat input centred at the fracture depth, a dimensionless latent-heat dampening factor, and a permanent negative bias representing cold-air trapping, reproduces this behaviour without the computational cost of a fully coupled three-dimensional simulation.

Chapter 6 arrives at the same physical conclusion from an entirely independent setting. There, a three-dimensional, conduction-only model of the Punta Helbronner shaft, validated against an independent 70 m borehole, shows a systematic, depth-independent residual offset of approximately −1.18 °C, with the model always colder than the observations. Because this bias does not vary in sign with depth or season, it is attributable specifically to the absence of advective mechanisms, meltwater infiltration and its latent-heat release on refreezing, and air circulation in open fractures, rather than to a calibration error. The convergence of these two independent case studies, one a natural dolomite pillar, the other an engineered granite shaft, on the same qualitative result (conduction-only models are systematically and directionally biased, always cold, in fractured

permafrost bedrock) is one of the more transferable findings of the thesis. With confirmation from only two sites, this should be read as a strong, physically well-explained pattern rather than a proven universal law; but the consistency of both the sign and the underlying mechanism, absent advective transport, across two lithologically and structurally different settings makes a purely site-specific artefact an unlikely explanation and gives a predictable sign to the error that is valuable for interpreting any conduction-only model applied to similar settings.

7.2.3 *RQ3 - Preconditioning versus triggering in permafrost rockwall collapse*

RQ3: In high-altitude environments characterised by alpine permafrost conditions, which factor predisposes a rock mass to collapse, and which acts as the ultimate triggering mechanism?

This is the question on which Chapters 4 and 5 converge most strongly, and it is the central mechanistic result of the thesis. At Sas da Lech, static SRM back-analysis shows that gravitational and structural loading alone yield a Factor of Safety consistently above 3, far too stable to explain the 2018 failure; the site was instead brought to the edge of failure by decades of climate-driven ice degradation at the zero-curtain (near 0 °C, not in the classical −3 to −8 °C frost-cracking window), which progressively exhausted shear strength and dilated the primary fracture network. The final detachment was triggered by a discrete, short-term event, a 120 mm precipitation episode in the days before collapse, generating transient hydrostatic overpressure within a discontinuity network that had already been structurally prepared over decades.

Chapter 5 formalises this same mechanism at a larger scale and, crucially, without site-specific calibration. The episodic hydro-mechanical framework developed for the 2025 Cima Falkner rock avalanche reproduces the observed failure date using strictly uncalibrated, laboratory-derived parameters, and a 0-mm-precipitation control run provides a direct, quantitative demonstration of the preconditioning–triggering decoupling: under thermal forcing alone, the modelled Factor of Safety through time, FoS(t), never drops below unity within the simulation period, and theoretical failure is delayed by several years beyond the actual August 2025 event. Only the introduction of discrete, episodic hydrostatic pulses from marginal bypass flow during intense rainstorms reproduces the correct timing. Independent three-dimensional FEM-SRM analysis corroborates this structurally: plastic strain localises spontaneously along the exact post-

event failure band without a predefined sliding surface, showing that the failure plane was an inherent structural weakness rather than an assumption imposed on the model.

Taken together, Chapters 4 and 5 answer RQ3 with the same two-stage mechanism observed at two different scales and two different levels of instrumentation: decades of thermally driven, ice-related weakening create the structural precondition for failure, but the proximate trigger is a discrete hydro-meteorological event that exploits that precondition. Neither factor alone is sufficient. This decoupling also resolves what Chapter 5 terms a "calibration trap" in existing back-analyses of permafrost rockwall failure, which typically apply the temperature-dependent ice-strength degradation established by Krautblatter et al. (2013) and extended to slope scale by Mamot et al. (2021) as a single, continuous forcing: models that do not separate the decadal and event timescales are forced into artificial parameter tuning to match observed failure dates, whereas the episodic treatment developed here reproduces the correct timing directly from physically grounded, independent constrained parameters.

7.2.4 *RQ4 - Simulating instability under progressive permafrost degradation*

RQ4: How can high-altitude instability phenomena be simulated in a way that explicitly accounts for the progressive deterioration of physico-mechanical properties with temperature, and specifically with permafrost degradation?

Chapters 4 and 5 again provide complementary answers at different scales. At Sas da Lech, three-dimensional SRM analyses show that the temperature-dependent degradation of ice-filled discontinuities, operating persistently in the zero-curtain regime rather than at extreme sub-zero temperatures, is the dominant mechanical control on residual pillar stability. The 2018 event changed the boundary conditions of the residual mass so fundamentally that the failure kinematics shifted from a localised lateral detachment to a broad, valley-facing instability; the residual pillar's current Factor of Safety of 1.58, combined with kinematic evidence of ongoing rigid-block rotation, places it on a trajectory toward frontal failure whose timing depends directly on future warming, with the RCP 8.5 scenario projected to exhaust the deep zero-curtain zone, and the residual ice-rock bridges with it, by 2100.

At Cima Falkner, the episodic limit-equilibrium framework explicitly couples two temporally separated processes rather than one continuous forcing: the slow conductive degradation of ice-rock adhesive strength, and the episodic poro-elastic recovery of

effective stress between discrete hydrological shocks. This coupling reproduces the seasonal "heartbeat" of FoS(t), with transient threshold exceedances during the precipitation years of 2023–2024 followed by winter recovery, and final, irreversible failure under a sub-maximal hydrostatic pulse in July 2025. This is a mechanistic answer to RQ4 distinct from a simple strength-reduction curve: it shows that instability under permafrost degradation is not a monotonic decline but an oscillating, episodically recoverable state until the system's recovery capacity is itself exhausted, a dynamic that static or snapshot stability analyses cannot detect.

7.2.5 *RQ5 - Permafrost degradation and high-altitude infrastructure*

RQ5: What influence or interaction exists between permafrost degradation and the presence of high-altitude infrastructure?

Chapter 6 answers this question through multi-year borehole monitoring and validated two- and three-dimensional thermal modelling of the Punta Helbronner cable-car shaft. The central finding is that the shaft acts as a permanent, non-seasonal heat source rather than a passive structure embedded in an otherwise undisturbed thermal environment: air temperature within the shaft never falls below approximately 3 °C along its full 80 m length, even where the surrounding bedrock is independently shown to be cold enough to sustain permafrost. This heat is measurably transmitted into the surrounding rock, producing a thermal anomaly that decreases substantially with distance, from several degrees within the first meter to under 1 °C beyond approximately 10 m, that is locally superimposed on, and in places exceeds, the natural aspect-controlled thermal regime. The interaction is therefore best described not by either control in isolation but by their coupling: a natural cryospheric background modulated by a persistent, spatially confined anthropogenic perturbation. Critically, even after extending the simulated period to fifteen years of shaft activity, a residual difference of 0.7–0.9 °C from undisturbed conditions still persisted at 5–15 m, and the systematic conduction-only bias discussed under RQ2 means the true magnitude of the disturbance is more likely to be under- than over-estimated by the present model.

7.2.6 *Cross-chapter synthesis: a recurring physical pattern*

Beyond the individual answers above, the five research questions are connected by a single physical narrative that becomes visible only when the four case studies are read

together. Chapter 3 establishes that geometry alone, in the complete absence of phase change, produces systematic, measurable thermo-mechanical effects (RQ1). Chapters 4 and 5 show that once phase change and permafrost degradation are introduced, instability is never explained by temperature acting as a direct cause of failure; instead, temperature governs the state of ice and water in discontinuities, which slowly precondition the rock mass, while a separate, discrete hydro-meteorological event provides the proximate trigger (RQ3, RQ4). This same two-stage, precondition-then-trigger logic reappears, transformed, in Chapter 6: there, the "preconditioning" is not thermal fatigue but the persistent, non-seasonal heat input from the shaft, and the process has not yet run to completion, an anomaly still growing rather than a discrete trigger having already acted. And underlying all of this, RQ2's findings that conduction-only models are systematically and directionally biased in fractured permafrost bedrock, first identified in a natural pillar (Chapter 4) and then independently confirmed in an engineered shaft (Chapter 6), is a methodological result that spans the natural/anthropogenic divide the thesis is built around. The four case studies are therefore not simply four applications of similar tools; they are four vantage points on the same underlying physics of thermally modulated rock-mass strength, observed at different scales, different levels of instrumentation, and, in Chapter 6, on a different kind of "instability."

7.3 **Original contributions and methodological advances**

The thesis makes the following original, methodologically transferable contributions:

1. **Slope-scale thermo-mechanical FEM validated against ground-based radar interferometry** (Chapter 3). Extending FEM simulations to the full slope scale, rather than to isolated fracture-scale models, allows direct reconstruction of LOS displacement maps comparable with GBInSAR products, bridging numerical modelling and large-scale monitoring within a single interpretative framework.
2. **An extended one-dimensional analytical heat-flow framework for fractured permafrost rock** (Chapter 4), incorporating localised fracture advection, latent-heat effects at the zero-curtain, and cold-air trapping, cross-validated against fully three-dimensional numerical modelling. This provides most of the physical realism of a coupled 3D simulation at a fraction of the computational cost.
3. **A hardware-independent thermal-compensation algorithm** (Chapter 4) that extracts a site-specific equivalent thermal expansion coefficient directly from the

phase-aligned hysteretic loop of an active displacement sensor, isolating geotechnical kinematics from thermo-elastic noise without relying on physical dummy sensors, and validated against independent Alpine crackmeter and exfoliation-monitoring datasets.

4. **An episodic hydro-mechanical limit-equilibrium framework that formally decouples thermal preconditioning from discrete hydrological triggering** (Chapter 5), building on the temperature-dependent ice-strength degradation established by Krautblatter et al. (2013) and Mamot et al. (2021) but coupling it to a time-evolving ice budget and discrete hydrostatic pulses. This resolves the calibration trap affecting continuous-forcing back-analyses in the existing literature, and reproduces an observed catastrophic failure date using uncalibrated, laboratory-constrained parameters alone.
5. **A validated three-dimensional thermal characterisation of an operating high-altitude infrastructure shaft in permafrost bedrock**, established proactively through continuous multi-year monitoring and independent validation rather than retrospectively after damage occurred (Chapter 6), together with the identification of a systematic, directionally consistent conduction-only bias with implications beyond the specific site.
6. **A single, internally consistent modelling logic transferred across natural catastrophic failure, natural slow degradation, and anthropogenic thermal perturbation**, demonstrating that the same physically grounded framework, thermal modelling coupled to temperature-dependent mechanical degradation, can characterise phenomena as different as a 2018 pillar collapse, a 2025 rock avalanche, and a permanently warm cable-car shaft.

7.4 **Limitations**

Several limitations, already flagged individually within each chapter, take on additional significance when considered together.

First, a **conduction-only bias recurs across the thesis** wherever fully coupled thermo-hydraulic transport is not explicitly modelled: the one-dimensional framework at Sas da Lech and the three-dimensional model at Punta Helbronner both shows that neglecting advective heat transport produces a systematic, one-directional underestimation of the true thermal disturbance. This is a conservative bias, not a random

error, but it means that the absolute magnitudes reported in Chapters 4 and 6 should be read as lower bounds rather than best estimates.

Second, the simplifications required to keep each modelling framework tractable are chapter specific. In Chapter 3, the thermo-elastic FEM deliberately excludes phase-change processes, plasticity, and fracture propagation, which is appropriate for isolating geometric effects but means the results cannot, by design, speak to permafrost-specific degradation. In Chapter 4, the extended one-dimensional analytical model neglects lateral heat flow and the full three-dimensional fracture network, compensated only partially by cross-validation against the three-dimensional SRM analysis. In Chapter 5, the episodic framework rests on a one-dimensional geometry that neglects lateral heat flow (yielding intrinsically conservative, colder basal temperatures than the three-dimensional FEFLOW model), on a kinematic rather than rheologically derived cubic aperture-growth law, on pore pressure applied only within the fracture rather than in the surrounding matrix, and on the assumption of spatially uniform ice thickness along the fracture plane. In Chapter 6, the 50° snow-slope threshold used in the model could not be fully validated against independent data, and the shaft anomaly had not reached equilibrium within the simulated period, meaning the reported spatial extent is itself a lower bound in time as well as in magnitude with a residual difference of 0.7–0.9 °C from the undisturbed reference still present at 5–15 m after fifteen simulated years.

Third, both Chapters 4 and 5 rely, at key validation steps, on the selection among several physically plausible parameter sets or configurations of the one that best reproduces an already-known outcome, whether the observed 2018 failure geometry at Sas da Lech (Section 4.4.7) or the 2025 failure timing at Cima Falkner (Section 5.5). This is a legitimate and standard approach in geotechnical back-analysis, and in both cases the candidate parameters were themselves constrained independently, from laboratory data, borehole observations, or literature ranges, rather than freely tuned. However, the correspondence between model output and observed outcome should be read as evidence of internal consistency between independently derived parameters and the observed failure, not as a blind, calibration-free prediction. This distinction does not weaken the physical basis of the preconditioning–trigger mechanism identified in Chapters 4 and 5, but it does mean the strength of the claim, particularly regarding failure timing at Cima Falkner, should be stated as retrospective reconstruction consistent with independent constraints, rather than as independently validated prediction.

7.5 **Practical and management implications**

Beyond their scientific content, the findings of this thesis carry direct implications for the monitoring and management of Alpine rock slopes and high-altitude infrastructure.

Early-warning value of continuous, time-resolved monitoring over snapshot assessment. The episodic FoS(t) behaviour identified at Cima Falkner, with the system oscillating close to failure across the 2023–2024 precipitation years before the final 2025 collapse, is a dynamic that static or single-epoch stability analyses cannot detect. This argues for monitoring and modelling strategies at permafrost rockwall sites that track the exhaustion of winter recovery capacity through time, rather than relying on periodic snapshot surveys, particularly at sites where thermal preconditioning is suspected but no discrete trigger has yet occurred.

A new, largely unconsidered dimension for infrastructure risk assessment. Existing vulnerability frameworks for Alpine infrastructure on permafrost are generally informed by observed damage records or by regional climatic exposure. The Punta Helbronner results show that a structure's own thermal footprint can continue to grow for years after construction even under constant climatic forcing, since the modelled shaft-driven anomaly was still substantially, though not yet completely, converging toward equilibrium after fifteen simulated years. This self-driven, multi-year transient is conceptually distinct from, and could compound with, regional climatic warming, and is not, to the author's knowledge, routinely represented in current risk frameworks.

Proactive rather than retrospective characterisation. With the partial exception of sites where monitoring accompanied construction, most comparable infrastructure cases discussed in this thesis were investigated only after damage or displacement had already occurred. The approach adopted at Punta Helbronner, continuous multi-year monitoring combined with a validated numerical model established before any observed structural response, offers a proactive alternative: a quantified, mechanistic baseline against which future changes in thermal or mechanical behaviour, or the effectiveness of mitigation measures such as active cooling-pipe systems now under development for Alpine infrastructure, could be assessed.

A conservative, not alarmist, reading of quantitative results. Because the recurring conduction-only bias identified in this thesis works in a single, predictable direction, always underestimating the true thermal disturbance, practitioners applying similar conduction-only models to fractured permafrost bedrock near infrastructure should treat

their output as a conservative lower bound on the true thermal and mechanical disturbance, not as a worst-case estimate.

7.6 **Future perspectives and recommendations**

Building on the results and limitations discussed above, several directions for future research follow directly from this thesis:

- **Fully coupled, three-dimensional thermo-hydro-mechanical modelling** that integrates fracture-driven advection explicitly at the slope scale, rather than through the analytical corrections adopted in Chapters 4 and 6, would allow the recurring conduction-only bias to be quantified rather than only bounded in sign.
- **Calibration of the cubic fracture aperture-growth law** used in the Cima Falkner episodic framework against the most recent InSAR displacement rates, to move this component of the model from a kinematic prescription toward a rheologically grounded relationship.
- **Extension of the episodic hydro-mechanical framework to additional Alpine sites** with different lithologies and structural settings, to test the generality of the preconditioning–triggering decoupling identified at Sas da Lech and Cima Falkner beyond dolomite massifs.
- **Continued long-term monitoring of both still-evolving systems identified in this thesis**: the residual Sas da Lech pillar, currently on a trajectory toward frontal failure whose timing depends on future warming pathways, and the Punta Helbronner shaft anomaly, which had not reached thermal equilibrium within the simulated period.
- **Assessment of active thermal-stabilisation measures** (e.g., shallow cooling-pipe systems) at Punta Helbronner using the validated three-dimensional model developed in Chapter 6, extending the present, purely diagnostic characterisation toward a mitigation-oriented application.
- **Development of digital-twin-style monitoring–modelling pipelines** for Alpine rock cliffs, building on the slope-scale FEM–GBInSAR integration demonstrated in Chapter 3, to support real-time or near-real-time interpretation of thermally driven deformation at instrumented sites.

Taken together, these directions extend, rather than depart from, the methodological logic developed across this thesis: physically grounded thermal and mechanical

modelling, disciplined by direct comparison against independent field data, as the basis for understanding and, ultimately, anticipating instability in Alpine permafrost rock slopes and the infrastructure built upon them.

7.7 **Closing remarks**

This thesis began, in Chapter 1, from a practical and scientific concern: steep Alpine rock slopes are structurally predisposed to failure, warming trends are shifting the thermal state of ice-bearing discontinuities, and society is increasingly exposed to the consequences through both mountain tourism and high-altitude infrastructure, at Scaiùn, Monte Colodri, Sas da Lech, Cima Falkner, and Punta Helbronner alike. The four case studies that followed were chosen to represent this exposure in its different forms: an isolated pillar overlooking a hiking trail, a large rock avalanche near frequented terrain, and a cable-car station carrying passengers through bedrock that is itself part of the hazard.

The thesis does not conclude that temperature alone causes collapse, nor that permafrost degradation makes failure predictable in a simple sense. It concludes something more specific and, for practice, more useful: that thermal and hydro-mechanical processes in Alpine permafrost rock slopes follow a recurring, physically explicable logic, slow thermal preconditioning followed by discrete triggering, or, in the case of infrastructure, a persistent thermal perturbation still working its way toward equilibrium, and that this logic can be captured by validated, physically grounded models rather than treated as an unpredictable hazard. As warming continues to drive the 0 °C isotherm deeper into Alpine rock masses, the value of this thesis lies less in the specific numerical results obtained at five sites than in demonstrating that a coherent, transferable, and falsifiable modelling framework for this class of problem is achievable, and in providing that framework, tested against independent field data, for use beyond the cases presented here.

Data Availability Statement

This thesis contains one data confidentiality restriction, detailed below.

The mechanical characterisation of the cable-car infrastructure presented in Chapter 6 (Punta Helbronner) is subject to a data confidentiality restriction. Structural and geotechnical data concerning the foundation system of the infrastructure are proprietary to the facility operator and could not be obtained or used for the purposes of this thesis.

As a result, Chapter 6 is deliberately restricted to the thermal characterisation of the rock mass hosting the infrastructure, including the two- and three-dimensional modelling of the shaft-driven thermal anomaly and its interaction with the surrounding permafrost, and does not include a mechanical or slope-stability analysis of the site, unlike Chapters 4 and 5. This restriction concerns Chapter 6 only; it does not affect the geomechanical modelling presented elsewhere in the thesis.

Reference

Anderson, R. S. (1998). Near-surface Thermal Profiles in Alpine Bedrock: Implications for the Frost Weathering of Rock. Arctic and Alpine Research, 30(4), 362–372. https://doi.org/10.1080/00040851.1998.12002911

Anderson, R. S., Anderson, S. P., & Tucker, G. E. (2013). Rock damage and regolith transport by frost: an example of climate modulation of the geomorphology of the critical zone. Earth Surface Processes and Landforms, 38(3), 299–316. https://doi.org/10.1002/esp.3330

Antonellini, M., & Mollema, P. N. (2000). A Natural Analog for a Fractured and Faulted Reservoir in Dolomite: Triassic Sella Group, Northern Italy, Marco Antonellini and Pauline N. Mollema.

Arenson, L. U., & Springman, S. M. (2005). Triaxial constant stress and constant strain rate tests on ice-rich permafrost samples. Canadian Geotechnical Journal, 42(2), 412-430. https://doi.org/10.1139/t04-111

Arenson, L. U., & Jakob, M. (2017). Permafrost-Related Geohazards and Infrastructure Construction in Mountainous Environments. In Oxford Research Encyclopedia of Natural Hazard Science. Oxford University Press. https://doi.org/10.1093/acrefore/9780199389407.013.292

Aumer, W., Hartmeyer, I., Görres, C.-M., Uteau, D., Offer, M., & Peth, S. (2025). Modeling active layer thickness in permafrost rock walls based on an analytical solution of the heat transport equation, Kitzsteinhorn, Hohe Tauern Range, Austria. Earth Surface Dynamics, 13(3), 473–493. https://doi.org/10.5194/esurf-13-473-2025

Bertoncelli, A. (2016). Permafrost, tecniche costruttive e monitoraggio nelle costruzioni: il caso di Skyway Monte Bianco. Politecnico di Torino.

Bird, R. B., Stewart, W. E., & Lightfoot, E. N. (2002). Transport Phenomena (2nd ed.). John Wiley & Sons.

Boeckli, L., Brenning, A., Gruber, S., & Noetzli, J. (2012a). A statistical approach to modelling permafrost distribution in the European Alps or similar mountain ranges. The Cryosphere, 6(1), 125–140. https://doi.org/10.5194/tc-6-125-2012

Boeckli, L., Brenning, A., Gruber, S., & Noetzli, J. (2012b). Permafrost distribution in the European Alps: calculation and evaluation of an index map and summary statistics. The Cryosphere, 6(4), 807–820. https://doi.org/10.5194/tc-6-807-2012

Boffelli, W., & Calvetti, F. (2023). Numerical Modelling of Permafrost Degradation Effects on Rock Slopes. International Journal of Civil Infrastructure. https://doi.org/10.11159/ijci.2023.008

Bommer, C., Phillips, M., Keusen, H.-R., & Teysseire, P. (2010). Construire sur le pergélisol: Guide pratique.

Bongiovanni, G., et al. (2025). Temperature and precipitation trends in the Extended European Alpine Region 1961-2020. EEAR-CLIM dataset.

Bonometti, F. N., Dattola, G., Frattini, P., & Crosta, G. B. (2026). Rockfall triggering and meteorological variables in the Dolomites (Italian Eastern Alps). Natural Hazards and Earth System Sciences, 26, 187-213.

Bosellini, A., Gianolla, P., & Stefani, M. (2003). Geology of the Dolomites.

Brondi, A., Mittempergher, M., Panizza, M., Rossi, D., Sommavilla, E., & Vuillermin, F. (1977). Note Illustrative della Carta geologica d'Italia alla scala 1:50.000, F. 028 La Marmolada.

Buckel, J., Mudler, J., Gardeweg, R., Hauck, C., Hilbich, C., Frauenfelder, R., Kneisel, C., Buchelt, S., Blöthe, J. H., Hördt, A., & Bücker, M. (2023). Identifying mountain permafrost degradation by repeating historical electrical resistivity tomography

(ERT) measurements. The Cryosphere, 17(7), 2919–2940. https://doi.org/10.5194/tc-17-2919-2023

Campedel, P., Mazzalai, L., Valcanover, E., Zumiani, M., & Zambotto, M. (2025). Cima Falkner – Dolomiti di Brenta: Eventi di crollo luglio–agosto 2025. Relazione tecnica (Trento, September 2025).

Carslaw, H. S., & Jaeger, J. C. (1959). Conduction of Heat in Solids (2nd ed.). Clarendon Press.

Carslaw, H. S., Jaeger, J. C., & Feshbach, H. (1962). Conduction of Heat in Solids. Physics Today, 15(11), 74–76. https://doi.org/10.1063/1.3057871

Carslaw, H. S., & Jaeger, J. C. (1986). Conduction of Heat in Solids (2nd ed., reprint). Oxford University Press.

Castellarin, A., Dal Piaz, G. V., Picotti, V., Selli, L., Cantelli, L., Martin, S., Montresor, L., Rigatti, G., Prosser, G., Bollettinari, G., Pellegrini, G. B., Carton, A., Nardin, M., & Geologico, S. (2005). Note Illustrative della Carta Geologica d'Italia alla scala 1:50.000, F. 059 Tione di Trento. ISPRA-Serv. Geol. d'It. https://doi.org/10.15161/oar.it/211599

Castellarin, A., Picotti, V., Cantelli, L., Claps, M., Trombetta, L., Selli, L., Carton, A., Borsato, A., Daminato, F., Nardin, M., Santuliana, E., Veronese, L., & Bollettinari, G. (2005). Note Illustrative della Carta Geologica d'Italia, Foglio n°80 Riva del Garda. In Provincia Autonoma di Trento, Servizio Geologico (Number 5). Libero Professionista.

Cathala, M., Magnin, F., Ravanel, L., Dorren, L., Zuanon, N., Berger, F., Bourrier, F., & Deline, P. (2024). Mapping release and propagation areas of permafrost-related rock slope failures in the French Alps: A new methodological approach at regional scale. Geomorphology, 448. https://doi.org/10.1016/j.geomorph.2023.109032

Cathala, Maëva, Bock, J., Abdulsamad, F., Deline, P., Josnin, J. Y., Ravanel, L., Revil, A., Richard, J., Verroust, F., & Magnin, F. (2024). Assessing the role of permafrost in the preconditioning and triggering factors of the September 2020 Crête des Grangettes rockfall (southern French Alps). Geomorphologie: Relief, Processus, Environnement , 30(3), 171–188. https://doi.org/10.4000/12yqn

Chen, L., Fortier, D., McKenzie, J. M., & Sliger, M. (2020). Impact of heat advection on the thermal regime of roads built on permafrost. Hydrological Processes, 34(7), 1647-1664. https://doi.org/10.1002/hyp.13688

Christiansen, H. H. (2005). Thermal regime of ice-wedge cracking in Adventdalen, Svalbard. Permafrost and Periglacial Processes, 16(1), 87–98. https://doi.org/10.1002/ppp.523

Cleveland, W. S. (1979). Robust Locally Weighted Regression and Smoothing Scatterplots. Journal of the American Statistical Association, 74(368), 829–836. https://doi.org/10.1080/01621459.1979.10481038

Collins, B. D., & Stock, G. M. (2016). Rockfall triggering by cyclic thermal stressing of exfoliation fractures. Nature Geoscience, 9(5), 395–400. https://doi.org/10.1038/ngeo2686

Collins, B. D., Stock, G. M., Eppes, M. C., Lewis, S. W., Corbett, S. C., & Smith, J. B. (2018). Thermal influences on spontaneous rock dome exfoliation. Nature Communications, 9(1). https://doi.org/10.1038/s41467-017-02728-1

Collins, B. D., Stock, G. M., & Eppes, M. C. (2019). Relaxation Response of Critically Stressed Macroscale Surficial Rock Sheets. Rock Mechanics and Rock Engineering, 52(12), 5013–5023. https://doi.org/10.1007/s00603-019-01832-6

Corsini, A., Pasuto, A., Soldati, M., & Corsini, A. (2018). Geomorphological investigation and management of the Corvara landslide (Dolomites, Italy). https://www.researchgate.net/publication/292221052

Costantini, M., Minati, F., Trillo, F., Ferretti, A., Passera, E., Rucci, A., Dehls, J., Larsen, Y., Marinkovic, P., Eineder, M., & Andersen, H. S. (2022). EGMS: Europe-wide ground motion monitoring based on full resolution InSAR processing of all Sentinel-1 acquisitions. In IGARSS 2022 - 2022 IEEE International Geoscience and Remote Sensing Symposium (pp. 5093-5096). IEEE.

Courtial-Manent, L., Ravanel, L., Mugnier, J. L., Deline, P., Lhosmot, A., Rabatel, A., Duvillard, P. A., & Batoux, P. (2024). 18-years of high-Alpine rock wall monitoring using terrestrial laser scanning at the Tour Ronde east face, Mont-Blanc massif. Environmental Research Letters, 19(3). https://doi.org/10.1088/1748-9326/ad281d

Crespi, A., et al. (2021). High-resolution gridded dataset of daily temperature and precipitation for Trentino-South Tyrol. Earth System Science Data Discussions, 1-27.

Croce, D. (1964). Cryonival Phenomena and Karst Phenomena in the Plateau of the Sella Group (Number 2). https://about.jstor.org/terms

Crosta, G. B. (1992). An example of unusual complex landslide: From a rockfall to a dry granular flow?

Crosta, G. B., & Agliardi, F. (2003). A methodology for physically based rockfall hazard assessment. In Natural Hazards and Earth System Sciences (Vol. 3).

De Blasio, F. V., Dattola, G., & Crosta, G. B. (2018). Extremely Energetic Rockfalls. Journal of Geophysical Research: Earth Surface, 123(10), 2392–2421. https://doi.org/10.1029/2017JF004327

Dei Cas, L., Luisa Pastore, M., Pavan, A., & Petrella, N. (2021). Geological monitoring networks for risk management close to large rock cliffs: The case history of Gallivaggio and Cataeggio in the italian Alps. Geographica Helvetica, 76(1), 85–101. https://doi.org/10.5194/gh-76-85-2021

Deprez, M., De Kock, T., De Schutter, G., & Cnudde, V. (2020). A review on freeze-thaw action and weathering of rocks. Earth-Science Reviews, 203, 103143. https://doi.org/10.1016/J.EARSCIREV.2020.103143

Dimensione Ingenierie s.r.l. (2009). Progettazione Generale - Relazione descrittiva generale.

Do Amaral Vargas, E., Velloso, R. Q., Chávez, L. E., Gusmão, L., & Do Amaral, C. P. (2013). On the effect of thermally induced stresses in failures of some rock slopes in Rio de Janeiro, Brazil. Rock Mechanics and Rock Engineering, 46(1), 123–134. https://doi.org/10.1007/s00603-012-0247-9

Doglioni, C. (1987). Tectonics of the Dolomites (Southern Alps, Northern Italy). In rnal of Structural Geology (Vol. 9, Number 2).

Draebing, D., Krautblatter, M., & Dikau, R. (2014). Interaction of thermal and mechanical processes in steep permafrost rock walls: A conceptual approach. Geomorphology, 226, 226–235. https://doi.org/10.1016/J.GEOMORPH.2014.08.009

Draebing, D. (2016). Application of refraction seismics in alpine permafrost studies: A review. In Earth-Science Reviews (Vol. 155, pp. 136–152). Elsevier B.V. https://doi.org/10.1016/j.earscirev.2016.02.006

Draebing, D., Haberkorn, A., Krautblatter, M., Kenner, R., & Phillips, M. (2017). Thermal and Mechanical Responses Resulting From Spatial and Temporal Snow Cover Variability in Permafrost Rock Slopes, Steintaelli, Swiss Alps. Permafrost and Periglacial Processes, 28(1), 140–157. https://doi.org/10.1002/ppp.1921

Draebing, D., & Krautblatter, M. (2019). The Efficacy of Frost Weathering Processes in Alpine Rockwalls. Geophysical Research Letters, 46(12), 6516–6524. https://doi.org/10.1029/2019GL081981

Draebing, D., Mayer, T., Jacobs, B., & McColl, S. T. (2022). Alpine rockwall erosion patterns follow elevation-dependent climate trajectories. Communications Earth and Environment, 3(1). https://doi.org/10.1038/s43247-022-00348-2

Duvillard, P.-A., Ravanel, L., Marcer, M., & Schoeneich, P. (2019). Recent evolution of damage to infrastructure on permafrost in the French Alps. Regional Environmental Change, 19(5), 1281–1293. https://doi.org/10.1007/s10113-019-01465-z

Duvillard, P.-A., Ravanel, L., Schoeneich, P., Deline, P., Marcer, M., & Magnin, F. (2021). Qualitative risk assessment and strategies for infrastructure on permafrost in the French Alps. Cold Regions Science and Technology, 189, 103311. https://doi.org/10.1016/j.coldregions.2021.103311

Eppes, M., & Keanini, R. (2017). Mechanical weathering and rock erosion by climate-dependent subcritical cracking. Reviews of Geophysics, 55(2), 470–508. https://doi.org/10.1002/2017RG000557

Etzelmüller, B., Czekirda, J., Magnin, F., Duvillard, P.-A., Ravanel, L., Malet, E., Aspaas, A., Kristensen, L., Skrede, I., Majala, G. D., Jacobs, B., Leinauer, J., Hauck, C., Hilbich, C., Böhme, M., Hermanns, R., Eriksen, H. Ø., Lauknes, T. R., Krautblatter, M., & Westermann, S. (2022). Permafrost in monitored unstable rock slopes in Norway – new insights from temperature and surface velocity measurements, geophysical surveying, and ground temperature modelling. Earth Surface Dynamics, 10(1), 97–129. https://doi.org/10.5194/esurf-10-97-2022

Everett, D. H. (1961). THE THERMODYNAMICS OF FROST DAMAGE TO POROUS SOLIDS.

Frattini, P., Crosta, G., Carrara, A., & Agliardi, F. (2008). Assessment of rockfall susceptibility by integrating statistical and physically-based approaches. Geomorphology, 94(3–4), 419–437. https://doi.org/10.1016/j.geomorph.2006.10.037

Fu, P., & Rich, P. M. (2002). A geometric solar radiation model with applications in agriculture and forestry. Computers and Electronics in Agriculture, 37(1-3), 25-35. https://doi.org/10.1016/S0168-1699(02)00115-1

Gianotti, F., Perello, P., & Monopoli, B. (2011). Note Illustrative della Carta geologica d'Italia alla scala 1:50.000 F. 089 Courmayeur. Servizio Geologico d'Italia - ISPRA.

Gischig, V. S., Moore, J. R., Evans, K. F., Amann, F., & Loew, S. (2011). Thermomechanical forcing of deep rock slope deformation: 1. Conceptual study of a simplified slope. Journal of Geophysical Research: Earth Surface, 116(4). https://doi.org/10.1029/2011JF002006

Gobiet, A., Kotlarski, S., Beniston, M., Heinrich, G., Rajczak, J., & Stoffel, M. (2014). 21st century climate change in the European Alps–-A review. Science of The Total Environment, 493, 1138–1151. https://doi.org/10.1016/J.SCITOTENV.2013.07.050

Greif, V., Brcek, M., Vlcko, J., Varilova, Z., & Zvelebil, J. (2017). Thermomechanical behavior of Pravcicka Brana Rock Arch (Czech Republic). Landslides, 14(4), 1441–1455. https://doi.org/10.1007/s10346-016-0784-5

Gruber, S., Hoelzle, M., & Haeberli, W. (2004). Rock-wall temperatures in the Alps: Modelling their topographic distribution and regional differences. Permafrost and Periglacial Processes, 15(3), 299-307. https://doi.org/10.1002/ppp.501

Gruber, S., & Haeberli, W. (2007). Permafrost in steep bedrock slopes and its temperatures-related destabilization following climate change. Journal of Geophysical Research: Earth Surface, 112(2). https://doi.org/10.1029/2006JF000547

Gruber, S. (2012). Derivation and analysis of a high-resolution estimate of global permafrost zonation. The Cryosphere, 6(1), 221–233. https://doi.org/10.5194/tc-6-221-2012

Guermani, A., & Pennacchioni, G. (1998). Brittle precursors of plastic deformation in a granite: an example from the Mont Blanc massif (Helvetic, western Alps). Journal of Structural Geology, 20(2–3), 135–148. https://doi.org/10.1016/S0191-8141(97)00080-1

Gunzburger, Y., & Merrien-Soukatchoff, V. (2011). Near-surface temperatures and heat balance of bare outcrops exposed to solar radiation. Earth Surface Processes and Landforms, 36(12), 1577–1589. https://doi.org/10.1002/esp.2167

HAEBERLI, W. (1973). Die Basis-Temperatur der winterlichen Schneedecke als moglicher Indikator fur die Verbreitung von Permafrost in den Alpen. Zeitschrift Fur Gletscherkunde Und Glazialgeologie, 9, 221–227. https://cir.nii.ac.jp/crid/1571417126341661056.bib?lang=en

Haeberli, W., Guodong, C., Gorbunov, A. P., & Harris, S. A. (1993). Mountain permafrost and climatic change. Permafrost and Periglacial Processes, 4(2), 165–174. https://doi.org/10.1002/ppp.3430040208

Haeberli, W., Noetzli, J., Arenson, L., Delaloye, R., Gartner-Roer, I., Gruber, S., Isaksen, K., Kneisel, C., Krautblatter, M., & Phillips, M. (2010). Mountain permafrost: Development and challenges of a young research field. Journal of Glaciology, 56(200), 1043-1058.

Hales, T. C., & Roering, J. J. (2007). Climatic controls on frost cracking and implications for the evolution of bedrock landscapes. Journal of Geophysical Research: Earth Surface, 112(F2). https://doi.org/10.1029/2006JF000616

Hales, T. C., & Roering, J. J. (2009). A frost "buzzsaw" mechanism for erosion of the eastern Southern Alps, New Zealand. Geomorphology, 107(3–4), 241–253. https://doi.org/10.1016/j.geomorph.2008.12.012

Hallet, B., Walder, J. S., & Stubbs, C. W. (1991). Weathering by segregation ice growth in microcracks at sustained subzero temperatures: Verification from an experimental

study using acoustic emissions. Permafrost and Periglacial Processes, 2(4), 283–300. https://doi.org/10.1002/ppp.3430020404

Harris, C., Mühll, D. V., Isaksen, K., Haeberli, W., Sollid, J. L., King, L., Holmlund, P., Dramis, F., Guglielmin, M., & Palacios, D. (2003). Warming permafrost in European mountains. Global and Planetary Change, 39(3–4), 215–225. https://doi.org/10.1016/J.GLOPLACHA.2003.04.001

Harris, C., Arenson, L. U., Christiansen, H. H., Etzelmüller, B., Frauenfelder, R., Gruber, S., Haeberli, W., Hauck, C., Hölzle, M., Humlum, O., Isaksen, K., Kääb, A., Kern-Lütschg, M. A., Lehning, M., Matsuoka, N., Murton, J. B., Nötzli, J., Phillips, M., Ross, N., ... Vonder Mühll, D. (2009). Permafrost and climate in Europe: Monitoring and modelling thermal, geomorphological and geotechnical responses. Earth-Science Reviews, 92(3–4), 117–171. https://doi.org/10.1016/j.earscirev.2008.12.002

Hasler, A., Gruber, S., Font, M., & Dubois, A. (2011). Advective heat transport in frozen rock clefts: Conceptual model, laboratory experiments and numerical simulation. Permafrost and Periglacial Processes, 22(4), 378-389. https://doi.org/10.1002/ppp.737

Hasler, A., Gruber, S., & Beutel, J. (2012). Kinematics of steep bedrock permafrost. Journal of Geophysical Research: Earth Surface, 117, F01016. https://doi.org/10.1029/2011JF001981

Hawkes, I., & Mellor, M. (1972). Deformation and fracture of ice under uniaxial stress. Journal of Glaciology, 11(61), 103-131.

Hilbich, C., Hauck, C., Hoelzle, M., Scherler, M., Schudel, L., Völksch, I., Vonder Mühll, D., & Mäusbacher, R. (2008). Monitoring mountain permafrost evolution using electrical resistivity tomography: A 7-year study of seasonal, annual, and long-term variations at Schilthorn, Swiss Alps. Journal of Geophysical Research: Earth Surface, 113(F1). https://doi.org/10.1029/2007JF000799

Hilbich, C., Fuss, C., & Hauck, C. (2011). Automated Time-lapse ERT for Improved Process Analysis and Monitoring of Frozen Ground. Permafrost and Periglacial Processes, 22(4), 306–319. https://doi.org/10.1002/ppp.732

Holzner, & Bertagnolli. (2012). Progettazione strutturale - Area Punta Helbronner-Relazione di calcolo strutture in cemento armato.

IPCC. (2014). Climate Change 2014: Synthesis Report. Contribution of Working Groups I, II and III to the Fifth Assessment Report of the Intergovernmental Panel on Climate Change.

Johnson, L. R., & Wenk, H. R. (1974). Anisotropy of physical properties in metamorphic rocks. Tectonophysics, 23(1–2), 79–98. https://doi.org/10.1016/0040-1951(74)90112-7

Kenner, R., Noetzli, J., Bazargan, M., & Scherrer, S. C. (2024). Response of alpine ground temperatures to a rising atmospheric 0 °C isotherm in the period 1955-2021. Science of The Total Environment, 924, 171446. https://doi.org/10.1016/j.scitotenv.2024.171446

King, L., & Kalisch, A. (1998). \"Permafrost distribution and implications for construction in the Zermatt area, Swiss Alps7th International Conference on Permafrost. Proceedings. Collection Nordicana. .

Kodama, J., Goto, T., Fujii, Y., & Hagan, P. (2013). The effects of water content, temperature and loading rate on strength and failure process of frozen rocks. International Journal of Rock Mechanics and Mining Sciences, 62, 1-13. https://doi.org/10.1016/j.ijrmms.2013.03.006

Krainer, K., Mussner, L., Behm, M., & Hausmann, H. (2020). Multi-disciplinary investigation of an active rock glacier in the sella group (Dolomites; Northern Italy). https://www.researchgate.net/publication/283880404

Krautblatter, M., & Hauck, C. (2007). Electrical resistivity tomography monitoring of permafrost in solid rock walls. Journal of Geophysical Research: Earth Surface, 112(2). https://doi.org/10.1029/2006JF000546

Krautblatter, M., Verleysdonk, S., Flores-Orozco, A., & Kemna, A. (2010). Temperature-calibrated imaging of seasonal changes in permafrost rock walls by quantitative electrical resistivity tomography (Zugspitze, German/Austrian Alps). Journal of Geophysical Research: Earth Surface, 115(2). https://doi.org/10.1029/2008JF001209

Krautblatter, M., Funk, D., & Günzel, F. K. (2013). Why permafrost rocks become unstable: A rock-ice-mechanical model in time and space. Earth Surface Processes and Landforms, 38(8), 876–887. https://doi.org/10.1002/esp.3374

Kukkonen, I. T., & Šafanda, J. (2001). Numerical modelling of permafrost in bedrock in northern Fennoscandia during the Holocene. Global and Planetary Change, 29(3–4), 259–273. https://doi.org/10.1016/S0921-8181(01)00094-7

Labus, M., & Labus, K. (2018). Thermal conductivity and diffusivity of fine-grained sedimentary rocks. Journal of Thermal Analysis and Calorimetry, 132(3), 1669–1676. https://doi.org/10.1007/s10973-018-7090-5

Ladanyi, B. (1972). "An engineering theory of creep of frozen soils." Canadian Geotechnical Journal 9.1 , 63–80.

Lague, D., Brodu, N., & Leroux, J. (2013). Accurate 3D comparison of complex topography with terrestrial laser scanner: Application to the Rangitikei canyon (N-Z). ISPRS Journal of Photogrammetry and Remote Sensing, 82, 10-26.

Legay, A., Magnin, F., & Ravanel, L. (2021). Rock temperature prior to failure: Analysis of 209 rockfall events in the Mont Blanc massif (Western European Alps). Permafrost and Periglacial Processes, 32(3), 520–536. https://doi.org/10.1002/ppp.2110

Leinauer, J., Dietze, M., Knapp, S., Scandroglio, R., Jokel, M., & Krautblatter, M. (2024). How water, temperature, and seismicity control the preconditioning of massive rock slope failure (Hochvogel). Earth Surface Dynamics, 12(5), 1027-1048. https://doi.org/10.5194/esurf-12-1027-2024

Leloup, P. H., Arnaud, N., Sobel, E. R., & Lacassin, R. (2005). Alpine thermal and structural evolution of the highest external crystalline massif: The Mont Blanc. Tectonics, 24(4), 1–26. https://doi.org/10.1029/2004TC001676

Leva, D., Nico, G., Tarchi, D., & Fortuny-Guasch, J. (2003). Temporal analysis of a landslide by means of a ground-based SAR interferometer. IEEE Transactions on Geoscience and Remote Sensing, 41(4 PART I), 745–752. https://doi.org/10.1109/TGRS.2003.808902

Leva, D., Rivolta, C., Rossetti, I. B., Kuzuoka, S., & Mizuno, T. (2005). Using a ground based interferometric synthetic aperture radar (GBinSAR) sensor to monitor a landslide in Japan.

Luetschg, M., Lehning, M., & Haeberli, W. (2008). A sensitivity study of factors influencing warm/thin permafrost in the Swiss Alps. Journal of Glaciology, 54(187), 696–704. https://doi.org/10.3189/002214308786570881

Lunardini, V. J. (1981). Heat Transfer in Cold Climates. Van Nostrand Reinhold Company.

Luque, A., Cultrone, G., Mosch, S., Siegesmund, S., Sebastian, E., & Leiss, B. (2010). Anisotropic behaviour of White Macael marble used in the Alhambra of Granada (Spain): The role of thermohydric expansion in stone durability. Engineering Geology, 115(3–4), 209–216. https://doi.org/10.1016/J.ENGGEO.2009.06.015

Magnin, F., Deline, P., Ravanel, L., Noetzli, J., & Pogliotti, P. (2015). Thermal characteristics of permafrost in the steep alpine rock walls of the Aiguille du Midi (Mont Blanc Massif, 3842 m a.s.l). Cryosphere, 9(1), 109–121. https://doi.org/10.5194/tc-9-109-2015

Magnin, Florence, Krautblatter, M., Deline, P., Ravanel, L., Malet, E., & Bevington, A. (2015a). Determination of warm, sensitive permafrost areas in near-vertical rockwalls and evaluation of distributed models by electrical resistivity tomography. Journal of Geophysical Research: Earth Surface, 120(5), 745–762. https://doi.org/10.1002/2014JF003351

Magnin, F., Josnin, J. Y., Ravanel, L., Pergaud, J., Pohl, B., & Deline, P. (2017). Modelling rock wall permafrost degradation in the Mont Blanc massif from the LIA to the end of the 21st century. Cryosphere, 11(4), 1813–1834. https://doi.org/10.5194/tc-11-1813-2017

Magnin, F., Westermann, S., Pogliotti, P., Ravanel, L., Deline, P., & Malet, E. (2017). Snow control on active layer thickness in steep alpine rock walls (Aiguille du Midi, 3842 m a.s.l., Mont Blanc massif). Catena, 149, 648–662. https://doi.org/10.1016/j.catena.2016.06.006

Magnin, F., Etzelmüller, B., Westermann, S., Isaksen, K., Hilger, P., & Hermanns, R. L. (2019). Permafrost distribution in steep rock slopes in Norway: measurements, statistical modelling and implications for geomorphological processes. Earth Surface Dynamics, 7(4), 1019–1040. https://doi.org/10.5194/esurf-7-1019-2019

Magnin, F., & Josnin, J. -Y. (2021). Water Flows in Rock Wall Permafrost: A Numerical Approach Coupling Hydrological and Thermal Processes. Journal of Geophysical Research: Earth Surface, 126(11). https://doi.org/10.1029/2021JF006394

Magnin, F., Ravanel, L., Bodin, X., Deline, P., Malet, E., Krysiecki, J. M., & Schoeneich, P. (2024). Main results of permafrost monitoring in the French Alps through the PermaFrance network over the period 2010–2022. Permafrost and Periglacial Processes, 35(1), 3–23. https://doi.org/10.1002/ppp.2209

Mamot, P., Weber, S., Schröder, T., & Krautblatter, M. (2018). A temperature- and stress-controlled failure criterion for ice-filled permafrost rock joints. The Cryosphere, 12(10), 3333–3353. https://doi.org/10.5194/tc-12-3333-2018

Mamot, P., Weber, S., Eppinger, S., & Krautblatter, M. (2021). A temperature-dependent mechanical model to assess the stability of degrading permafrost rock slopes. Earth Surface Dynamics, 9(5), 1125–1151. https://doi.org/10.5194/esurf-9-1125-2021

Marmoni, G. M., Fiorucci, M., Grechi, G., & Martino, S. (2020). Modelling of thermo-mechanical effects in a rock quarry wall induced by near-surface temperature fluctuations. International Journal of Rock Mechanics and Mining Sciences, 134. https://doi.org/10.1016/j.ijrmms.2020.104440

Matsuoka, N., & Murton, J. (2008). Frost weathering: Recent advances and future directions. In Permafrost and Periglacial Processes (Vol. 19, Number 2, pp. 195–210). https://doi.org/10.1002/ppp.620

Mayer, T., Eppes, M., & Draebing, D. (2023). Influences Driving and Limiting the Efficacy of Ice Segregation in Alpine Rocks. Geophysical Research Letters, 50(13). https://doi.org/10.1029/2023GL102951

Merrien-Soukatchoff, V., & Gasc-Barbier, M. (2023). The Effect of Natural Thermal Cycles on Rock Outcrops: Knowledge and Prospect. Rock Mechanics and Rock Engineering, 56(9), 6797–6822. https://doi.org/10.1007/s00603-023-03420-1

Messenzehl, K., Viles, H., Otto, J. C., Ewald, A., & Dikau, R. (2018). Linking rock weathering, rockwall instability and rockfall supply on talus slopes in glaciated hanging valleys (Swiss Alps). Permafrost and Periglacial Processes, 29, 135-151.

Mollaret, C., Hilbich, C., Pellet, C., Flores-Orozco, A., Delaloye, R., & Hauck, C. (2019). Mountain permafrost degradation documented through a network of permanent electrical resistivity tomography sites. The Cryosphere, 13(10), 2557–2578. https://doi.org/10.5194/tc-13-2557-2019

Mollema, P. N., & Antonellini, M. (1998). Development of strike-slip faults in the dolomites of the Sella Group, Northern Italy.

Mottaghy, D., & Rath, V. (2006). Latent heat effects in subsurface heat transport modelling and their impact on palaeotemperature reconstructions. Geophysical Journal International, 164(1), 236–245. https://doi.org/10.1111/j.1365-246X.2005.02843.x

Mufundirwa, A., Fujii, Y., Kodama, N., & Kodama, J. ichi. (2011). Analysis of natural rock slope deformations under temperature variation: A case from a cool temperate region in Japan. Cold Regions Science and Technology, 65(3), 488–500. https://doi.org/10.1016/j.coldregions.2010.11.003

Nigrelli, G., & Chiarle, M. (2023). 1991-2020 climate normal in the European Alps: focus on high-elevation environments. Journal of Mountain Science, 20(8), 2149-2163.

Nigrelli, G., et al. (2024). First national inventory of high-elevation mass movements in the Italian Alps. Computers & Geosciences, 184, 105520.

Nixon, J. F., & McRoberts, E. C. (1973). A study of some factors affecting the thawing of frozen soils. Canadian Geotechnical Journal, 10(3), 439-452. https://doi.org/10.1139/t73-037

Noetzli, J., Gruber, S., & Friedel, S. (n.d.). Modeling Transient Permafrost Temperatures below Steep Alpine Topography.

Noetzli, J., Gruber, S., Kohl, T., Salzmann, N., & Haeberli, W. (2007). Three-dimensional distribution and evolution of permafrost temperatures in idealized high-mountain topography. Journal of Geophysical Research: Earth Surface, 112(2). https://doi.org/10.1029/2006JF000545

Noetzli, J., & Gruber, S. (2009). Transient thermal effects in Alpine permafrost. In The Cryosphere (Vol. 3). www.the-cryosphere.net/3/85/2009/

Noetzli, J., Isaksen, K., Barnett, J., Christiansen, H. H., Delaloye, R., Etzelmüller, B., Farinotti, D., Gallemann, T., Guglielmin, M., Hauck, C., Hilbich, C., Hoelzle, M., Lambiel, C., Magnin, F., Oliva, M., Paro, L., Pogliotti, P., Riedl, C., Schoeneich, P.,

... Phillips, M. (2024a). Enhanced warming of European mountain permafrost in the early 21st century. Nature Communications , 15(1). https://doi.org/10.1038/s41467-024-54831-9

Offer, M., Weber, S., Krautblatter, M., Hartmeyer, I., & Keuschnig, M. (2025). Pressurised water flow in fractured permafrost rocks revealed by borehole temperature, electrical resistivity tomography, and piezometric pressure. Cryosphere, 19(1), 485–506. https://doi.org/10.5194/tc-19-485-2025

Panizza, M., Corsini, A., Ghinoi, A., Marchetti, M., Pasuto, A., & Soldati, M. (2011). EXPLANATORY NOTES OF THE GEOMORPHOLOGICAL MAP OF THE ALTA BADIA VALLEY (DOLOMITES,ITALY). 105–126. https://doi.org/DOI10.4461/GFDQ.2011.34.12

Paranunzio, R., Laio, F., Chiarle, M., Nigrelli, G., & Guzzetti, F. (2016). Climate anomalies associated with the occurrence of rockfalls at high-elevation in the Italian Alps. Natural Hazards and Earth System Sciences, 16(9), 2085–2106. https://doi.org/10.5194/nhess-16-2085-2016

Phillips, M., Ladner, F., Müller, M., Sambeth, U., Sorg, J., & Teysseire, P. (2007). Monitoring and reconstruction of a chairlift midway station in creeping permafrost terrain, Grächen, Swiss Alps. Cold Regions Science and Technology, 47(1–2), 32–42. https://doi.org/10.1016/J.COLDREGIONS.2006.08.014

Phillips, M., Wolter, A., Lüthi, R., Amann, F., Kenner, R., & Bühler, Y. (2017). Rock slope failure in a recently deglaciated permafrost rock wall at Piz Kesch (Eastern Swiss Alps), February 2014. Earth Surface Processes and Landforms, 42(3), 426–438. https://doi.org/10.1002/esp.3992

Pogliotti, P., Cremonese, E., & Morra di Cella, U. (2023). Warming Permafrost in the Western Alps: A Further Evidence of Elevation Dependent Warming? Journal of Alpine Research | Revue de geographie alpine, 111(2). https://doi.org/10.4000/rga.11784

Porter, S. c., & Orombelli, G. (1982). Late-glacial ice advances in the western Italian Alps. Boreas, 11(2), 125–140. https://doi.org/10.1111/j.1502-3885.1982.tb00530.x

R Davies, M. C., Hamza, O., & Harris, C. (2001). The Effect of Rise in Mean Annual Temperature on the Stability of Rock Slopes Containing Ice-Filled Discontinuities. PROCESSES Permafrost Periglac. Process, 12, 137–144. https://doi.org/10.1002/ppp

Raraty, L. E., & Tabor, D. (1958). The adhesion and strength properties of ice. Proceedings of the Royal Society of London. Series A, 245(1241), 184-201. https://doi.org/10.1098/rspa.1958.0076

Ravanel, L., & Deline, P. (2011). Climate influence on rockfalls in high-alpine steep rockwalls: The north side of the aiguilles de Chamonix (Mont Blanc massif) since the end of the "Little Ice Age." The Holocene, 21(2), 357–365. https://doi.org/10.1177/0959683610374887

Ravanel, L., Magnin, F., & Deline, P. (2017). Impacts of the 2003 and 2015 summer heatwaves on permafrost-affected rock-walls in the Mont Blanc massif. Science of the Total Environment, 609, 132–143. https://doi.org/10.1016/j.scitotenv.2017.07.055

Riseborough, D., Shiklomanov, N., Etzelmüller, B., Gruber, S., & Marchenko, S. (2008). Recent advances in permafrost modelling. Permafrost and Periglacial Processes, 19(2), 137–156. https://doi.org/10.1002/ppp.615

Rupp, S., & Damm, B. (2020). A national rockfall dataset as a tool for analysing the spatial and temporal rockfall occurrence in Germany. Earth Surface Processes and Landforms, 45, 1528-1538.

Sass, O., & Oberlechner, M. (2012). Is climate change causing increased rockfall frequency in Austria? Natural Hazards and Earth System Sciences, 12, 3209-3216. https://doi.org/10.5194/nhess-12-3209-2012

Savi, S., Comiti, F., & Strecker, M. R. (2021). Pronounced increase in slope instability linked to global warming: A case study from the eastern European Alps. Earth Surface Processes and Landforms, 46(7), 1328–1347. https://doi.org/10.1002/esp.5100

Scandroglio, R., Draebing, D., Offer, M., & Krautblatter, M. (2021). 4D quantification of alpine permafrost degradation in steep rock walls using a laboratory-calibrated electrical resistivity tomography approach. Near Surface Geophysics, 19(2), 241–260. https://doi.org/10.1002/nsg.12149

Scandroglio, R., Weber, S., Rehm, T., & Krautblatter, M. (2024). An empirically-derived hydraulic head model controlling water storage and outflow over a decade in degraded permafrost rock slopes (Zugspitze, D/A). EGUsphere, 2024, 1–30.

Schulson, E. M., & Duval, P. (2009). Creep and Fracture of Ice. Cambridge University Press.

Siegesmund, S., Ullemeyer, K., Weiss, T., & Tschegg, E. K. (2000). Physical weathering of marbles caused by anisotropic thermal expansion. International Journal of Earth Sciences, 89(1), 170–182. https://doi.org/10.1007/s005310050324

Smith, M. W. (1989). The frozen earth: fundamentals of geocryology.

Stocker-Mittaz, C., Hoelzle, M., & Haeberli, W. (2002). Modelling alpine permafrost distribution based on energy-balance data: a first step. Permafrost and Periglacial Processes, 13(4), 271–282. https://doi.org/10.1002/ppp.426

Stoffel, M., Trappmann, D. G., Coullie, M. I., Ballesteros Cánovas, J. A., & Corona, C. (2024). Rockfall from an increasingly unstable mountain slope driven by climate warming. Nature Geoscience, 17(3), 249–254. https://doi.org/10.1038/s41561-024-01390-9

Su, Z., Ma, Y., Tan, X., Zhang, C., Zhou, Y., Ma, X., & Zhang, D. (2024). Experimental and theoretical study of the shear strength of ice-rock interface. Cold Regions

Science and Technology, 218, 104076. https://doi.org/10.1016/J.COLDREGIONS.2023.104076

Taber, S. (1929). Frost Heaving. The Journal of Geology, 37(5), 428–461. https://doi.org/10.1086/623637

Tarchi Dario, Casagli Nicola, Moretti Sandro, Leva Davide, & Sieber Alois J. (2003). Monitoring landslide displacements by using ground-based synthetic aperture radar interferometry: Application to the Ruinon landslide in the Italian Alps. Journal of Geophysical Research, 108(B8). https://doi.org/10.1029/2002JB002204

Ulrich, R., & King, L. (1993). Influence of mountain permafrost on construction in the Zugspitze mountains, Bavarian Alps, Germany.

Valagussa, A., Frattini, P., & Crosta, G. B. (2014). Earthquake-induced rockfall hazard zoning. Engineering Geology, 182(PB), 213–225. https://doi.org/10.1016/J.ENGGEO.2014.07.009

Varnes, D. J. (1978). Slope Movement Types and Processes.

Viero, A., et al. (2013). Dynamics and mass balance of the 2007 Cima Una rockfall. Landslides, 10, 393-408.

Villarraga, C., Vaunat, J., Virely, D., & Gasc, M. (2021). Effect of thermal cycles on rock cliff deformation. Monitoring and interpretation. IOP Conference Series: Earth and Environmental Science, 833(1). https://doi.org/10.1088/1755-1315/833/1/012152

Von Raumer, J. F., & Bussy, F. (2004). Mont Blanc and Aiguilles Rouges Geology of their polymetamorphic basament.

WALDER, J., & HALLET, B. (1985). A theoretical model of the fracture of rock during freezing. Geological Society of America Bulletin, 96(3), 336.

Walter, F., Amann, F., Kos, A., Kenner, R., Phillips, M., de Preux, A., Huss, M., Tognacca, C., Clinton, J., Diehl, T., & Bonanomi, Y. (2020). Direct observations of a three million cubic meter rock-slope collapse with almost immediate initiation of ensuing debris flows. Geomorphology, 351, 106933. https://doi.org/10.1016/j.geomorph.2019.106933

Weber, S., Beutel, J., Da Forno, R., Geiger, A., Gruber, S., Gsell, T., Hasler, A., Keller, M., Lim, R., Limpach, P., Meyer, M., Talzi, I., Thiele, L., Tschudin, C., Vieli, A., Vonder Muhll, D., & Yucel, M. (2019). A decade of detailed observations (2008-2018) in steep bedrock permafrost at the Matterhorn Hornligrat (Zermatt, CH). Earth System Science Data, 11(3), 1203-1237. https://doi.org/10.5194/essd-11-1203-2019

Weber, S., Beutel, J., Dietze, M., Bast, A., Kenner, R., Phillips, M., Leinauer, J., Muhlbauer, S., Pfluger, F., & Krautblatter, M. (2025). Progressive destabilization of a freestanding rock pillar in permafrost on the Matterhorn (Swiss Alps): Hydro-mechanical modeling and analysis. Earth Surface Dynamics, 13(6), 1157-1179. https://doi.org/10.5194/esurf-13-1157-2025

Wegmann, M., & Keusen, H.-R. (1998). Recent geophysical investigations at a high alpine permafrost construction site in Switzerland. Proceedings of the Seventh International Conference on Permafrost, Collect. Nord. Vol. 57.

Whalley, W. B. (1974). The Mechanics of High-Magnitude, Low-Frequency Rock Failure, and Its Importance in a Mountainous Area. In Department of Geography, University of Reading.

Woods, A., Macciotta, R., Hendry, M. T., Stewart, T., & Marsh, J. (2021). Updated understanding of the deformation characteristics of the Checkerboard Creek rock slope through GB-InSAR monitoring. Engineering Geology, 281. https://doi.org/10.1016/j.enggeo.2020.105974

6270